UNIVERSIDAD NACIONAL AUTÓNOMA DE MEXICO
PROGRAMA DE POSGRADO EN ASTROFÍSICA
INSTITUTO DE CIENCIAS NUCLEARES

MODELOS Y OBSERVACIONES DE FLUJOS DE ESTRELLAS JÓVENES

TESIS
QUE PARA OPTAR POR EL GRADO DE:
DOCTOR EN CIENCIAS (ASTROFISICA)

PRESENTA:
ANTONIO CASTELLANOS RAMÍREZ

TUTORES:
ALEJANDRO CRISTIAN RAGA RASMUSSEN
INSTITUTO DE CIENCIAS NUCLEARES
ARY RODRÍGUEZ GONZÁLEZ
INSTITUTO DE CIENCIAS NUCLEARES

MÉXICO, CDMX, DICIEMBRE 2018

"Cause all my world's sad and weary,
all my days were windin' down.
Then you showed me a better way.
My three little girls"

A mis sobrinas: Tere, Julia y Alicia. Y a mi sobrino Rafita.

"I hope you don't mind, I hope you don't mind that I put down in words
How wonderful life is while you're in the world"

A Rosita "brazos de sol".

Agradecimientos

Me dicen el desaparecido
fantasma que nunca está.
Me dicen el desagradecido
pero esa no es la verdad.
Yo llevo en el cuerpo un dolor
que no me deja respirar.
Llevo en el cuerpo una condena
que siempre me echa a caminar.

Quiero comenzar agradeciendo a Ary Rodríguez. Él es el principal responsable de que yo haya decidido trabajar en temas del medio interestelar y realizar mi trabajo de doctorado en este campo. Todos y cada uno de los momentos que compartimos son recuerdos invaluables para mí. El primer borrador del artículo de las *superburbujas* es uno de los recuerdos más gratos de mis años en el posgrado.

A mis dos asesores, Ary y Alex Raga. Ellos son mis maestros y tutores, pero sobretodo, grandes amigos. Pienso que he sido muy afortunado en trabajar con ellos dos.

Al grupo de los Astroplasmas: Raga, Pablo, Esquivel, Fabio, Ary, Liliana y Claudio. Ellos hacen que el ambiente de trabajo durante los estudios de posgrado sea el mejor que uno pueda encontrar y han contribuído de manera importante en mi desarrollo, tanto académico como personal. Las reuniones en el café, en la casa del Ary, o en la del *jefe*, han sido momentos muy gratos de una gran familia donde todos somos partes iguales. Muchas gracias por tener siempre la puerta abierta.

Muy en especial, mi agradecimiento a Pablo por permitirme trabajar en su cubículo durante todo este tiempo. Este lugar ha sido mi hogar y tengo un gran cariño por él.

A los sinodales de esta tesis: Jorge Cantó, Susana Lizano, Sergiy Silich, Will Henney y Pablo Velázquez. Por el tiempo dedicado a leer este texto. Sus sugerencias y comentarios mejoraron de manera notable este trabajo. Muy en particular a Jorge, quien ha estado presente en todas mis evaluaciones y de quien he aprendido mucho con cada una de las observaciones y comentarios realizados a lo largo de mis estudios de posgrado.

A Bertha, por echarme siempre la mano con los trámites, la información y todo lo referente a la normatividad del posgrado.

A mis *cuates* Hugo y Alejandro. Ellos no hicieron nada relevante durante este proceso, como no sea brindarme su amistad, pero seguro me la *iban a armar* si no estaban en los agradecimientos de la tesis.

A *Rosita*, por su apoyo y amor incondicional. Por estos dos años que han sido maravillosos.

A los integrantes del ñoño-journal, por plácidos momentos de discusiones.

Tengo un enorme agradecimiento a mi *alma mater*, la UNAM. En particular al Instituto de Ciencias Nucleares, el cual ha sido mi casa durante muchos, muchos años.

Agradezco finalmente al programa de becas de posgrado del CONACYT, y al proyecto PAPIIT IN109518, los cuales me proporcionaron el apoyo económico para el desarrollo de mis estudios durante estos años.

Prefacio

Las estrellas se pueden clasificar en estrellas de baja y alta masa dependiendo de si sus masas son menores o mayores que 8 $M_\odot$. En el primer caso es sencilla su detección y se conoce relativamente bien el proceso de formación y evolución. En cuanto a las segundas, éstas son difíciles de detectar al inicio de su vida ya que se encuentran embebidas en un medio de nubes muy grandes y densas, llenas de gas y polvo, además de tener un tiempo de formación muy corto (10^4 años comparado con 10^5 años de las estrellas de baja masa) y de que la cantidad de estrellas masivas es baja, lo que implica que se conoce menos su proceso de formación.

Actualmente se piensa que las estrellas se forman en nubes moleculares a partir del colapso debido a inestabilidades gravitacionales de regiones frías de gas y polvo, con su correspondiente acreción hacia la región colapsada conocida como protoestrella. Estas nubes moleculares están formadas de una mezcla de material primigenio con gas eyectado en forma de flujos como chorros, vientos o explosiones de supernova de estrellas de generaciones anteriores. Es decir, las estrellas y el medio interestelar se encuentran atados mediante un proceso cíclico.

Los flujos estelares son inherentes en cualquier etapa evolutiva de la vida de una estrella, desde la formación de las protoestrellas, en forma de chorros (algunos con alto grado de colimación), pasando por los vientos estelares, los cuales están presentes en la mayor parte de la vida de una estrella, hasta la muerte de estas, ya sea separándose suavemente de sus capas más externas si la estrella es de baja o intermedia masa, o como una explosión violenta de supernova en el caso en que la estrella sea muy masiva.

En la década de los 50's del siglo pasado, las primeras observaciones de jets estelares vinieron de la mano de George Herbig y Guillermo Haro, quienes detectaron unas nebulosas peculiares que fueron llamadas posteriormente objetos Herbig Haro o HH. Inicialmente se pensó que estas nebulosas eran estrellas jóvenes. Sin embargo, en la década de los 70's, sus espectros fueron interpretados como provenientes de ondas de choque. Una década después, se identificó estos objetos con chorros de gas altamente colimado alimentados por estrellas jóvenes.

Paralelamente, durante las décadas de 1960 y 1970, se detectaron otros fenómenos relacionados con flujos estelares. Por ejemplo, se observaron perfiles P-Cygni, los cuáles son indicadores de fuertes vientos estelares emergiendo de estrellas jóvenes y masivas.

Los flujos de estrellas jóvenes juegan un papel importante en la evolución de su entorno y de la galaxia que las contiene. Tanto los vientos estelares como los chorros inyectan energía

al medio ambiente, lo cual modifica las condiciones físicas del medio interestelar, además de inducir fuertemente la formación estelar en el gas interestelar vecino. Estos dos fenómenos pueden crear cavidades en la nube materna a medida que los flujos estelares barren el medio por donde avanzan, generando turbulencia.

Igualmente, al final de la vida de una estrella masiva, una explosión de supernova altera el estado del medio que rodea a la estrella (y la galaxia), generando turbulencia y produciendo movimientos en el gas, alterando la composición del medio interestelar y afectando la futura formación estelar. Este fenómeno es tanto local como global, es decir, el movimiento del medio da lugar a la formación de nuevas regiones densas de gas y polvo en donde puede surgir un nuevo brote de formación estelar, dando lugar a una nueva generación de estrellas. Por otro lado, los chorros colimados contribuyen de manera fundamental en la formación de una estrella, pues permiten que una protoestrella acrete material al disminuir su momento angular a través de este tipo de flujos.

Otro proceso en donde los flujos de estrellas jóvenes juegan un papel importante es en la química del medio interestelar. Los fuertes choques producidos por los flujos tanto de estrellas masivas como de las estrellas de baja masa pueden llegar a disociar moléculas y alterar la química del medio, redistribuyéndola de manera importante. Así mismo, la turbulencia generada por estos flujos dan paso a la mezcla química del gas, alterando la distribución molecular del gas.

La formación de polvo se da principalmente en cascarones alrededor de estrellas evolucionadas como las gigantes rojas o aquellas en la rama asintótica de las gigantes (AGB) a través de la inyección de materiales esenciales para la formación de polvo, por ejemplo silicatos cristalinos y amorfos, grafito, entre otros. El polvo también se produce en cantidades menores en cascarones circumestelares de novas y nebulosas planetarias.

Debido al rápido progreso de las observaciones espectroscópicas (radio, infrarrojo, óptico), se ha podido constatar que las moléculas y el polvo se encuentran en todas partes en el Universo, salvo en las zonas muy calientes. La importancia de la química en la astronomía ha sido puesta en evidencia en los últimos tiempos dado el gran desarrollo de las observaciones milimétricas y submilimétricas.

El modelado químico del medio interestelar es fundamental para interpretar adecuadamente las observaciones astronómicas de las líneas espectrales o de las abundancias de las especies moleculares que residen en regiones del medio interestelar.

La astroquímica aborda problemas de reacciones químicas en gases astrofísicos. Toma en cuenta procesos de ionización, reacciones en fase gaseosa, interacciones entre moléculas y polvo, y efectos fotoquímicos. Es de importancia en la dinámica de algunas regiones del medio interestelar debido al hecho de que las propiedades térmicas se determinan por la abundancia

y el estado molecular/atómico/iónico de las especies. Por otro lado, la hidrodinámica afecta de forma importante la composición química del medio interestelar, ya que las tasas de reacción dependen de la densidad y la temperatura del gas.

El objetivo general de este trabajo es elaborar un estudio observacional y teórico de los flujos de estrellas jóvenes. En particular, se estudian las condiciones cinemáticas, dinámicas, y la emisión de rayos X en burbujas empujadas por el viento de estrellas masivas. También, se estudia el espectro de líneas de emisión y su variabilidad en el tiempo en objetos Herbig Haro analizando imágenes obtenidas con el Telescopio Espacial Hubble (HST) y realizando simulaciones numéricas.

Además, se presenta un código numérico que resuelve las ecuaciones de la cinética química. Éste se implementa en códigos de la dinámica de gases para estudiar la influencia de los flujos estelares en el comportamiento químico del medio interestelar.

Este trabajo de tesis está dividido por tanto en tres capítulos. El primero trata sobre burbujas generadas por vientos de estrellas masivas. En el segundo se discuten observaciones y modelos de objetos HH. Finalmente, el capítulo tres se refiere a la astroquímica. En particular a la elaboración de un código que resuelve ecuaciones de una red química con aplicaciones en la astrofísica.

En cada uno de los capítulos se han incluído los artículos que conforman cada tema y que dan nombre a las secciones de la tesis. Estos artículos se han añadido en el formato original del documento publicado por la revista correspondiente, y al inicio de cada sección se presenta un breve resumen (con los resultados obtenidos). Finalmente, se ha agregado un capítulo que contiene las conclusiones principales de los trabajos presentados en esta tesis.

Índice general

Capítulo 1

Vientos de estrellas masivas

1.1. Introducción

Las estrellas masivas, cuyo rango de masa está por arriba de 8 $M_\odot$, son importantes agentes de la evolución de las galaxias, siendo las principales responsables de la inyección de energía y metales en el medio interestelar (ISM) por medio de vientos estelares y explosiones de supernova. Estos flujos también alimentan la presión turbulenta, la cual soporta parcialmente la autogravedad de las nubes moleculares. Estas estrellas son dominantes en la determinación de la composición molecular/atómica/iónica de las nubes, puesto que controlan la emisión de fotones UV y de rayos cósmicos, los cuales son fuentes importantes de calentamiento, ionización y disociación del gas interestelar.

Las estrellas masivas tienen una importante pérdida de masa que se encuentra en el rango entre $10^{-9} - 10^{-6}$ $M_\odot$/yr (para las estrellas en la secuencia principal). La velocidad terminal de sus vientos es del orden de $\sim 10^3$ km s^{-1}. Por tanto, estas estrellas inyectan energía (en forma de energía mecánica), masa y momento de forma contínua a través de vientos estelares la mayor parte de su vida y en forma de supernova al final de su evolución. Los flujos eyectados producen ondas de choque, las cuales al propagarse en el medio interestelar comprimen y calientan el material apilándolo en un cascarón de material denso.

En general este tipo de estrellas se encuentran en grupos de estrellas de distintas masas y tamaños denominados cúmulos estelares. La combinación de los fuertes vientos individuales dentro del cúmulo produce eyecciones de material denominado "viento del cúmulo". La estructura alimentada por el viento recibe el nombre de "burbuja" o "superburbuja", dependiendo de si la fuente es una estrella masiva individual, o si es un cúmulo de estrellas masivas. Las burbujas típicamente presentan un tamaño de unas pocas decenas de parsecs, mientras que las superburbujas presentan un tamaño $\sim 10 - 100$ pc.

Las burbujas empujadas por el viento de una estrella individual evolucionan junto con ésta. Mientras la estrella se encuentra en la fase de secuencia principal va generando una burbuja de gas coronal en su entorno. Cuando la evolución de la estrella llega a la fase de la supergigante roja, la masa perdida se expande en la región barrida por el viento generado por la estrella en la fase previa. Finalmente, cuando la estrella masiva evoluciona a la fase de

Wolf-Rayet, el viento generado por ésta barre el material del viento de la supergigante roja, formando una nueva burbuja.

Una vez que la estrella masiva ha formado una región H II (la zona en donde el gas es fotoinizado por la radiación UV de la estrella) la burbuja coronal comienza a expandirse a través del gas ionizado. En este trabajo se considera por separado (como es común, ver Weaver et al. 1977; Chu & Mac Low 1990) el concepto de burbuja, independiente de las regiones fotoionizadas. Para una discusión acerca de esto también se pueden revisar Arthur (2009) y Raga et al. (2012).

El término burbuja fue acuñado por vez primera por Castor et al. (1975). Los primeros modelos de estas estructuras se realizaron, independientemente, bajo dos hipótesis: a) conservación de momento (Steigman et al., 1975), donde el viento estelar afecta directamente el cascarón de la burbuja cediéndole momento, y b) conservación de energía (Dyson & de Vries, 1972; Castor et al., 1975), en donde el viento estelar es chocado adiabáticamente, aumentando la temperatura e incrementando la presión, misma que es responsable de la expansión del cascarón.

El viento, de una estrella individual o de cúmulo, al interactuar con el medio circundante produce ondas de choque que barren y calientan el material, formando un cascarón en expansión. El efecto generado por estos vientos consiste en un patrón de dos choques: el choque principal, que barre el medio, acelerándolo, comprimiéndolo y calentándolo; y el choque interno o de reversa, que desacelera el viento de la estrella (cúmulo), calentando el material y comprimiéndolo también.

Para el caso tanto de la emisión UV como de rayos X, el modelo de Weaver et al. (1977) es el más completo (ver también Chu & Mac Low 1990). Este modelo supone un medio homogéneo y ha sido considerado el modelo estándar de burbujas.

Básicamente las estructuras de una burbuja o de una superburbuja son muy similares. Éstas se detallan a continuación (ver esquema en la Figura 1.1). Sus elementos son:

i) Una región de viento libre, la cual está formada por el viento sin perturbar (en el caso de un cúmulo estelar esta región se encuentra fuera del radio del cúmulo, en donde los vientos estelares, luego de haber interaccionado entre ellos forman un viento de cúmulo).

ii) Una región de viento chocado por el choque interno. Este es un gas coronal y emite en rayos X.

iii) La zona externa, formada por el medio interestelar chocado que ha barrido el choque principal (cascarón). Esta es la región más densa de la burbuja y emite tanto en rayos X suaves como en el óptico. Cuando el cascarón se enfría, emite solamente en el óptico.

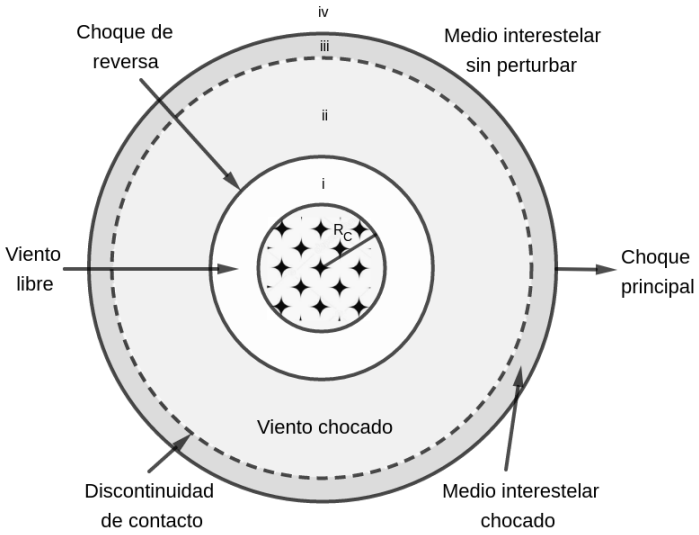

Figura 1.1: Diagrama de una superburbuja producida por un cúmulo de estrellas masivas. Se muestra: i) la región de "viento de cúmulo" libre, ii) la región de viento chocado por el choque de reversa, iii) la región de medio interestelar chocado por el choque principal y iv) el medio interestelar sin perturbar. Para el caso de una burbuja producida por una sola estrella masiva, $R_c \sim R_*$, el radio estelar.

IV) El medio interestelar sin perturbar, afuera del cascarón barrido.

El modelo ha sido comparado con observaciones de superburbujas, dando como resultado que la emisión de rayos X observada siempre excedía las predicciones teóricas (Chu & Mac Low, 1990; Wang & Helfand, 1991).

Basada en las observaciones de (Rosado et al., 1981, 1982) y Rosado (1986), Oey (1996a) propone dos tipos de superburbujas: de alta y de baja velocidad. Las de alta velocidad están caracterizadas por una velocidad de expansión del cascarón $v_S \geq 25$ km s^{-1}. Para exceder esta velocidad en superburbujas típicas (de 100 pc de radio aproximadamente), es necesario tener una aceleración adicional, como por ejemplo una explosión de supernova. La energía liberada por la supernova proporciona una fuente de calentamiento (del gas dentro de la superburbuja) adicional, lo que puede explicar el exceso de rayos X en las observaciones. Así mismo, el "empujón" debido a la explosión produce una aceleración al cascarón, lo que puede explicar las velocidades observadas. Estos efectos también explican la morfología observada de algunas superburbujas (ver el caso de DEM L50 y DEM L152 más abajo en el texto).

En el caso del modelo estándar de burbujas, cuando se añade una explosión de supernova, no se toma en cuenta el enriquecimiento de la metalicidad debido a este evento. Para un plasma en un rango de temperatura entre 10^6 y 10^7 K, la emisividad de los rayos X es proporcional a la metalicidad. De acuerdo con el trabajo de Silich et al. (2001) para un

plasma cuya metalicidad aumenta por un factor 10, digamos por una explosión de supernova, entonces debe haber un aumento proporcional en la luminosidad de los rayos X suaves.

Según este modelo, la metalicidad no influye de manera relevante en el aspecto, tamaño, velocidad de expansión y cantidad de materia barrida por la evolución de la superburbuja. Sin embargo, como se puntualizó arriba, el efecto de la metalicidad es aumentar la emisividad de rayos X de la burbuja, dejando su estructura interior sin alterar. No obstante, estas hipótesis aun no han podido ser verificadas, puesto que se carece de evidencia observacional de enriquecimiento de metales en la emisión de rayos X de las superburbujas.

La detección de manera directa de la emisión de rayos X de las burbujas empujadas por el viento de una estrella masiva es en general difícil, puesto que suelen estar rodeadas de material poco denso y no muy caliente, el cual presenta baja emisión en rayos X. Se han detectado este tipo de estructuras para estrellas Wolf-Rayet (Chu et al., 2003; Toalá et al., 2015), ya que sus vientos suelen ser más densos que los de las estrellas O. NGC 6888 (Gruendl et al., 2000; Moore et al., 2000; Toalá et al., 2016) y S308 (ver Chu 2008 y referencias ahí) son las únicas burbujas de este tipo en ser detectadas en óptico y rayos X.

Por otro lado, se han detectado una buena cantidad de superburbujas empujadas por vientos de cúmulos de estrellas masivas en donde adicionalmente ha ocurrido alguna explosión de supernova. En algunos casos, como son N 70 y N 185 (Reyes-Iturbide et al., 2014; Rodríguez González et al., 2011), de acuerdo con las observaciones la explosión de la supernova ha ocurrido cerca del centro del cúmulo. Por tanto, se observa una morfología esférica, como se muestra en la Figura 1.2, para el caso de N 70. En otros casos, como los de DEM L50 y DEM L152 (Jaskot et al., 2011) la explosión de supernova ha ocurrido cerca del borde del cúmulo, por lo que se observa una morfología que contiene una protuberancia en el lugar donde ha ocurrido la supernova (ver Figura 1.3).

En este primer capítulo de la tesis se pretende explorar de manera numérica los efectos de la metalicidad, conducción térmica y la detonación de una supernova en la emisión de rayos X en superburbujas empujadas por los vientos de estrellas masivas en un cúmulo, a fin de entender de una mejor manera la emisión observada en algunas de estas superburbujas.

1.2. The soft and hard X-rays thermal emission from star cluster winds with a supernova explosion

En este capítulo vamos a presentar una serie de modelos numéricos con la finalidad de explorar los efectos de explosiones de supernova, de la metalicidad, así como de la conducción térmica en la emisión térmica de rayos X (suaves y duros) en una superburbuja de cúmulo

Figura 1.2: Superburbuja N70. Se forma por la interacción del viento de 13 estrellas masivas de acuerdo con Oey (1996b). La burbuja presenta una morfología esférica, así como una alta probabilidad de contener una explosión de supernova cerca del centro del cúmulo. En la imagen se presenta una composición de tres colores: Óptico (B) 429 nm, (V) 554 nm y Hα. Créditos: ESO

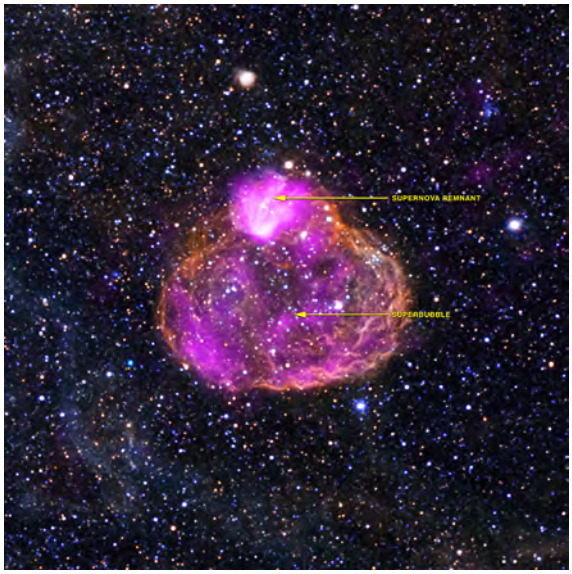

Figura 1.3: Superburbuja DEM L50. Se forma por interacción del viento de 18 estrellas masivas de acuerdo con Jaskot et al. (2011). Se observa una morfología semielíptica con una protuberancia en la parte superior, lejos del centro del cúmulo. De acuerdo con las observaciones, se ha presentado una explosión de supernova en esta región. La composición de la imagen es: rayos X (E= 0.3–2.8 keV) magenta; Óptico, Hα + [N II] rojo y [O III] verde. Créditos: rayos X, NASA/CXC/Univ of Michigan/A.E.Jaskot, Óptico, NOAO/CTIO/MCELS

masivo de estrellas.

En este artículo mi contribución ha sido en la elaboración y simulación de los modelos, la busca de parámetros adecuados para llevar a cabo las simulaciones, la revisión de la bibliografía y la búsqueda de objetos observacionales para comparar con las simulaciones.

Los vientos de estrellas masivas dentro de un cúmulo estelar aportan una cantidad considerable de energía al medio interestelar, los cuales al interaccionar entre ellos generan un viento de cúmulo cuya expansión barre y calienta el medio circundante, formando una estructura llamada *superburbuja*. La superburbuja está formada de gas coronal, y emite en rayos X. A partir de los modelos tradicionales de burbujas empujadas por vientos de estrellas masivas (Weaver et al., 1977; Chu & Mac Low, 1990), no se puede explicar la emisión en rayos X detectadas observacionalmente en algunos cúmulos de estrellas masivas.

Se ha sugerido (Chu & Mac Low, 1990) que la presencia de una explosión de supernova dentro del cúmulo estelar en los modelos teóricos, podría producir el efecto necesario para aumentar la temperatura de la superburbuja y generar una emisión de rayos X similar a la observada (ver por ejemplo Reyes-Iturbide et al. 2014; Rodríguez González et al. 2011; Jaskot et al. 2011).

El objetivo de nuestros modelos numéricos es explicar los valores de las luminosidades en rayos X suaves (en el rango $0{,}2-2$ keV) observadas en algunas superburbujas de cúmulos de estrellas, como por ejemplo: N70 (Rodríguez González et al., 2011), N185 (Reyes-Iturbide et al., 2014), DEM L50 y DEM L152 (Jaskot et al., 2011), con luminosidades: $L_x \approx 2.4{\times}10^{35}$, $2.1{\times}10^{35}$, $2{,}0-4{,}0\times10^{36}$ y $5{,}4-5{,}7\times10^{35}$ erg s^{-1}, respectivamente. En los primeros dos casos, las observaciones muestran una aparente explosión de supernova en el centro del cúmulo, mientras que los dos últimos presentan explosiones de supernova fuera del centro. Además del incremento de la luminosidad X, este hecho también afecta la morfología de la superburbuja; en los dos primeros casos ésta es esférica, mientras que en los últimos dos es de tipo semielíptica con una protuberancia en la región cercana a la explosión.

Las simulaciones numéricas se llevaron a cabo utilizando un código numérico paralelizado que resuelve las ecuaciones de la dinámica de gases en una malla cartesiana 3D uniforme, el cual incluye pérdidas radiativas (una función de enfriamiento atómica) y la conducción térmica.

La simulación tiene 15 estrellas masivas emitiendo vientos, colocadas aleatoriamente dentro del radio del cúmulo. Los vientos son impuestos en regiones esféricas, cuyo radio debe ser resuelto adecuadamente por la malla computacional para garantizar la esfericidad del viento. Se supone que todas las estrellas tienen la misma tasa de pérdida de masa y los vientos poseen la misma velocidad.

Para tener una visión global del efecto de la explosión de la supernova en la emisión de

rayos X, la imposición de la supernova dentro de la burbuja formada por los vientos se efectúa a 4 diferentes tiempos. Además, se han calculado modelos donde se varía la posición de la explosión: uno en el centro del cúmulo y dos modelos con la explosión fuera del centro (cerca del radio del cúmulo y a la mitad de éste). En la explosión de la supernova se considera una inyección de energía total, de la cual la mitad se inyecta como energía cinética y el resto como energía térmica (Rodríguez González et al., 2011).

Finalmente, para explorar el efecto de la metalicidad en la emisión de rayos X, se han realizado algunas simulaciones con las mismas metalicidades para los tres componentes (el medio interestelar, los vientos estelares y la supernova) y algunos modelos con metalicidades diferentes. También, se han calculado un par de modelos con conducción térmica.

Los resultados obtenidos de nuestras simulaciones numéricas son los siguientes:

- Las luminosidades en rayos X suaves para los modelos sin conducción térmica y con la explosión de la supernova en el centro del cúmulo, tanto en el caso de metalicidad homogénea como metalicidad variable, son consistentes con los valores observacionales para el caso de N 70 y N 185. Sin embargo, el pico de luminosidad no es lo suficientemente intenso para alcanzar los valores observados en DEM L50 y DEM L152 .

- En los modelos con conducción térmica y con explosión de la supernova en el centro del cúmulo se incrementan los valores de la luminosidad, sin alcanzar los valores que intentamos reproducir.

- En los modelos con la explosión de la supernova lejos del centro, el incremento de la luminosidad es mayor. En particular, para el caso con la supernova en el borde del cúmulo, la luminosidad de rayos X suaves alcanzada por los modelos numéricos coincide en buena medida con las luminosidades observadas reportadas para DEM L50 y DEM L152.

Monthly Notices of the ROYAL ASTRONOMICAL SOCIETY

MNRAS **450,** 2799–2811 (2015) doi:10.1093/mnras/stv795

The soft and hard X-rays thermal emission from star cluster winds with a supernova explosion

A. Castellanos-Ramírez,[1⋆] A. Rodríguez-González,[1] A. Esquivel,[1] J. C. Toledo-Roy,[1] J. Olivares[2,3] and P. F. Velázquez[1]

[1]*Instituto de Ciencias Nucleares, Universidad Nacional Autónoma de México, Apdo. Postal 70-543, 04510 México, D.F., Mexico*
[2]*Université Grenoble Alpes, IPAG, F-38000 Grenoble, France.*
[3]*CNRS, IPAG, F-38000 Grenoble, France*

Accepted 2015 April 9. Received 2015 April 8; in original form 2014 July 3

ABSTRACT

Massive young star clusters contain dozens or hundreds of massive stars that inject mechanical energy in the form of winds and supernova explosions, producing an outflow which expands into their surrounding medium, shocking it and forming structures called superbubbles. The regions of shocked material can have temperatures in excess of 10^6 K, and emit mainly in thermal X-rays (soft and hard). This X-ray emission is strongly affected by the action of thermal conduction, as well as by the metallicity of the material injected by the massive stars. We present three-dimensional numerical simulations exploring these two effects, metallicity of the stellar winds and supernova explosions, as well as thermal conduction.

Key words: stars: winds, outflows – ISM: bubbles – open clusters and associations: general – galaxies: star clusters: general – X-rays: ISM.

1 INTRODUCTION

It is well known that massive O-B-type stars inject a considerable amount of mechanical energy into the interstellar medium (ISM), in form of stellar winds or supernova (SN) explosions. The energy input by these events is sufficient to drive strong shocks that expand into the ISM generating a structure called bubble.

The model, proposed by Weaver et al. (1977) and later expanded by Chu & Mac Low (1990) and Chu et al. (1995), is considered the standard model of bubbles driven by stellar winds. It considers the injection of mechanical energy to the ISM from stellar winds that results in the formation of a bubble. This bubble is surrounded by a cool shell of ISM material that has been swept by the expanding shock front. The shocked (and thereby heated and compressed) material in the interior of the bubble emits considerably in X-rays, whereas the outer, cooler shell emits at optical wavelengths.

The original Weaver et al. (1977) model considers a single stellar wind source. Sometime later, in order to explain what is now known as *superbubbles*, the model was extended to include multiple wind sources (see Chu & Mac Low 1990; Chu et al. 1995; Cantó, Raga & Rodríguez 2000; Silich, Tenorio-Tagle & Rodríguez-González 2004).

The simplest model of superbubble formation is as follows. Consider a cluster with N stars each having different mass-loss rate $\dot{M}_{\mathrm{w},i}$ and a wind velocity $v_{\mathrm{w},i}$. Since the stars inject mechanical energy in the form of stellar winds, the total mechanical luminosity is given by

$$L_{\mathrm{w}} = \sum_{i=1}^{N} \frac{1}{2} \dot{M}_{\mathrm{w},i} v_{\mathrm{w},i}^2 \, .$$

At first, the stellar winds collide with each other and with the environment inside the cluster radius. Thus, the space between the stars is filled with hot shocked material from the winds. This happens until a stationary flow is established, giving rise to a common cluster wind that forms a *supershell*. As this supershell expands through the surrounding ISM, it creates a superbubble structure with the following structure (Weaver et al. 1977; Rodríguez-González et al. 2011; Velázquez et al. 2013):

(i) The innermost region located near the stars (where their winds collide) produces thermal hard X-ray emission (if the stellar winds have terminal velocities larger than 1000 km s^{-1}), and driving the expansion of the bubble through a pressure difference between the hot and dense interior and the colder and less dense environment.

(ii) After the individual winds from the stars coalesce into a cluster wind, it expands freely from the cluster radius outwards. In this zone, X-ray emission is important only close to the cluster radius, and it consists mostly of soft X-rays.

(iii) Behind the main shock pushing into the ISM a reverse shock is formed. The reverse shock encounters the freely expanding wind and compresses and heats it to soft X-ray-emitting temperatures.

⋆ E-mail: antonio.castellanos@nucleares.unam.mx

The region filled by shocked wind is quite extended and dominates the emission in X-rays, particularly in the soft energy bands.

(iv) The outermost region of the superbubble consists of a shell of shocked ISM that has been swept up by the main shock. Beyond this zone, there is only unperturbed ISM material.

The original wind-blown bubble (WWB) model proposed by Weaver et al. (1977) overpredicts the X-ray luminosity. One reason is that this model includes thermal conduction and in consequence produces a denser interior that in the case without it, which in turn increases the X-ray luminosity. Furthermore, the WWB models do not take into account the radiative losses within the cluster radius, and this can have a significant impact on the luminosity (see Rodríguez-González et al. 2011). Recent examples of this are the works of Dunne et al. (2003) and Reyes-Iturbide et al. (2009), which predict X-ray luminosities that exceed that of the observations by about one order of magnitude.

On the other hand, there are others models that predict an X-ray emission that underestimates the observed values (for instance, see the work of Harper-Clark & Murray 2009; Rogers & Pittard 2014, in which only the cluster wind region is considered), a problem for which different solutions have been explored. Chu & Mac Low (1990) proposed that in order to increase the luminosity of X-rays (so as to match the observations) one should consider shock waves produced by the explosion of SNe inside the star cluster. Stevens & Hartwell (2003) presented models where the luminosity of soft X-rays is obtained as a function of the mass-loss rate, the cluster radius and the wind terminal velocity. They do not take into account mass loading, but they consider it can be relevant for the study of soft X-rays in this type of massive clusters. The work of Silich et al. (2001) deals with the effect on the X-ray emission of the high metal content injected by the massive stellar winds and the SN remnants. Rodríguez-González et al. (2011) showed that SNe occurring near the centre of the cluster are not capable of reproducing (completely) the luminosity observed in X-rays, and neither do they help explain the kinematics of the shell (without consider thermal conduction). They instead showed that off-centre SN explosions (for N70 and N185, see also Reyes-Iturbide et al. 2014) could help explain the two or three orders of magnitude difference between the luminosity observed and the standard model predictions. However, in these models the X-ray luminosity agrees with the observed value for only ∼10 000 yr, making the probability of observing them in this regime rather low. On the other hand, Velázquez et al. (2013) presented models of the M 17 superbubble where they considered the contribution of the gas of the parental cloud in the evolution. They showed that the mass loading from the parental cloud can help increase the luminosity of soft X-rays by up to an order of magnitude. In such work, neither the metallicity nor thermal conduction was considered.

The Large Magellanic Cloud (LMC) is filled with superbubbles with important soft X-rays emission. Some of these superbubbles (for instance, DEM L50 and DEM L152; see Jaskot et al. 2011) show evidence for off-centre SN events that seem to interact with the external shell pushed by the stellar winds. In the observations made by Jaskot et al. (2011), the gas of the SN remnant is still seen. This remnant is located close to the superbubble edge. These objects have luminosities up to an order of magnitude higher than those predicted by the model of Weaver et al. (1977).

Moreover, the numerical models that appear in Jaskot et al. (2011) produce luminosities that are two orders of magnitude lower than the observations ($\sim 10^{36}$ erg s^{-1}). Therefore, the authors explored the effect of the metallicity and of mass loading by clouds to bridge the luminosity deficit in soft X-rays. They calculated the mass of metal-enriched material injected by the SN explosions (Maeder 1992; Oey & Massey 1995; Silich et al. 2001; Silich, Tenorio-Tagle & Añorve-Zeferino 2005; Añorve-Zeferino, Tenorio-Tagle & Silich 2009) and found that metallicities from 3 to 10 times solar can be achieved, and using the equations of Silich et al. (2001), they concluded that the effect is not sufficient to account for the differences. They conclude that the main mechanism that can explain such an important enhancement of the total X-rays luminosity is mass loading.

Recently, Rogers & Pittard (2014) presented a study of the soft X-ray emission during the various evolutionary stages of massive stars embedded in a dense giant molecular cloud (GMC), going through the red supergiant and Wolf–Rayet stages up to the SN phase. They showed that the inclusion of the GMC results in a short-lived attenuation of the X-ray emission of the cluster, during the time before an important fraction of the material is carried away from the wind interaction region. After this occurs, the luminosity remains practically constant.

The X-ray emission of a star changes substantially as it goes through distinct evolutionary stages. For instance, the X-ray luminosity drops abruptly during the red giant phase and increases substantially once in the Wolf–Rayet phase. Rogers & Pittard (2014) show that, in spite of the differences between their models and some observations, their results agree reasonably with other observations, such as the case of M 17 and the Rosette Nebula. They found that the emission produced by their model during the early wind-dominated phase is smaller compared to the prediction from the standard model (Weaver et al. 1977; Chu & Mac Low 1990), but larger than the emission expected in models that only consider the emission at the interaction region of the winds of massive stars (the cluster wind). Finally, for stars in the main sequence, they found luminosities two or three orders of magnitude above those predicted by the standard model, lasting for more than 4.5 kyr.

In this work, we present a series of numerical models exploring the effects of SN explosions, metallicity and heat conduction in the thermal soft and hard X-ray luminosity of a massive star cluster. The paper is organized as follows: in Section 2 we present the numerical set-up of our models, describe the implementation of the thermal conduction and the metallicity in the gas dynamics equations, and in Section 3 we show the resulting synthetic emission in the soft and hard X-ray bands as well as a brief discussion of our results. In Section 4, we have made some comparisons of our numerical models with four interesting observed bubbles. Finally, a summary is given in Section 5.

2 THE NUMERICAL SIMULATIONS

With the purpose of exploring the effects of the interaction and influence of the SN explosions and metallicity, as well as thermal conduction in the cluster stellar winds, we performed a series of numerical simulations, and estimated the soft and hard X-ray emission that would be produced.

We used the HUACHO code (see Esquivel et al. 2009; Raga et al. 2009) to perform all numerical simulations. The code solves the hydrodynamic equations (1)–(3) on a three-dimensional uniform Cartesian mesh, using a second-order finite volume method with HLLC fluxes (Toro, Spruce & Speares 1994) and a piecewise linear reconstruction of the variables at the cell interfaces with a minmod

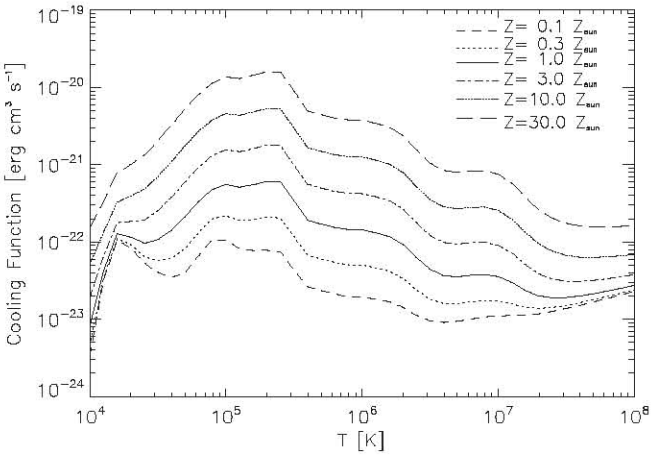

Figure 1. Cooling function for a range of metallicities between 0.1 and 30 $Z_\odot$.

slope limiter. The code also includes radiative losses and isotropic thermal conduction:

$$\frac{\partial \rho}{\partial t} + \nabla \cdot (\rho \boldsymbol{u}) = 0, \quad (1)$$

$$\frac{\partial (\rho \boldsymbol{u})}{\partial t} + \nabla \cdot (\rho \boldsymbol{u}\boldsymbol{u} + \mathbf{I} P) = 0, \quad (2)$$

$$\frac{\partial E}{\partial t} + \nabla \cdot [\boldsymbol{u}(E + P)] = L_{\rm rad}(Z, T) + \nabla \cdot \boldsymbol{q}, \quad (3)$$

where ρ, $\boldsymbol{u}$, T, P and E are the mass density, velocity, temperature, thermal pressure and energy density, respectively, $\mathbf{I}$ is the identity matrix, γ is the heat capacity ratio, $L_{\rm rad}(Z, T)$ is the energy-loss rate and $\boldsymbol{q}$ is the heat flux due to electron conduction (see Section 2.2). The system is closed with an ideal gas law given by $E = \rho|\boldsymbol{u}|^2/2 + P/(\gamma - 1)$. To find the energy-loss rate, we use a tabulated cooling function from the freely available CHIANTI data base (Landi et al. 1996; Dere et al. 1997). As we show in Fig. 1, we have constructed a cooling function with a range of metallicities of 0.1–30 $Z_\odot$.

The computational domain is a cube of 140 pc on a side, discretized by 256^3 cells in a uniform grid, yielding a resolution of 0.5469 pc.[1] From the number of massive stars, one can estimate the mass of the star cluster (∼3500 $M_\odot$ using STARBURST99; Leitherer & Heckman 1995). In our model, we did not consider the total mass of the paternal cloud, but we selected the size of the simulation box so that it contains a typical superbubble of radius (∼50 pc, i.e. DEM L50 and DEM L152).

The simulations include 15 stellar wind sources placed randomly within the cluster radius ($R_c = 10$ pc, and the distribution is the same for all the simulations). The stellar winds are imposed in spherical regions of radius $R_w = 6.03 \times 10^{18}$ cm (1.95 pc), corresponding to 5 pixels of the grid, and have a temperature $T_w = 10^5$ K. All the stars have the same mass-loss rate, $\dot{M}_w = 10^{-6}$ $M_\odot$ yr^{-1} and wind velocity of $v_w = 1500$ km s^{-1}. We turned on the stellar winds at the beginning of the simulation. The rest of the computational domain was initially filled by a homogeneous environment with temperature $T_0 = 10^4$ K and density $n_0 = 2$ cm^{-3}.

[1] We have tested that the resolution is sufficient in terms of the numerical convergence of the overall features of the simulations. However, some details of the flow and the exact values of the luminosities still depend on the resolution; see the discussion at the end of Section 3.

Table 1. Parameters of the simulations.

Model	SN locus (pc)	SN detonation time (10^5 yr)	Metallicity ($Z_\odot$)	Thermal conduction
sr0tsn2z0.3	0	2	0.3	No
sr0tsn3z0.3	0	3	0.3	No
sr0tsn5z0.3	0	5	0.3	No
sr0tsn2zv	0	2	Variable[a]	No
sr0tsn3zv	0	3	Variable[a]	No
sr0tsn5zv	0	5	Variable[a]	No
sr0tsn7.5zv	0	7.5	Variable[a]	No
sr0tsn2zvC	0	2	Variable[a]	Yes
sr0tsn5zvC	0	5	Variable[a]	Yes
sr5tsn5zv	5	5	Variable[a]	No
sr10tsn5zv	10	5	Variable[a]	No

Notes. [a]For these models the metallicity of the ISM is 0.3 $Z_\odot$, 3 $Z_\odot$ for the stellar winds and 10 $Z_\odot$ for the SN ejecta.

We impose an SN inside the bubble formed by the winds at four different times: 2, 3, 5 and 7.5×10^5 yr (each corresponding to a different model). These times were chosen to control the distance from the site of the SN to the superbubble shell. Since we do not follow the evolution of the star cluster that produces the shell (as Rogers & Pittard 2014), these times are related to the superbubble dynamical age that would be observed and not with the star cluster age. The superbubble dynamical age is smaller than that of the stars because it does not include the time needed to clear up the material between the stars and forms a common bubble. While in most of the models, the SN is placed at the centre of the star cluster, we have included two off-centre models: one in which the SN is placed 5 pc from the centre, and the other where it is near the edge of the bubble (10 pc from the centre). The SN explosion was imposed by injecting a total energy of 1×10^{51} erg and 2 $M_\odot$ of mass in a region with a radius of 2 pc. Half of this energy was injected as kinetic energy (with velocity following an increasing linear profile with radius, and constant density and temperature inside the imposition region), and the rest is thermal energy (Toledo-Roy et al. 2014).

To explore the effect of metallicity, we have performed some runs with a homogeneous metallicity for all the three components (the ISM, the stellar winds and the SN) and some models with a different metallicity for each of these components. In the homogeneous metallicity models, we have used a metallicity of 0.3 $Z_\odot$. For the variable metallicity models, following Silich et al. (2001), we use $Z_{\rm ISM} = 0.3\,Z_\odot$ for the ISM, $Z_{\rm wind} = 3.0\,Z_\odot$ for the mass injected in the form of winds, and $Z_{\rm SN} = 10\,Z_\odot$ for the SN ejecta. We have also included thermal conduction in two of the models.

The parameters of the simulations are listed in Table 1. As can be seen from the table, we named the models to reflect the parameters used: the number after 'sr' corresponds to the location of the SN in pc; it is followed by 'tsn' and another number to indicate the time of the SN detonation since the winds sources were turned on (in units of 10^5 yr); next there is the letter 'z' followed by the number 0.3 for the uniform metallicity models or the letter 'v' for the variable metallicity runs; for the models with thermal conduction a letter 'C' is appended at the end of the model name.

2.1 Adding the effect of metallicity to the cooling

The cooling in the code is added as a source term after updating the hydrodynamic variables. At the end of each timestep, we estimate the cooling by interpolating a tabulated cooling curve which is, for

a given metallicity, a function of the temperature. The energy loss is then subtracted to the internal energy of each cell at every timestep.

For the runs with a uniform metallicity this is a simple linear interpolation (in temperature) of a single table that is generated by the CHIANTI data base. For the runs with varying metallicity we created a series of tables for metallicities in the range of 0.1–30 $Z_\odot$; these are plotted in Fig. 1. Along with the gas-dynamic equations (equations 1–3) we consider the metallicity Z as a passive scalar by including an extra equation of the form

$$\frac{\partial Z\rho}{\partial t} + \nabla \cdot (Z\rho \boldsymbol{u}) = 0. \quad (4)$$

Using the metallicity value at each cell we do a bilinear interpolation (with metallicity spaced linearly and temperature logarithmically) to estimate the cooling to be applied there. For the ISM the metallicity is set to $0.3\,Z_\odot$ at the start of the simulation. For the winds and SNe the gas is injected into the simulation either with $Z_{\rm wind} = Z_{\rm SN} = 0.3\,Z_\odot$ (for the homogeneous models) or $Z_{\rm wind} = 3\,Z_\odot$ and $Z_{\rm SN} = 10\,Z_\odot$ for the inhomogeneous models.

The average metallicity in each region can be calculated (using Silich et al. 2001) as

$$\tilde{Z} = \frac{M_{\rm z,ej} + M_{\rm z,ism}}{M_{\rm ej} + M_{\rm ism}} \quad (5)$$

where $M_{\rm z,\,ej}$ and $M_{\rm z,\,ism}$ are the masses of the metallic ejecta (by winds and/or SN) and swept-up interstellar gas, respectively, while $M_{\rm ej}$ and $M_{\rm ism}$ are the total masses of the ejected and swept-up interstellar gas.

In general, the most metal-enriched regions are found behind the contact discontinuity that separates the main and reverse shocks. Even though some mixing occurs at the interface (mainly due to hydrodynamical instabilities and/or turbulence), since the swept-up ISM mass is larger than the ejected mass the metallicity of the shell remains close to that of the ISM.

2.2 Thermal conduction

In order to include the effect of thermal conduction by free electrons in our numerical simulation, we add a heat flux term ($\nabla \cdot \boldsymbol{q}$) in the right hand side of the energy equation (3).

The heat conduction due to collisions with free electrons in a plasma is given by the classical Spitzer (1962) law:

$$\boldsymbol{q} = -k\nabla T, \quad (6)$$

where k is the thermal conductivity given by

$$k = \beta\, T^{5/2}, \quad (7)$$

where, for a fully ionized hydrogen plasma $\beta \approx 6 \times 10^{-7}\,{\rm erg\,s^{-1}\,K\,cm^{-1}}$ (see Spitzer 1962). The result relies on the assumption that the mean free path is small compared to the scale-length of temperature variations ($\lambda \ll T/|\nabla T|$).

When the mean free path of the electrons is comparable or larger than temperature scalelength the heat flux saturates. In this regime the heat flux can be estimated by the local sound speed ($c_{\rm s}$) and pressure (P), as described by Cowie & McKee (1997):

$$q_{\rm sat} = 5\phi_{\rm s} c_{\rm s} P, \quad (8)$$

where $\phi_{\rm s}$ is a factor of order unity (we have used $\phi_{\rm s} = 1.1$).

At every timestep, we compute the heat fluxes in the classical and the saturated regimes, keep the smaller one and introduce its divergence as a source term to the energy equation. We have to mention that the thermal conduction time-scale is smaller than the hydrodynamic one determined by the standard CFL condition . For this reason, we apply a sub-stepping method to include the source term (we take of the order of 100 sub-steps to integrate the source term for each hydrodynamical step).

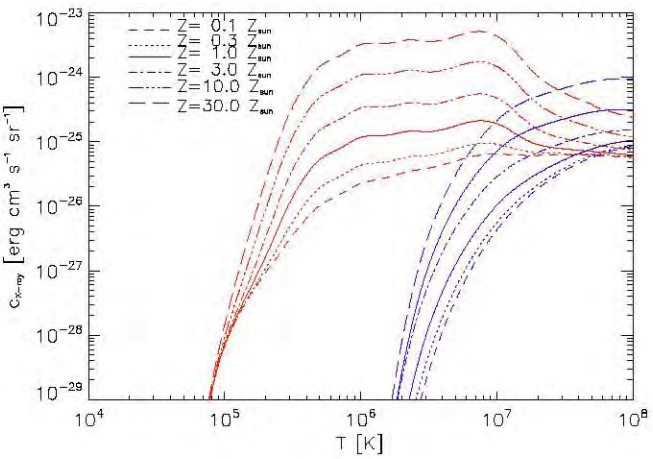

Figure 2. Thermal soft (0.1–2 keV, in red lines) and hard (2–10 keV, in blue lines) X-ray emission coefficients for a range of metallicities between 0.1 and 30 $Z_\odot$.

2.3 X-ray emission coefficients

We take the output from the hydrodynamical simulations to estimate the X-ray luminosity in all the models. We consider that the emission coefficient in the low-density regime is $j_\nu(n, Z, T) = n_{\rm e}^2 \chi(Z, T)$, where $n_{\rm e}$ is the electron density, and $\chi(Z, T)$ is a function of the temperature (T) and the metallicity (Z). For a given metallicity, the function χ can be computed and integrated over an energy band using the CHIANTI atomic data base and its associated IDL software (Landi et al. 1996; Dere et al. 1997). We have computed $\chi(Z, T)$ for various metallicities ($Z = 0.1$, 0.3, 1, 3 and $10\,Z_\odot$), using the ionization equilibrium model by Mazzota et al. (1998), over a range of temperatures from 10^4 to 10^9 K. The emission coefficients were integrated over two energy bands: soft X-rays (0.1–2 keV), and hard X-rays (2–10 keV). The result is a two-dimensional table of coefficients that is a function of temperature and metallicity. Fig. 2 shows the thermal soft (red lines) and hard (blue lines) X-ray emission coefficients, respectively, as function of temperature for several metallicities.

From the results of the simulations, we obtain the density, temperature and metallicity in every computational cell and perform a bilinear interpolation to get χ, and then use it to determine the emissivity for the two energy bands. The contribution of all cells is then added to compute the total X-ray luminosity both for soft and hard X-rays.

3 RESULTS

The colour maps of Figs 3 and 4 show the density and temperature at three different evolutionary times. These were chosen to show the effect of the SN explosion in the X-ray emission (see the next section). We present a time slightly before the SN explosion (top row), at the peak of luminosity after the explosion (middle row) and once the total luminosity has diminished back to a value near its pre-SN level (bottom row). The columns correspond to three different models: in the left-hand and central columns the SN occurs at the centre of the cluster, without thermal conduction, and with thermal conduction, respectively, and in the rightmost column the SN is 10 pc off-centre (the position of the SN is indicated by a star in the

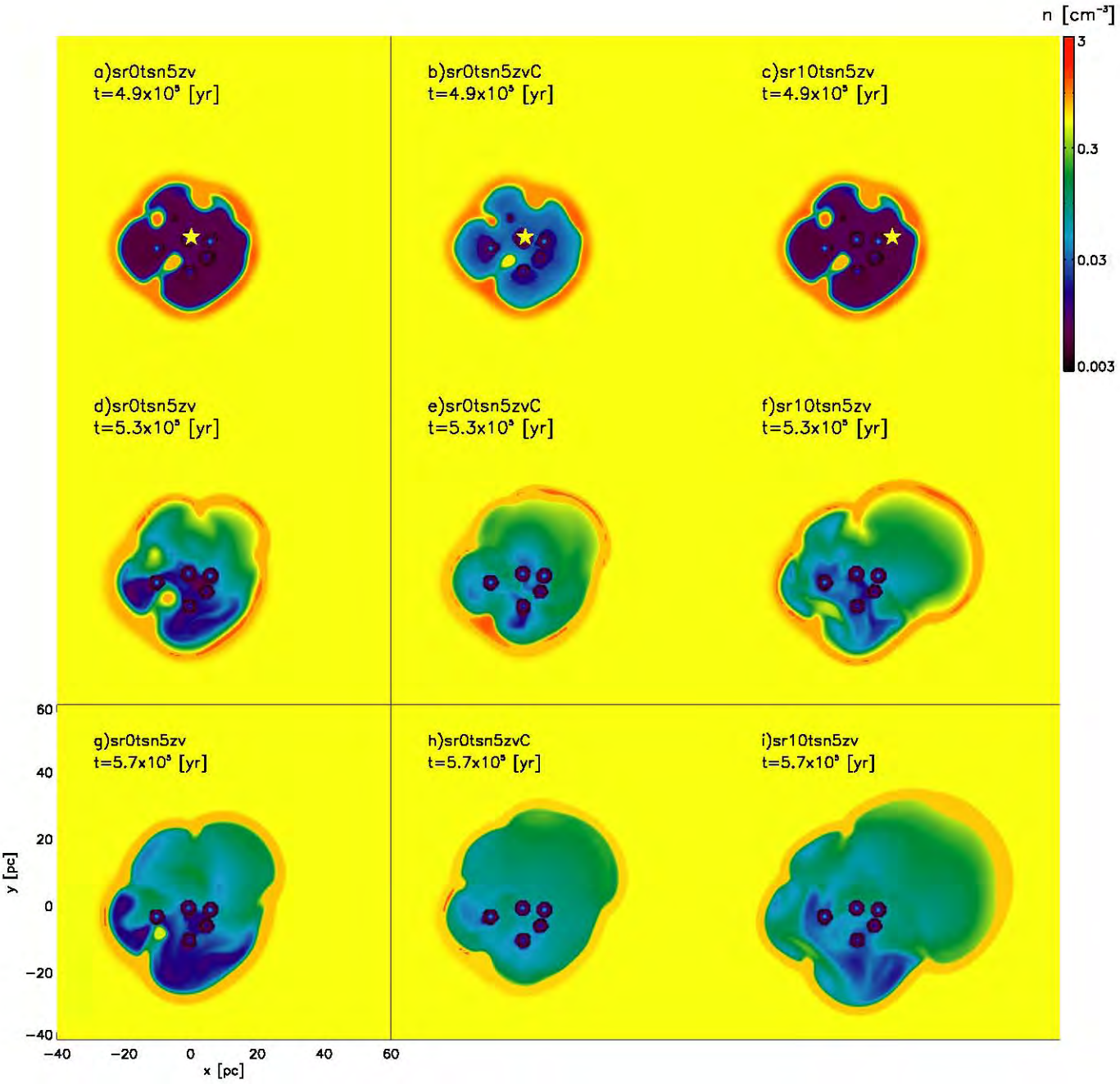

Figure 3. Density maps at different stages of the evolution and for different models. The columns correspond to three distinct models: in the panels of the left-hand column, the SN explosion occurs at the centre of the cluster (model sr0tsn5zv; panels a, d and g); those of the central column show the same model but including thermal conduction (sr0tsn5zvC; panels b, e and h); and in those of the right-hand column the SN explosion occurs 10 pc off-centre (sr10tsn5zv; panels c, f and i). For all models shown here, the SN explosion occurs at $t = 5 \times 10^5$ yr and the metallicity of the gas varies across components, as discussed in the text. The rows correspond to three relevant evolutionary stages: just before the SN explosion (top row), at the peak of X-ray luminosity (middle row) and once the luminosity has approximately returned to its original level (bottom row). The position of the SN is marked with a star in the panels of the top row. The spatial scale is the same across all panels and is shown in panel g.

top row). Following the time sequence in the columns of this figure, it can be seen that the SN ejecta reach the edge of the wind bubble and push it further into the ambient medium. Due to the particular position of the stars in these models, the gas distribution inside the wind bubble favours the expansion of the SN eject towards the upper-right corner of the simulation box, and thus the blowout is more pronounced in this direction, the effect being larger if the SN explodes off-centre (at the edge of the star cluster; see the rightmost panels).

3.1 Soft X-ray emission

Following the pressure-driven model discussed by Chu & Mac Low (1990), the soft X-ray luminosity can be estimated from

$$L_{\rm X} = 3.29 I(\tau) \xi L_{37}^{33/35} n_0^{17/35} t_6^{19/35} \ ({\rm erg\,s^{-1}}), \quad (9)$$

where

$$I(\tau) = \frac{125}{33} - 5\tau^{1/2} + \frac{5}{3}\tau^3 - \frac{5}{11}\tau^{11/3}, \quad (10)$$

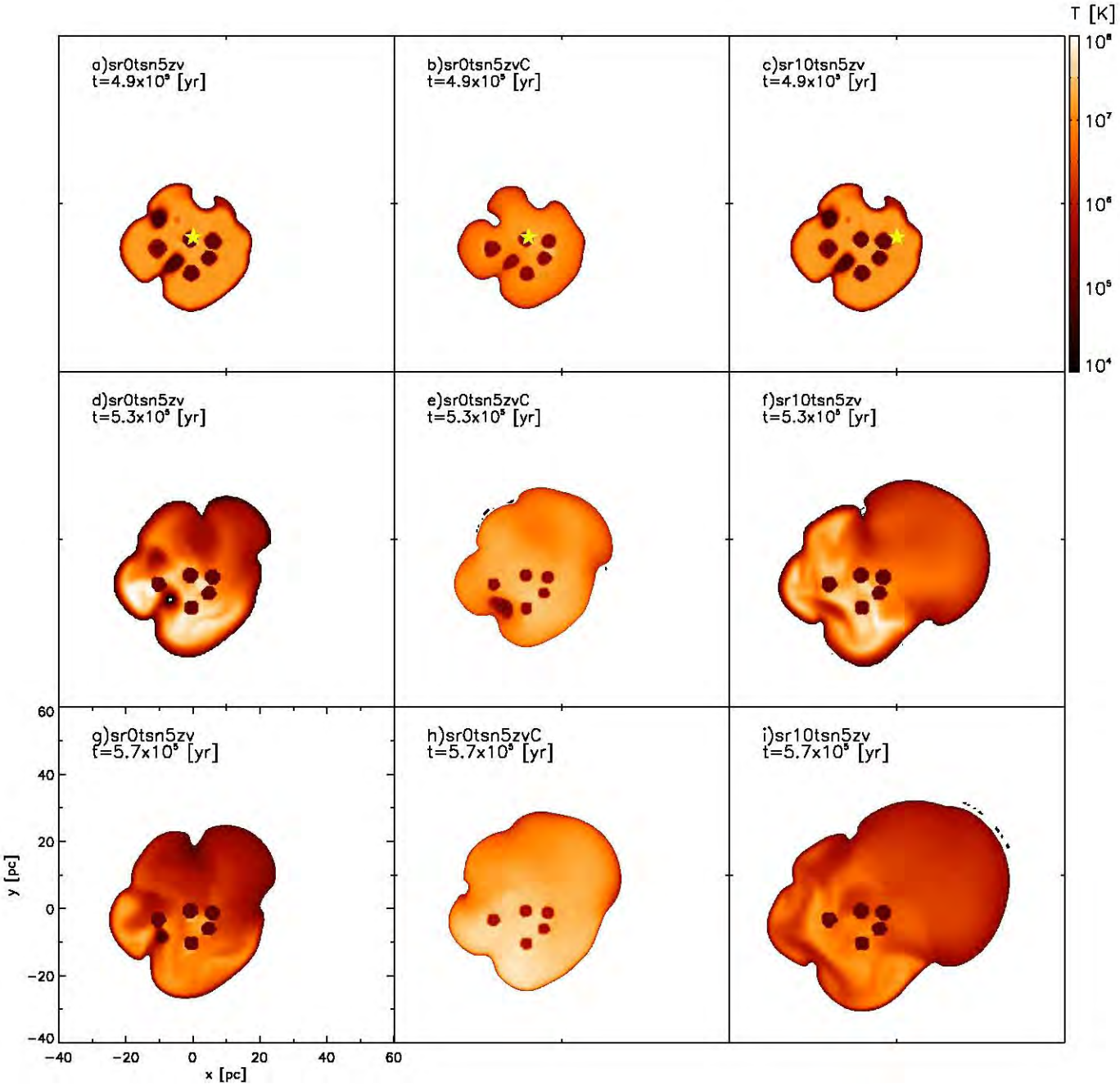

Figure 4. Temperature maps, corresponding to the same panels as in Fig. 3.

with

$$\tau = 0.16 L_{37}^{-8/35} n_0^{-2/35} t_6^{6/35}, \quad (11)$$

ξ is the gas metallicity, $L_{37} = L_{\rm w}/10^{37}$, where $L_{\rm w}$ is the mechanical luminosity of the cluster (in erg s^{-1}), n_0 is the ISM density and t_6 is the cluster lifetime in Myr. In all the models presented here, the mechanical energy injected by the winds is 1.1×10^{37} erg s^{-1}. With this mechanical energy, the total X-ray luminosity for the stellar wind contribution is $\sim 10^{33}$ erg s^{-1} (see equation 9, and also Chu & Mac Low 1990), for an ISM density of 2 cm^{-3} and metallicity of 0.3 $Z_\odot$ after an evolution time of 2×10^5 yr.

We have computed the soft X-ray emission for all the models at 10^4 yr intervals. Fig. 5 shows the evolution of the total soft X-ray luminosities for all models without thermal conduction and with the SN placed at the centre of the star cluster. The red lines show the models with uniform metallicity, and the blue ones with variable metallicity.

The X-ray luminosity before the SN event is in agreement with the value predicted by Chu & Mac Low (1990). Shortly after the SN explosion, the luminosity increases dramatically. We calculated the time interval in which the soft X-ray luminosity remains above 10^{34}, 10^{35} and 10^{36} erg s^{-1} ($\Delta t_{\rm s,\,34}$, $\Delta t_{\rm s,\,35}$ and $\Delta t_{\rm s,\,36}$, respectively). The maximum luminosity achieved and these time intervals are shown in Table 2.

From Fig. 5, we can see that the general shape of the luminosity curve after the SN explosion is quite similar in all the models. All models reached the same maximum luminosity of $\sim 3 \times 10^{35}$ erg s^{-1}, and have $\Delta t_{\rm s,\,34} \sim 6 \times 10^4$ yr and

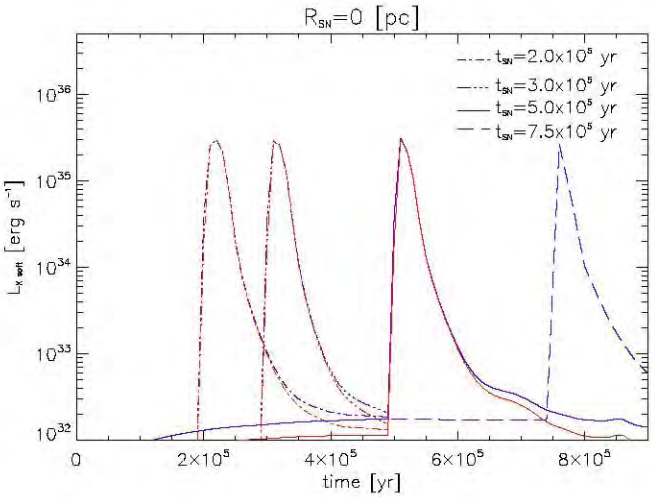

Figure 5. Evolution of the total soft X-ray luminosities for models with the supernova explosion occurring at the centre of the star distribution. The red lines are the models with homogeneous metallicity (for a supernova event at $t = 2$, 3, 5 and 7.5×10^5 yr dash–dotted, solid, triple-dot–dashed and dashed lines, respectively). The blue lines are the models with different metallicities ($Z_{\rm ISM} = 0.3\ Z_\odot$, $Z_{\rm wind} = 3\ Z_\odot$ and $Z_{\rm SN} = 10\ Z_\odot$ for the interstellar medium, stellar wind and supernova explosion, respectively, for SN explosions at $t = 2$, 3 and 5×10^5 yr).

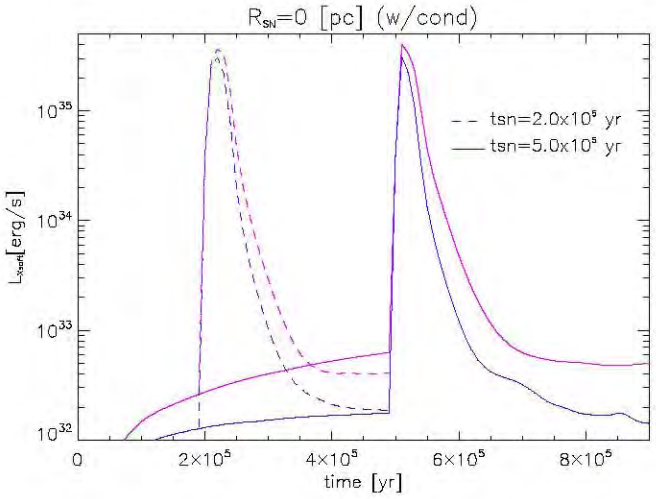

Figure 6. Evolution of the total soft X-rays luminosities for models with supernova explosion in the centre of the star distribution with inhomogeneous metallicity. The magenta line are the models with thermal conduction and the blue lines are the models without thermal conduction process (for supernova event at $t = 2$ and 5×10^5 yr dashed and solid lines, respectively).

Table 2. Maximum soft X-ray luminosity and time intervals in which the soft X-ray emission remains above 10^{34}, 10^{35} and 10^{36} erg s^{-1}.

Model	$L_{\rm max,\ soft}$ (erg s^{-1})	$\Delta t_{\rm s,\ 34}$ (10^4 yr)	$\Delta t_{\rm s,\ 35}$ (10^4 yr)	$\Delta t_{\rm s,\ 36}$ (10^4 yr)
sr0tsn2z0.3	2.98×10^{35}	6.42	3.55	–
sr0tsn3z0.3	2.83×10^{35}	5.60	3.05	–
sr0tsn5z0.3	2.98×10^{35}	6.01	2.84	–
sr0tsn2zv	3.01×10^{35}	6.72	3.63	–
sr0tsn3zv	2.92×10^{35}	5.96	3.13	–
sr0tsn5zv	3.08×10^{35}	6.34	2.92	–
sr0tsn7.5zv	2.68×10^{35}	6.13	2.90	–
sr0tsn2zvC	3.65×10^{35}	8.20	4.30	–
sr0tsn5zvC	4.03×10^{35}	9.00	3.96	–
sr5tsn5zv	4.16×10^{35}	7.61	3.79	–
sr10tsn5zv	1.23×10^{36}	13.81	7.27	3.02

$\Delta t_{\rm s,\ 35} \sim 3 \times 10^4$ yr. In these models, in which the SN explosion occurs at the centre of the stellar distribution, luminosities above 10^{36} erg s^{-1} are never reached. Our results show only small differences in the soft X-ray emission between models with uniform metallicity and those with variable metallicity. The similarity of the emission across the models indicates that the emission is dominated by swept-up ISM material. This is partly because the high-metallicity gas (winds and SN) is kept at a temperature too high for thermal soft X-rays to be important. Thermal conduction allows energy transport with reduced bulk motions, resulting in a denser inner region. Weaver et al. (1977) estimated a significant increase in the soft X-ray luminosity (up to two orders of magnitude) with respect to models without thermal conduction. Fig. 6 displays the evolution of the soft X-rays luminosities for the two models with thermal conduction (sr0t2e5zvC and sr0t5e5zvC, magenta lines), and their counterpart without thermal conduction (sr0t2e5zv and sr0t5e5zv, blue lines). As can be seen, thermal conduction does increase the maximum luminosity of the models, but only by a factor of ∼1.25, and the luminosity returns to a value a factor of two larger after the SN explosion. The time of emission above 10^{34} erg s^{-1} also increases by a similar factors of 1.2 and 1.6 for the SN imposed after 2×10^5 and 5×10^5 yr, respectively. Approximately the same timespan increase is found for emission above 10^{35} erg s^{-1}; see Table 2. These increments in the time interval with emission above 10^{34} and/or 10^{35} erg s^{-1} will enhance the chance of such luminosities being observed.

We can see that the inclusion of different metallicities and/or thermal conduction induces only small discrepancies in the soft X-ray emission.

From this model, it is clear that the SN explosions are a crucial ingredient for the thermal X-ray emission. The presence of an SN can explain the extra X-ray luminosity observed in several superbubbles. However, when the SN event occurs in the centre of the cluster, the soft X-ray luminosity only reaches a few times 10^{35} erg s^{-1}, still falling short of some of the observed values (e.g. those of Jaskot et al. 2011). We find that models with a centred explosion seem to still be underluminous.

A possibility that results in luminosities above 10^{36} erg s^{-1} is to place the SN at a distance from the centre of the star cluster. For these reasons, we have included models sr5tsn5zv and sr10tsn5zv where the SN occurs at $R_{\rm SN} = 5$ and 10 pc from the star cluster centre, respectively, both at $t_{\rm SN} = 5 \times 10^5$ yr. Fig. 7 shows the soft X-ray luminosities for these two models compared to a model with an SN placed at the cluster centre (sr0tsn5zv).

We can see that the X-ray luminosities increase when the SN explodes closer to the edge of the bubble. The maximum soft X-ray luminosity increases by a factor of ∼1.25 between the model with SN explosion at $R_{\rm SN} = 0$ and $R_{\rm SN} = 5$ pc and a factor of ∼4 when the SN explodes near the cluster radius ($R_{\rm C} = 10$ pc), reaching a maximum luminosity of $L_{\rm max} = 1.23 \times 10^{36}$ erg s^{-1}.

For model sr10tsn5zv, the only one that reached 10^{36} erg s^{-1}, the time interval spent above 10^{36} erg s^{-1} was 30 kyr. In addition, this last model predicts a time spent above 10^{35} erg s^{-1} of 72 kyr, and one above 10^{34} erg s^{-1} of 14 kyr. These numbers are ∼3 times larger than those of the model with the SN explosion occurring at the centre of the star cluster.

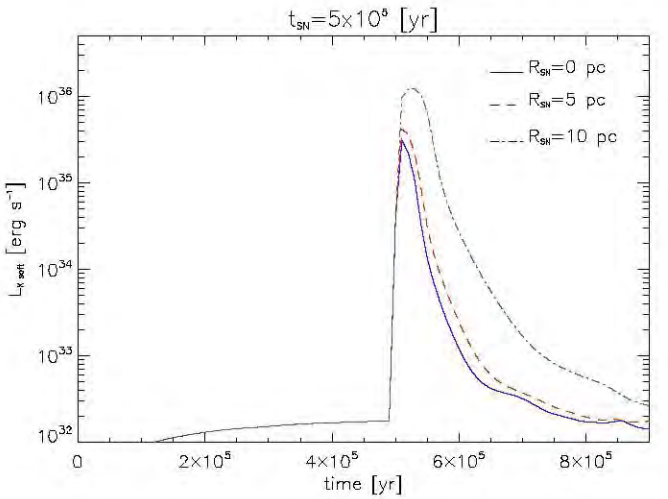

Figure 7. Evolution of the total soft X-rays luminosities for models with supernova explosion at $t = 5 \times 10^5$ yr, and with inhomogeneous metallicity. The blue, red and olive lines are the model with supernova event in $R = 0$, 5 and 10 pc, respectively.

From these results we can see that, on the one hand, for the case of the SN at the cluster centre the soft X-ray luminosity increase is not very sensitive to the time at which it is detonated. The luminosity increase is only slightly larger for SN explosions that occur later in the evolution of the superbubble. On the other hand, when the SN is off-centre the luminosity increase depends considerably on the distance to the centre of the cluster.

The colour maps of Fig. 8 show the soft X-ray emissivity in the same layout as in Fig. 3. Note that the blowout region (located at the upper-right corner of the simulation box) provides the largest contribution to the luminosity increase seen 30 kyr after the explosion (middle panels). By 200 kyr after the explosion (bottom panels), the emissivity has almost returned to values comparable to its pre-SN level; however, due to the now larger X-ray-emitting volume, the luminosity remains slightly above the original level (see Fig. 7).

An interesting exercise is to compare the predicted luminosity statistics of our simulations with those of observed superbubbles. For this purpose, we have taken a sample of 26 bubbles with luminosities greater than 10^{34} erg s^{-1} from the literature (Oey 1996; Dunne, Points & Chu 2001; Jaskot et al. 2011; Reyes-Iturbide et al. 2014). Out of these, 18 have luminosities above 10^{35} erg s^{-1} while only 3 are observed with $L_{\rm soft} > 10^{36}$ erg s^{-1}. We can use our numerical results to predict how many bubbles out of these 26 should have luminosities above these two levels. In order to do this, we computed, from Table 2, the ratios of the times spent above these levels to the overall time where luminosity is above 10^{34} erg s^{-1} for model sr10tsn5zv (the only one that reaches 10^{36} erg s^{-1}). We find that $\Delta t_{\rm s,\,36}/\Delta t_{\rm s,\,34} \sim 52.6$ and $\Delta t_{\rm s,\,35}/\Delta t_{\rm s,\,34} \sim 21.9$ per cent. Thus, assuming that all bubbles in this observed sample reach a luminosity of 10^{36} erg s^{-1} at some point in their evolution, this model predicts that about 14 should have a luminosity above 10^{35} erg s^{-1} while about six should be observed above 10^{36} erg s^{-1}. Though the values do not coincide exactly, they reasonably match the luminosity ratios of $L_{36}/L_{34} \sim 12$ and $L_{36}/L_{35} \sim 70$ per cent observed in the sample. Here, L_n is a soft X-ray luminosity that is greater than or equal to 10^n erg s^{-1}.

There could be several explanations for this difference. For one, it is hard to judge whether this small sample of superbubbles is representative of the general population, and thus some variability can be expected in the statistics. At the same time, our numerical results suggest that the position of an SN explosion occurring inside the bubbles determines whether a luminosity of 10^{36} erg s^{-1} is reached at all during their lifetimes. Thus, if not all of the observed bubbles have had off-centre SN explosion, it is to be expected that fewer of them would be observed above 10^{36} erg s^{-1} than what our models predict.

3.2 Hard X-ray emission

Hard X-ray emission is produced in the hottest regions inside the bubble where individual winds interact, when the gas flow is faster than an $\sim$1000 km s^{-1}, as well as during the early stages of the SN remnant evolution and where the cluster wind and/or the SN remnant are heated by the reverse shock. Thus, one should expect that metallicity should have a significant effect on the hard X-ray emission.

In Table 3, we show the maximum thermal hard X-ray luminosity, and the time intervals for which the luminosity remains above 10^{33} erg s^{-1} ($\Delta t_{\rm h,\,33}$) and 10^{34} erg s^{-1} ($\Delta t_{\rm h,\,33}$).

Fig. 9 shows the evolution of the thermal hard X-rays luminosity for all models with the SN placed at the centre. In the models with different metallicities, all three components exhibit maximum luminosities ($\sim 3 \times 10^{34}$ erg s^{-1}) that are $\sim$3 times larger than those of the models with homogeneous metallicity ($\sim 1.0 \times 10^{34}$ erg s^{-1}). We have to mention that the thermal hard X-ray emission produced inside the star cluster (regions of wind collisions) is underestimated by the models with homogeneous metallicity due to the rather low metallicity of the wind sources (0.3 $Z_\odot$). In the models with the variable metallicity, the wind is injected with a more appropriate metal content (3 $Z_\odot$), thus the hard X-ray luminosity in these models should be closer to reality.

We can see from Table 3 that the maximum hard X-ray luminosity is significantly larger in the models with variable metallicity, typically an increase of $\sim$3.5 times. The time interval that the emission remains above 10^{33} erg s^{-1} is similar, although slightly larger in the models with more realistic metallicity. In contrast, the time that the emission remains above 10^{34} erg s^{-1} is much larger (a factor of $\sim$4) than that obtained in the models with homogeneous metallicity.

An important fact to notice is that the ratio of the maximum luminosities in soft X-rays to hard X-rays is of the order of 10. Velázquez et al. (2013) explored the ratios between soft and hard X-ray emission in the young star cluster M 17. This particular cluster is partially immersed in the cluster parental cloud, and their models resulted in a ratio of soft to hard X-rays of two orders of magnitude. From our models, we notice that the time intervals of high luminosity for soft X-rays ($\Delta t_{\rm s,\,34}$ and $\Delta t_{\rm s,\,35}$) are larger than those obtain for hard X-rays ($\Delta t_{\rm h,\,33}$ and $\Delta t_{\rm h,\,34}$).

This shows that very young star clusters with an SN event can produce hard X-ray luminosities that are only an order of magnitude fainter than the soft X-rays. However, this happens only for a short interval at the earlier stages of the SN remnant. After that the hard X-ray emission drops abruptly.

Fig. 10 shows the evolution of the hard X-ray luminosity for the two models with thermal conduction and their counterpart without thermal conduction. The maximum luminosities and the time intervals of high hard X-ray emission are remarkably similar in spite of the thermal conduction. Although small differences can be seen, the position of the SN explosion in the cluster does not have a significant influence in the overall and maximum thermal hard X-ray luminosity (see Fig. 11).

It is also interesting to note that for an SN exploding at the centre of the cluster the highest luminosity achieved is much lower if the

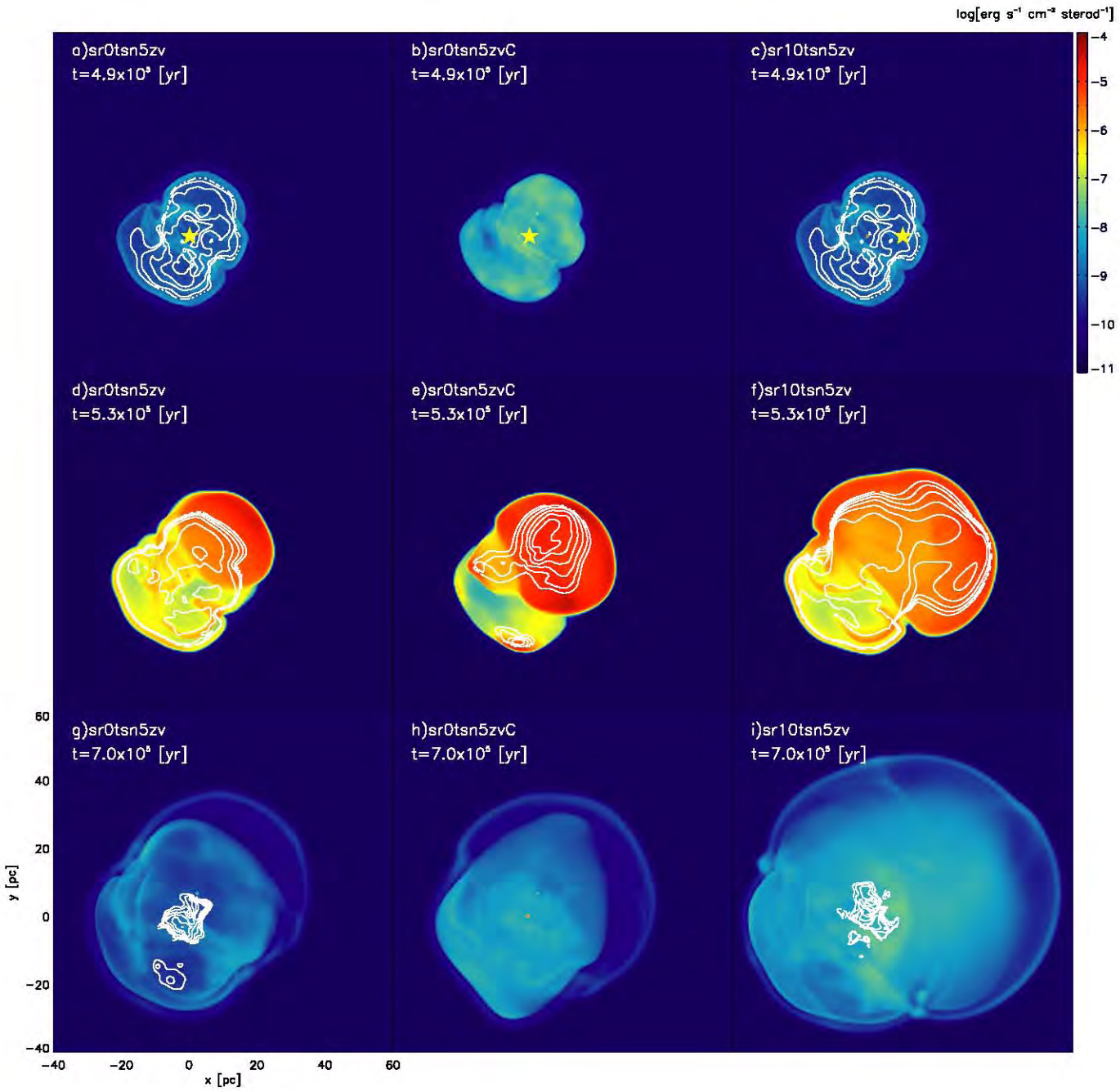

Figure 8. Comparison of the X-ray emissivity in the soft (colour maps, with the shown logarithmic scale given in erg s^{-1} cm^{-2} sr^{-1}) and hard (contours, logarithmically spaced levels from 10^{-11} to 10^{-8} erg s^{-1} cm^{-2} sr^{-1}) bands at the three different stages shown in Fig. 3.

explosion occurs at later times (cf. the long dashed curve in Fig. 9 to the others).

The distribution of the hard X-ray emission before the SN explosion, at peak luminosity and after the luminosity returns to its previous level can be seen as the (logarithmically spaced) contour levels in Fig. 8. The emission during peak luminosity (middle row) is slightly more extended in the case where the SN is detonated off-centre (panel f), but returns to being concentrated inside the star cluster after the effect of the explosion has had time to decay (bottom row). The impact of thermal conduction on the hard X-ray emission is also evident. As can be seen, before (top row) or sometime after (bottom row) the SN explosion the hard-band emission is at a much higher level in the cases without thermal conduction (left- and right-hand columns). However, during the luminosity peak (middle row) all models display important hard X-ray emission regardless of the inclusion of thermal conduction. The difference lies mainly in that in the case including thermal conduction (panel e) the emission is slightly more centralized than in the cases without.

We must note that the resolution used in the models is not enough to capture all the details of the flow. The use of higher resolution allows larger compression factors as well as more small-scale structure inside the bubbles. To estimate the uncertainty in the X-ray luminosities due to poor resolution, we have taken a test case (model sr0tsn5z0), and reproduce the set-up in the WALICXE-3D code (Toledo-Roy et al. 2014). This code has adaptive mesh refinement, which allows us to increase the resolution at a lower computational

Table 3. Maximum hard X-ray luminosity and time intervals in which the hard X-ray emission remains above 10^{33} and 10^{34} erg s^{-1}.

Model	$L_{\rm max,\,hard}$ (erg s^{-1})	$\Delta t_{\rm h,\,33}$ (10^4 yr)	$\Delta t_{\rm h,\,34}$ (10^4 yr)
sr0tsn2z0.3	2.88×10^{34}	2.00	1.35
sr0tsn3z0.3	2.88×10^{34}	1.99	1.35
sr0tsn5z0.3	2.88×10^{34}	1.96	1.33
sr0tsn2zv	1.02×10^{35}	2.03	1.84
sr0tsn3zv	1.02×10^{35}	2.02	1.85
sr0tsn5zv	1.02×10^{35}	2.00	1.83
sr0tsn7.5zv	2.81×10^{32}	0.00	0.00
sr0tsn2zvC	9.90×10^{34}	2.03	1.84
sr0tsn5zvC	9.93×10^{34}	2.00	1.82
sr5tsn5zv	9.07×10^{34}	2.00	1.81
sr10tsn5zv	9.84×10^{34}	3.57	1.99

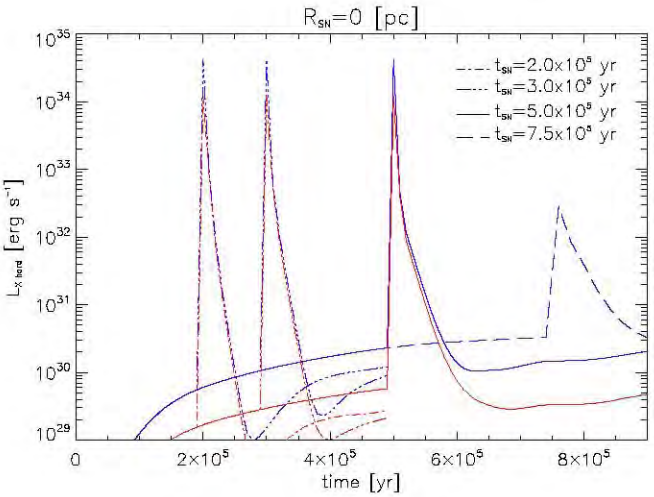

Figure 9. Same as Fig. 5 for hard X-rays luminosities.

cost, but the thermal conduction is not fully implemented. We ran the test case at an equivalent resolution of 512^3 and 1024^3 cells, and while the details of the flow are different, the integrated X-ray luminosities seem to reach convergence. The peak luminosity in the higher resolution runs is a factor of $\sim$2 larger than in the 256^3 model sr0tsn5z0. And the times above 10^{34}, 10^{35} and 10^{36} erg s^{-1} are larger by a factor of $\sim$1.5. All the results presented above have an uncertainty of this order of magnitude due to the limited resolution.

4 COMPARISONS WITH OBSERVATIONS

It is useful to compare our numerical models to the observations of particular superbubbles. We have thus turned our attention to four superbubbles located in the LMC: N70, N185, DEM L50, and DEM L152. These superbubbles have some particular features (as we will show) that make them compatible with our results.

N70 is a superbubble with a radius of approximately 53 pc. According to the observations, there is an SN located closer to the centre than the edge of the cluster. The X-ray luminosity reported by Reyes-Iturbide et al. (2014) is about $2.4(\pm0.4) \times 10^{35}$ erg s^{-1}. We can see that our numerical results are in good agreement with these observations, in particular the models with the SN explosion in the centre of the cluster.

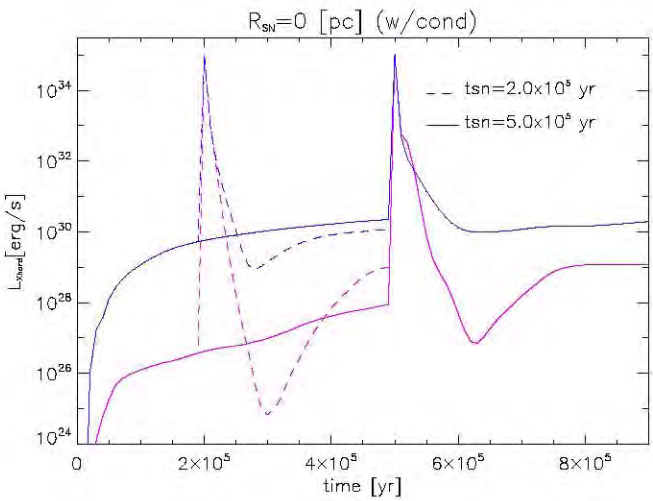

Figure 10. Same as Fig. 6 for hard X-rays luminosities.

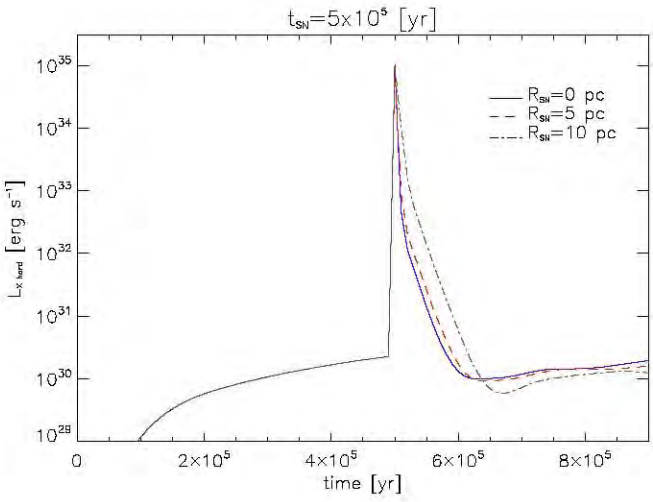

Figure 11. Same as Fig. 7 for hard X-rays luminosities.

The case of N185 is quite similar to that of N70. N185 has a spherical shape with an approximate radius of 43 pc (Oey 1996). The X-ray luminosity obtained by Reyes-Iturbide et al. (2014) is $2.1\ (\pm0.7) \times 10^{35}$ erg s^{-1}. Following Rosado et al. (1982), a possibility to explain the high velocity of this superbubble is that an SN explosion occurred. From its spherical shape, we conclude that the SN explosion must be located near the centre of the cluster. As in the previous case, our numerical models are in good agreement with the observed X-ray luminosities.

Two other interesting cases are DEM L50 and DEM L152. These are two superbubbles with very intense X-ray emission. According to observations DM L152 has a radius of approximately 50 pc (Jaskot et al. 2011), and DEM L50 has roughly the same radius (Oey 1996). Jaskot et al. (2011) reported an X-ray luminosity in the range $2.0–4.0 \times 10^{36}$ erg s^{-1} for DEM L50 and an emission of $5.4–5.7 \times 10^{35}$ erg s^{-1}. These two superbubbles contrast with N70 and N185 in that they contain an off-centre SN explosion, which is clearly distinguishable in the observations. Only numerical model sn10tsn5zv predicts a luminosity comparable to the observed values. The luminosities predicted by other models are not high enough to match with these observed values.

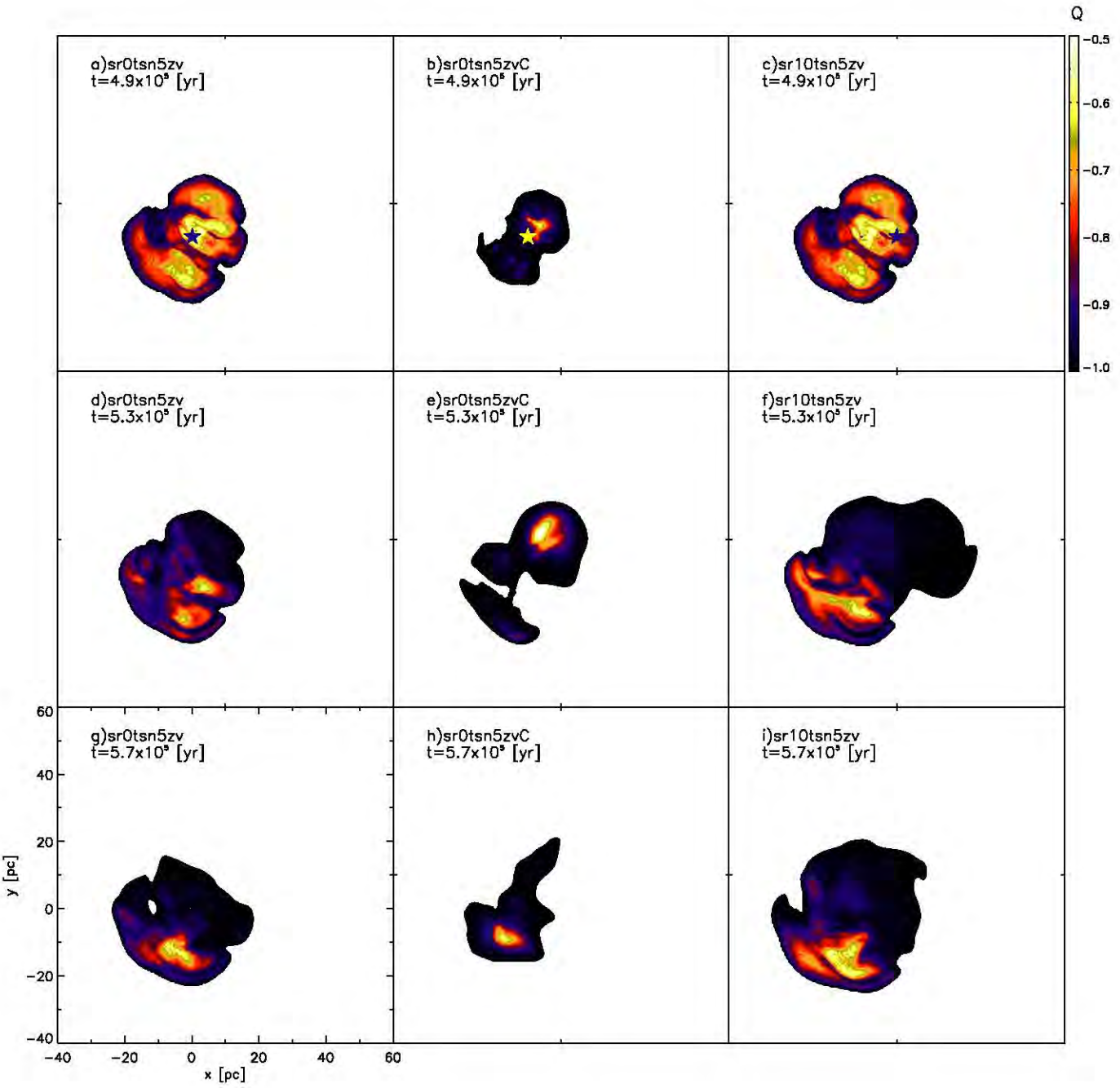

Figure 12. Hardness maps for the same cases shown in Fig. 3.

In order to better compare with observations, we have calculated the hardness ratio for three of our models (see Fig. 12). These models are those discussed in Section 3: two with a centred SN explosion that differ in the presence of thermal conduction, and the third with the SN explosion 10 pc off-centre. Following Jaskot et al. (2011), the hardness ratio is defined as

$$Q = \frac{H - S}{H + S}, \tag{12}$$

where H is the flux energy in the 2–10 keV energy band (corresponding to hard X-rays) and S is the flux energy in the 0.1–2 keV energy band (corresponding to soft X-rays). After computing the fluxes and obtaining Q for each cell in the simulation, we integrate along the z-axis in order to project the result into a 2D map, assuming that the X-ray absorption due to the material inside the bubble can be neglected.

In Fig. 12 we observe that, before the SN explosion occurs, in models without thermal conduction (left- and right-hand columns) the hardness ratio peaks at ~ -0.55 at the centre of the stellar distribution, and decreases as we approach the edge of the cluster (the shell of swept-up ISM material emits mainly soft X-rays). In the case of the model that includes thermal conduction (middle column), we observe that $Q \sim -1$ in most of the bubble, indicating that hard X-ray emission is largely negligible. As a result, the material ejected by the stars is cooled quickly from hard X-ray-emitting temperatures

(10^8 K) to temperatures in the range 10^5–10^6 K where soft X-ray emission is favoured.

The SN explosion drastically alters the hardness maps for the models without thermal conduction. The SN shock wave sweeps the cluster volume, devoiding the centre of the bubble of hard X-ray-emitting gas and forming regions with $Q \sim -0.6$ closer to the edge of the bubble. In the model with thermal conduction, the hard X-ray emission is small to begin with, and the effect of the explosion on the hardness ratio is not as noticeable.

The predicted Q values obtained in our numerical models are similar to those obtained by Jaskot et al. (2011) for DEM L50 and DEM L152. Nevertheless, the specific details and assumptions of our simulations make it hard to establish direct comparisons to specific observed bubbles. In order to use the hardness ratio to predict some of the physical processes that occur or have occurred in the superbubbles, we would need to separately simulate the specific physical details, such as the position and mass and energy injection rates of each star, the ISM density, of each particular bubble, which is out of the scope of this work.

5 CONCLUSIONS

In this paper, we present 3D hydrodynamical models of the evolution of the soft and hard thermal X-ray luminosities produced inside superbubbles driven by massive stellar winds including the effect of an SN explosion and thermal conduction.

In all models, we include the injection of mass and energy by a cluster of wind sources and a single SN event. We have varied the position of the SN with respect to the centre of the cluster as well as the detonation time. Also, we have worked out models with a uniform metallicity and models in which the environment, the winds and the SN have different metallicities. The metallicities are used to calculate the radiative cooling rate, and has an effect on the emissivity in X-rays. We have also taken into account the effects of thermal conduction in two of the models.

In the models with different metallicities, we used $Z = 0.3\,Z_\odot$ for the environment, $3\,Z_\odot$ for the winds and $10\,Z_\odot$ for the SN ejecta. Our models show that the contribution of the metallicity of the winds and the SN remnant is negligible for the soft X-ray emission of superbubbles, but becomes important for the hard X-ray component. In these models, the ratio of soft to hard maximum luminosity can be as extreme as 10 (i.e. the hard X-ray luminosity reaches 10 per cent of the one for soft X-rays).

The models with thermal conduction result in a noticeable increase in the total luminosity of soft X-rays, by a factor of $\sim$1.25. However, this factor is smaller than the two orders of magnitude difference predicted in the standard model of Weaver et al. (1977) and Chu & Mac Low (1990). The differences are likely to come from the fact that the standard model of Weaver et al. (1977) considers just a single star, and the extension to a star cluster in Chu & Mac Low (1990) and Chu et al. (1995) does not account for the cooling of the gas due to the interaction of the stellar winds. Thermal conduction has a slightly larger effect on the total integrated emission of hard X-rays, increasing the luminosity by a factor of $\sim$2.6.

The most important contribution to the emission of soft and hard X-rays is produced by the injection of mass and energy by SN explosions. In soft X-rays, the luminosity increases by up to two orders of magnitude when we consider an SN explosion placed at the cluster centre, and up to three orders when it explodes at the edge the star cluster.

Another important factor to consider is the time during which the luminosity remains high (i.e. observable). We show that when off-centre SN events occur (close to the shell) the luminosity can increase by one or two orders of magnitude above that predicted by the standard model without SN, and that it can be maintained by a few tens of thousands of years. Indeed, as the SN explosion occurs closer to the shell of swept-up ISM, the maximum luminosity of soft X-rays as well as the time interval during which luminosity is enhanced increase.

An important increase in the maximum soft X-ray luminosity is produced when the SN ejecta collide with the dense shell of swept-up ISM gas left behind by its interaction with the cluster wind. In these cases, X-ray luminosities of 10^{36} erg s^{-1} can be achieved. On the other hand, superbubbles where the SN explosions have not taken place near the shell, such as N70 and N185 (Jansen et al. 2011; Reyes-Iturbide et al. 2014), have lower X-ray luminosity, and can be explained using our models with a slightly off-centre SN.

In clusters without SN events, or with an SN placed at the centre of the cluster, the contribution to the luminosity made by the SN is hard to observe, in particular because the observable flux increase in the soft X-ray emission lasts for a short time. This could be happening in massive stellar clusters in the Galaxy, such as Arches, Quintuplet and NGC 3603, that have a hundred massive stars with a total observed X-ray emission of $\sim 10^{34}$ erg s^{-1}.

ACKNOWLEDGEMENTS

We acknowledge support from CONACyT grants 167611 and 167625, and DGAPA-UNAM grant IG100214 and IN 109715. We thank the anonymous referee for very relevant comments that resulted in a substantial revision of the original version of this paper.

REFERENCES

Añorve-Zeferino G. A., Tenorio-Tagle G., Silich S., 2009, MNRAS, 394, 1284
Cantó J., Raga A. C., Rodríguez L. F., 2000, ApJ, 536, 896
Chu Y.-H., Mac Low M.-M., 1990, ApJ, 365, 510
Chu Y.-H., Chang H.-W., Su Y.-L., Mac Low M.-M., 1995, ApJ, 450, 157
Cowie L. L., McKee C. F., 1977, ApJ, 211, 135
Dere K. P., Landi E., Mason H. E., Monsignori Fossi B. C., Young P. R., 1997, A&AS, 125, 149
Dunne B. C., Points S. D., Chu Y.-H., 2001, ApJS, 136, 119
Dunne B. C., Chu Y.-H., Chen C.-H. R., Lowry J. D., Townsley L., Gruendl R. A., Guerrero M. A., Rosado M., 2003, ApJ, 590, 306
Esquivel A., Raga A. C., Cantó J., Rodríguez González A., 2009, A&A, 507, 855
Harper-Clark E., Murray N., 2009, ApJ, 693, 1696
Jansen F. et al., 2001, A&A, 365, L1
Jaskot A. E., Strickland D. K., Oey M. S., Chu Y.-H., García-Segura G., 2011, ApJ, 729, 28
Landi E., Del Zanna G., Young P. R., Dere K. P., Mason H. E., Landini M., 2006, ApJS, 162, 261
Leitherer C., Heckman T. M., 1995, ApJS, 96, 9
Maeder A., 1992, A&A, 264, 105
Mazzotta P., Mazzitelli G., Colafrancesco S., Vittorio N., 1998, A&AS, 133, 403
Oey M. S., 1996, ApJ, 467, 666
Oey M. S., Massey P., 1995, ApJ, 452, 210
Raga A. C., Esquivel A., Velázquez P. F., Cantó J., Haro-Corzo S., Riera A., Rodríguez-González A., 2009, ApJ, 707, L6
Reyes-Iturbide J., Velázquez P. F., Rosado M., Rodríguez-González A., González R. F., Esquivel A., 2009, MNRAS, 394, 1009

Reyes-Iturbide J., Rosado M., Rodríguez-González A., Velázquez P. F., Sánchez-Cruces M., Ambrocio-Cruz P., 2014, ApJ, 148, 102
Rodríguez-González A., Velázquez P. F., Rosado M., Esquivel A., Reyes-Iturbide J., Toledo-Roy J. C., 2011, ApJ, 733, 34
Rogers H., Pittard J. M., 2014, MNRAS, 441, 964
Rosado M., Georgelin Y. M., Georgelin Y. P., Laval A., Monnet G., 1982, A&A, 115, 61
Silich S., Tenorio-Tagle G., Añorve-Zeferino G. A., 2005, ApJ, 635, 1116
Silich S., Tenorio-Tagle G., Terlevich R., Terlevich E., Netzer H., 2001, MNRAS, 324, 191
Silich S., Tenorio-Tagle G., Rodríguez-González A., 2004, ApJ, 610, 226
Spitzer L., Jr 1962, Physics of Fully Ionized Gases. Wiley Interscience, New York
Stevens I. R., Hartwell J. M., 2003, MNRAS, 339, 280
Toledo-Roy J. C., Esquivel A., Velázquez P. F., Reynoso E. M., 2014, MNRAS, 442, 229
Toro E. F., Spruce M., Speares W., 1994, Shock Waves, 4, 25
Velázquez P. F., Rodríguez-González A., Esquivel A., Rosado M., Reyes-Iturbide J., 2013, ApJ, 767, 69
Weaver R., McCray R., Castor J., Shapiro P., Moore R., 1977, ApJ, 218, 377

This paper has been typeset from a TEX/LATEX file prepared by the author.

Capítulo 2

Flujos de estrellas jóvenes de baja masa

2.1. Introducción.

Las estrellas, mediante sus eyecciones de gas, influyen en la tasa de formación estelar. Los flujos estelares inyectan masa, momento y energía al medio interestelar, y también son responsables de la presencia del polvo en el medio. Este polvo tiene un efecto fundamental en el medio interestelar a través de sus propiedades ópticas, térmicas y químicas.

Es aceptado en general (McKee & Ostriker, 2007) que la formación de estrellas de baja masa inicia cuando una nube molecular fría y densa colapsa bajo la acción de su propia gravedad. Durante este colapso la nube comienza a fragmenarse y forma núcleos más pequeños y densos que comienzan a acretar material y eventualmente colapsan para formar protoestrellas. A fin de que la estrella jóven continúe acretando material, este debe perder momento angular. La eyección colimada de material, el chorro, es resultado de este proceso (ver Figura 2.1). Alrededor de 1950 y de manera independiente Herbig y Haro (Herbig, 1951; Haro, 1952) observaron en la nebulosa de Orión, dos nudos que emitían de manera intensa en Hα y en las líneas rojas de [S II](ver Figura 2.2). Fue el singular e inesperado espectro de emisión de estos nudos lo que llamó la atención. Además del espectro de líneas de Balmer, estos objetos (bautizados como objetos Herbig-Haro o HH por Ambartsumian 1954) emiten débilmente en un amplio rango del contínuo, además de un buen número de líneas prohibidas en el óptico: [S II], [N II], [Fe II], así como [O I], [O II] e incluso [O III]. El hecho de que tienen líneas fuertes de átomos neutros y de iones de baja energía de ionización (por ejemplo líneas de [C I], [S II], [O I] y [Fe I]) los diferencia en forma clara de las regiones fotoionizadas.

Los objetos HH son nebulosas compactas dentro de regiones de formación estelar que emiten espectros de líneas de emisión óptica características. Estos objetos se forman de la interacción entre el flujo de gas expulsado supersónicamente por una estrella jóven y el medio ambiente, la cuál genera ondas de choque que calientan e ionizan el gas.

En general, los chorros o jets presentan una serie de nudos alineados que se alejan de la

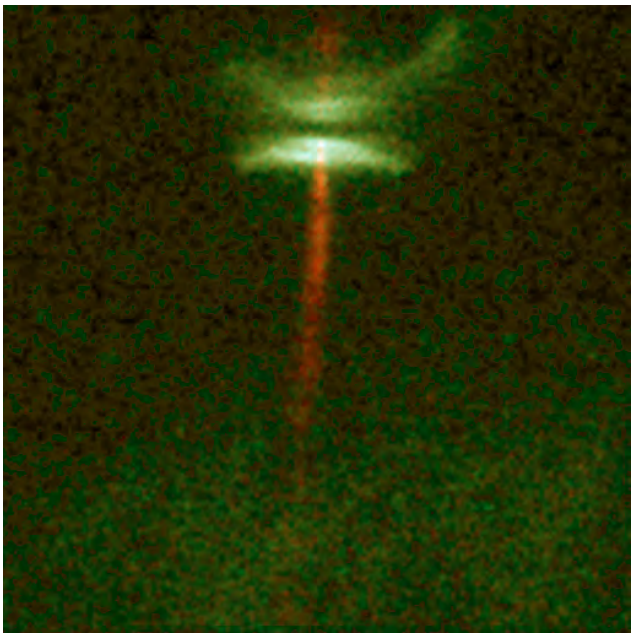

Figura 2.1: Objeto protoestelar HH 30. Se muestra una estrella recién formada rodeada de un disco de polvo. La luz de ésta ilumina la parte de arriba y abajo del disco, haciéndolos visibles. La región más densa del disco oculta a la estrella. El chorro rojizo emana como resultado del colapso del material que forma la estrella. La imagen es en el óptico (R), 675 nm. Créditos: C. Burrows (STScI & ESA), the WFPC 2 Investigation Definition Team, and NASA

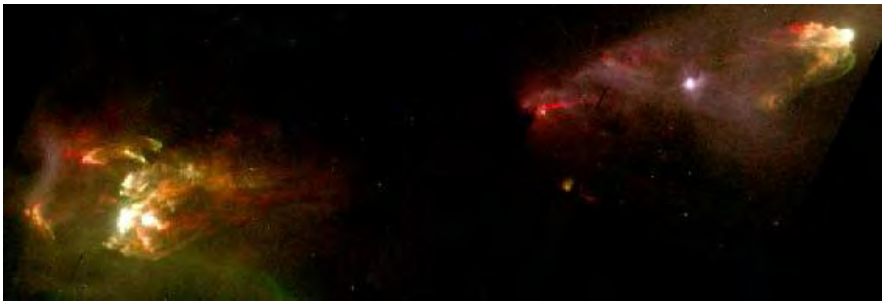

Figura 2.2: Objetos HH 1 y 2. Se encuentran ubicados cerca de la Nebulosa de Orión. La estrella fuente es ocultada por una nube de polvo y su localización es aproximadamente a medio camino entre los dos objetos. La imagen presenta una combinación de Hα en verde y [S II] en rojo. Créditos: J. Hester (ASU), WFPC2 Team, NASA

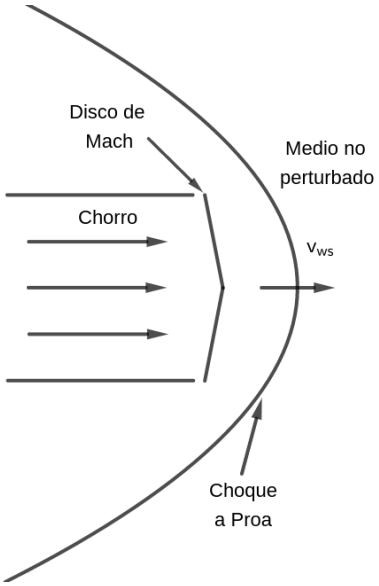

Figura 2.3: Diagrama de una superficie de trabajo. El chorro, que tiene velocidad supersónica, interactúa con el medio interestelar. Esta interacción genera dos choques: un choque principal (a proa) que barre el material del medio y un disco de Mach, que frena el material del mismo chorro. La estructura completa se mueve a una velocidad v_{ws}.

fuente emisora; el material que se encuentra más alejado de la fuente se denomina la cabeza del chorro, muchas veces siendo la región más extensa y brillante del objeto. La emisión de los nudos a lo largo del chorro es debida a ondas de choque que se generan dentro del chorro.

La cabeza de un chorro supersónico tiene una estructura de dos choques, la cuál se muestra en el diagrama de la Figura 2.3: un choque a proa que barre y acelera el material del medio interestelar, y un disco de Mach, que frena el material del chorro.

Los nudos se producen debido a la variabilidad de la emisión del flujo eyectado, que induce discontinuidades en el chorro, dando lugar a superficies de trabajo internas (ver Figura 2.4). Se produce entonces una cabeza principal y una cadena de nudos cerca de la fuente del jet. En el caso en que el jet se propague en un medio de menor densidad, la cabeza presenta mayor velocidad que las superficies de trabajo internas. Esto se traduce morfológicamente en una condensación rápida y brillante (la cabeza del chorro) muy alejada de la fuente, seguida de varios nudos más lentos y de menor intensidad cerca de la fuente. Si el chorro se mueve en un medio de mayor densidad, las superficies de trabajo internas se mueven a mayor velocidad que la cabeza, y eventualmente la alcanzan.

En general los jets se mueven en medios que son mayormente neutros, así que la zona inmediata post-choque emite líneas de Balmer excitadas colisionalmente. Después de esta zona (región de alta temperatura), se forma una zona de enfriamiento, donde la temperatura decrece y las distintas especies se recombinan. Esta región emite líneas prohibidas (como

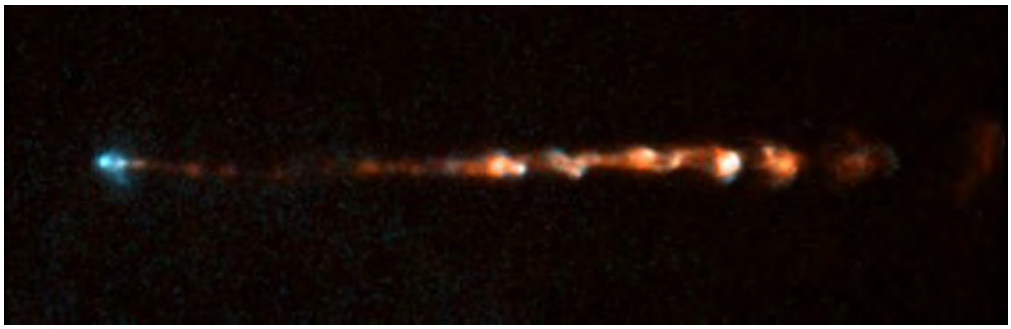

Figura 2.4: Imagen del objeto HH 34. Las regiones brillantes en los grumos son los nudos donde el material de mayor velocidad alcanza material del mismo chorro que avanza más lento (debido a la variabilidad en la velocidad de eyección). Esta interacción produce la emisión observada. La composición de colores en la imagen corresponde al óptico, Hα (cian) y [S II] (naranja). Créditos: NASA, ESA, and P. Hartigan (Rice University)

[S II], [O I] y [N II]) y líneas de recombinación de hidrógeno y helio.

Los choques a proa son más fuertes cerca de la cabeza y más débiles en las alas. Esto se debe a que en la cabeza el choque es perpendicular a la velocidad del material y en las alas el choque es oblícuo. En Raga et al. (2015a) se muestran resultados recientes sobre la emisión en choques a proa.

Los objetos HH presentan movimientos propios grandes (Herbig & Jones, 1981), así como altas velocidades radiales (Schwartz, 1981), por lo que tienen movimientos supersónicos con respecto al medio ambiente, donde la velocidad del sonido es aproximadamente de 3 km s^{-1} (en un gas neutro a una temperatura de 10^3 K). Su emisión óptica es debida a líneas que ocurren una vez que el gas se enfría detrás de la onda de choque (Schwartz, 1978).

De acuerdo con (Reipurth & Bally, 2001; Bally et al, 2002), los objetos HH son nebulosas relativamente pequeñas, de entre 20 y 30″. Muestran forma de choque a proa y/o una estructura tipo chorro (una colección o cadena de nudos). Estos objetos tienen velocidades de unos cuantos cientos de km s^{-1} hasta $\sim$ 1000 km s^{-1} dependiendo si vienen de estrellas de baja o alta masa. Las densidades de estos objetos se encuentran en un rango entre 10^2 y 10^5 cm^{-3}, mientras que sus grados de ionización van de entre 1 a 10 % para objetos de baja excitación, hasta casi 100 % para los objetos de alta excitación.

HH 1 y 2 fueron los primeros objetos HH descubiertos (Herbig, 1951; Haro, 1952). Estos son los objetos HH más brillantes en el cielo (junto con HH 80/81) y consisten en dos cabezas de jet alejándose uno del otro, separados por una distancia (proyectada) de 2′,5. Se encuentran localizados aproximadamente a 400 pc en la nube molecular Orion A (Bally et al, 2002).

Muchas de las características generales de los flujos HH fueron encontradas primero en este par de objetos. Por ejemplo, las primeras mediciones de movimientos propios en objetos HH se realizaron en HH 1 y 2 (Herbig & Jones, 1981). Estas mediciones mostraron que HH 1

y 2 forman parte de un chorro bipolar con velocidades entre 200 y 300 km s^{-1}, alejándose de la fuente emisora. Estas mismas observaciones muestran que el chorro se encuentra a una inclinación de 10°con respecto al plano del cielo y que posee una velocidad de aproximadamente 330 km s^{-1}.

Así mismo, HH 1 y 2 fueron los primeros en ser detectados en radio (Pravdo et al., 1985) , ultravioleta (Ortolani & D'Odorico, 1980) y rayos X (Pravdo et al., 2001). La fuente emisora de este chorro bipolar fue detectada en el contínuo de radio por Pravdo et al. (1985). Se encuentra localizada aproximadamente en el punto medio entre HH 1 y HH 2. Posteriormente se mostró que esta fuente, VLA 1, presenta una estructura de nudos ópticos alineados con el eje del sistema HH 1/2 (Bohigas et al., 1985) en dirección hacia HH 1. También se encontró un contrajet, el cual va en dirección hacia HH 2 y es visible sólo en el infrarrojo (Noriega-Crespo & Raga, 2012).

En esta segunda parte del trabajo, se explora de forma observacional y teórica el espectro de líneas de emisión así como los movimientos propios de los objetos HH 1 y 2 utilizando nuevas observaciones del Telescopio Espacial Hubble (HST). Se calcula la emisión de las líneas de Balmer producidas por procesos de recombinación y excitaciones colisionales. También se realiza una simulación numérica para modelar la intensidad en función de la posición y el tiempo de los nudos del jet HH 1 en las líneas rojas de [S II].

2.2. Recombination and collisionally excited Balmer lines

El trabajo presentado en este capítulo permite calcular de una manera sencilla la emisión de líneas de Balmer para modelos de ondas de choque.

La contibución en este artículo ha sido en la elección de parámetros atómicos y en el cálculo de las líneas de Balmer con recombinaciones + excitaciones colisionales.

En este modelo consideramos el equilibrio estadístico para los niveles excitados del átomo de hidrógeno. Se supone que estos niveles son poblados por recombinaciones de los electrones con el H II, transiciones espontáneas desde los niveles de mayor energía y excitaciones colisionales hacia arriba desde el estado base; mientras que las transiciones espontáneas hacia abajo son las responsables de despoblar los niveles de energía.

Como principales suposiciones del modelo, se consideran despreciables los términos correspondientes a las transiciones colisionales entre los niveles excitados, así como la fotoionización y la ionización colisional desde los niveles excitados, además de suponer que una buena parte de los átomos neutros se encuentran en el estado base. En este sentido, el modelo está

pensado para aplicarse en el régimen de baja densidad.

Las ecuaciones del equilibrio estadístico tienen una solución sencilla para los coeficientes de recombinación y de excitación colisional efectivos en términos de la "matriz de cascada", la cual describe una cascada de transiciones espontáneas (para los casos "B" y "A") alimentada tanto por recombinaciones como por excitaciones colisionales. De esta solución se obtienen los coeficientes de emisión para las transiciones entre pares de niveles de energía.

Como un resultado importante de este cálculo, se obtuvo que en el rango de temperaturas debajo de aproximadamente 10^4 K la tasa de energía por recombinación domina, mientras que, para temperaturas mayores la tasa de energía debida a las excitaciones colisionales es dominante.

Si se supone que la mayor parte de los electrones proviene del H II, entonces se obtiene que los cocientes de líneas para el caso ópticamente delgado provenientes de una región homogénea son solo función de la temperatura y de la fracción de ionización. Como resultado de este hecho, se encuentra que los cálculos correspondientes de cocientes de líneas de Balmer muestran una transición entre un régimen de baja temperatura, y uno de alta temperatura. En ambos casos se obtiene una débil dependencia tanto de la temperatura como de la fracción de ionización.

En el caso de bajas temperaturas, los cocientes de líneas están dominados claramente por los procesos de recombinación, mientras que en el caso de altas temperaturas dominan las excitaciones colisionales. En la transición entre estos dos regímenes, la dependencia de los cocientes de líneas con respecto a la temperatura y la fracción de ionización es fuerte.

Esta caracterıística permite diferenciar observacionalmente entre regiones de líneas de Balmer de recombinación y regiones con líneas excitadas colisionalmente, lo cual tiene una aplicación directa en la observación de ondas de choque, ver los capítulos 2.3 (Raga et al., 2015a) y 2.4 (Raga et al., 2015c) de esta tesis.

Finalmente, se obtuvo que en el caso de un gas en equilibrio coronal (donde existe balance entre las ionizaciones colisionales y las recombinaciones radiativas del H), la emisión de las líneas de Balmer siempre está dominada por las excitaciones colisionales. Esto significa que para obtener líneas de recombinación de Hα y Hβ, es necesario tener fracciones de ionización de H substancialmente mayores que la de equilibrio coronal, es decir, una baja fracción de neutros. En la zona inmediatamente detrás del choque, la fracción de neutros es mayor a la del caso en equilibrio coronal, y por lo tanto la emisión Hα y Hβ está dominada por las excitaciones colisionales.

Revista Mexicana de Astronomía y Astrofísica, **51**, 229–237 (2015)

RECOMBINATION AND COLLISIONALLY EXCITED BALMER LINES

A. C. Raga, A. Castellanos-Ramírez, A. Esquivel, A. Rodríguez-González, & P. F. Velázquez

Instituto de Ciencias Nucleares, Universidad Nacional Autónoma de México, Mexico.

Received 2014 November 24; accepted 2015 July 28

RESUMEN

Presentamos un modelo para el equilibrio estadístico de los niveles de H, considerando recombinaciones a los niveles excitados, excitaciones colisionales partiendo desde el nivel fundamental y transiciones radiativas espontáneas. Este problema tiene una simple solucion en términos de la "matriz de cascada", que describe una cascada de transiciones espontáneas alimentada tanto por recombinaciones como por excitaciones colisionales. Las predicciones resultantes de cocientes de líneas de Balmer muestran una transición entre un régimen de baja temperatura y uno de alta temperatura (dominados por recombinaciones y por excitaciones colisionales, respectivamente), ambos con sólo una dependencia débil de la temperatura. Esta clara característica permite una diferenciación observacional directa entre regiones de líneas de Balmer de recombinación y regiones con líneas excitadas colisionalmente. Encontramos que para un gas en equilibrio coronal las líneas de Hα y Hβ se excitan colisionalmente a todas las temperaturas. Para obtener líneas de Hα y Hβ de recombinación, es necesario tener fracciones de ionización de H substancialmente mayores que la de equilibrio coronal (por ejemplo, como las presentes en un gas fotoionizado).

ABSTRACT

We present a model for the statistical equilibrium of the levels of H, considering recombinations to excited levels, collisional excitations up from the ground state and spontaneous radiative transitions. This problem has a simple "cascade matrix" solution, describing a cascade of downwards spontaneous transitions fed by both recombinations and collisional excitations. The resulting predicted Balmer line ratios show a transition between a low temperature and a high temperature regime (dominated by recombinations and by collisional excitations, respectively), both with only a weak line ratio vs. temperature dependence. This clear characteristic allows a direct observational identification of regions in which the Balmer lines are either recombination or collisionally excited transitions. We find that for a gas in coronal ionization equilibrium the Hα and Hβ lines are collisionally excited for all temperatures. In order to have recombination Hα and Hβ it is necessary to have higher ionization fractions of H than the ones obtained from coronal equilibrium (e.g., such as the ones found in a photoionized gas).

Key Words: Herbig-Haro objects — hydrodynamics — ISM: individual objects (HH1, HH2) — ISM: kinematics and dynamics — shock waves

1. INTRODUCTION

Seaton (1959a,b) presented calculations of the recombination cascade of hydrogen (H), considering the transitions between different principal (i.e., energy) quantum numbers n, and assuming an equilibrium distribution between the angular momentum levels l corresponding to a given n. The effect of considering explicitly the different values of l was studied by Pengelly & Seaton (1964). Brocklehurst (1970, 1971) calculated the statistical equilibrium for the (n, l) levels of H, also including redistribution between the different l values (at constant n) due to collisions with protons, as well as collisions with electrons producing transitions between different n

values. More recent results on the recombination cascade of hydrogenic ions (including redistribution between different angular momentum levels through collisions with protons) are presented by Storey & Hummer (1995). Even more recently, Storey & Sochi (2014) analyzed the collisional excitation and recombination of the excited levels of H resulting from non-thermal electron distribution functions.

Aggarwal (1983) calculated the electron impact collisional excitation rates for the $1 \rightarrow 2$ and $1 \rightarrow 3$ transitions, and suggested that they could have an important effect on the prediction of low lying lines of H. This effect was evalued in more detail by Hummer & Storey (1987). More recently, Stasińska & Izotov (2001) and Luridiana et al. (2003) calculated photoionized region models from which they concluded that for some parameters the collisional excitations from the $n = 1$ levels can have an effect of $\approx 5\%$ in the predicted Balmer line intensities.

The effect of collisional excitations upwards from the $n = 1$ levels of H of course can have a dominant effect in astrophysical shocks. Immediately after the shock, one has a high temperature region (of $\approx 10^5$ K for a 100 km s^{-1} shock) in which H can be partially neutral, though rapidly becoming collisionally ionized. In this region, the $1 \rightarrow n$ electron collision excitations dominate over the recombinations to the excited levels of H. This effect was included in the shock models of Raymond (1979), who added the contribution of the collisional excitations of the low lying levels of H to the recombination cascade.

In this paper, we present a simple model for the statistical equilibrium of the excited levels of H including both the recombinations and the upwards electron collisional excitations from the ground state. This model can be solved with the traditional "cascade matrix" solution (see, e.g., the book of Osterbrock & Ferland 2006), with a cascade of downwards spontaneous transitions which is fed both by recombinations and by collisional excitations from the ground state.

In § 2, we discuss the statistical equilibrium and the calculation of line emission coefficients, giving the results obtained for the Hα emission. In § 3, we present the results obtained for the Hα/Hβ and Hβ/Hγ ratios. These results are summarized in § 4. Finally, the paper has two appendices which give all the necessary parameters for solving the 5-level H atom problem, and analytic fits giving the predicted line intensities and/or line ratios as a function of temperature and ionization fraction of the gas.

2. THE STATISTICAL EQUILIBRIUM AND THE EMISSION COEFFICIENTS

Let us consider the statistical equilibrium for the excited levels of H, under the assumption that they are populated by recombinations (due to electron collisions with HII), spontaneous transitions from higher energy levels and upward collisional excitations from the ground ($n = 1$) state, and depopulated only by downwards spontaneous transitions. For the energy level $k > 1$, we then have:

$$n_e \left[n_{HII} \alpha_k(T) + n_{HI} q_{1,k}(T) \right] + \sum_{m>k} n_m A_{mk} = n_k \sum_{m<k} A_{km} \, . \quad (1)$$

In this equation, $\alpha_k(T)$ is the radiative recombination coefficient to level k, $q_{1,k}(T)$ is the electron collisional excitation coefficient for the $1 \rightarrow k$ transition, the A_{km} are the Einstein spontaneous transition coefficients, n_e is the electron number density, n_{HII} is the ionized H number density, and n_{HI} the neutral H density.

In this equilibrium equation, we neglect the collisional transitions between the excited levels, and the photo and collisional ionizations from the excited levels. Furthermore, we assume that the number density of the $n = 1$ level is equal to n_{HI} (i.e., that the vast majority of neutral atoms are in the ground state). This amounts to a "low density regime" assumption, in which the only active collisional transitions (as well as the photoionizations) are the ones starting from the ground state. This is a clearly valid assumption for the permitted transitions of H at interstellar medium densities.

The solution to the statistical equilibrium equations (see equation 1) can be written as:

$$n_k = n_e \left[n_{HII} \alpha_k^{(eff)}(T) + n_{HI} q_{1,k}^{(eff)}(T) \right] , \quad (2)$$

with an effective recombination coefficient defined in the usual way as:

$$\alpha_k^{(eff)}(T) = \frac{\sum_{m \geq k} C_{mk} \alpha_m(T)}{\sum_{m<k} A_{km}} , \quad (3)$$

and an analogously defined effective collisional excitation coefficient:

$$q_k^{(eff)}(T) = \frac{\sum_{m \geq k} C_{mk} q_{1,m}(T)}{\sum_{m<k} A_{km}} , \quad (4)$$

in terms of the "cascade matrix" C_{mk}. This matrix can be calculated recursively by first computing the

probability P_{km} of having a direct $k \rightarrow m$ transition:

$$P_{km} = \frac{A_{km}}{\sum_{l<k} A_{kl}}\,, \tag{5}$$

and then using these branching ratios to calculate iteratively the terms of the cascade matrix

$$C_{km} = C_{k,m+1} P_{m+1,m} + P_{km}\,, \tag{6}$$

which give the probability of having a $k \rightarrow m$ transition either directly or by a cascade of intermediate spontaneous transitions. The diagonal elements of the matrix are given a value of 1 (i.e., $C_{kk} = 1$). A discussion of the cascade matrix formalism can be found in the book of Osterbrock & Ferland (2006).

Once the effective recombination and collisional excitation coefficients have been obtained, one can calculate the emission coefficients for the $k \rightarrow m$ transition as:

$$j_{km} = \frac{n_e}{4\pi}\left[n_{HII}\epsilon^r_{km}(T) + n_{HI}\epsilon^c_{km}(T)\right]\,, \tag{7}$$

where

$$\epsilon^r_{km}(T) = \alpha^{(eff)}_k(T) A_{km} E_{km}\,,$$

and

$$\epsilon^c_{km}(T) = q^{(eff)}_{1,k}(T) A_{km} E_{km}\,,$$

(with E_{km} being the energy of the $k \rightarrow m$ transition).

We should note that in the above derivation we have considered the energy levels of H to have equilibrium populations for their angular momentum levels (i.e., that for a given n, the angular momentum levels l have relative populations proportional to their statistical weights $4l + 2$). As shown in the classical paper of Brocklehurst (1971), more detailed models for the population of the levels of H (considering the transitions between the different angular momenta due to collisions with protons) give small deviations (of order $\sim 2\%$) in the predictions of the ratios between the lower lying Balmer line intensities. We do not consider these effects in the present paper.

With the Einstein coefficients A_{km}, the collisional excitation coefficients $q_{1,m}(T)$ and the recombination coefficients $\alpha_m(T)$ we can calculate the effective recombination and collisional excitation coefficients $\alpha^{(eff)}_m(T)$ and $q^{(eff)}_m(T)$ (given by equations 3 and 4, and the recombination and collisional enegy rates (ϵ^r_{km} and ϵ^c_{km}, see equation 7). As described in detail in Appendix A, we have done this calculation for the $n = 1 \rightarrow 5$ levels of H, considering "case A" (i.e., with optically thin lines) and "case B" (in which the Lyman transitions are optically thick).

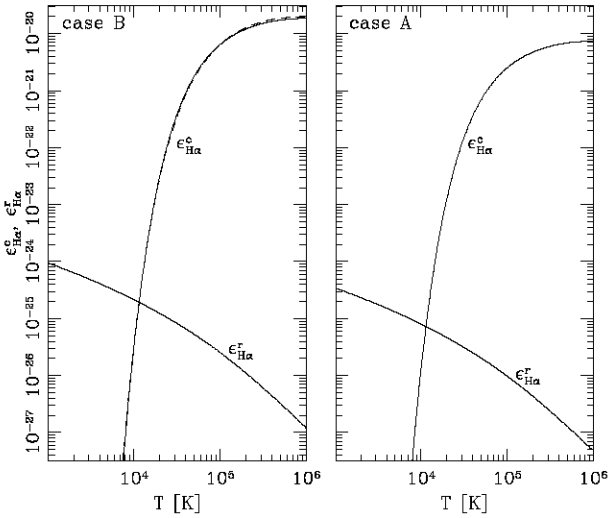

Fig. 1. Contributions to the Hα emission coefficients of the recombination cascade ($\epsilon^r_{H\alpha}$) and the collisional excitation cascade ($\epsilon^c_{H\alpha}$) as a function of temperature, for the "case B" (left) and "case A" (right) approximations (see the discussion in § 2). The solid lines give the numerical results from the cascade calculations, and the dashed lines give the analytic fits to the "case B" results, described in Appendix B (left frame).

In Figure 1, we show the recombination and collisional energy rates $\epsilon^r_{H\alpha}$ and $\epsilon^c_{H\alpha}$ (see equation 7) as a function of temperature for "case B" (left, optically thick Lyman lines) and "case A" (right, optically thin Lyman lines). For the "case B" coefficients, we have also calculated analytic fits, which are described in Appendix B (dashed lines in the left panel of Figure 1). It is clear that for temperatures below $\approx 10^4$K the recombination energy rate is dominant, but for larger temperatures the collisional excitation energy rate dominates by many orders of magnitude. Because of this, even if the product $n_e n_{HI}$ is very small (i.e., because H is mostly ionized), the collisional excitation contribution to the Hα emission becomes dominant at high enough temperatures. This effect is discussed in more detail in the following Section.

3. THE Hα/Hβ AND Hβ/Hγ LINE RATIOS

We now assume that most of the free electrons come from the HII, and set $n_e = n_{HII} = x n_H$ and $n_{HI} = (1 - x) n_H$, where n_H is the total H density.

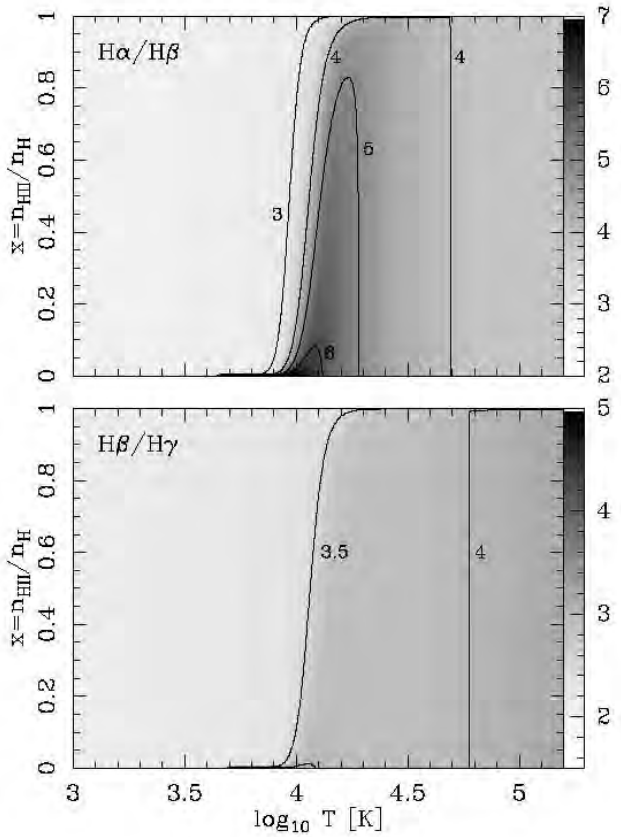

Fig. 2. Case B (i.e. optically thick Lyman lines) Hα/Hβ (top) and Hβ/Hγ ratios (bottom) as a function of temperature and H ionization fraction ($x = n_{HII}/n_H$) calculated with the emission coefficients given by equation 8. The line ratios are shown with labeled contours and with linear greyscales given by the bars on the right.

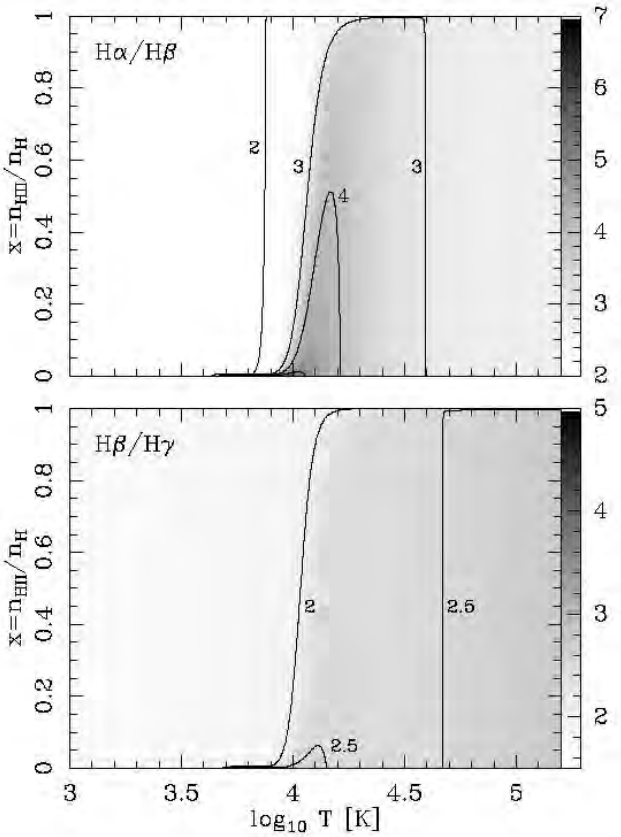

Fig. 3. Case A (i.e. optically thin Lyman lines) Hα/Hβ (top) and Hβ/Hγ ratios (bottom) as a function of temperature and H ionization fraction ($x = n_{HII}/n_H$) calculated with the emission coefficients given by equation 8. The line ratios are shown with labeled contours and with linear greyscales given by the bars on the right.

Then, from equation (7) we obtain the line emission coefficients as:

$$j_{km} = \frac{x n_H^2}{4\pi} \left[x \epsilon^r_{km}(T) + (1-x) \epsilon^c_{km}(T) \right] . \quad (8)$$

Therefore, the observed ratios of optically thin lines from a homogeneous region (which are proportional to the ratios of the corresponding emission coefficients) are only a function of the temperature T and the H ionization fraction x (since the dependence on the H density n_H cancels out as all emission coefficients are proportional to n_H^2, see equation 8).

In Figures 2 and 3 we show the resulting Hα/Hβ and Hβ/Hγ ratios as function of T and x for the "case B" (Figure 2) and "case A" (Figure 3) approximations (see § 2 and Appendix A). It is clear that at temperatures smaller than $\approx 10^4$K, we obtain an almost constant value for the line ratios (as has been shown repeated times for the H recombination lines, see e.g. Brocklehurst 1971), a region around $T \approx 10^4$K in which the line ratios show a relatively strong dependence on both x and T, and a high temperature regime in which the line ratios again are almost constant.

This behavior is also shown in Figures 4 (case B) and 5 (case A), in which the line ratios are shown as a function of temperature for three fixed values of the ionization fraction of H ($x = 10^{-3}$, 0.5 and 0.999). It is clear that the line ratios have a "low temperature regime" (dominated by the recombination cascade) and a "high temperature regime" (dominated by the collisional excitation cascade) in which the line ratios are independent of the H ionization fraction x. In the transition between these two regimes, the line ratios depend on both T and x.

In the low temperature regime, the temperature dependence of the line ratios is weak, reflecting the weak (and similar) temperature dependencies of the

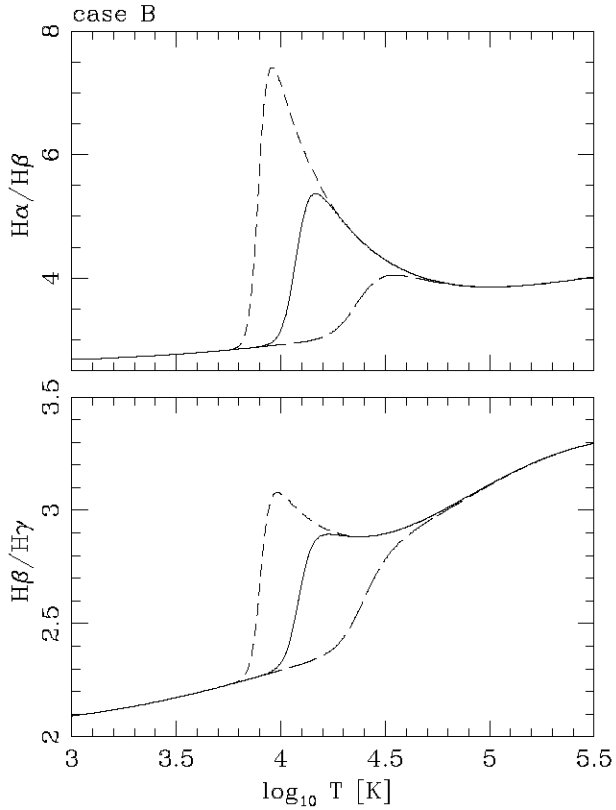

Fig. 4. Case B Hα/Hβ (top) and Hβ/Hγ ratios (bottom) as a function of temperature for three different values of the H ionization fraction: $x = n_{HII}/n_H = 0.999$ (long dashes), 0.5 (solid line), and 0.001 (short dashes).

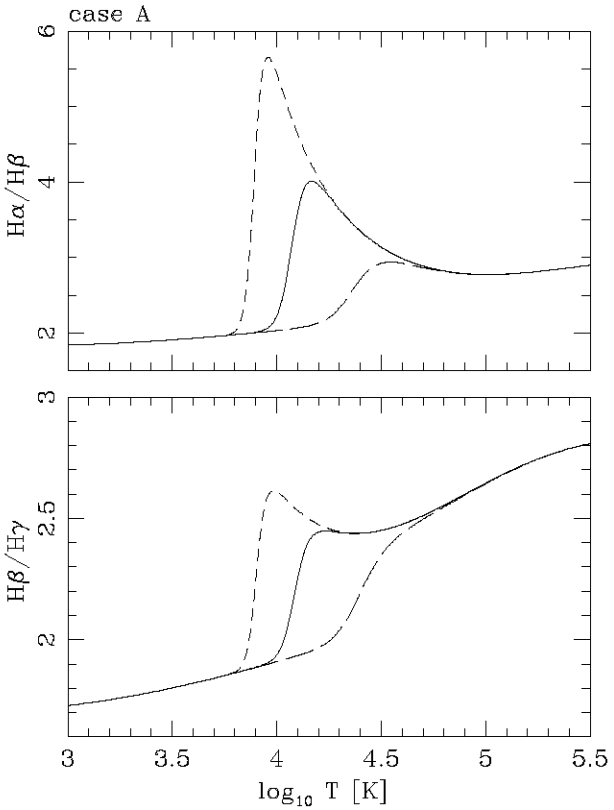

Fig. 5. Case A Hα/Hβ (top) and Hβ/Hγ ratios (bottom) as a function of temperature for three different values of the H ionization fraction: $x = n_{HII}/n_H = 0.999$ (long dashes), 0.5 (solid line), and 0.001 (short dashes).

recombination coefficients to the excited levels of H. In the high temperature regime, the temperature dependence of the line ratios is also small. This is because the populations of the excited levels m through collisional excitations are dominated by the direct excitation to level m. Therefore, the temperature dependence of the n_m/n_k ratio (which determines the ratios of lines starting from the pair of levels) is given by a term of the form:

$$\frac{n_m}{n_k} \propto e^{-(E_m - E_k)/k_B T}\,, \qquad (9)$$

where we have neglected the (weak) temperature dependence of the collisional excitation coefficients (see Appendix A). It is clear that for $T \gg (E_m - E_k)/k_B$ (where k_B is Boltzmann's constant) the line ratios basically become independent of T. These temperatures are $(E_4 - E_3)/k_B = 7681$ K for the Hα/Hβ ratio and $(E_5 - E_4)/k_B = 3551$ K for the Hβ/Hγ ratio. In Appendix B we give approximate analytic forms for calculating the case B Hα/Hβ and Hβ/Hγ ratios.

From Figures 2-5 we see that for ionization fractions $x \to 1$, the line ratios preserve their recombination cascade values up to increasing values of the temperature. This result is intuitively clear, since for $x = 1$ (i.e., for a neutral fraction $1 - x = 0$) no collisional excitations (up from the $n = 1$ level) take place. This is seen in equation (8), from which for $x = 1$ we obtain $j_{km} \propto \epsilon^r_{km}(T)$.

In order to quantify this effect, we calculate the neutral fraction $1 - x_c$ (as a function of T) for which the Hα emission has equal contributions from collisional excitations and from the recombination cascade. We find this neutral fraction by setting the two terms within the square brackets of equation 8 equal to each other, from which we obtain:

$$1 - x_c = \frac{1}{1 + \epsilon_c(H\alpha)/\epsilon_r(H\alpha)}\,. \qquad (10)$$

From our 5-level H atom calculation, we compute the $1 - x_c$ neutral fraction (at which the recombination cascade and collisional excitation contributions

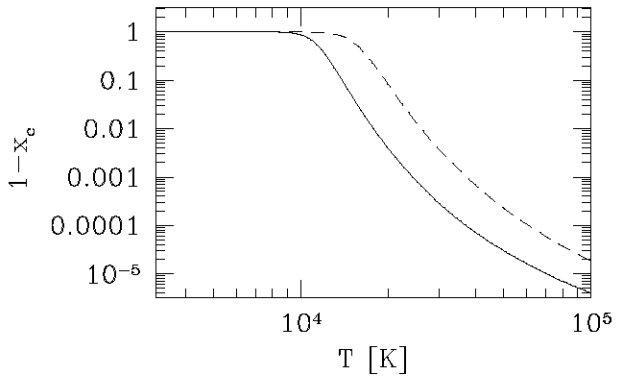

Fig. 6. The solid line shows the neutral H fraction $1-x_c$ (above which the contribution of collisional excitation to the Hα emission dominates over the recombination cascade) as a function of T. Indistinguishable $1-x_c$ vs. T curves are obtained from cases A and B. The dashed line shows the neutral H fraction given by the coronal ionization equilibrium condition. The coronal equilibrium neutral fraction is higher than $1-x_c$ at all temperatures.

to Hα are equal) as a function of temperature, and show the results in Figure 6.

This figure can be interpreted as follows. For neutral fractions larger than $1-x_c$, the Hα emission is dominated by the collisional excitation contribution. Therefore, for temperatures $T < 10^4$ K, in order to have an important contribution from collisional excitations one needs to have neutral fractions very close to 1 (so that the recombination cascade term of equation 8 becomes very low). However, for $T > 10^4$ K the collisional excitation contribution becomes dominant for monotonically decreasing $1-x_c$ values (see Figure 6).

Interestingly, if we compare the temperature dependence of the neutral fraction corresponding to coronal ionization equilibrium (i.e., the ionization state determined from the equilibrium between collisional ionizations and radiative recombinations of H), we see that coronal equilibrium gives higher neutral fractions at all temperatures. Therefore, the Hα emission of a gas in coronal ionization equilibrium is dominated by the collisional excitation contribution at all temperatures.

4. DISCUSSION

We have derived a simple model of a spontaneous transition cascade fed by both recombinations and electron impact excitations upwards from the ground level of H. With this model, the level populations and the line emission coefficients can be written in terms of the usual "effective recombination coefficients" (equation 3) and of equivalently defined "effective collisional excitation coefficients" (equation 4).

We calculated the recombination and the collisional contributions to the emission coefficients of the Hα, Hβ and Hγ lines as a function of temperature and H ionization fraction $x = n_{HII}/n_H$ and found that the Balmer line ratios have a transition from a "low temperature" to a "high temperature" regime, with approximately temperature-independent ratios in both regimes. The low temperature regime of course corresponds to the recombination cascade, which is known to produce line ratios with only a weak temperature dependence. The high temperature regime corresponds to collisionally excited H lines in the regime in which kT is much larger than the energy difference between the upper levels giving rise to the pair of lines in the ratio (for which the line ratio again shows only a weak dependence on temperature).

The details of the transition between the low and the high temperature regimes of the line ratios depend on the ionization fraction x of the gas (see Figures 2 and 3). For low values of x, the Hα/Hβ and Hβ/Hγ line ratios show strong peaks as a function of temperature, before settling onto the high temperature regime values. These peaks disappear for values $x \approx 1$, and a monotonic transition between the low and high temperature line ratio regimes is then obtained (see Figures 4 and 5).

The existence of this clear transition between a low and a high temperature regime (in which the H level populations are dominated by recombinations and by collisional excitations, respectively) has interesting implications for observations of shock waves. For example, in high angular resolution observations of Herbig-Haro (HH) objects one might detect both the Balmer line emission of the hot, immediate post-shock region (with temperatures in excess of $\approx 10^5$K, where one would see the effect of the collisional excitations) and of the cooler ($\approx 10^3 \rightarrow 10^4$K) recombination region (dominated by the recombination cascade). The first region would be characterized by an Hα/Hβ ratio of ≈ 4 (see the high temperature regime of this ratio in Figure 4), and the second region by the recombination Hα/H$\beta \approx 2.8$ value (see the low temperature regime in Figure 4 or, e.g., Pengelly & Seaton 1964). This effect is seen in the new Hα and Hβ images of HH 1 and 2 of Raga et al. (2015).

Our results might also be applicable for observations of Balmer dominated, non-radiative shocks (in which the Balmer line emission is due to collisional excitation in the immediate post-shock region, see,

e.g., the reviews of Raymond 2001 and Heng 2010). With high signal-to-noise observations of the Hα, Hβ and Hγ lines, it would be possible to use the predictions of the high temperature regime Hα/Hβ and Hβ/Hγ line ratios (see the $T > 10^5$K region of Figure 4 and the interpolations given by equations B18-B19) to obtain a simultaneous determination of the extinction and of the average temperature of the emitting gas.

Very interestingly, we find that for a gas in coronal ionization equilibrium (i.e., the equilibrium resulting from the balance between collisional ionizations and radiative recombinations of H) the Hα emission is dominated by the collisional excitation contribution (see Figure 6). In order for the recombination cascade to have a dominant contribution to the Hα emission one needs a gas with considerably higher ionization fraction (i.e., lower neutral fraction) than the coronal equilibrium value. This situation is found, e.g., in photoionized regions (in which high ionizations are found even for relatively low temperature values as a result of the high photoionization rate) and in recombination regions of shock waves (in which the recombining gas relaxes toward, but never reaches, coronal equilibrium). On the other hand, the immediate post-shock collisional ionization regions have neutral fractions higher than coronal equilibrium, so that they have an Hα emission which is clearly dominated by the collisional excitation contribution.

Finally, the work presented in this paper gives a straightforward method for calculating the Balmer line emission from shock wave models. This can be done by solving the recombination+collisional excitation cascade model (for which all parameters are given in Appendix A) or by using the analytic fits which have been obtained for the case B emission coefficients and line ratios (see Appendix B).

We acknowledge support from CONACyT grants 101356, 101975 and 167611, DGAPA-UNAM grants IN105312 and IG100214. We an acknowledge anonymous referee for comments which led to the results presented in Figure 6.

APPENDICES

A. COEFFICIENTS FOR THE RECOMBINATION AND COLLISIONAL EXCITATION CASCADE

In this Appendix we give the atomic parameters and coefficients used to calculate the statistical equilibrium for the $n = 3 \rightarrow 5$ levels of H (see equations 2-6). We have taken the Einstein A coefficients and the collision strengths Ω by appropriately grouping the parameters given in the Chianti database (Dere et al. 1997; Landi et al. 2006). To describe the temperature dependencies of the collision strengths of the $1 \rightarrow k$ transitions we calculated least squares polynomials of the form

$$\Omega_{1,k}(T) = \sum_{p=0}^{5} a_p t^k \,, \tag{A11}$$

with $t = \log_{10}(T/10^4\mathrm{K})$ in the $T = 10^3 \rightarrow 10^8$K temperature range. The values of the a_k coefficients for the transitions to levels $k = 2 \rightarrow 5$ (as well as the A coefficients) are given in Table 1.

The $q_{1,k}$ collisional excitation coefficients were then calculated with the standard relation

$$q_{1,k}(T) = \frac{8.629 \times 10^{-6}}{2T^{1/2}} \Omega_{1,k}(T) e^{-E_{1,k}/k_B T} \,, \tag{A12}$$

with T in K, and where we considered that the statistical weight of the ground state is $g_1 = 2$.

We calculated the recombination coefficients α_k to the excited levels of H following Seaton (1959a), and we then calculated least squares fits of the form

$$\log_{10} \alpha_k = \sum_{p=0}^{4} b_p t^k \,, \tag{A13}$$

with $t = \log_{10}(T/10^4\mathrm{K})$, in the $T = 10^3 \rightarrow 10^6$K temperature range. The coefficients for the polinomials interpolating the $\alpha_k(T)$ are given in Table 2 for $k = 1 \rightarrow 5$.

With these coefficients we calculated the recombination cascade and the collisionally excited cascades described in § 2. The "case A" calculation was done with the Einstein A coefficients given in Table 1, and the "case B" calculation was done setting to zero the A coefficients of the Lyman transitions (i.e., setting $A_{k,1} = 0$ for all k).

B. ANALYTIC FITS FOR THE "CASE B" EMISSION

In this Appendix we present analytic fits to the temperature dependence of the "case B" recombination and collisional excitation contributions to the Hα emission and to the temperature dependence of the Hα/Hβ and Hβ/Hγ ratios of the "case B" recombination and collisional contributions:

$$\epsilon_r(H\alpha) = \frac{4.85 \times 10^{-23}}{T^{0.568} + 3.85 \times 10^{-5} T^{1.5}} \,, \tag{B14}$$

TABLE 1

EINSTEIN A COEFFICIENTS AND FITS FOR THE COLLISION STRENGTHS

transition	A^{a} [s^{-1}]	a_0	a_1	a_2	a_3	a_4	a_5
$1 \rightarrow 2$	4.695×10^8	0.7925	0.9385	−1.5361	2.2035	−0.5345	0.0409
$1 \rightarrow 3$	5.567×10^7	0.2500	0.2461	−0.3297	0.3892	−0.0928	0.0071
$1 \rightarrow 4$	1.279×10^7	0.1125	0.1370	−0.1152	0.1209	−0.0276	0.0020
$1 \rightarrow 5$	4.128×10^6	0.0773	0.0678	−0.0945	0.0796	−0.0177	0.0013

[a]Also: $A_{32} = 4.410 \times 10^7 s^{-1}$, $A_{42} = 8.419 \times 10^6 s^{-1}$, $A_{43} = 8.986 \times 10^6 s^{-1}$, $A_{52} = 2.530 \times 10^6 s^{-1}$, $A_{53} = 2.201 \times 10^6 s^{-1}$ and $A_{54} = 2.699 \times 10^6 s^{-1}$.

TABLE 2

FITS FOR THE RECOMBINATION COEFFICIENTS

levels	b_0	b_1	b_2	b_3	b_4
1	−12.8049	−0.5323	−0.0344	−0.0305	−0.0017
2	−13.1119	−0.6294	−0.0998	−0.0327	0.0001
3	−13.3377	−0.7161	−0.1435	−0.0386	0.0077
4	−13.5225	−0.7928	−0.1749	−0.0412	0.0154
5	−13.6820	−0.8629	−0.1957	−0.0375	0.0199

to better than 3% in the $10^3 \rightarrow 10^6$K temperature range,

$$\epsilon_c(H\alpha) = \frac{3.57 \times 10^{-17}}{T^{0.5}} e^{-140360/T} \times \left(1 + \frac{7.8}{1 + 5 \times 10^5/T}\right), \quad \text{(B15)}$$

to better than 8% in the $10^4 \rightarrow 10^6$K temperature range,

$$\frac{\epsilon_r(H\alpha)}{\epsilon_r(H\beta)} = 2.674 + \frac{1.383}{1 + (9 \times 10^4/T)^{0.8}}, \quad \text{(B16)}$$

to better than 1% in the $10^3 \rightarrow 10^6$K temperature range,

$$\frac{\epsilon_r(H\beta)}{\epsilon_r(H\gamma)} = 1.984 + \frac{0.96}{1 + (9 \times 10^4/T)^{0.64}}, \quad \text{(B17)}$$

to better than 0.7% in the $10^3 \rightarrow 10^6$K temperature range,

$$\frac{\epsilon_c(H\alpha)}{\epsilon_c(H\beta)} = 3.35e^{-7681/T} + \frac{1.05}{(1 + 4.5 \times 10^4/T)^4}, \quad \text{(B18)}$$

to better than 0.7% in the $10^4 \rightarrow 10^6$K temperature range, and

$$\frac{\epsilon_c(H\beta)}{\epsilon_c(H\gamma)} = 3.35e^{-3551/T} + \frac{1.26}{(1 + 10^4/T)^3}, \quad \text{(B19)}$$

to better than 0.8% in the $10^4 \rightarrow 10^6$K temperature range.

In these interpolation fomulae, T is the temperature in K. The fits to the recombination and collisionally excited Hα emission (equations B14-B15) are shown in Figure 1.

REFERENCES

Aggarwal, K. M. 1983, MNRAS, 202, 15
Brocklehurst, M. 1970, MNRAS, 148, 417
Brocklehurst, M. 1971, MNRAS, 153, 471
Dere, K. P., Landi, E., Mason, H. E., Monsignori Fossi, B. C., & Young, P. R. 1997, A&AS, 125, 149
Heng, K. 2010, PASA, 27, 23
Hummer, D. G., & Storey, P. J. 1987, MNRAS, 224, 801
Landi, E., Del Zanna, G., Young, P. R., Dere, K. P., Mason, H. E., & Landini, M., 2006, ApJS, 162, 261
Luridiana, V., Peimbert, A., Peimbert, M. & Cerviño, M. 2003, ApJ, 592, 846
Osterbrock, D. E., & Ferland, G. J. 2006, Astrophysics of gaseous nebulae and active galactic nuclei, University Science Books (Sausalito, USA)
Pengelly, R. M., & Seaton, M. J. 1964, MNRAS, 127, 165
Raga, A. C., Reipurth, B., Castellanos-Ramírez, A., Chiang, H-F, & Bally, J. 2015, ApJ, in press
Raymond, J. C. 1979, ApJS, 39, 1
Raymond, J. C. 2001, SSRv, 99, 209
Seaton, M. J. 1959a, MNRAS, 119, 81
Seaton, M. J. 1959b, MNRAS, 119, 90
Stasińska, G., Izotov, Y. 2001, A&A, 378, 817
Storey, P. J., Sochi, T. 2014, MNRAS, in press

A. Castellanos-Ramírez, A. Esquivel, A. C. Raga, A. Rodríguez-González, P. F. Velázquez: Instituto de Ciencias Nucleares, Universidad Nacional Autónoma de México, Apdo. Postal 70-543, 04510 D.F., México (raga, juan.rodriguez@nucleares.unam.mx).

2.3. Collisionally Excited Filaments in Hubble Space Telescope Hα and Hβ images of HH 1/2

En este capítulo se describen nuevas imágenes en Hα y Hβ del sistema HH 1/2 tomadas con el HST. Dichas imágenes muestran algunos efectos interesantes que no se han observado hasta ahora en estudios de la estructura de emisión de líneas en los objetos HH.

Mi contribución en este trabajo ha sido básicamente en el desarrollo de la teoría de las líneas de Balmer con recombinaciones + excitaciones colisionales y en la interpretación de los cocientes de línea de HH 1/2.

La región de HH 1 y HH 2 fue observada con los filtros Hα (F656N) y Hβ (F487N) el 16 de Agosto del 2014 con la cámara WFC3 del HST. La reducción de las imágenes se llevó a cabo utilizando las técnicas usuales con el HST. Con la finalidad de evitar regiones muy extendidas dominadas por el ruido al momento de calcular el cociente de líneas, elegimos un valor mínimo para las emisiones. También, para realizar el cálculo de las razones Hα/Hβ intrínsecas, debemos aplicar una corrección de desenrojecimiento.

El procedimiento es como sigue: calculamos las razones observadas para todos los pixeles tal que la intensidad del flujo Hβ observado sea mayor que el mínimo fijado. Luego obtenemos un valor medio $<$ Hα/Hβ $>_{\rm obs}$= 3,8, para ambos HH 1 y HH 2. Comparando este valor con aquel obtenido para el caso B de la cascada de recombinación, 2.8, y utilizando la curva de extinción galáctica promedio, obtenemos un valor del exceso de color $E(B-V) = 0{,}27$. Este valor obtenido es un poco menor que el valor estándar de 0.35 (Brugel et al., 1981). Para calcular los cocientes desenrojecidos, multiplicamos los valores observados por un factor 2.8/3.8, asumiendo básicamente que la extinción hacia HH 1 y 2 no depende de la posición.

Los valores desenrojecidos de Hα/Hβ en el caso de HH 2 toman valores en el rango de 2 a 6. Los valores más altos se localizan en regiones de estructura filamentaria en el borde principal de la parte delantera del choque

En el mapa del cociente Hα/Hβ intrínseco para HH 1 (donde se ha utilizado el mismo criterio para el valor mínimo del flujo de Hβ), se observa que Hα/H$\beta > 4$ en un filamento delgado en el lado este de la cabeza.

De los mapas obtenidos se observa, en ambos objetos, que para valores bajos en la intensidad de Hβ se obtiene una distrubución ancha de los cocientes de línea centrada en Hα/H$\beta \approx 2{,}8$ (el valor correspondiente a la cascada de recombinación). Para pixeles con intensidades Hβ más brillantes, la distribución de Hα/Hβ se extiende a valores ~ 5 para HH 1, y ~ 6 para HH 2, lo cuál es consistente con excitaciones colisionales desde el nivel $n = 1$ al nivel $n = 3$ y 4 del hidrógeno en un gas a temperatura $T = 1{,}5 \times 10^4$ K (ver capítulo anterior y Raga et al. 2015b).

Esto es prueba fehaciente de la presencia de líneas de Balmer excitadas colisionalmente y, junto con el hecho de que las regiones con alto Hα/Hβ están restringidas a zonas delgadas de la cabeza principal de HH 1 y 2, es evidencia concluyente de que se observan regiones de excitación colisional inmediatamente después de las ondas de choque. Por otro lado, la mayor parte de la emisión Hα proviene de las zonas de recombinación, en las cuales las líneas de Balmer son producidas por la cascada de recombinación.

A lo largo de este trabajo, se ha supuesto que la extinción es uniforme sobre las regiones de emisión de HH 1 y 2. Las estructuras en la vecindad de los objetos podrían producir cambios en la extinción que afecten los resultados obtenidos. Si esto fuera un efecto dominante, esperaríamos ver una fuerte anti-correlación entre Hα/Hβ y la intensidad de Hβ, con cocientes grandes para Hβ débiles. Nuestras observaciones no muestran ese efecto.

Así, estas nuevas imágenes de Hα y Hβ muestran por primera vez de forma concluyente que se está detectando la zona inmediata post-choque de objetos HH (donde el hidrógeno está siendo ionizado y excitado colisionalmente). La detección de estas regiones contribuye de un modo claro a desarrollar modelos de choques a proa de objetos HH, en los cuales la posición del choque relativa a las regiones de recombinación está constreñida por las observaciones.

The Astrophysical Journal Letters, 798:L1 (6pp), 2015 January 1 doi:10.1088/2041-8205/798/1/L1

COLLISIONALLY EXCITED FILAMENTS IN *HUBBLE SPACE TELESCOPE* Hα AND Hβ IMAGES OF HH 1/2

A. C. Raga[1], B. Reipurth[2], A. Castellanos-Ramírez[1], Hsin-Fang Chiang[2], and J. Bally[3]
[1] Instituto de Ciencias Nucleares, Universidad Nacional Autónoma de México, Ap. 70-543, 04510 México, D.F., México; raga@nucleares.unam.mx
[2] Institute for Astronomy, University of Hawaii at Manoa, Hilo, HI 96720, USA
[3] Center for Astrophysics and Space Astronomy, University of Colorado, UCB 389, Boulder, CO 80309, USA
Received 2014 November 7; accepted 2014 November 19; published 2014 December 10

ABSTRACT

We present new Hα and Hβ images of the HH 1/2 system, and we find that the Hα/Hβ ratio has high values in ridges along the leading edges of the HH 1 bow shock and of the brighter condensations of HH 2. These ridges have $H\alpha/H\beta = 4 \rightarrow 6$, which is consistent with collisional excitation from the $n = 1$ to the $n = 3$ and 4 levels of hydrogen in a gas of temperatures $T = 1.5 \rightarrow 10 \times 10^4$ K. This is therefore the first direct evidence that the collisional excitation/ionization region of hydrogen just behind Herbig–Haro shock fronts is detected.

Key words: Herbig–Haro objects – ISM: individual objects (HH1/2) – ISM: jets and outflows – shock waves – stars: winds, outflows

1. INTRODUCTION

HH 1 and 2 were the first Herbig–Haro (HH) objects discovered (Herbig 1951; Haro 1952), and they have played an important role in the field of HH objects (see the historical review of Raga et al. 2011). For example, *Hubble Space Telescope* (*HST*) images (Schwartz et al. 1993; Hester et al. 1998), proper motions (ground-based: Herbig & Jones 1981; *HST*: Bally et al. 2002; IR: Noriega-Crespo et al. 1997; radio: Rodríguez et al. 2000), and detections in radio continuum (Pravdo et al. 1985), UV (Ortolani & D'Odorico 1980), and X-rays (Pravdo et al. 2001) were first obtained for HH 1 and 2.

The HH 1/2 system has a central source detected in radio continuum (see, e.g., Rodríguez et al. 2000) and a bipolar jet system with a NW jet (directed toward HH 1), which is visible optically, and a SE jet (directed toward HH 2), which is visible only in the IR (see Noriega-Crespo & Raga 2012). HH 1 has a "single bow shock" morphology, and HH 2 is a collection of condensations, some of which also have bow-shaped morphologies (see, e.g., Bally et al. 2002). The emission line structure of these objects has been studied spectroscopically, with one-dimensional (Solf et al. 1988) and two-dimensional (Solf et al. 1991; Böhm & Solf 1992) coverage of the objects. It should be pointed out that the HH 1/2 outflow lies very close to the plane of the sky, so that projection effects do not have to be considered when interpreting the observations of these objects.

The spatial structure of the optical line emission has been studied at higher angular resolution with *HST* images. Schwartz et al. (1993) obtained Hα, [S II] 6716+6730, and [O I] 6300 images. Later images of HH 1 and 2 were all taken with filters isolating the Hα and the red [S II] lines (Bally et al. 2002; Hartigan et al. 2011).

In this Letter, we describe a pair of new *HST* images of HH 1 and 2 obtained with filters isolating the Hα and Hβ lines. These images were obtained in consecutive exposures, so that they are not affected by proper motions (which become evident in *HST* observations of the HH 1/2 complex separated by more than a few weeks) or by differences in the pointing, and they therefore yield an accurate depiction of the spatial distribution of the Hα/Hβ ratio in these objects. These images show effects that have not been detected previously in ground-based studies of the emission line structure of HH 1 and 2 (see, e.g., Solf et al. 1991 and Böhm & Solf 1992) or in *HST* images of other HH objects (since *HST* Hβ images of HH objects have not been previously obtained).

This Letter is organized as follows. The new *HST* images are described in Section 2. The spatial distribution of the Hα/Hβ ratio, the line ratios as a function of Hβ intensity, and the distribution functions of the line ratios are presented in Section 3. Finally, an interpretation of the results is presented in Section 4.

2. THE OBSERVATIONS

The region around HH 1 and 2 was observed with the Hα (F656N) and Hβ (F487N) filters on 2014 August 16 with the Wide Field Camera 3 (WFC3) on the *HST*. The Hα image was obtained with a 2686 s exposure and the Hβ image with a slightly longer 2798 s exposure. The images were reduced with the standard pipeline, and a simple recognition/replacement algorithm was used to remove the cosmic rays. The final images have 4130 × 4446 pixels, with a pixel size of 0.″03962.

The images contain only two stars: the Cohen-Schwartz star (Cohen & Schwartz 1979) and "star No. 4" of Strom et al. (1985). These two stars have been used to determine astrometric positions in CCD images of the HH 1/2 region since the work of Raga et al. (1990), yielding better positions for HH 1 (which is closer to the two stars) than for HH 2. We have carried out paraboloidal fits to the point-spread functions of these two stars, and find no evidence for offsets and/or rotation, which shows the excellent tracking of the *HST* during the single pointing in which the two images were obtained. Also, we have analyzed the Hα−Hβ difference images of the two stars and find no offsets between the two frames.

The full Hα frame is shown in Figure 1, as well as zoomed in views of the regions around HH 1 and HH 2 in both Hα and Hβ. As seen in the top frame, the Hα map shows the extended collection of HH 2 knots (to the SE) and the more compact distribution of the HH 1 knots (toward the NW). The central frames of Figure 1 show the Hα emission of HH 2 (left) and HH 1 (right) on a larger scale. In the fainter Hβ emission (bottom panel of Figure 1), only the brighter regions of HH 1 and 2 are detected. We have defined two boxes (labeled A and B in the bottom frame of Figure 1) enclosing the regions of the two objects that are detected in Hβ. In the following section, the regions within these two boxes are used in order to study the spatial dependence of the Hα/Hβ ratio.

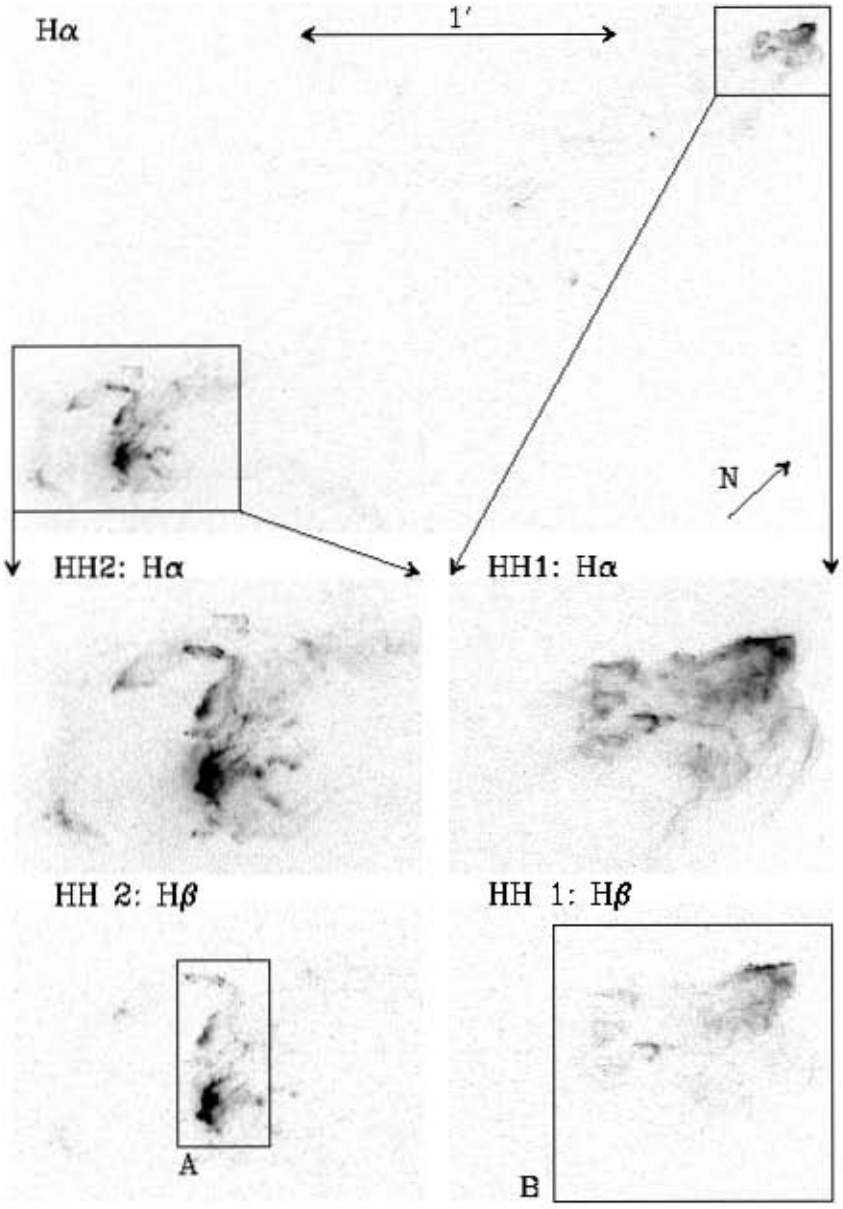

Figure 1. Top: Hα frame of HH 1 and 2 obtained with the WFC3 camera of the *HST* (the scale and orientation of the images is shown). The central and the bottom frames show the Hα and Hβ images (respectively) of regions containing HH 2 (left) and HH 1 (right). Also, on the Hβ frames we show boxes that include the brighter regions of HH 1 and HH 2 (boxes B and A, respectively), which have been used for calculating the Hα/Hβ ratios shown in Figures 2–5. The images are displayed with a logarithmic grayscale.

As discussed in detail by O'Dell et al. (2013), the F656N filter is contaminated by emission from the [N II] 6548 line, and both the F656N and F487N filters have contributions from the nebular continuum. Using the fact that at all measured positions within HH 1 and 2, the [N II] 6548/Hα ratio does not exceed a value of $\approx$0.35 (see, e.g., Brugel et al. 1981a and Solf et al. 1988) and the transmission curve of the F656N filter (see O'Dell et al. 2013 and the WFC3 Instrument Handbook), one then finds a peak contribution of $\approx$2% to the measured flux. For estimating the effects of the continuum in the F656N and F487N images, one can use the continuum and line fluxes obtained by Brugel et al. (1981a, 1981b) and the bandpasses of the filters to obtain estimates of $\approx$0.4 and 5% (for the F656N and F487N filters, respectively). Therefore, when interpreting the Hα/Hβ ratios obtained from our *HST* images, it is necessary to keep in mind that there is an uncertainty of $\sim$5% due to a possible spatial dependence in the Hβ line to continuum ratio within the F487N filter. As this uncertainty is $\sim$1 order of magnitude smaller than the Hα/Hβ ratio variations described below, we do not discuss it further.

3. THE Hα/Hβ RATIOS

Figure 2 shows the Hα map (right) and Hα/Hβ ratio map (left) for HH 2. To avoid having extended regions dominated by noise, in order to calculate the line ratio map, it is necessary to place a lower bound on the line fluxes. We have chosen to calculate the ratios only in regions in which the observed Hβ flux is larger than $I_0 = 5.4 \times 10^{-18}$ erg s^{-1} pixel^{-1}.

For calculating the intrinsic Hα/Hβ ratios, we have applied the following reddening correction. We first calculate the observed ratios for all of the pixels with Hβ intensities larger than I_0 (see above) for the A and B boxes (shown in the

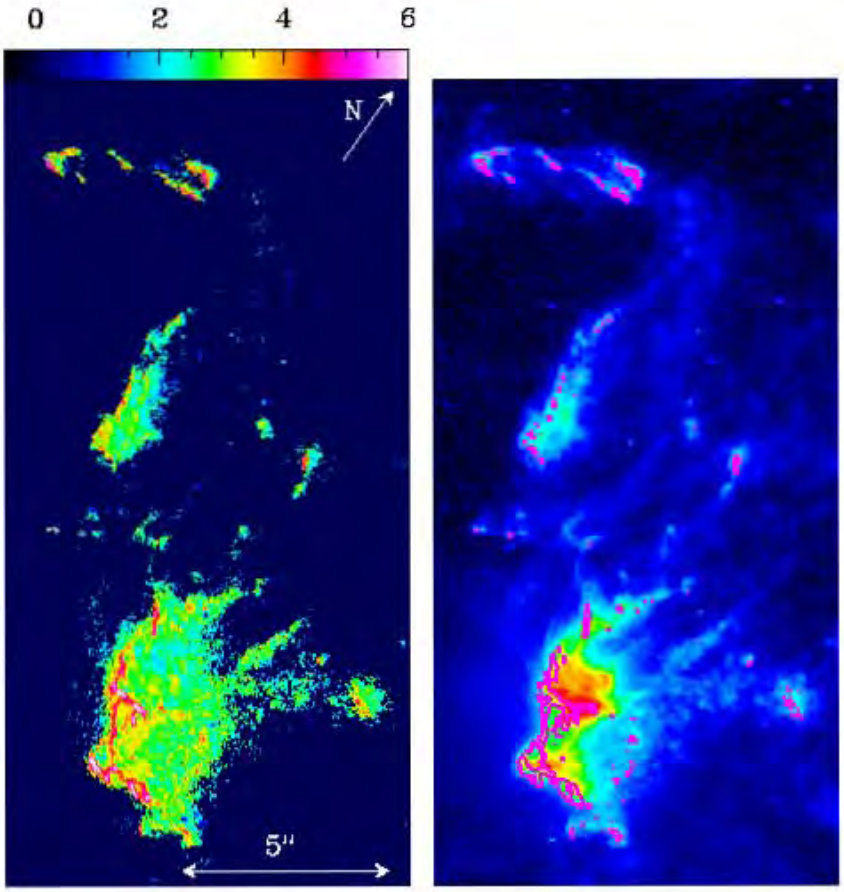

Figure 2. Hα emission (right, shown with a logarithmic color scale) and dereddened Hα/Hβ ratio (left, shown with the linear color scale given by the top bar) for HH 2. The outflow source lies toward the NNW. On the Hα image (right frame) we have included a (dereddened) Hα/Hβ = 4 contour (in purple). This contour shows that the higher values of the line ratio are distributed in a ridge along the leading edge of the emitting condensations.

bottom frames of Figure 1). For HH 2, we obtain a mean line ratio $\langle H\alpha/H\beta\rangle_{obs} = 3.82$ and for HH 1 we obtain an almost identical $\langle H\alpha/H\beta\rangle_{obs} = 3.79$ value. Considering an observed line ratio of 3.8 for both objects, comparing with the case B recombination cascade intrinsic Hα/Hβ ratio of 2.8 and using the average Galactic extinction curve, we obtain an $E(B-V) = 0.27$ color excess. This value is somewhat lower than the $E(B-V) \approx 0.35$ value deduced for HH 2 by Brugel et al. (1981a), using the method of Miller (1968), based on the fixed ratios between the auroral and transauroral lines of [S II] (i.e., not assuming a recombination cascade Hα/Hβ ratio). In order to calculate the dereddened Hα/Hβ ratios, we therefore multiply the observed ratios by a factor of 2.8/3.8, basically assuming that the extinction toward HH 1 and 2 is position-independent.

The dereddened Hα/Hβ ratios of HH 2 (see Figure 2) have values in the 2 → 6 range, with the regions of higher values corresponding to filamentary structures in the leading edge of the emitting knots (i.e., in the edges directed away from the outflow source). In order to illustrate the positions of these "high Hα/Hβ" regions, we have superimposed an Hα/Hβ = 4 contour on the Hα emission map (purple contour in the right frame of Figure 2).

Figure 3 shows the Hα map (bottom) and dereddened Hα/Hβ ratio map (top) for HH 1. We have calculated the ratios only for pixels with an observed Hβ flux larger than $I_0 = 5.4 \times 10^{-18}$ erg s^{-1} pixel^{-1} (i.e., the same cutoff used for HH 2; see above). The region with Hα/Hβ > 4 is a thin filament on the E side of the leading edge of HH 1 (see the purple contour on the Hα emission map in the bottom frame of Figure 3). It is clear that HH 1 shows a strong side-to-side asymmetry with respect to the outflow axis, as the SW region of the leading edge does not show high Hα/Hβ ratios (see the top frame of Figure 3). The Hα emission also shows a strong side-to-side asymmetry.

Figure 4 shows the dereddened Hα/Hβ line ratio as a function of the (observed) Hβ flux for all of the pixels with $I_{H\beta} > I_0$ (see above) for HH 1 (top frame) and HH 2 (bottom frame). It is clear that for low values of the Hβ intensity in both HH 1 and 2 we have a relatively broad distribution of line ratios (the width of this distribution representing the relatively large errors of the line ratio at low intensities) centered on the Hα/Hβ = 2.8 recombination cascade value. For pixels with brighter Hβ intensities, we see a distribution of Hα/Hβ ratios extending from ≈3 to larger values of ∼5 (for HH 1) or ∼6 (for HH 2).

This result is seen more clearly in Figure 5, where we show the normalized distributions of the line ratios of pixels with $I_0 < I_{H\beta} < I_1 = 2.5 \times 10^{-17}$ erg s^{-1} pixel^{-1} (distribution f_1, top frame), of pixels with $I_1 < I_{H\beta} < I_2 = 4.7 \times 10^{-16}$ erg s^{-1} pixel^{-1} (distribution f_2, center), and of all pixels with $I_2 < I_{H\beta}$ (distribution f_3, bottom frame of Figure 5, with appropriate pixels found only in HH 2). For both HH 2 (left column) and HH 1 (right column of Figure 5), we see that the distribution f_1 of the lower intensity pixels is approximately symmetrical, centered at an Hα/Hβ ≈ 2.8 line ratio. The

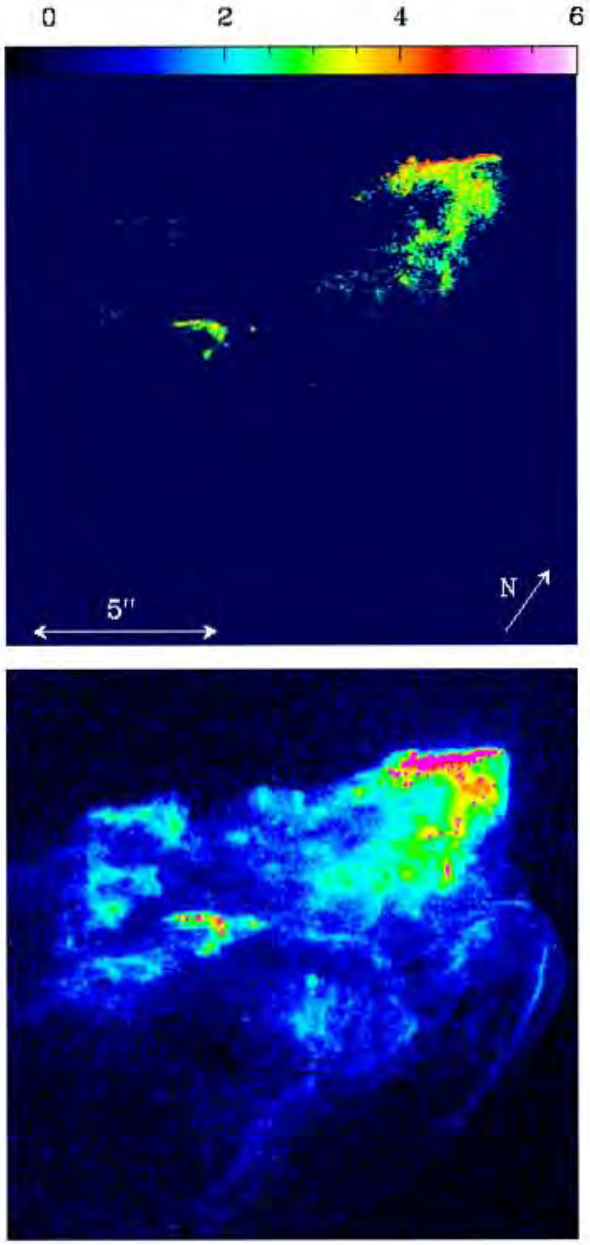

Figure 3. Hα emission (bottom, shown with a logarithmic color scale) and dereddened Hα/Hβ ratio (top, shown with the linear color scale given by the top bar) for HH 1. The outflow source lies toward the SSE. On the Hα image (bottom frame) we have included a (dereddened) Hα/Hβ = 4 contour (in purple). This contour shows that the higher values of the line ratio are distributed in a ridge along the E side of the leading edge of HH 1.

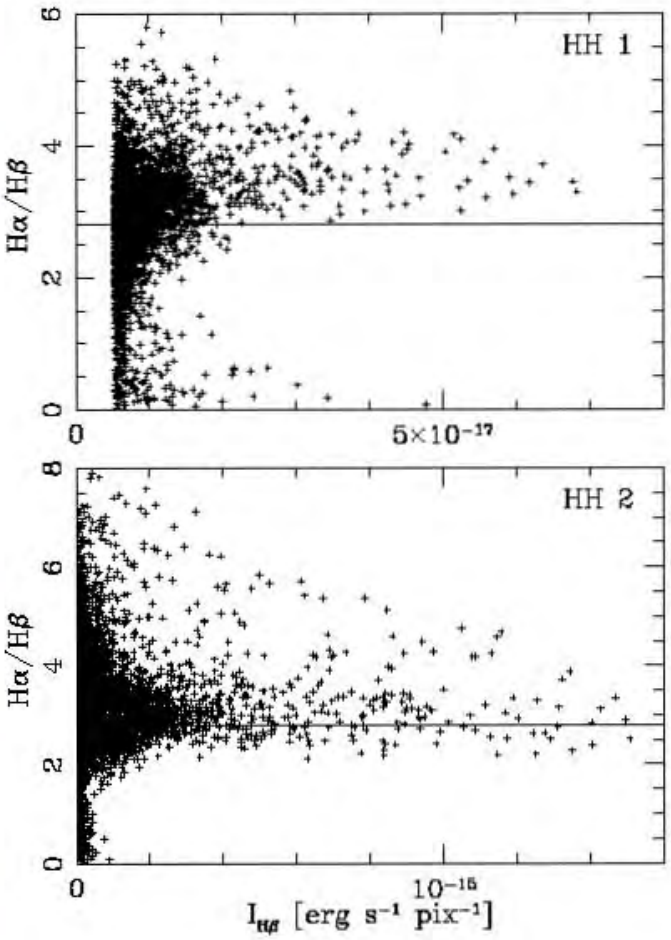

Figure 4. Dereddened Hα/Hβ ratio as a function of the observed Hβ flux for the pixels of HH 1 (top) and HH 2 (bottom). For the lower Hβ intensities, we see that the line ratios straddle a value of ≈2.8 (shown with a horizontal line in both frames), corresponding to the recombination cascade Hα/Hβ ratio. For larger Hβ intensities, we find line ratios extending from ≈3 to ≈5 (for HH 1) or 6 (for HH 2).

distributions for higher intensity pixels (f_2 and f_3; see above and the middle and bottom frames of Figure 5) start at values of Hα/Hβ ∼ 2–2.5, have a peak at a line ratio of ≈3.3 and have a wing extending to Hα/Hβ ∼ 5 for HH 1 and ∼6 for HH 2. In the following section, we show that these high Hα/Hβ ratios coincide with the values expected for collisional excitation of the $n = 3$ and 4 levels of H.

4. DISCUSSION

From our new Hα and Hβ *HST* images, we can compute dereddened Hα/Hβ maps for the brighter regions of HH 1 and 2. For the reddening correction, we assume that the mean value of the Hα/Hβ ratio coincides with the recombination cascade value of 2.8, as found previously by Brugel et al. (1981a), who calculated the reddening correction with Miller's method, based on the ratios of auroral to transauroral [S II] lines.

We find that in limited spatial regions the (dereddened) Hα/Hβ ratio has values of ∼4 → 6, which are inconsistent with the recombination cascade value. These high Hα/Hβ regions are filaments along the leading edges (i.e., the edges away from the outflow source) of the brighter emitting regions of HH 1 and 2 (see Figures 2 and 3).

Raga et al. (2015) show that the $r_{\alpha\beta}$ = Hα/Hβ ratio for a "case B" cascade fed by collisional excitations from the ground state of hydrogen has the approximate form:

$$r_{\alpha\beta} = 3.40\, e^{E_{43}/(kT)} + \frac{0.95}{(1 + 5 \times 10^4\,\mathrm{K}/T)^4}, \qquad (1)$$

where k is Boltzmann's constant and E_{43} is the energy difference between the $n = 4$ and $n = 3$ energy levels (so that E_{43}/k = 7680 K). The first term of this functional form has a temperature dependence derived from the ratio of the $n = 1 \rightarrow 3$ and $n = 1 \rightarrow 4$ collisional excitation coefficients (assuming temperature-independent collision strengths), and the second term is a correction necessary to match the results of a five-level, collisionally fed cascade matrix description of the hydrogen atom in the $T = 10^3 \rightarrow 10^6$ K temperature range (see Raga et al.

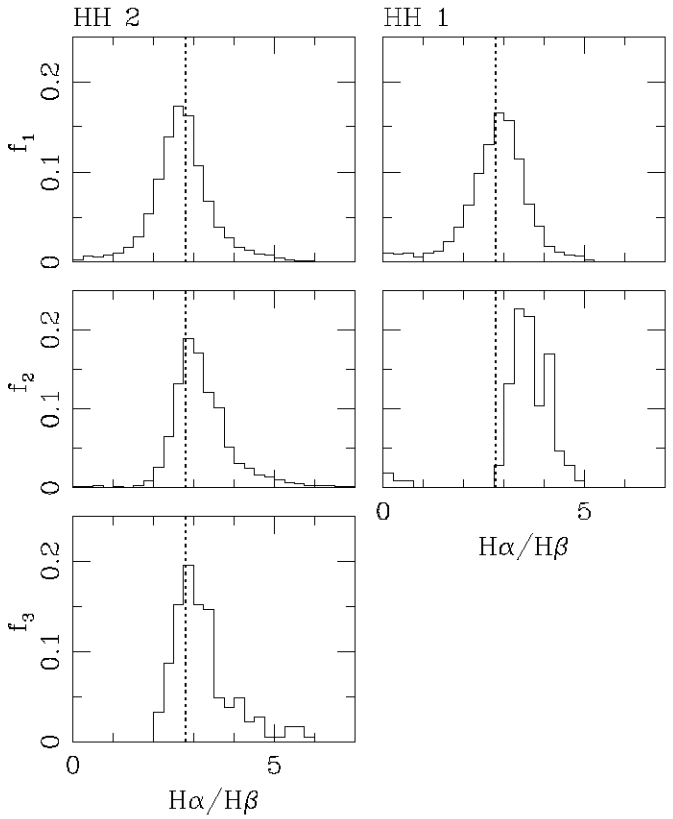

Figure 5. Distribution functions for the number of pixels within Hα/Hβ ratio bins for HH 2 (left) and HH 1 (right). We show three different distributions: f_1 (top) corresponding to pixels with $I_0 = 5.4 \times 10^{-18}$ erg s^{-1} pixel^{-1} $< I_{H\beta} < I_1 = 2.5 \times 10^{-17}$ erg s^{-1} pixel^{-1}, f_2 (center) of pixels with $I_1 < I_{H\beta} < I_2 = 4.7 \times 10^{-16}$ erg s^{-1} pixel^{-1}, and f_3 (bottom) of pixels with $I_2 < I_{H\beta}$. The distribution function of the lower intensity pixels (f_1, top frames) is approximately symmetrical, centered at a line ratio of ≈2.8, corresponding to the recombination cascade value (the dashed vertical line in all plots corresponds to Hα/Hβ = 2.8). The distribution functions for higher intensity pixels (f_2 and f_3, central and bottom frames) all show extended wings to higher values of Hα/Hβ.

2015). It is clear that the functional form of r (see Equation (1)) has high values for low temperatures and has an asymptotic value of 4.35 for $T \rightarrow \infty$.

From Equation (1), one obtains $r(T = 1.5 \times 10^4\,\mathrm{K}) = 5.6$ and $r(T = 10^5\,\mathrm{K}) = 3.9$. Therefore, the wing of the line ratio distributions extending to Hα/H$\beta \sim 4 \rightarrow 6$ (see Figure 5) can straightforwardly be explained as produced in regions with temperatures in the $1.5 \rightarrow 10 \times 10^4$ K range emitting collisionally excited Balmer lines.

This clear evidence that we are observing collisionally excited Balmer lines together with the fact that the high Hα/Hβ regions are restricted to the leading edges of the outward moving condensations of HH 1 and 2 is quite conclusive evidence that we are observing the region of collisional excitation of H lines right after the shock waves driven into the surrounding medium by the condensations. Most of the Hα emission, however, comes from a region further away from the shock, in which the Balmer lines are produced through the standard recombination cascade (as evidenced by the Hα/H$\beta \sim 3$ ratios; see Figures 2 and 3).

The theoretical prediction of these two regions of Balmer line emission (a collisionally excited Balmer line region immediately after the shock, and the recombination region with Balmer lines dominated by the recombination cascade) in HH shock wave models is already mentioned by Raymond (1979), and the Hα emission from the two regions was studied in more detail by Raga & Binette (1991). These two regions are of course present in all shock models (for example, in the plane-parallel, time-dependent shock models of Teşileanu et al. 2009).

In non-radiative shocks observed in some supernovae remnants or in pulsar cometary nebulae, the observed emission comes exclusively from the region of collisional excitation right behind the shocks (see, e.g., the review of Heng 2010). In HH objects, the only previous observational evidence of the emission from the immediate post-shock region (as opposed to the emission from the recombination region) were the Hα filaments seen in *HST* images of some bow shocks, notably in the *HST* images of HH 47 (Heathcote et al. 1996), HH 111 (Reipurth et al. 1997), and HH 34 (Reipurth et al. 2002). However, as only Hα was observed, it was not possible to guarantee that these filaments did correspond to the region of collisionally excited Balmer lines.

Our new Hα and Hβ images for the first time show in a quite conclusive way that we have a detection of the immediate post-shock region of HH objects (in which H is being collisionally ionized and the levels of H are being collisionally excited). The detection of this region provides a clear way forward for developing models of HH bow shocks, in which the position of the shock wave relative to the recombination region is directly constrained by the observations.

We should note that throughout this Letter we have assumed that the extinction is uniform over the emission regions of HH 1 and 2. In principle, it could be possible that foreground structures in the vicinity of the objects might produce changes in the extinction on angular scales comparable to the size of the objects. However, estimates of the density of the pre-bow shock material of HH 1 and 2 (based on observations of the post-shock density and on plane-parallel shock models; see, e.g., Hartigan et al. 1987) give values ∼100–300 cm^{-3}. Clearly, such a low-density environment will not produce appreciable extinction on spatial scales comparable to the size of the HH objects. Because of this, if one wants to attribute the observed changes in the Hα/Hβ ratio to an angular dependence of the extinction, it is necessary to assume that still undetected, sharp-edged, high-density regions are present in the immediate vicinity of HH 1 and 2.

Support for this work was provided by NASA through grant HST-GO-13484 from the Space Telescope Science Institute. A.R. and A.C.R. acknowledge support from the CONACyT grants 101356, 101975, and 167611 and the DGAPA-UNAM grants IN105312 and IG100214.

REFERENCES

Bally, J., Heathcote, S., Reipurth, B., et al. 2002, AJ, 123, 2627
Böhm, K. H., & Solf, J. 1992, AJ, 104, 1193
Brugel, E. W., Böhm, K. H., & Mannery, E. 1981a, ApJS, 47, 117
Brugel, E. W., Böhm, K. H., & Mannery, E. 1981b, ApJ, 234, 874
Cohen, M., & Schwartz, R. D. 1979, ApJL, 233, L77
Haro, G. 1952, ApJ, 115, 572
Hartigan, P., Frank, A., Foster, J. M., et al. 2011, ApJ, 736, 29
Hartigan, P., Raymond, J. C., & Hartmann, L. W. 1987, ApJ, 316, 323
Heathcote, S., Morse, J. A., Hartigan, P., et al. 1996, AJ, 112, 1141
Heng, K. 2010, PASA, 27, 23
Herbig, G. H. 1951, ApJ, 113, 697
Herbig, G. H., & Jones, B. F. 1981, AJ, 86, 1232
Hester, J. J., Stapelfeldt, K. R., & Scowen, P. A. 1998, AJ, 116, 372
Miller, J. S. 1968, ApJL, 154, L57
Noriega-Crespo, A., Garnavich, P. M., Curiel, S., Raga, A. C., & Ayala, S. 1997, ApJL, 486, L55

Noriega-Crespo, A., & Raga, A. C. 2012, ApJ, 750, 101
O'Dell, C. R., Ferland, G. J., Henney, W. J., & Peimbert, M. 2013, AJ, 145, 92
Ortolani, S., & D'Odorico, S. 1980, A&A, 83, L8
Pravdo, S. H., Feigelson, E. D., Garmire, G., et al. 2001, Natur, 413, 708
Pravdo, S. H., Rodríguez, L. F., Curiel, S., et al. 1985, ApJL, 293, L35
Raga, A. C., Barnes, P. J., & Mateo, M. 1990, AJ, 99, 1912
Raga, A. C., & Binette, L. 1991, RMxAA, 22, 265
Raga, A. C., Castellanos-Ramírez, A., Esquivel, A., Rodríguez-González, A., & Velázquez, P. F. 2015, RMxAA, submitted
Raga, A. C., Reipurth, B., Cantó, J., Sierra-Flores, M. M., & Guzmán, M. V. 2011, RMxAA, 47, 425
Raymond, J. C. 1979, ApJS, 39, 1
Reipurth, B., Hartigan, P., Heathcote, S., Morse, J., & Bally, J. 1997, AJ, 114, 757
Reipurth, B., Heathcote, S., Morse, J., Hartigan, P., & Bally, J. 2002, AJ, 123, 362
Rodríguez, L. F., Delgado-Arellano, V. G., Gómez, Y., et al. 2000, AJ, 119, 882
Schwartz, R. D., Cohen, M., Jones, B. F., et al. 1993, AJ, 106, 740
Solf, J., Böhm, K. H., & Raga, A. C. 1988, ApJ, 334, 229
Solf, J., Raga, A. C., Böhm, K. H., & Noriega-Crespo, A. 1991, AJ, 102, 1147
Strom, S. E., Strom, K. M., Grasdalen, G. L., et al. 1985, AJ, 90, 2281
Teşileanu, O., Massaglia, S., Mignone, A., Bodo, G., & Bacciotti, F. 2009, A&A, 507, 581

2.4. High Angular Resolution Multi-line Study of HH 1 and 2

El trabajo presentado en este capítulo muestra una serie de imágenes obtenidas con el HST entre el 14 y el 17 de Agosto del 2014, las cuales incluyen un número relativamente extenso de líneas de emisión. Estas son: Hα, Hβ, [O I] 6300, [O II] 3726+29, [O III] 5007 y [S II] 6716+30. Estas observaciones permiten hacer un estudio detallado de la distribución espacial de la excitación del espectro de emisión de líneas con alta resolución angular.

Mi contribución en este artículo fue básicamente en la actualización de parámetros atómicos y en el cálculo de diagnosticos de plasma para interpretar las observaciones multi-línea de HH 1/2.

Con los datos obtenidos se elaboraron mapas de Hα y mapas de la distribución espacial de los cocientes de líneas respecto de Hα observados para HH 1 y HH 2. Como en el capítulo 2.3 (Raga et al., 2015a), se utiliza un mínimo de intensidad para el cálculo del cociente de línea, para eliminar las zonas con cocientes de muy baja señal a ruido.

Encontramos en el caso de HH 1 que el cociente Hβ/Hα tiene un valor constante de 0.35 (correspondiente al caso B de la cascada de recombinación), excepto en una región delgada a lo largo del ala este, donde los valores son cercanos a 0.22, correspondientes a las líneas de Balmer excitadas colisionalmente producidas en la región inmediatamente después del choque.

Además, se encuentra que la cabeza del choque tiene dos alas asimétricas (Raga et al., 1988): el ala este, más brillante en Hα, Hβ, [S II], y [O I], y el ala oeste, cuyas emisiones brillantes se dan en [O II] y [O III]. Esta asimetría puede interpretarse como un choque a proa moviéndose en un medio con un gradiente transversal de densidad, con el ala oeste moviéndose en una región de menor densidad y el ala este moviéndose en una región de mayor densidad (Henney, 1996).

En el caso de HH 2 se observa una región central de condensaciones brillantes detectadas en la emisión de alta excitación [O III], alineada en la dirección noroeste-sureste. Estas condensaciones están rodeadas de nudos menos brillantes (en la periferia) en las líneas de baja excitación ([O I] y [S II]). Se observa que los valores de Hβ/Hα permanecen casi constantes, correspondiendo al caso B de la cascada de recombinación, excepto en unas crestas angostas localizadas alrededor del borde principal de las condensaciones brillantes, donde la excitación colisional se hace presente.

Otro resultado novedoso consiste en que los mapas de cocientes de líneas muestran un arreglo en dos estructuras tipo choque a proa: una principal, con baja excitación, y otra secundaria (siguiendo de cerca a la principal) de mayor excitación. Esto sugiere que la re-

gión más brillante de HH 2 podría corresponder a la superposición de dos choques a proa fragmentados.

Además de lo anterior, los cocientes de líneas se utilizaron para graficar diagramas de dos cocientes para HH 1 y 2. Para estos diagramas usamos los cocientes de todas las líneas respecto de [O II] (porque se obtienen mejores resultados que con los cocientes respecto a Hα) y los utilizamos para comparar las observaciones con las predicciones de los modelos de choque planos (Hartigan et al., 1987). Sorprendentemente se distinguen fuertes correlaciones lineales, prácticamente en todas las posibles combinaciones de dos cocientes de líneas. Este resultado es una propiedad llamativa de la emisión de HH 1 y 2.

A partir de estas correlaciones, es posible realizar una predicción de la temperatura en términos de los cocientes de líneas (en este trabajo se utilizó el cociente de líneas [O I]/[S II], porque O I y S II coexisten espacialmente en las zonas de recombinación, ver por ejemplo Raga & Binette 1991 y Bacciotti & Eislöffel 1999). Las temperaturas resultantes, $T_{[O\ I]/[S\ II]}$, muestran que se tiene básicamente un valor constante ($\sim 10^4$ K) en casi todo el objeto, con excepción de una tira delgada de valores altos ($> 2\times10^4$ K) que se ubica en el ala este de HH 1. Este filamento coincide espacialmente con los valores altos de Hα/Hβ mostrados en el capítulo 2.3 (Raga et al., 2015a), los cuales tienen los valores esperados de cocientes de líneas de Balmer para excitación colisional. Así, los altos valores obtenidos para $T_{[O\ I]/[S\ II]}$ representan muy probablemente la contribución a la emisión de regiones de ionización colisional justo después del choque.

Para HH 2, los resultados muestran valores altos de $T_{[O\ I]/[S\ II]}$ ($> 3 \times 10^4$ K) localizados alrededor de la proa de las condensaciones más brillantes. Al igual que en HH 1, estas regiones coinciden con los valores grandes de Hα/Hβ.

The Astronomical Journal, 150:105 (12pp), 2015 October doi:10.1088/0004-6256/150/4/105

HIGH ANGULAR RESOLUTION MULTI-LINE STUDY OF HH 1 AND 2

A. C. Raga[1], Bo Reipurth[2], A. Castellanos-Ramírez[1], Hsin-Fang Chiang[2], and J. Bally[3]
[1] Instituto de Ciencias Nucleares, Universidad Nacional Autónoma de México, Ap. 70-543, 04510 D.F., México; raga@nucleares.unam.mx
[2] Institute for Astronomy, University of Hawaii at Manoa, Hilo, HI 96720, USA
[3] Center for Astrophysics and Space Astronomy, University of Colorado, UCB 389, Boulder, CO 80309, USA
Received 2015 March 9; accepted 2015 August 4; published 2015 September 8

ABSTRACT

We present new *Hubble Space Telescope* (*HST*) narrow band images of the bright Herbig–Haro (HH) objects HH 1 and 2 in the light of the Hα, Hβ, [O I] 6300, [O II] 3726+28, [O III] 5007 and [S II] 6716+30 emission lines. The resulting emission and line ratio maps give an improved picture of the physical structure of these HH objects, showing the presence of spatially limited, high excitation/ionization ridges. We find that HH 1 has a morphology that could be interpreted in terms of a single, asymmetric bow shock, and that many of the clumps of HH 2 fall in two bow-shaped structures of different excitations. We also construct two-line ratio plots showing clear trends, which are much simpler than the highly complex spatial distributions of the emission, and are therefore interesting for testing shock models of HH objects (we only present a comparison with previously published, steady plane-parallel shock models). We have also used the temperature-sensitive [O I]/[S II] line ratio to evaluate the temperature range and to obtain temperature maps of HH 1 and 2. We find that this line ratio picks out emitting regions with temperatures $\approx 10^4$ K, except along the leading edges of the HH 1 and 2 bow shocks (in which temperatures of $\sim 3 \rightarrow 5 \times 10^4$ K are obtained).

Key words: Herbig–Haro objects – ISM: individual objects (HH1/2) – ISM: jets and outflows – shock waves – stars: winds, outflows

1. INTRODUCTION

HH 1 and 2 form one of the brightest Herbig–Haro (HH) outflow systems. As indicated by their numbers, they were the first HH objects to be discovered (Herbig 1951; Haro 1952). Also, many of the important characteristics of HH objects were first observed in HH 1 and 2. Examples of this are high proper motions (Herbig & Jones 1981) and radio (Pravdo et al. 1985), ultraviolet (Ortolani & D'Odorico 1980) and X-ray (Pravdo et al. 2001) emission, all first observed in HH 1 and 2. Raga et al. (2011) discuss the observational and theoretical work that has been done on HH 1 and 2 (up to 2010).

Hubble Space Telescope (*HST*) Hα and [S II] 6716+30 images of HH 1 and 2 have been presented by Hester et al. (1998), Bally et al. (2002) and Hartigan et al. (2011). An earlier paper by Schwartz et al. (1993) presented Hα, [S II] 6716+30 and [O III] 5007 *HST* images of HH 2 (HH 1 falling outside of the observed field). In particular, the paper of Bally et al. (2002) presents a detailed discussion of the morphologies of HH 1 and 2, and of the differences between the Hα and red [S II] emission. The multi-epoch images have also been used for detailed proper motion studies of these objects (Bally et al. 2002; Hartigan et al. 2011).

We have obtained new *HST* narrow-band images of the HH 1/2 region for a more extended set of emission lines: Hα, Hβ, [S II] 6716+30, [O I] 6300, [O II] 3726+29 and [O III] 5007 (in the following, we omit the wavelength in the notation for the observed forbidden lines). These images allow us to do an unprecedentedly detailed study of the spatial dependence of the excitation of the emission line spectra of HH 1 and 2 at high angular resolution. This study is limited in the number of studied emission lines compared to previous, ground-based studies such as the spectrophotometric observations of HH 1 by Solf et al. (1988), which study over 100 emission lines. On the other hand, our new study gives the 2D angular distribution of the line emission (the work of Solf et al. 1988 is restricted to a single slit cutting through HH 1), and at a much higher spatial resolution.

The paper is organized as follows. In Section 2, we describe the new *HST* observations. In Section 3, we present emission line maps and line ratio maps for HH 1 (Section 3.1) and HH 2 (Section 3.2). In Section 4, we place the line ratios of the pixels within the HH 1 and HH 2 emitting regions on two-line ratio plots. The characteristics of these line ratios are described, and possible temperature diagnostic ratios are derived. The resulting temperatures are then used for producing temperature maps of HH 1 and 2. Finally, the results are discussed and summarized in Section 5.

2. THE OBSERVATIONS

A field including the emission of HH 1 and 2 was observed with WFC3 through the Hα (F656N), Hβ (F487N), [O I] 6300 (F631N), [O II] 3726+29 (F373N), [O III] 5007 (F502N) and [S II] 6716+30 (F673N) filters, with exposures of 2686 (Hα), 2798 (Hβ), 2798 ([O I]), 5484 ([O II]), 2798 ([O III]) and 2798 ([S II]) seconds. The observations were carried out between 2014 August 14 and 17, so that the effects of the proper motions of HH 1 and 2 are completely negligible during this limited time-interval.

The images were reduced with the standard pipeline, and a simple recognition/replacement algorithm was used to remove the cosmic rays. The final images have a pixel size of $0\farcs03962$ and were all registered with the Hα frame using the observed positions of the Cohen–Schwartz star (Cohen & Schwartz 1979) and "star no. 4" of Strom et al. (1985). Since the work of Raga et al. (1990) all of the position determinations on CCD frames of the HH 1 and 2 knots have been done using only these two stars. We find that the pixel size of all of the frames is identical (to within the errors of the fits to the point-spread functions of the two stars), and that only a translation and a rotation have to be applied.

Using the filter bandpasses given in the WFC3 Instrument Handbook, we compute the fluxes in the observed lines. Clearly, the Hα filter has a contribution from the [N II] 6548 line (at $\sim$5% of peak transmission, see the discussion of O'Dell et al. 2013), but since very large values of the [N II]/Hα ratio are unlikely to be present in HH 1 and 2 (as these line ratios at lower angular resolutions never reach high values in HH spectra, see, e.g., Brugel et al. 1981a and Solf et al. 1988), the contribution of the [N II] 6548 line to the flux obtained from the F656N (Hα) filter will be at most of order $\sim$2%. Also, the fluxes measured with the narrow-band filters include a contribution from the continuum (believed to be a combination of the recombination continuum and a collisionally enhanced two-photon continuum in HH 1 and 2, see, e.g., Solf et al. 1988). If we take the continuum of HH 1 and 2 observed by Brugel et al. (1981b), we estimate that it has a contribution of $\sim$10% to the fluxes obtained from the F487N (Hβ), F502N ([O III]) and F373N ([O II]) filters, and smaller contributions (of $\sim$1%) to the fluxes obtained from the red filters.

In the following sections, we present the calibrated emission line images with the observed fluxes and we also compute ratios between the observed lines. The line fluxes and line ratios are obtained after applying a reddening correction. For this correction, we consider the $E(B-V)=0.27$ color excess determined by Raga et al. (2015) for HH 1 and 2, and the average Galactic extinction curve. This reddening correction results in correction factors of 3.84, 2.45, 2.36, 1.87, 1.80 and 1.77 (in magnitudes: $A=1.46$, 0.97, 0.93, 0.68, 0.64 and 0.62) for the [O II], Hβ, [O III], [O I], Hα and [S II] fluxes, respectively.

3. THE SPATIAL DISTRIBUTION OF THE LINE INTENSITIES AND LINE RATIOS

3.1. HH 1

In Figure 1, we show the region around HH 1 in the six calibrated (and dereddened) images. We see the following characteristics:

1. the Hβ image closely resembles the Hα map, but the fainter regions are not well detected in the Hβ image,
2. the lower excitation lines ([O I] and [S II]) show a structure which qualitatively resembles Hα, but with stronger relative emission in the extended E wing of HH 1,
3. the intermediate excitation [O II] emission quite closely follows the Hα morphology except in a region along the W wing (and $\leqslant$5″ from the tip of HH 1) in which [O II] is clearly brighter and more extended,
4. the high excitation [O III] emission is concentrated in two narrow ridges, following the two bow wings out to $\sim$4″ from the tip of HH 1.

In Figure 2, we show the Hα intensity map, and maps of the spatial distribution of the (dereddened) ratios of all of the other observed lines to Hα. We calculate the line ratios with Hα in the denominator because line ratios in HH objects (as well as in other emission line objects) have traditionally been presented with one of the Balmer lines in the denominator (which is generally a reasonable thing to do, because the Balmer lines are bright and are usually detected over most of the emitting region). The line ratios have been calculated only for the regions with (dereddened) Hα intensities $I_{\rm H\alpha} \geqslant 9\times10^{-18}\,{\rm erg\,s^{-1}\,cm^{-2}\,pix^{-1}}$. The five resulting ratio maps have the following characteristics:

1. Hβ/Hα: this ratio shows a relatively constant value of $\approx$0.35 (corresponding to the case B recombination cascade value) except in a ridge along the leading edge of the E wing, in which values of $\approx$0.22 are found. Raga et al. (2015) have interpreted this ridge as evidence for collisional excitation of the Balmer lines in the immediate post-shock region,
2. [S II]/Hα: this ratio shows low values along the two wings in the region within $\sim$3″ from the tip. It then shows a bow-like ridge which trails the HH 1 tip by about $\sim$2″ (see the discussion of Bally et al. 2002). The higher values for this ratio are found along the extended E wing, at $\geqslant$10″ from the tip. In the axial region of the object one also sees localized ridges of high or low values for this line ratio,
3. [O I]/Hα: this ratio has a spatial distribution that shows basically the same features as the [S II]/Hα line ratio map,
4. [O II]/Hα: this ratio appears to show two bow-shaped structures. One of these structures includes the tip of HH 1 and has a short W wing, and an extended E wing, forming an extended region with [O II]/Hα $\sim$ 1. A second, bow structure with high [O II]/Hα $\sim$ 2 trails the leading bow by $\sim$2″. Other ridges are seen trailing the HH 1 tip by $\sim$10″,
5. [O III]/Hα: this map presents low values ($\sim$0.1) except along the bow-shaped structure (clearly seen in the [O II]/Hα map) that trails the HH 1 tip by $\sim$2″. The higher values (with [O III]/Hα $\sim$ 1) are seen along the W wing of this structure.

We finally note that HH 1 has a clear side-to-side asymmetry: the E wing is more extended, and brighter in the Balmer, [S II] and [O I] lines, and the W wing is more compact, and brighter in the [O II] and [O III] lines. This effect is seen both in the images (Figure 1) and in the line ratio maps (Figure 2).

3.2. HH 2

As can be seen in Figure 3, HH 2 has a central region of bright condensations (knots A, G and H, see e.g., Bally et al. 2002) surrounded by a number of fainter condensations. The brighter condensations lie in an elongated region (with a width of $\sim$5″–10″ and a length of $\sim$20″–30″) aligned in a NE-SW direction. The fainter, peripheral condensations are particularly bright in the low excitation lines (see the [O I] and [S II] maps of Figure 3), and only the brighter condensations are detected in the high excitation [O III] emission.

Figure 4 shows the dereddened line ratios, which were calculated only for regions with $I_{\rm H\alpha} \geqslant 9\times10^{-18}\,{\rm erg\,s^{-1}\,cm^{-2}\,pix^{-1}}$. Here we point out some of the many features seen in these maps:

1. an almost constant Hβ/Hα ratio, with values corresponding to the case B recombination cascade, except for narrow ridges around the leading edges of the brighter condensations, in which collisional excitation is present (see the discussion of Raga et al. 2015),
2. the [S II]/Hα and [O I]/Hα ratios have low values (of $\sim$0.5 and $\sim$0.3, respectively) in the brighter

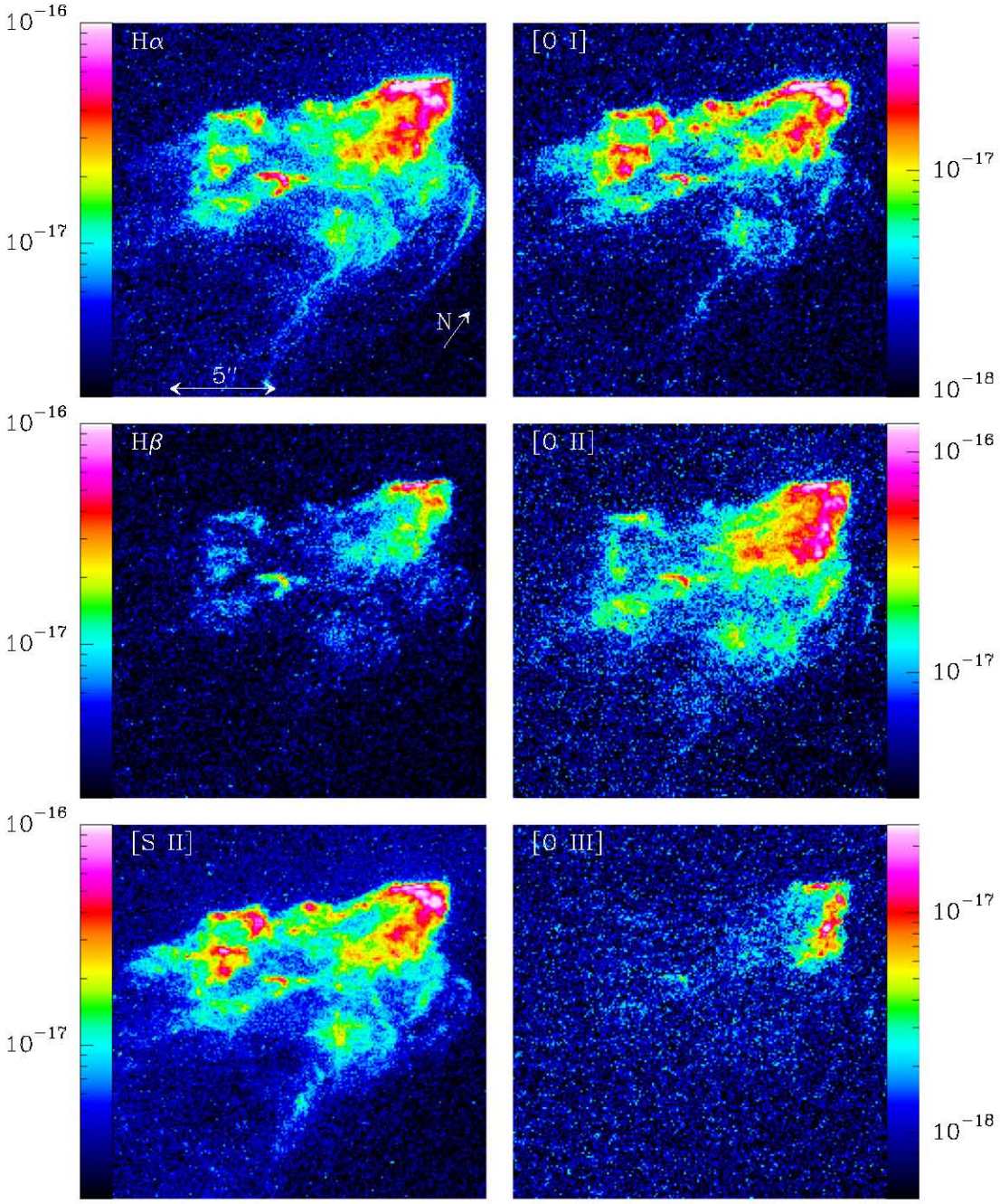

Figure 1. Narrow-band images of HH 1, in filters isolating the emission lines given on the top left of each plot. The angular scale and the orientation are given in the top left frame. The calibrated, dereddened fluxes are displayed with the logarithmic color scale given (in erg s^{-1} cm^{-2} pix^{-1}) by the bars attached to each plot. The outflow source lies $\approx 70''$ to the SSE from the northern tip of HH 1.

condensations, and higher values (of $\sim$1 or larger) in the fainter, peripheral condensations,

3. the [O II]/Hα ratio shows large values (of $\sim$2) in an arc-like region which trails the bright condensations of HH 2,
4. the [O III]/Hα ratio has its higher values (>0.5) in localized regions, which mostly lie in the arc-like [O II]/Hα ridge.

In Figure 5, we show a grayscale Hα image of the central region of HH 2 together with two contours, one of them corresponding to [S II]/H$\alpha = 0.4$ (in red) and the other one to [O II]/H$\alpha = 1.5$. The high [O II]/Hα region (enclosed by the blue contour) forms an arc-like structure trailing the low [S II]/Hα valley (enclosed by the red contour, which surrounds a region of low [S II]/Hα ratios, see the bottom left frame of Figure 4). This suggests that the brighter region of HH 2 might correspond to a superposition of two fragmented main bow shocks.

An interesting feature that is seen in the spatially resolved line ratios of Figures 4 and 5: the line ratios corresponding to the emission of the brighter knots of HH 2 show an extension to regions ahead (i.e., further away from the outflow source) of the emission peaks. While this faint emission has line ratios which closely follow the ones of the nearby, bright condensations, it has been observed that it has broader line profiles (see, e.g., Böhm & Solf 1992). This peculiar effect has been

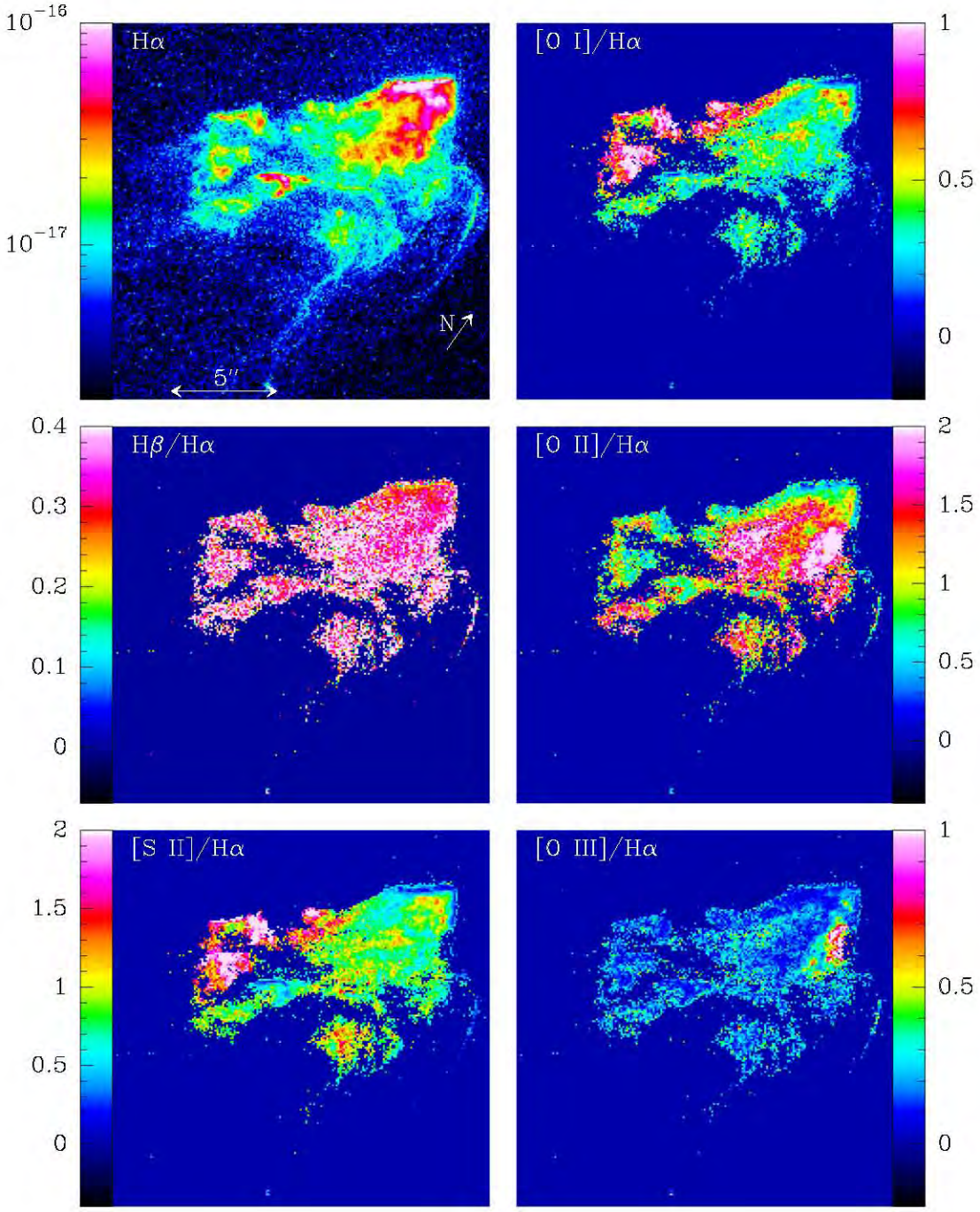

Figure 2. Hα map (top left) and reddening corrected line ratio maps of the other observed lines over Hα (see the labels on the top left of each frame) of HH 1. The line ratio maps are displayed with the linear color scale given by the bars attached to each plot. The scale and orientation of the images are shown on the Hα image (top left). The line ratios have been computed only for the regions with $I_{\rm H\alpha} \geqslant 9 \times 10^{-18}$ erg s^{-1} cm^{-2} pix^{-1}.

successfully modeled as the emission from the bright condensations being scattered on dust in the nearby environment of HH 2 (Riera et al. 2005). Therefore, the extensions to the faint surroundings that we observe around the brighter HH 2 knots probably correspond to the scattering of the emission from the knots off the neighboring environment.

4. DIAGNOSTIC LINE RATIOS

From our six narrow-band images we can obtain line ratio maps, and then obtain two-line ratio graphs in which we plot points corresponding to the individual pixels of the HH 1 and HH 2 emitting regions. For this exercise, we take ratios of all lines to the "intermediate excitation" [O II] 3726+29 emission.

We have switched to taking ratios to the [O II] line emission because if one wants to compare with predictions from plane shock models, better results are obtained if one takes ratios to lines other than Hα or Hβ. This is because the Balmer emission from plane, steady shocks has two components: a relatively weak peak in the immediate post-shock region (in which collisionally excited Balmer lines are produced), and a stronger emission peak in the high density/low temperature tail of the recombination region (in which we have recombination Balmer

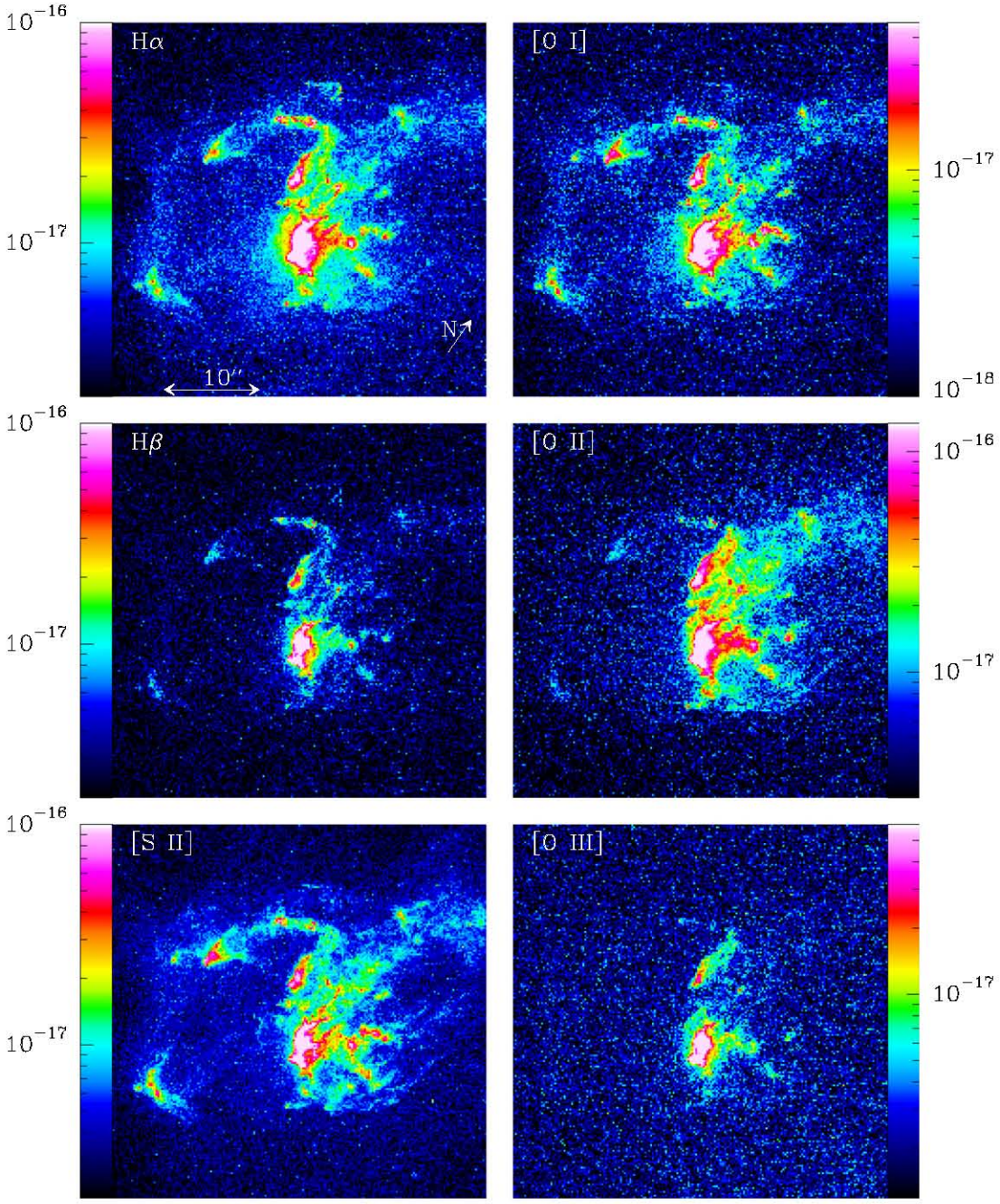

Figure 3. Narrow-band images of HH 2, in filters isolating the emission lines given on the top left of each plot. The angular scale and the orientation are given in the top left frame. The fluxes are displayed with the logarithmic color scale given (in erg s^{-1} cm^{-2} pix^{-1}) by the bars attached to each plot. The outflow source lies ≈80″ to the NNW from the brighter condensations of HH 2.

lines, see, e.g., Raga & Binette 1991). Because of the long time-scales necessary for its formation, this "recombination Balmer line region" is likely to differ considerably between the plane-parallel shock prediction and the time-dependent, 3D structure that we have in HH objects (as was first pointed out by Dopita et al. 1982, who studied the continuum spectrum of HH objects). Therefore, a better agreement between plane-parallel shock predictions and observations is indeed expected for line ratios not involving the Balmer lines.

In Figure 6, we plot the locations of all pixels with $I_{H\alpha} \geqslant 2.7 \times 10^{-17}$ erg s^{-1} cm^{-2} pix^{-1} of HH 1 (left column) and HH 2 (right column) in line ratio plots corresponding to Hα/[O II] (top), Hβ/[O II], [O I]/[O II] and [O III]/[O II] (bottom) as a function of [S II]/[O II]. We have chosen to put the [S II]/[O II] ratio along the x-axis as an indicator of decreasing excitation of the spectrum (of the individual pixels) for increasing values of the line ratio.

In this Figure we also show the predictions from the "self-consistent pre-ionization" stationary, plane-parallel models of Hartigan et al. (1987) with a $n = 100\,cm^{-3}$ pre-shock density and shock velocities between 20 and 400 km s^{-1}. It is clear that while the shock models give line ratios in the same range as the observations, many of the observed line ratios do not agree in detail with the model predictions.

For HH 1 (left column of Figure 6), all of the line ratios (except possibly for the [O III]/[O II] ratio) show a clump of

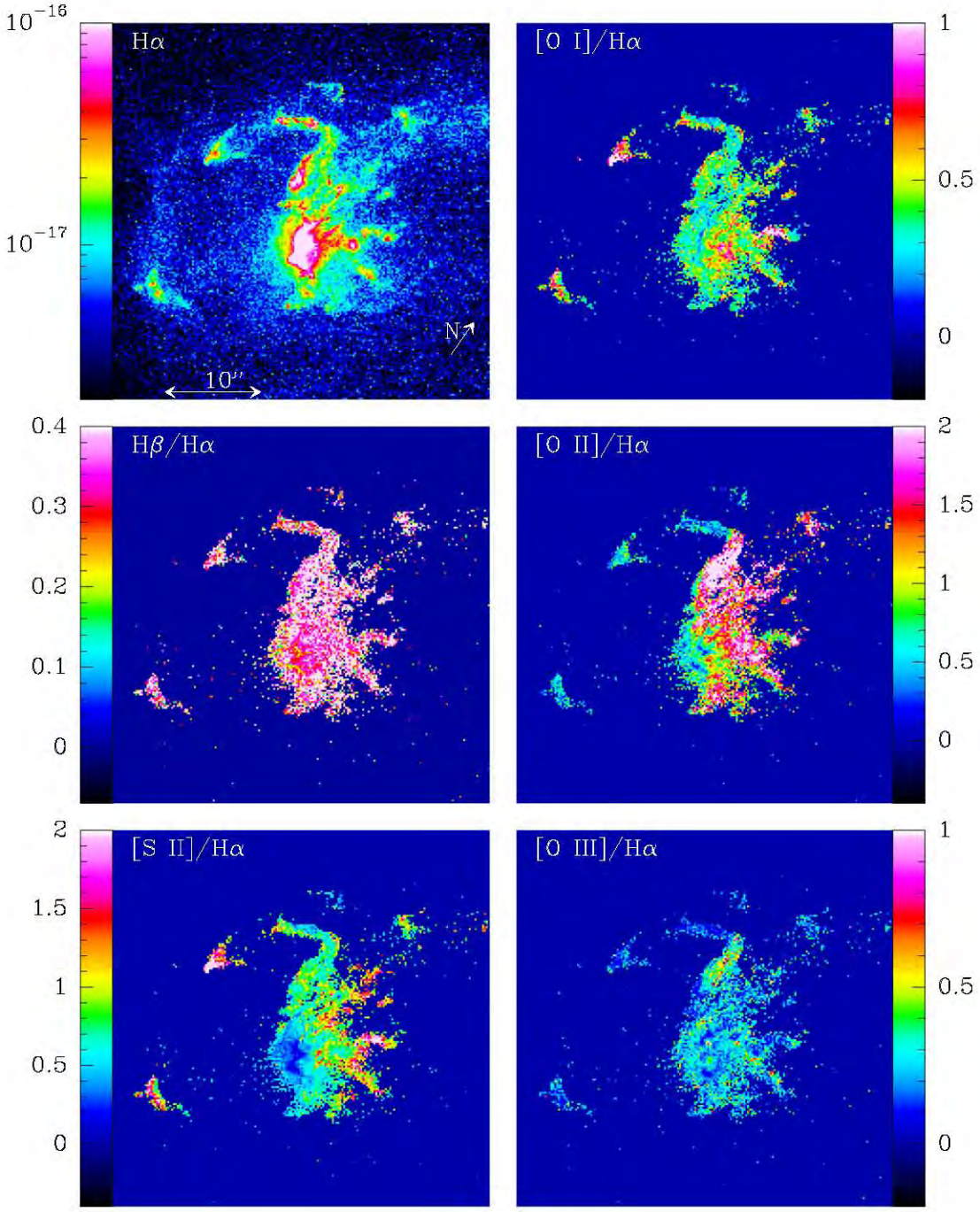

Figure 4. Hα map (top left) and reddening corrected line ratio maps of the other observed lines over Hα (see the labels on the top left of each frame) of HH 2. The line ratio maps are displayed with the linear color scale given by the bars attached to each plot. The scale and orientation of the images are shown on the Hα image (top left). The line ratios have been computed only for the regions with $I_{\rm H\alpha} \geqslant 9 \times 10^{-18}$ erg s^{-1} cm^{-2} pix^{-1}.

points at [S II]/[O II] < 1 values, and then an approximately linear trend for larger values of [S II]/[O II]. These trends are also seen in the HH 2 emission (right column of Figure 6), though with considerably larger dispersions. In HH 2, we see points in the [S II]/[O II] < 1 region which appear to lie along a second, higher slope trend.

Remarkable trends as the ones seen in Figure 6 are seen in many of the possible two-line ratio plot combinations, and they appear to be pointing at some basic underlying principle in the production of the line emission of HH 1 and 2. This basic feature can be understood as follows.

The clearest correlation in our two-line ratio maps is seen in the [O I]/[O II] versus [S II]/[O II] plots (see Figure 6). The fact that most of the points lie along a straight line implies that they all share the same slope $r =$ [O I]/[S II] (which can be verified by calculating the [O I]/[S II] ratio, which indeed has very similar values for all of the regions emitting these lines in HH 1 and 2).

In HH 1, it appears that sulphur is always at least singly ionized, probably as a result of the presence of an FUV radiation field which photoionizes S I. Empirical evidence for this is the fact that the [S I] 4506 and 7725 lines are not detected

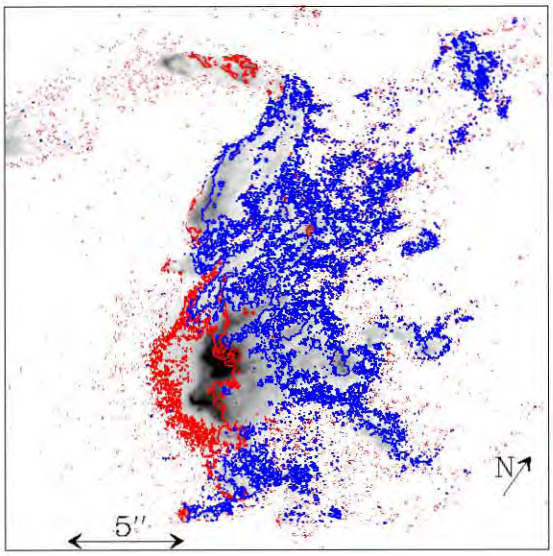

Figure 5. Hα map of the central, bright region of HH 2 (displayed with a logarithmic grayscale), and constant line ratio contours corresponding to [S II]/Hα = 0.4 (red) and [O II]/Hα = 1.5 (blue). The regions enclosed by the red contour correspond to minima in the line ratio, and the regions enclosed by the blue contour correspond to maxima. The scale and orientation of the image are shown. The regions with low [S II]/Hα (enclosed by the red contour) and with high [O II]/Hα (enclosed by the blue contour) have bow-like structures.

in the high signal-to-noise spectra of HH 1 of Solf et al. (1988). Interestingly, carbon does appear to at least partially recombine in HH 1 (as relatively weak emission is observed in the [C I] 8727, 9823 and 9849 lines, see Solf et al. 1988). Because of this, when computing models of HH shock waves it is standard practice to assume that the lowest ionization state of sulphur is S II.

The [S II] emission extends to regions of higher temperatures than the [O I] emission because S II has a higher ionization potential than O I. However, most of the [S II] emission comes from the cooler, lower ionization, denser region (further downstream from the shock wave) in which the [O I] emission is produced. This effect can be seen in plots of the emission coefficients of the [S II] and [O I] lines as a function of distance from the shocks (see, e.g., Raga & Binette 1991; Hartigan et al. 1994; Bacciotti & Eislöffel 1999). Diagnostic line ratios for flows with shock waves are discussed by Podio et al. (2006), Hartigan & Morse (2007) and in the review of Dougados et al. (2010), p. 793.

We can therefore assume that the [S II] and [O I] emission come from regions with similar average values of the temperature, density and ionization fraction. We can then compute the line ratio in an approximate way with a "single parcel model," and use the observed line ratios in the usual "plasma diagnostic" sense. The line ratio would then be given by:

$$\frac{[\mathrm{O\ I}]}{[\mathrm{S\ II}]} = \frac{n_\mathrm{O}}{n_\mathrm{S}} f(T), \tag{1}$$

where n_O is the oxygen and n_S the sulphur number density, and $f(T)$ is a function of the temperature (derived from the appropriate multi-level atom/ion statistical equilibrium problem). In this equation we have assumed that in the region emitting these lines, oxygen is mostly in the form of O I and sulphur in the form of S II, and that the line emission is in the low density regime (i.e., that both emission coefficients are $\propto n_\mathrm{e}$, where n_e is the electron density). We should note that in hotter regions closer to the shocks it is clear that both oxygen and sulphur will have higher ionization states (as [O II], [O III] and [S III] lines are detected in the spectra of HH 1 and 2, see, e.g., Brugel et al. 1981a). However, in the region emitting the [O I] and the [S II] lines, indeed most of oxygen is in the form of O I and sulphur as S II (see Raga & Binette 1991).

Clearly, in the low density regime the emission coefficients are proportional to the collisional excitation coefficients (up from the ground state), which have very similar dependencies for the red [O I] and [S II] lines, since their upper levels lie at similar energies above the ground state. Because of this, $f(T)$ is a relatively weak function of T.

We determine $f(T)$ by solving 5-level atom statistical equilibrium problems (with the parameters of the book by Pradhan & Nahar 2011), and we find the fit :

$$f(T) = 0.0115\left(\frac{T}{10^4\ \mathrm{K}}\right) - 0.0018 \tag{2}$$

which reproduces the numerical results to within 5% in the $T = 5000 \rightarrow 30000$ K temperature range.

Then, the fact that we observe very similar $r = [\mathrm{O\ I}]/[\mathrm{S\ II}]$ ratios in all of HH 1 and 2 directly implies that the emission in each pixel comes from gas with similar temperatures (see Equation (1)). This can be quantified by inverting Equations (1)–(2) to obtain a prediction of the temperature of the gas as a function of the observed [O I]/[S II] line ratio:

$$T_{[\mathrm{O\ I}]/[\mathrm{S\ II}]} = 8.70 \times 10^5\ \mathrm{K}\left(\frac{n_\mathrm{S}}{n_\mathrm{O}}\frac{[\mathrm{O\ I}]}{[\mathrm{S\ II}]} + 0.0018\right). \tag{3}$$

We compute this temperature for all of the pixels of HH 1 and 2, considering the oxygen and sulphur abundances $n_\mathrm{O}/n_\mathrm{H} = 10^{8.51-12}$ and $n_\mathrm{S}/n_\mathrm{H} = 10^{7.06-12}$ obtained for M42 by Esteban et al. (2004). The resulting predicted temperatures are plotted as a function of the [S II]/[O II] line ratio in Figure 7. It is clear that all of the points with [S II]/[O II] > 1 have temperatures of $\approx 10^4$ K for HH 1, and temperatures between $\sim(1 \rightarrow 1.5) \times 10^4$ K for HH 2. Therefore, the linear correlation observed between the [O I]/[O II] and the [S II]/[O II] ratios (see Figure 6) directly implies that the emission of the [O I] and [S II] lines always comes from regions of temperatures $\approx 10^4$ K.

We show the spatial distribution of $T_{[\mathrm{O\ I}]/[\mathrm{S\ II}]}$ in HH 1 and 2 in Figure 8. In HH 1, we see that $T_{[\mathrm{O\ I}]/[\mathrm{S\ II}]}$ has a basically constant value of $\approx 10^4$ K over all of the object, except for a ridge of higher temperatures ($> 2 \times 10^4$ K) along the E wing of HH 1. This ridge coincides spatially with the high Hα/Hβ ratio ridge found by Raga et al. (2015), which has the line ratio values expected for collisional excitation of the Balmer lines. Therefore, the high $T_{[\mathrm{O\ I}]/[\mathrm{S\ II}]}$ ridge seen in Figure 8 probably represents a contribution to the emission from the region of collisional ionization right behind the bow shock.

For HH 2, we see high ($> 3 \times 10^4$ K) $T_{[\mathrm{O\ I}]/[\mathrm{S\ II}]}$ values along the leading edges of the brighter condensations (see Figure 9). These high $T_{[\mathrm{O\ I}]/[\mathrm{S\ II}]}$ regions coincide with the high Hα/Hβ ridges described by Raga et al. (2015), which are likely to correspond to the immediate post-shock regions of collisional excitation and ionization.

In Figure 9 we present the [O III]/[O II] versus [O II]/[O I] line ratio plots for the pixels within the HH 1 (top) and HH 2

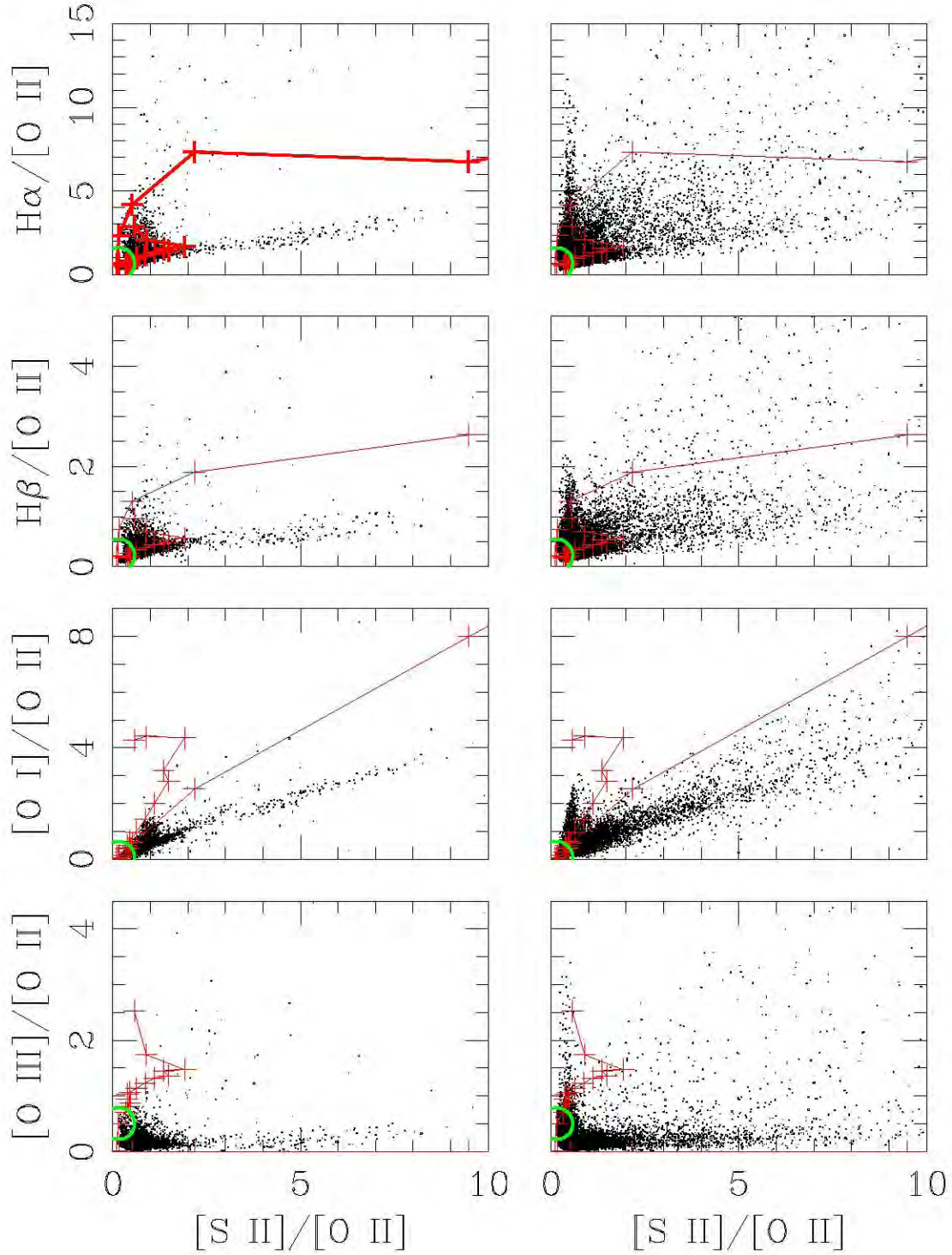

Figure 6. Hα/[O II] (top), Hβ/[O II], [O I]/[O II] and [O III]/[O II] (bottom) vs. [S II]/[O II] two-line ratio plots (for the pixels with $I_{H\alpha} \geqslant 2.7 \times 10^{-17}$ erg s^{-1} cm^{-2} pix^{-1}) of the emitting regions of HH 1 (left) and HH 2 (right). The line ratios predicted from the self-consistent pre-ionization, steady, plane-parallel shock models (with a pre-shock density of 100 cm^{-3} and shock velocities of 20, 30, 40, 60, 80, 90, 100, 110, 120, 130, 140, 160, 180, 200, 220, 240, 260, 280, 300, 350 and 400 km s^{-1}) of Hartigan et al. (1987) are shown with the red crosses joined by a red line. The 100 km s^{-1} shock velocity model is indicated with the green circle, and the extension to high [S II]/[O II] ratios corresponds to the lower velocity shocks. It is clear that some, but not all, of the features seen in the observed line ratios appear to be reproduced by the shock models. The red line along the *x*-axis of the bottom plots corresponds to the shock models with shock velocities $\leqslant$80 km s^{-1}, which have basically no [O III] emission.

(bottom) emitting regions, together with the locus (in this two-line ratio plot) of the plane-parallel shock models of Hartigan et al. (1987). This plot is particularly interesting in that it involves lines from the different ionization states of a single element. It is quite impressive that most of the observed points fall within a region bracketed by the predictions from the shock models, and can therefore be interpreted as a superposition (along the line of sight) of the emission from shocks of different velocities. However, in order to explain the observed line ratios, one would have to argue that in most of the HH 1

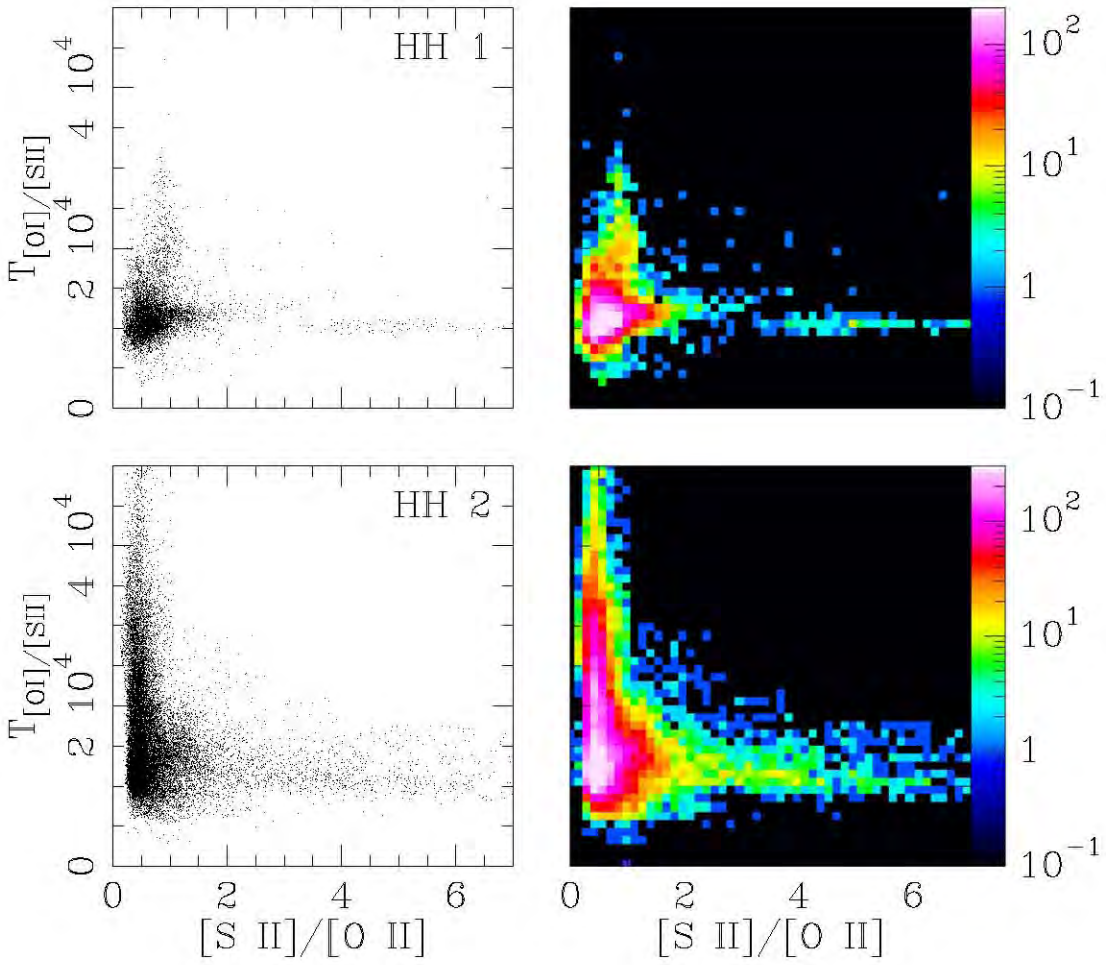

Figure 7. Temperatures deduced from the [O I]/[S II] line ratios as a function of [S II]/[O II] for the pixels in the emitting regions of HH 1 (top) and HH 2 (bottom). The points correspond to all of the pixels with $I_{H\alpha} \geqslant 2.7 \times 10^{-17}$ erg s^{-1} cm^{-2} pix^{-1}. The plots in the left column show the values obtained for the individual pixels, and the plots in the right column show the same data with a color scale giving the number of pixels with values falling into the square bins shown in the plots.

and 2 pixels one sees the combination of a faster shock with a very low velocity shock (of shock velocity $\sim$20 $\rightarrow$ 40 km s^{-1}).

Finally, we present the spatial distributions of the [O III]/[O II] and [O II]/[O I] line ratios in HH 1 (Figure 10) and HH 2 (Figure 11). In HH 1, we see that the region around the northern tip and the W wing (extending to $\sim 3''$ from the tip) have a series of localized maxima of the [O III]/[O II] ratio (see Figure 10). The [O II]/[O I] ratio has a curved ridge (with values $\geqslant$5) in the region of the tip of HH 1. This region is trailed by a valley (with [O II]/[O I] $\approx$ 1) at $\sim 2''$ from the tip and extending toward the E wing. This valley is trailed by another ridge, with the highest values of [O II]/[O I] along the W wing, at distances of $\geqslant 3''$ from the tip of HH 1 (see Figure 10). In HH 2 we see that the [O III]/[O II] ratio has highest values in the leading edge of the brighter condensations (see Figure 11), and that the [O II]/[O I] ratio has highest values along a broken ridge that follows the "second bow" (also seen in the [S II]/Hα ratio, see Figure 5).

It is a priori somewhat puzzling that in HH 1 and 2 the regions with higher [O III]/[O II] in many cases coincide spatially with regions of low [O II]/[O I] (and vice versa), as one would naively expect that regions with higher excitation might show simultaneous increases of both ratios. However, plane-parallel shock models predict increasing [O III]/[O II] and decreasing [O II]/[O I] ratios as a function of increasing shock velocities (for shock velocities $\geqslant$40 km s^{-1}), as can be seen in the line ratios of the shock models of Hartigan et al. (1987) in Figure 10. Therefore, the anti-correlation of these two line ratios seen in HH 1 and 2 is in qualitative agreement with the predictions from shock models.

5. DISCUSSION AND CONCLUSIONS

We have obtained simultaneous *HST* images of the HH 1/2 region in a set of 6 emission lines: Hα, Hβ, [O I] 6300, [O II] 3726+28, [O III] 5007 and [S II] 6716+30. This represents a larger set of *HST* narrow-band images than has ever been observed before in an HH object. For example, Heathcote et al. (1998) obtained Hα, [S II] and [O III] maps of HH 80/81, but most of the *HST* images of other HH objects are restricted to Hα and [S II]. Raga et al. (2015) presented an analysis of the Hα and Hβ HH 1/2 images, and in the present paper we discuss the results obtained from the full set of images.

For HH 1, we find that the bow head has two asymmetric wings: the E wing is brighter in Hα, Hβ, [S II] and [O I], and the W wing is brighter in [O II] and [O III]. This asymmetry in the excitation of the two wings was previously suggested by the ground-based [O III] and Hα images of Raga et al. (1988). Henney (1996) interpreted this asymmetry in terms of a bow shock moving into an environment with a cross-axis density gradient (with the W wing moving into a lower, and the E wing

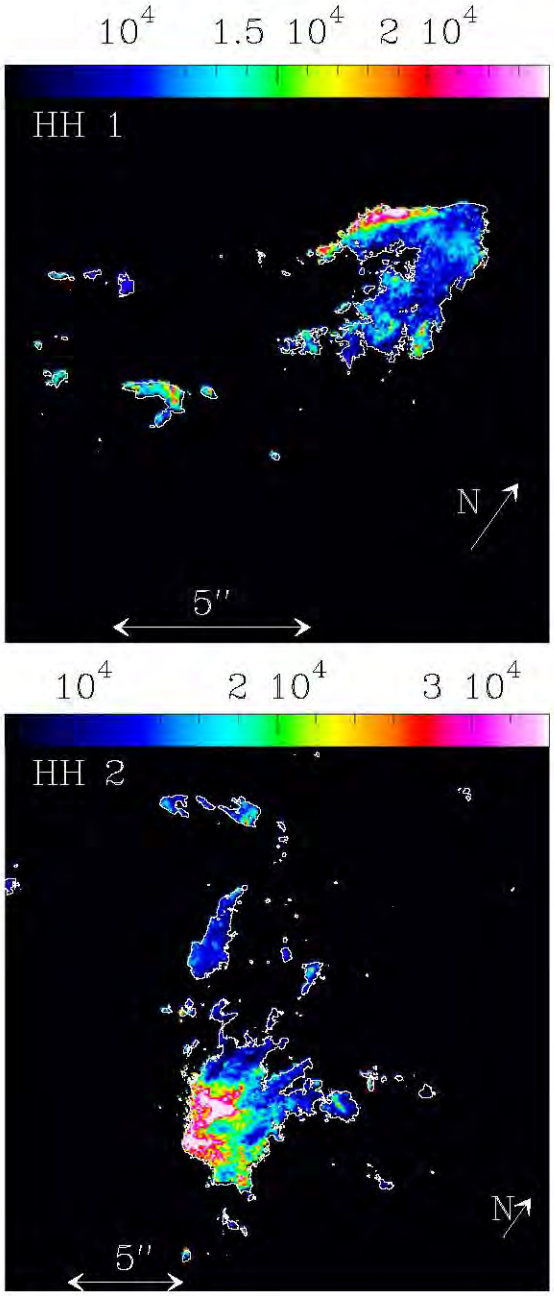

Figure 8. Spatial distribution of the temperatures predicted from the [O I]/[S II] line ratios for the regions of HH 1 (top) and HH 2 (bottom) with $I_{H\alpha} \geqslant 2.7 \times 10^{-17}$ erg s^{-1} cm^{-2} pix^{-1}. The temperature stratifications are displayed with the linear color scales given (in K) by the bars on top of each of the two frames.

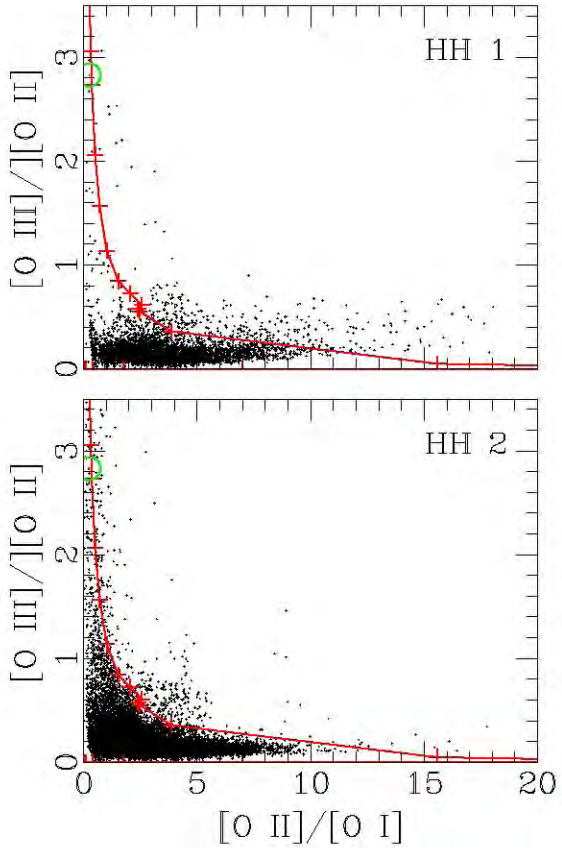

Figure 9. [O III]/[O II] vs. [O II]/[O I] for the pixels with $I_{H\alpha} \geqslant 2.7 \times 10^{-17}$ erg s^{-1} cm^{-2} pix^{-1}) of the emitting regions of HH 1 (top) and HH 2 (bottom). The line ratios predicted from the self-consistent pre-ionization, steady, plane-parallel shock models of Hartigan et al. (1987) are shown with the red crosses joined by a red line. The 100 km s^{-1} shock velocity model is indicated with the green circle, and the extension to low [O III]/[O II] ratios corresponds to the lower velocity shocks.

into a higher density environment). Our present images show that the W wing possibly belongs to a second bow structure (which could correspond to a bow shock or to an internal shock within the impinging jet), so that the interpretation of the observed structure requires additional elements.

The situation is of course more complex for HH 2, which shows a rather chaotic collection of emitting knots. However, we find that the line ratio maps (see Figures 4 and 5) show an arrangement into two bow-like structures: a leading, lower excitation and a trailing, higher excitation bow. This possible arrangement might provide a guiding idea for trying to produce structures resembling HH 2 with 3D numerical simulations. Reproducing the observations of HH 2 will of course not be straightforward, since the narrow-band images (see Section 3.2) and spatially resolved spectra (Riera et al. 2005) indicate that regions of this object are dominated by the light of the brighter condensations being scattered on dust in the surrounding environment. In order to identify correctly the regions of scattered light it will probably be necessary to carry out detailed spectro-polarimetric observations (see Henney & Axon 1995).

An unexpected result of our observations is obtained by placing the pixels from HH 1 and 2 in two-line ratio plots. We find that many of the possible combinations of two-line ratios result in plots which show strong, linear correlations between all of the points. These correlations are stronger for the emitting region of HH 1, but are also seen (with larger dispersions) for HH 2. A particularly remarkable correlation is observed in the [O I]/[O II] versus [S II]/[O II] plots (see Figure 6).

These correlations are a result of the fact that many of the line ratios depend mostly on the temperature, and that the temperature of the region emitting a given line is always within a rather narrow range. The best temperature indicator of our limited set of lines is the [O I]/[S II] ratio, which has a relatively weak temperature dependence, but results from lines coming from very similar spatial regions in the recombination regions of shock waves (see, e.g., Raga & Binette 1991; Bacciotti & Eislöffel 1999). The observed values of this line ratio imply

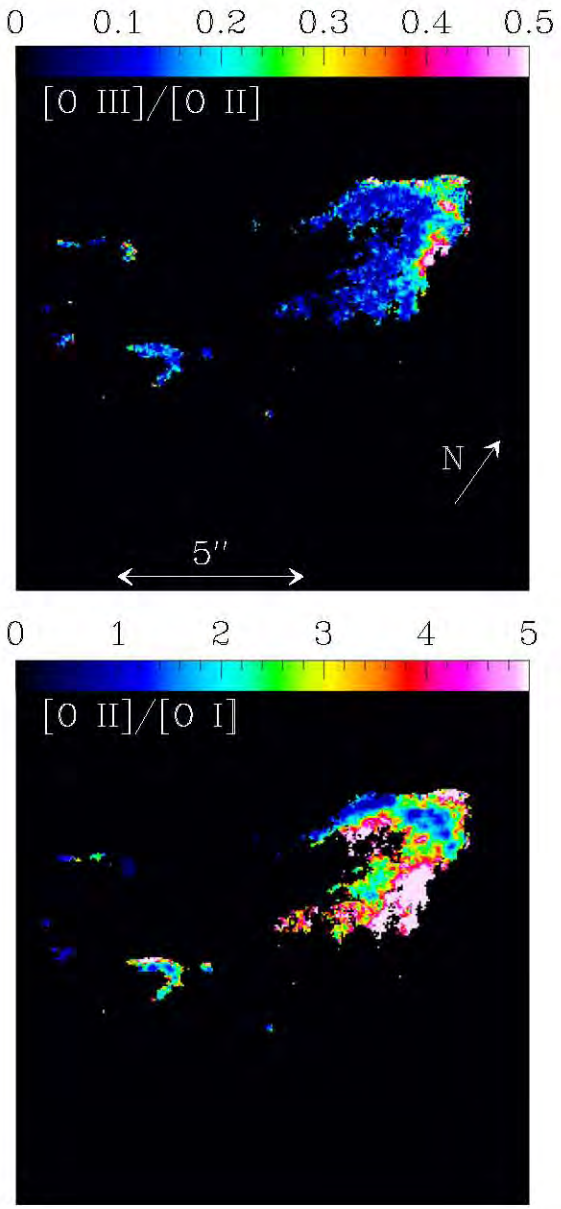

Figure 10. [O III]/[O II] (top) and [O II]/[O I] (bottom) line ratio maps of HH 1 (calculated for the pixels with $I_{H\alpha} \geqslant 2.7 \times 10^{-17}$ erg s^{-1} cm^{-2} pix^{-1}). The line ratios are displayed with the linear color scales given by the bars on top of each of the two frames.

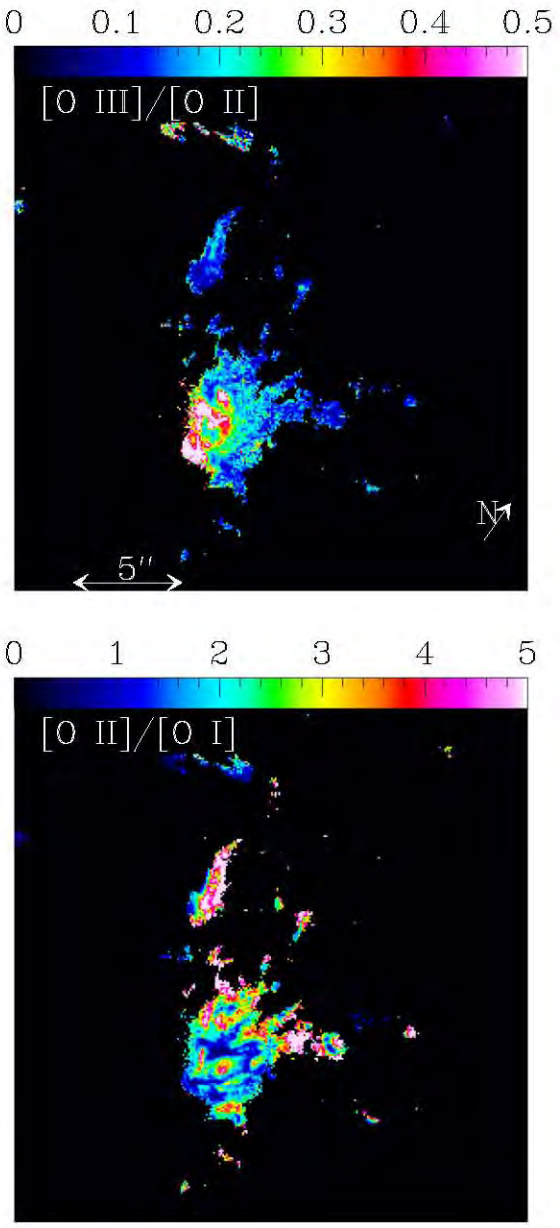

Figure 11. [O III]/[O II] (top) and [O II]/[O I] (bottom) line ratio maps of HH 2 (calculated for the pixels with $I_{H\alpha} \geqslant 2.7 \times 10^{-17}$ erg s^{-1} cm^{-2} pix^{-1}). The line ratios are displayed with the linear color scales given by the bars on top of each of the two frames.

temperatures of $\sim 10^4$ K for most of the emitting region (see Figure 7).

If one plots the spatial distribution of the predicted temperature, one finds that the [O I]/[S II] ratio gives temperatures of $\approx 10^4$ K for most of the HH 1 and 2 emitting regions, except for high temperatures ($>2 \times 10^4$ K) in ridges along the leading edges of the brighter condensations (see Figure 8). These ridges coincide with the regions in which Raga et al. (2015) found high Hα/Hβ ratios, implying collisional excitation of the Balmer lines. Therefore, the high temperature implied for these ridges by the observed [O I]/[S II] ratios is consistent with the fact that we are seeing a hot region close to the shock waves in which the material is being collisionally ionized.

In the two-line ratio plots (Figure 6), we have included the values obtained from a series of plane-parallel shock models (with self-consistent pre-ionization, a pre-shock number density of 100 cm^{-3} and shock velocities from 20 to 400 km s^{-1}) of Hartigan et al. (1987). Some but not all of the features of the two-line ratio plots appear to be reproduced by the shock models. This is probably to be expected, since a wider range of parameters might be present (e.g., different pre-shock densities and pre-ionization states), the plane-parallel approximation is probably not correct for many of the emitting regions, and the steady approximation is not likely to be applicable (with strong effects on the predicted line ratios, see Innes et al. 1987). Also, a comparison with the predictions from "shock models" (in which the emission from all of the cooling/recombination region is added together) might be inappropriate because in some regions we might be resolving the structure of the cooling regions. Finally, at any given point in HH 1 and 2

we are likely to be observing superpositions of different flow structures which contribute to the local emission.

The two-line ratio plots (Figure 6) offer the intriguing possibility of carrying out comparisons with gasdynamic (or MHD) models of HH bow shocks. Even though it will always be a somewhat hopeless task to attempt to reproduce the complex morphologies and kinematics of HH 1 and 2 (or for the sake of the argument, of any HH object observed with high angular resolution), it should be a less thankless task to attempt to reproduce the general trends and ranges of the two-line ratio plots. The fact that these diagrams show relatively simple trends (see Figure 6), and that these trends are shared by the morphologically quite different HH 1 and HH 2, suggests that they are the direct consequence of the global parameters of the objects and the physical processes involved, and are not dependent on the detailed structure that the flow might have at a given time.

Either axisymmetric or 3D simulations of an HH bow shock should stably reproduce the two-line ratio correlations observed in HH 1 and 2 (see Figure 6), provided that they include the physical processes relevant for the production of the emission line spectrum. This caveat is of course the main challenge in attempting to compute appropriate numerical models, and we will definitely give it a try.

The numerical simulations will have to be done in at least two steps: high spatial resolution axisymmetric simulations (to have an appropriate resolution of the recombination regions in order to try to reproduce the observed line ratios), and lower resolution 3D simulations (in order to model the successive, off-axis bow structures observed in HH 1 and 2). The results from these simulations will have to be compared not only with the observed line ratios (in which the positional information has been removed) but also with the images, radial velocities and proper motions of these HH objects.

Support for this work was provided by NASA through grant *HST*-GO-13484 from the Space Telescope Science Institute. AR and ACR acknowledge support from the CONACyT grants 101356, 101975 and 167611 and the DGAPA-UNAM grants IN105312 and IG100214.

REFERENCES

Bacciotti, F., & Eislöffel, J. 1999, A&A, 342, 717
Bally, J., Heathcote, S., Reipurth, B., et al. 2002, AJ, 123, 2627
Böhm, K. H., & Solf, J. 1992, AJ, 104, 1193
Brugel, E. W., Böhm, K. H., & Mannery, E. 1981a, ApJS, 47, 117
Brugel, E. W., Böhm, K. H., & Mannery, E. 1981b, ApJ, 234, 874
Cohen, M., & Schwartz, R. D. 1979, ApJL, 233, L77
Dopita, M. A., Binette, L., & Schwartz, R. D. 1982, ApJ, 261, 183
Dougados, C., Bacciotti, F., Cabrit, S., & Nisini, B. 2010, Jets from Young Stars IV, Lecture Notes in Physics, Vol. 793 (Berlin: Springer)
Esteban, C., Peimbert, M., García-Rojas, J., et al. 2004, MNRAS, 355, 229
Haro, G. 1952, ApJ, 115, 572
Hartigan, P., Frank, A., Foster, J. M., et al. 2011, ApJ, 736, 29
Hartigan, P., & Morse, J. A. 2007, ApJ, 660, 426
Hartigan, P., Morse, J. A., & Raymond, J. C. 1994, ApJ, 436, 125
Hartigan, P., Raymond, J. C., & Hartmann, L. W. 1987, ApJ, 316, 323
Heathcote, S., Reipurth, B., & Raga, A. C. 1998, AJ, 116, 1940
Henney, W. J. 1996, RMxAA, 32, 2
Henney, W. J., & Axon, D. J. 1995, ApJ, 454, 233
Herbig, G. H. 1951, ApJ, 113, 697
Herbig, G. H., & Jones, B. F. 1981, AJ, 86, 1232
Hester, J. J., Stapelfeldt, K. R., & Scowen, P. A. 1998, AJ, 116, 372
Innes, D. E., Giddings, J. R., & Falle, S. A. E. G. 1987, MNRAS, 227, 1021
O'Dell, C. R., Ferland, G. J., Henney, W. J., & Peimbert, M. 2013, AJ, 145, 92
Ortolani, S., & D'Odorico, S. 1980, A&A, 83, L8
Podio, L., Bacciotti, F., Nisini, B., et al. 2006, A&A, 456, 189
Pradhan, A., & Nahar, S. 2011, Atomic Astrophysics and Spectroscopy (Cambridge: Cambridge Univ. Press)
Pravdo, S. H., Feigelson, E. D., Garmire, G., et al. 2001, Natur, 413, 708
Pravdo, S. H., Rodríguez, L. F., Curiel, S., et al. 1985, ApJL, 293, L35
Raga, A. C., Barnes, P. J., & Mateo, M. 1990, AJ, 99, 1912
Raga, A. C., & Binette, L. 1991, RMxAA, 22, 265
Raga, A. C., Mateo, M., Böhm, K. H., & Solf, J. 1988, AJ, 95, 1783
Raga, A. C., Reipurth, B., Cantó, J., Sierra-Flores, M. M., & Guzmán, M. V. 2011, RMxAA, 47, 425
Raga, A. C., Reipurth, B., Castellanos-Ramírez, A., Chiang, H.-F., & Bally, J. 2015, ApJL, 798, L1
Riera, A., Raga, A. C., Reipurth, B., et al. 2005, RMxAA, 41, 371
Schwartz, R. D., Cohen, M., Jones, B. F., et al. 1993, AJ, 106, 740
Solf, J., Böhm, K. H., & Raga, A. C. 1988, ApJ, 334, 229
Strom, S. E., Strom, K. M., Grasdalen, G. L., et al. 1985, AJ, 90, 2281

2.5. Variability of the emission line fluxes and ratios of HH 1/2

En el trabajo correspondiente a este capítulo se comparan datos espectrofotométricos obtenidos en 1978 (Brugel et al., 1981) con los flujos de líneas de emisión de imágenes calibradas obtenidas con el Telescopio Espacial Hubble (HST) en 1994 (Hester et al., 1998) y 2014 (Raga et al., 2015a).

La contribución hecha en este trabajo fue en la búsqueda de datos históricos de la emisión de líneas de HH 1/2 y en el desarrollo del modelo interpretativo.

Las observaciones de 1978 fueron realizadas con un espectrofotómetro multicanal, el cual tiene una apertura que cubre la mayor parte de las regiones emisoras de HH 1 y 2. El espectro incluye las líneas de [O II] 3726+28, [O III] 5007, [O I] 6300, Hα y Hβ y [S II] 6716+6730. En las observaciones de 1994, las líneas obtenidas son: [O III] 5007, Hα y [S II] 6716+30. Finalmente, las imágenes obtenidas en 2014 incluyen líneas de emisión de: Mg II 2798, [O II] 3726+28, [O III] 5007, [O I] 6300, Hα, Hβ y [S II] 6716+30. Además, a fin de evaluar la evolución temporal de la línea de Mg II 2798, se consideran los flujos obtenidos en 1980 con el Explorador Internacional Ultravioleta (IUE,Böhm-Vitense et al. 1982).

Los resultados obtenidos se enumeran a continuación.

Para HH 1:

- La luminosidad de Hα se incrementó cerca de 4 % entre 1978 y 1994, decreciendo aproximadamente un 24 % en el periodo de 1994 a 2014.
- La línea Mg II 2798 (relativa a Hα) no presenta un cambio apreciable. Esto significa que las variaciones en el espectro intrínseco son pequeñas y que la extinción hacia este objeto ha permanecido constante es este periodo de tiempo.
- La intensidad de las líneas [O II] 3726+29 (relativas a Hα) se ha incrementado cerca de 40 % en el periodo 1978 a 2014.
- Hβ tiene un valor bajo comparado con Hα en las observaciones de 1978, lo cual indica que las regiones con líneas excitadas colisionalmente contribuyen más al espectro de aquella época que en el de 2014.
- La línea [O III] 5007 se incrementa por un factor 2 de 1978 a 1994 y luego decrece aproximadamente 20 % en el 2014.
- La línea [O I] 6300 presenta un leve incremento en el periodo 1978 a 2014.
- Las líneas [S II] 6716+30 (relativas a Hα) crecen un factor 2 en el periodo 1978 a 2014.

Para HH 2:

- La luminosidad de Hα se incrementa por un factor $\sim$ 2.4 de 1978 a 1994; mientras que entre 1994 y 2014 crece un factor $\sim$ 1.75.
- La línea Mg II 2798 se incrementó un factor 2, sin embargo presenta algunos problemas técnicos ya que la apertura del espectrógrafo del IUE no cubre toda la región que emite en HH 2.
- Las líneas [O II] 3726+29 (relativas a Hα) han crecido aproximadamente 20 % en el periodo 1978 a 2014.
- La línea [O III] 5007 tiene un incremento de aproximadamente 40 % de 1978 a 1994 y en 2014 regresa al valor que tenía en 1978.
- Las líneas Hβ, [O I] 6300, y [S II] 6716+30 (relativas a Hα) presentan muy pequeñas variaciones.

Con el fin de interpretar la dependencia temporal de la emisión de líneas observadas, se desarrolló un modelo simple de una superficie de trabajo, que ha arrojado resultados muy interesantes.

Los resultados del análisis observacional muestran que en el periodo 1978-2014 en HH 2 los cocientes de línea obtenidos son básicamente independientes del tiempo (lo que indica un choque de velocidad prácticamente constante), mientras que la luminosidad se incrementa de manera importante (aproximadamente por un factor 4). Se descarta el hecho de que este aumento en la luminosidad sea producido por un cambio en la extinción del objeto a medida que el objeto se aleja de la fuente emisora, puesto que esto implicaría que los cocientes de línea observados deberían ser dependientes del tiempo.

Por tanto, el hecho de que HH 2 sea más brillante puede interpretarse (utilizando un modelo de una superficie de trabajo) como un jet denso que tiene tanto velocidad como pérdida de masa constante y que se mueve en un medio con densidad creciente. En este modelo, el incremento en la luminosidad es proporcional al incremento de la densidad del medio.

Para el caso de HH 1, las observaciones muestran que la intensidad de las líneas han permanecido prácticamente constantes, con un decremento de aproximadamente 30 % en el periodo 1978-2014. Esta variación de la luminosidad en el tiempo se interpreta en el modelo de la superficie de trabajo como indicativo de que HH1 se mueve en un medio de densidad decreciente.

Revista Mexicana de Astronomía y Astrofísica, **52**, 347–355 (2016)

VARIABILITY OF THE EMISSION LINE FLUXES AND RATIOS OF HH 1/2

A. C. Raga,[1] B. Reipurth,[2] A. Castellanos-Ramírez,[1] and J. Bally[3]

Received April 18 2016; accepted June 7 2016

RESUMEN

Comparamos datos espectrofotométricos obtenidos en 1978 (por Brugel et al. 1981a) con los flujos de líneas de emisión de imágenes calibradas obtenidas con el Hubble Space Telescope (HST) en 1994 y 2014. Esta comparación muestra que los cocientes de líneas de emisión de estos objetos se han mantenido sorprendentemente invariantes durante los últimos 36 años. Por otro lado, las intensidades de las líneas sí han cambiado, y muestran un incremento por un factor de ≈ 4 para HH 2, y un decremento de $\approx 30\%$ para HH 1. Estos resultados apoyan la idea de que HH 1 y 2 son cabezas de jets densos, viajando en un medio ambiente con densidad decreciente (para HH 1) o creciente (para HH 2).

ABSTRACT

We compare spectrophotometric data of HH 1 and 2 obtained in 1978 (by Brugel et al. 1981a) with the emission line fluxes from calibrated Hubble Space Telescope (HST) images obtained in 1994 and 2014. This comparison shows that the emission line ratios of these objects have remained surprisingly invariant during the past 36 years. On the other hand, the line intensities have indeed changed, with HH 2 brightening by a factor of ≈ 4 and HH 1 becoming $\approx 30\%$ fainter. These results would be consistent with HH 1 and 2 being leading working surfaces of heavy jets travelling into an environment of decreasing (for HH 1) or increasing (HH 2) densities.

Key Words: Herbig-Haro objects — ISM: individual objects (HH1/2) — ISM: jets and outflows — shock waves — stars: formation — stars: winds, outflows

1. INTRODUCTION

Even though it is clear that the Herbig-Haro objects HH 1 and 2 have strong time-variabilites (Herbig 1969, 1973; Herbig & Jones 1981; Brugel et al. 1985; Raga et al. 1990a; Böhm et al. 1993; Eislöffel et al. 1994), the study of their time-dependent emission spectrum has proven to be quite difficult. The difficulties arise from the heterogeneity of the data.

The older images of HH 1 and 2 (before ≈ 1985) are relatively broad band photographic plates, and have been analyzed by Herbig (1969, 1973) for time variabilities. The analysis presented in these papers to some extent stands alone, since it is not straightforward to relate it to more recent observations (obtained with different techniques).

More recent CCD images of HH 1 and 2 obtained through narrow-band filters, cover very few emission lines, and in general lack any calibration. As far as we are aware, the only attempts to use ground based CCD images for an evaluation of the variability of HH 1 and 2 were presented by Raga et al. (1990a) and by Eislöffel et al. (1993).

Spectrophotometric observations of HH 1 and 2 have generally been obtained either with "short" (Hartigan et al. 1987) or "long" (Solf et al. 1988; Giannini et al. 2015) spectrograph slits. Though the obtained spectra are generally well calibrated, it is difficult to disentangle the time-variability of the angularly extended HH 1 and 2 objects from effects due to different slit sizes and positions of the successive

[1]Instituto de Ciencias Nucleares, Universidad Nacional Autónoma de México, Ciudad de México, México.
[2]Institute for Astronomy, Univ. of Hawaii at Manao, Hilo, USA.
[3]Center for Astrophysics and Space Astronomy, Univ. of Colorado, Colorado, USA.

observations. Also, spectrophotometric observations of Brugel et al. (1981a, b) are available, which cover at least most of the emitting regions of HH 1 and 2 (see below and § 2).

The HH 1 and 2 images obtained with the Hubble Space Telescope (Hester et al. 1998; Bally et al. 2002; Hartigan et al. 2011; Raga et al. 2015a, b; Raga et al. 2016) have calibrated fluxes, and are therefore appropriate for studying the time-dependence of the emission. An analysis of the time-variability of the [O III] 5007, Hα and [S II] 6716+30 emission of HH 1 in this images was presented by Raga et al. (2016). Also, a "pre-COSTAR" set of HST images of HH 2 (in Hα, [S II] and [O III]) was obtained by Schwartz et al. (1993).

In Figure 1 we present a comparison between a photograph of HH 2 obtained by Herbig in 1959 (in red light, with the Lick Observatory 120-inch reflector shortly after its inauguration), and the addition of an Hα and a [S II] 6716+30 frame obtained with the Hubble Space Telescope in 2014 (see Raga et al. 2015a, b). The two images have been scaled and centered in an approximate way. From this figure, it is clear that the structure of HH 2 has changed in a dramatic way over the past ≈ 55 years.

In the present paper, we use the two sets of HST images which cover a broader range of emission lines, namely,

- the 1994 images of Hester et al. (1998), which include filters isolating the [O III] 5007, Hα and [S II] 6716+30 lines,
- the 2014 observations of Raga et al. (2015a,b) which include the Mg II 2798 (not described in the published papers), [O II] 3726+28, Hβ, [O III] 5007, [O I] 6300, Hα and [S II] 6716+30 lines.

The second (2014) set of HST images covers most of the bright near-UV to optical emission lines of HH 1 and 2, and is therefore appropriate for studying the time-evolution of the spectra of these objects. Unfortunately, the first (1994) set has only three images, and can only be used for an analysis of the time-evolution of the three line combinations.

For an analysis of more emission lines, we can use the spectrophotometric observations of Brugel et al. (1981a). These authors used a multi-channel spectrophotometer with apertures that covered most of the emitting regions of HH 1 and 2. These observations can be directly compared with line fluxes calculated by angularly integrating the 1994 and 2014 sets of HST images over the emitting areas of HH 1 and HH 2.

In this way, we use the immensely detailed HST images only for obtaining an angularly integrated emission line spectrum of HH 1 and 2, and we compare the resulting spectra with the spectrophotometric observations of Brugel et al. (1981a). We feel that the somewhat brutal angular integration of the HST images is justified by the very interesting comparison that can be made with the older spectrophotometric results.

The paper is organized as follows. The HST images and the older, spectrophotometric data sets are discussed in § 2. The 2014 Mg II 2798 HST image (which has not been presented before in the literature) is also presented in this section. § 3 presents an evaluation of the time-evolution of the emission line spectra of HH 1 and 2. § 4 discusses a simple working surface model which is used for interpreting the observed time-dependence of the line emission. Finally, the results are discussed in § 6.

2. THE OBSERVATIONS

2.1. *The reddening correction*

Brugel et al. (1981a) used Miller's (1968) method, which is based on the fixed ratio of the transauroral (4069, 4076Å) to the auroral (10318, 10336Å) [S II] lines, and obtained $E(B-V) = 0.47$ for HH 1 and $E(B-V) = 0.35$ for HH 2. Raga et al. (2015b) used the average of the Hα/Hβ ratios of the individual emitting pixels of HH 1 and 2 to derive $E(B-V) \approx 0.27$ for the two objects.

In this paper, we present the observed line fluxes and ratios, as well as the values corrected for a standard Galactic extinction curve with $E(B-V) = 0.27$. This extinction curve (see Fitzpatrick 1999) corresponds to the $R = A_V/E(B-V) = 3.1$ case of Cardelli et al. (1988). This choice is not unique, since there has been a considerable amount of discussion as to which extinction curve is actually relevant for the HH 1/2 region (see, e.g., Böhm-Vitense et al. 1982 and Böhm et al. 1991). The choice of extinction curve of course has a particularly strong effect in the UV.

2.2. *The first epoch spectrophotometric observations*

In September 1978, Brugel et al. (1981a) observed HH 1 and 2 with the MCSP II spectrophotometer (see Oke 1969) at the Palomar 5.1 m telescope. In the configuration that was used the spectrophotometer had an aperture of 6″ diameter (see Brugel et al. 1981b), and several positions (2 for HH 1 and 3 for HH 2) were used to cover the emitting regions of HH 1 and 2. We have now co-added

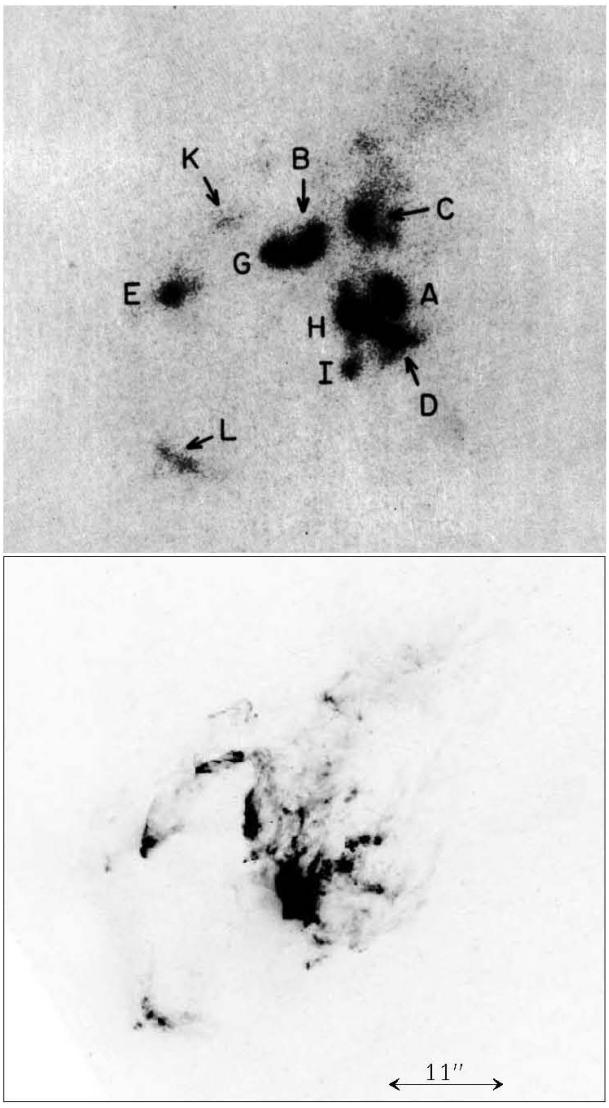

Fig. 1. Comparison between a photograph of HH 2 (obtained by G. Herbig in 1959 at the Lick Observatory 120-inch reflector, top) and an Hα+[S II] image (obtained in 2014 with the HST, shown with a linear greyscale). The two images have been approximately scaled and centered relative to each other. The identifications of the condensations of HH 2 are given in the top frame, and the angular scale is shown in the bottom frame. N is up and E to the left.

the spectra from the two HH 1 apertures and the three HH 2 apertures to obtain two spectra: one for HH 1 and one for HH 2.

These spectra include the [O II] 3726+28, Hβ, [O III] 5007, [O I] 6300 and Hα lines. Unfortunately, the channels of the MCSP cover the [S II] 6716 but not the [S II] 6730 line. Because of this, we have taken the [S II] 6716+6730/Hα ratio from a lower quality spectrum obtained by Brugel et al. (1981a) at the KPNO 2.1 m telescope.

Finally, for the Mg II 2798 line we have taken the fluxes obtained in 1980 with the International Ultraviolet Explorer (IUE) by Böhm-Vitense et al. (1982). The IUE spectrograph had a $23'' \times 10''$ aperture, which included most of the emitting regions of HH 1 and 2. As this UV observation was carried out only a couple of years after the Brugel et al. (1981a) optical observations. In the following we consider them as taken at the same time.

2.3. *The HST images*

We consider two epochs of HST images:

1. the [S II] 6716+30, Hα and [O III] 5007 images of Hester et al. (1998), obtained in 1994.6,

2. the [S II] 6716+30, Hα, [O I] 6300, [O III] 5007, Hβ, and [O II] 3726+28 images of Raga et al. (2015a), obtained in 2014.6.

To the 2014.6 set of images, we have added a Mg II 2798 image (a 5484 s exposure through the F280N filter) which was not analyzed by Raga et al. (2015a). Figure 2 shows the brighter region of HH 2 in the Hα, Hβ, and Mg II 2798 dereddened images, and the Mg II/Hβ line ratio map. HH 1 is barely visible in the Mg II 2798 frame, but an angularly integrated flux for HH 1 can be obtained.

There are two other epochs of HST images of HH 1 and 2 (see Bally et al. 2002 and Hartigan et al. 2011), but we do not include them in the present study because they only cover the [S II] 6716+30 and Hα lines.

As discussed by Raga et al. (2015a), the continuum emission of HH 1 and 2 affects the line fluxes obtained from the HST images. This continuum contamination is more important for the blue lines, and it could be as large as $\approx 30\%$ for the Mg II 2798 line. However, this is unlikely to have a large effect for the qualitative interpretation of the emission proposed in the present paper.

In order to compare the HST line fluxes with the spectrophotometric data of Brugel et al. (1981a), we carry out angular integrations over the emitting areas of HH 1 and 2 in the HST frames. In order to do this, we add the emission within the 5×10^{-15} erg s^{-1}cm^{-2}arcsec^{-2} (dereddened) Hα isophotes of HH 1 and 2. In this way, we avoid defining arbitrary "boxes" around both objects.

2.4. *The Mg II 2798 image*

Figure 2 shows the Mg II 2798 HST image obtained in 2014 (see subsection 2.3). We see that the Mg II emission has an angular extent comparable to that of the Hβ emission (fainter, more extended regions being seen in Hα). Because of this, we have chosen to calculate the Mg II/Hβ ratio map (which depends much less on the reddening correction than the Mg II/Hα ratio), which is also shown in Figure 2. We do not display the Mg II emission of HH 1 because it is quite faint, so that it is only appropriate for obtaining an angularly integrated line flux.

From the line ratio map, we see that most of the Mg II emitting region of HH 2 (within condensation H) has a Mg II/Hβ ratio of $\approx 1 \rightarrow 2$. If one looks at the predictions from the plane-parallel shock models of Hartigan et al. (1987), one sees that these line ratios are consistent with shock velocities between 110 and 160 km s^{-1}.

There is also a small region in the NE of condensation H with Mg II/H$\beta \approx 5$, implying a shock velocity of ≈ 260 km s^{-1} (see Hartigan et al. 1987).

3. THE TIME-DEPENDENT LINE RATIOS AND FLUXES

In Table 1, we present the observed and dereddened Hα fluxes obtained in the three epochs of observations described in § 2. This table gives the measured (F) as well as the dereddened (F_0) fluxes, which were obtained assuming a standard Galactic extinction curve with $E(B-V) = 0.27$ (for both HH 1 and 2, see § 2.1). We have also computed the Hα luminosities with the dereddened fluxes and a distance of 414 pc to HH 1 and 2.

It is clear that the Hα luminosity of HH 1 has a slowly decreasing trend, with a decrease of $\approx 4\%$ from 1978.7 to 1994.6 and a somewhat larger decrease of $\approx 24\%$ from 1994.6 to 2014.6. On the other hand, HH 2 has an Hα luminosity which increases by a factor of ≈ 2.4 from 1978.7 to 1994.6 and by a factor of ≈ 1.75 from 1994.6 to 2014.6.

In Table 2, we present the observed and dereddened line ratios of HH 1 and 2. For both objects, the spectrum has a surprisingly small time-dependence. For HH 1:

- the Mg II 2798 line (relative to Hα) has not changed appreciably from 1980.7 to 2014.6. Unless we have a strange coincidence, this result seems to imply both that the variations of the intrinsic spectrum are small and that the extinction to HH 1 has remained invariant during this time-period,
- the [O II] 3726+29 lines have grown by $\approx 40\%$ from 1978.7 to 2014.6,
- the Hβ line has a relatively low value compared to Hα in the 1978.7 spectrum. This might be an indication that the regions of HH 1 with collisionally excited lines could have contributed more to the spectrum of HH 1 than in 2014.6 (when the regions of high Hα/Hβ ratio have small angular extents, see Raga et al. 2015b),
- the [O III] 5007 line grew by a factor of 2 from 1978.7 to 1994.6, and then decreased by $\approx 20\%$ in the 2014.6 observations,
- the [O I] 6300 line has had a small increase from 1978.7 to 2014.6,
- the [S II] 6716+30 lines have grown (relative to Hα) by a factor of ≈ 2 from 1978.7 to 2014.6.

For HH 2:

- the Mg II 2798 line has grown by a factor of 2 from 1980.7 to 2014.6. This could be due to the fact that the aperture of the IUE spectrograph (used for the 1980.7 observations see § 2) might not have included all of the emitting region of HH 2. Also, the continuum contamination in the HST image could be responsible for part of this increased flux (however, a corresponding increase should then be seen in HH 1),
- the [O II] 3726+29 lines have grown (relative to Hα) by $\approx 20\%$ from 1978.7 to 2014.6,
- the [O III] 5007 line grows by $\approx 40\%$ from 1978.7 to 1994.6, and in 2014.6 returns to a value very similar to the 1978.7 value,
- the Hβ, [O I] 6300 and [S II] 6716+30 lines have very small variations (relative to Hα).

4. INTERPRETATION IN TERMS OF A WORKING SURFACE MODEL

4.1. *General considerations*

The variations in the emission line ratios for HH 1 are not large, but might be significant (in particular, for the [S II] and [O II] lines). The spectrum of HH 2 shows smaller line ratio variations, except for the Mg II 2798 line (an effect which might be due to part of the emitting region falling outside the IUE spectrograph aperture of the 1980.7 observations). Therefore, we conclude that the emission line spectra of HH 1 and 2 have at most shown small variabilities in their *relative* line intensities (see Table 2).

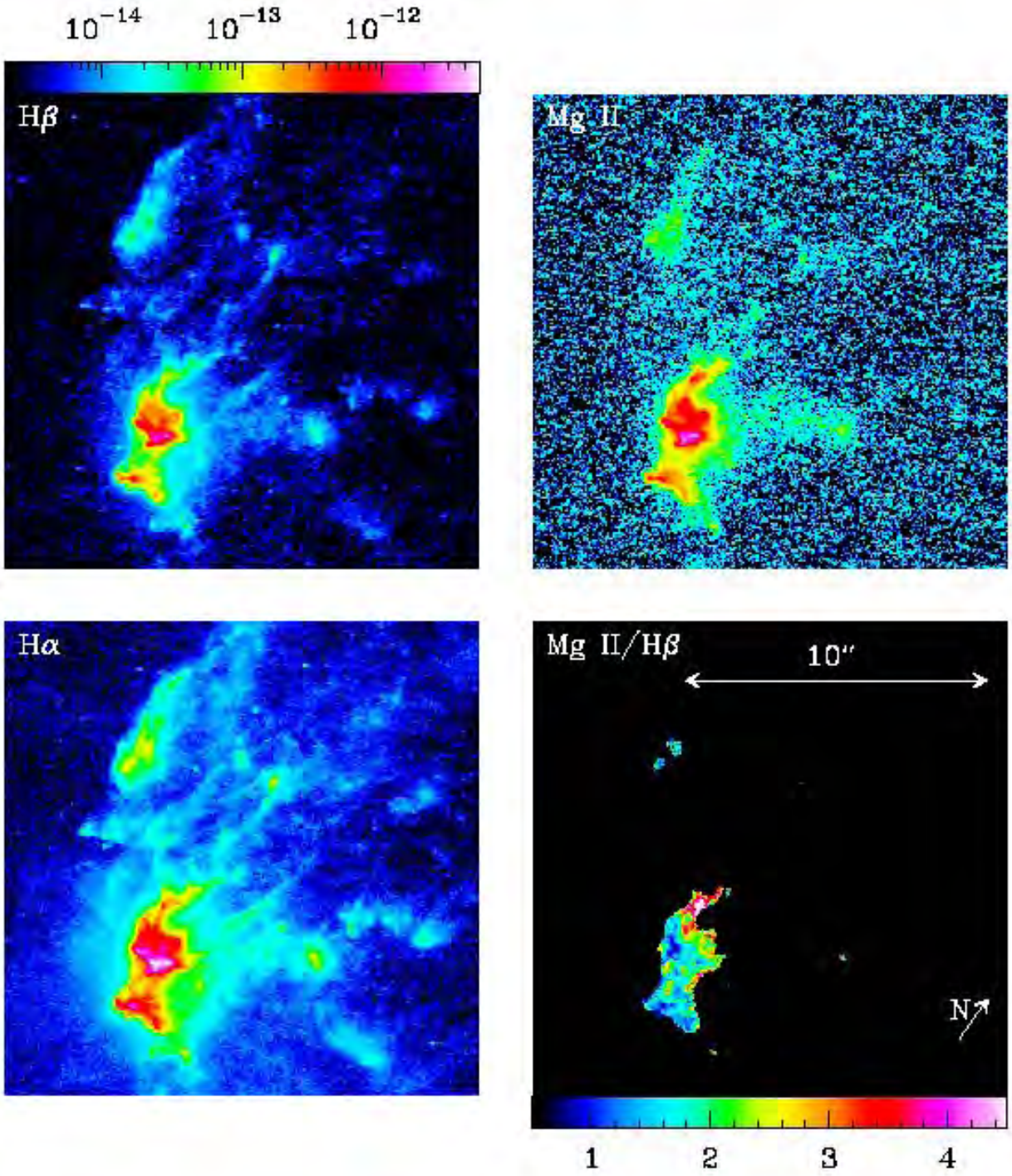

Fig. 2. Hβ (top left), Hα (bottom left), Mg II 2798 (top right) and Mg II/Hβ line ratio (bottom right) maps of HH 2. The emission maps are shown with the logarithmic color scale (in erg s^{-1} cm^{-2} $arcsec^{-2}$) displayed in the top left bar. The line ratio map is shown with the linear color scale displayed in the bottom right bar. The angular scale and orientation of the frames are shown in the bottom right frame. The color figure can be viewed online.

TABLE 1

Hα LINE FLUXES AND LUMINOSITIES

Epoch	HH 1			HH 2		
	$F_{H\alpha}$[1]	$F_{H\alpha,0}$[1]	$L_{H\alpha}$[2]	$F_{H\alpha}$[1]	$F_{H\alpha,0}$[1]	$L_{H\alpha}$[2]
2014.6	4.16	7.50	4.05×10^{-3}	33.67	60.75	3.28×10^{-2}
1994.6	5.50	9.92	5.36×10^{-3}	19.21	34.67	1.87×10^{-2}
1978.7	5.77	10.41	5.63×10^{-3}	7.88	14.21	7.68×10^{-3}

[1]Observed (F) and dereddened (F_0) Hα fluxes in units of 10^{-13} erg s^{-1} cm^{-2}.

[2]Luminosities (in units of $L_\odot$) assuming a distance of 414 pc.

HH 1 shows a small decrease in Hα flux of ≈ 30% from 1978 to 2014. On the other hand, the Hα flux of HH 2 shows a clear, monotonic increase as a function of time.

Unless we have a combination of effects cancelling each other out, we can conclude that the invariance of the line ratios implies that:

- a time-independent interstellar extinction correction (such as the one which we have applied, see § 2) appears to be appropriate,
- the shock velocities associated with HH 1 and 2 do not change substantially as a function of time.

As can be seen from steady, plane-parallel shock models (see, e.g., Raymond 1979 and Hartigan et al. 1987), the emission line ratios of the spectrum emitted by a shock are generally a strong function of shock velocity, and only depend weakly on the preshock density. Also, shocks (of a given shock velocity) with a cooling function dominated by processes in the "low density regime" have line fluxes that scale linearly with the preshock density.

Therefore, an increase in the emission line flux (and at the same time keeping approximately constant line ratios) such as is seen in HH 2 implies that the emission is produced in shocks with approximately time-independent shock velocities, and with a pre-shock density that increases with time. How can this situation be obtained in a working surface of a jet? This question is addressed in the following section.

4.2. *The luminosity of a working surface*

A working surface is composed of a "jet shock" that slows down the jet material (on interaction with the environmental gas) and a "bow shock" which accelerates ambient material. From the standard, ram-pressure balance argument, for the two-shock working surface one obtains a velocity of motion (Raga et al. 1990b):

$$v_{ws} = \frac{\beta(1+\alpha)}{1+\beta} v_j \,, \tag{1}$$

where v_j is the jet velocity, $\beta = \sqrt{\rho_j/\rho_a}$ (where ρ_j and ρ_a are the jet and ambient densities, respectively) and $\alpha = v_a/v_j$ (where v_a is a possibly non-zero velocity away from the source of the ambient medium into which the jet is propagating). Equation (1) applies for the leading head of the jet (by setting $\alpha = 0$) or to an "internal working surface" within a variable jet (see Raga et al. 1990b), moving into previously ejected, slower jet material.

The jet shock has a shock velocity:

$$v_{js} = v_j - v_{ws} = \frac{1-\alpha}{1+\beta} v_j \,, \tag{2}$$

and the shock velocity of the bow shock is:

$$v_{bs} = v_{ws} - v_a = \frac{\beta(1-\alpha)}{1+\beta} v_j \,. \tag{3}$$

Now, in a highly radiative shock most of the kinetic energy flux arriving at the shock ends up being radiated away. Therefore, assuming that the jet and bow shocks have approximately the same surface area σ, the luminosities of the jet shock and the bow shock are:

$$L_{js} = \frac{\sigma \rho_j v_{js}^3}{2} = \frac{\dot{M}_j}{2} \left(\frac{1-\alpha}{1+\beta}\right)^3 v_j^2$$

$$= \frac{\dot{M}_j}{2} \frac{(1-\alpha)^3 v_{ws}^2}{\beta^2 (1+\beta)(1+\alpha)^2} \,, \tag{4}$$

$$L_{bs} = \frac{\sigma \rho_a v_{bs}^3}{2} = \frac{\dot{M}_j}{2} \left(\frac{1-\alpha}{1+\beta}\right)^3 \beta v_j^2$$

$$= \frac{\dot{M}_j}{2} \frac{(1-\alpha)^3 v_{ws}^2}{\beta (1+\beta)(1+\alpha)^2} \,, \tag{5}$$

TABLE 2

EMISSION LINES WITH RESPECT TO Hα = 100

Ion	λ [Å]	Epoch	HH 1		HH 2	
			F	F_0	F	F_0
Mg II	2798	2014.6	10	39	16	60
		1980.7	8	33	8	31
[O II]	3726+29	2014.6	54	115	36	76
		1978.7	31	66	27	58
Hβ	4861	2014.6	26	35	24	33
		1978.7	17	23	22	30
[O III]	5007	2014.6	14	19	16	21
		1994.6	18	23	21	28
		1978.7	9	12	15	20
[O I]	6300	2014.6	40	42	43	45
		1978.7	34	36	41	43
Hα	6563		100	100	100	100
[S II]	6716+30	2014.6	87	85	46	45
		1994.6	68	66	40	41
		1978.7	49	48	38	37

where we have used equations (1-3) to write the shock luminosities in terms of the jet velocity v_j (second set of equalities) and in terms of the working surface velocity v_{ws} (third set of equalities). In these equations, $\dot{M}_j = \sigma\rho_j v_j$ is the total mass per unit time arriving at the working surface.

The total luminosity of the working surface then is:

$$L_{ws} = L_{js} + L_{bs} = \frac{\dot{M}_j}{2}\frac{(1-\alpha)^3}{(1+\alpha)^2}\left(\frac{v_{ws}}{\beta}\right)^2 . \quad (6)$$

As discussed in the previous section, the fact that the emission line ratios of HH 1 and 2 have changed very little implies that the shocks giving rise to the observed emission have relatively constant shock velocities. Unless one is prepared to believe in the presence of a calibrated balancing of different effects, the fact that we have constant jet shock or bow shock velocities (depending on which of the two shocks dominates the emission) implies constant values of v_j, $\beta = \sqrt{\rho_j/\rho_a}$ and $\alpha = v_a/v_j$ (see equations 2 and 3).

A less restrictive requirement is obtained for the regime of high β and low α. In this $\rho_j \gg \rho_a$ regime, the bow shock dominates the working surface luminosity (see equations 4-5), and $v_{ws} \approx v_j$ (see equation 1). Therefore, if any possible time-variability of the ejection of the jet manifests itself only over time periods longer than a few decades (which are covered by the observations), we would have an approximately constant $v_{bs} \approx v_{ws} \approx v_j$ (see equations 1 and 3), and the luminosity (dominated by the bow shock emission) would be given by equation (6) with constant v_{ws} (and $\alpha \ll 1$):

$$L_{ws} \approx \frac{\dot{M}_j}{2}\left(\frac{\rho_a}{\rho_j}\right)^2 v_{ws}^2 . \quad (7)$$

4.3. *Application of the working surface model to HH 1 and 2*

The emission line spectrum of HH 2, which shows basically time-independent line ratios (indicating a constant shock velocity) and a strongly increasing luminosity can then be directly interpreted as a jet (of constant velocity and mass loss rate) travelling in an environment of increasing density. From equation (7) we see that the increase in the environmental density is expected to be proportional to the observed increase in the luminosity.

For HH 1, we observe a small decrease in luminosity as a function of time (see Tables 1 and 2). In terms of our working surface model, this would then imply that HH 1 is moving into an ambient medium of slowly decreasing density (see equation 7).

Let us note that a "high β", "heavy jet" situation is consistent with the high proper motions observed in HH 1 and 2. These proper motions have remained almost constant from the mid-twentieth century (see Herbig & Jones 1981; Bally et al. 2002), implying that the presence of environmental inhomogeneities do not produce appreciable effects (as would be the case for a low β outflow, see equation 1). Interestingly, a small acceleration of the HH 1 proper motions has recently been measured (Raga et al. 2016), which would be consistent with a high β jet moving into a medium of decreasing density (see equation 1).

Implicit in this discussion is the expectation of a time-independent ratio between the luminosity of the lines we are studying (see Tables 1 and 2) and the continuum and line luminosities (at optical, UV and IR wavelengths) not considered in the present study. This appears to be a reasonable assumption given the fact that we are apparently having almost time-independent shock velocities in HH 1 and 2.

4.4. *The mass loss rate of the HH 1/2 system*

From Table 2, we see that the ratio of the luminosities of all of the lines (including Hα) we are considering to Hα lies in the range of 3 to 4 for HH 1 and 2. In the 1978.7 observations of Brugel et al. (1981a), one finds that the remaining lines (observed

by these authors, but not included in our present paper) contribute an extra $\approx 30\%$ to the luminosities of HH 1 and 2. The continuum of HH 1 and 2 has a luminosity of ≈ 2 times the Hα luminosity in the $\lambda = 3000$ to 8000 Å wavelength range (Brugel et al. 1981b).

The continuum in the $\lambda = 1300$ to 3000 Å wavelength range (Böhm-Vitense et al. 1982) has a luminosity of ≈ 15 times Hα. However, the reddening correction in the far UV is very uncertain (Böhm et al. 1991).

Considering the line and continuum contributions described above, we see that the total luminosity of HH 1 and 2 is at least ≈ 10 times the Hα luminosity. Therefore, in the first (1978.7) epoch, both HH 1 and HH 2 had total luminosities of $\approx 7 \times 10^{-2}\, L_\odot$ (see Table 1). Inserting this value in equation (7), we then obtain an estimate:

$$\dot{M}_j \approx 1.5 \times 10^{-8}\, M_\odot\, \mathrm{yr}^{-1} \times \left(\frac{L_{ws}}{7 \times 10^{-2} L_\odot}\right) \left(\frac{200\,\mathrm{km\,s^{-1}}}{v_{ws}}\right) \left(\frac{\rho_j}{\rho_a}\right)^2 , \quad (8)$$

where we have used an estimate of 200 km s^{-1} for the velocity of HH 1 and 2 (see, e.g., Bally et al. 2002).

Since HH 1 and 2 appear to correspond to high β ($= \sqrt{\rho_j/\rho_a}$) working surfaces (see above), we would then conclude that the mass loss rate associated with each lobe of the outflow has a value $\dot{M}_j \approx 10^{-7} M_\odot \mathrm{yr}^{-1}$. This estimate of the mass loss rate lies within the range of mass loss rates deduced by Nisini et al. (2005) from observations of the optical and IR emission of the HH 1 jet.

5. CONCLUSIONS

A comparison of spectra of HH 1/2 obtained in three epochs, namely

1. 1978.7: spectrophotometric data of Brugel et al. (1981a),
2. 1994.6: 3 narrow-band HST images (Hester et al. 1998),
3. 2014.6: 7 narrow-band HST images (Raga et al. 2015a, b),

shows that the emission-line ratios do not change appreciably over this rather extended time period. This result is not completely surprising because the proper motion velocities of these objects have remained almost constant over a long time period (see Herbig & Jones 1981 and Bally et al. 2002).

More surprising is the fact that while the line intensities of HH 1 have remained almost constant (showing only a small decrease of $\approx 30\%$ in the 1978-2014 period), HH 2 has brightened by a remarkably large factor of ≈ 4. This scaling up of the brightness of HH 2 is unlikely to be the result of a change in the extinction to the object (as it travels away from the outflow source), because such a change would be directly visible as a time-dependence of the observed line ratios.

Therefore, we conclude that HH 2 appears to be moving into an ambient medium of increasing densities, while preserving the same shock velocity. This situation is consistent with the leading working surface of a "heavy" jet (i.e., with high $\beta = \sqrt{\rho_j/\rho_a}$, where ρ_j is the jet density and ρ_a the ambient density) moving into an inhomogeneous environment. Such a scenario is not unreasonable for the HH 1/2 system, which are located above the L1641 cloud, and with HH 2 (which is slightly redshifted) moving into a region in which denser condensations are present (see Girart et al. 2005; Lefloch et al. 2005).

A simple analytic model of a working surface shows that for a high β working surface the luminosity is proportional to ρ_a/ρ_j. Therefore, the increase of ≈ 4 in the brightness of HH 2 could be explained with a similar rise in the density of the environment into which HH 2 is travelling.

Of course, in this high β regime the changes in environmental density will also lead to (small) changes in the motion of the HH objects. The small decrease in the brightness of HH 1 (interpreted as the result of a decrease in the environmental density) would then be coupled with a small increase in the velocity of the object. It seems that such an effect is indeed observed (Raga et al. 2016).

Clearly, it will be necessary to carry out a new analysis of the proper motions of HH 2 (including the new HST images of Raga et al. 2015a, b) to see whether or not its increase in brightness is coupled with a small decrease in its proper motion velocities.

Another remaining point is that it is clear that the total (radiative) luminosity of an HH object provides a direct measure of the mechanical luminosity of the associated stellar outflow (see § 4.2). In § 4.4, we have used an estimate of the luminosities of HH 1 and 2 to obtain an estimate of the mass loss rate associated with this outflow. The luminosity that we have used is based on the optical line intensities (which have been measured at different epochs), the optical continuum (obtained only around 1980), and the line and continuum UV emission (also obtained around 1980). Notably, we did not include the IR

line and continuum emission (part ot this information is present in Spitzer and Herschel observations of the HH 1/2 region, see Noriega-Crespo & Raga 2012 and Fischer et al. 2010). A detailed analysis of current observations covering all of the relevant wavelength ranges would provide more reliable luminosities for HH 1 and 2, therefore leading to better estimates of the mass loss rate of the outflow.

Support for this work was provided by NASA through grant HST-GO-13484 from the Space Telescope Science Institute. AR acknowledges support from the CONACyT grants 167611 and 167625 and the DGAPA-UNAM grants IA103315, IA103115, IG100516 and IN109715.

REFERENCES

Bally, J., Heathcote, S., Reipurth, B., Morse, J., Hartigan, P., & Schwartz, R. 2002, AJ, 123, 2627
Böhm, K. H., Raga, A. C., Binette, L. 1991, PASP, 103, 85
Böhm, K. H., Noriega-Crespo, A., Solf, J. 1993, ApJ, 416, 647
Böhm-Vitense, E., Cardelli, J. A., Nemec, J. M., Böhm, K. H. 1982, ApJ, 262, 224
Brugel, E. W., Böhm, K. H., Mannery, E. 1981a, ApJS, 47, 117
. 1981b, ApJ, 243, 874
Brugel, E. W., Böhm, K. H., Böhm-Vitense, E., Shull, J. M. 1985, ApJ, 292, L75
Cardelli, J. A., Clayton, C. C., Mathis, J. S. 1988, ApJ, 239, L33
Eislöffel, J., Mundt, R., Böhm, K. H. 1994, AJ, 108, 1042
Fischer, W. J., Megeath, S. T., Ali, B. et al. 2010, A&A, 518, L122
Fitzpatrick, E. L. 1999, PASP, 111, 63
Giannini, T., Antoniucci, S., Nisini, B., Bacciotti, F., Podio, L. 2015, ApJ, 814, 52
Girart, J. M., Viti, S., Estalella, R., Williams, D. A. 2005, A&A, 439, 601
Hartigan, P., Raymond, J., Hartmann, L. W. 1987, ApJ, 316, 323
Hartigan, P. et al. 2011, ApJ, 736, 29
Herbig, G. H. 1969, CoKon, 65 (Vol VI, 1), 75
. 1973, IBVS, 832
Herbig, G. H., Jones, B. F. 1981, AJ, 86, 1232
Hester, J. J., Stapelfeldt, K. R., Scowen, P. A. 1998, AJ, 116, 372
Lefloch, B., Cernicharo, J., Cabrit, S., Cesarsky, D. 2005, A&A, 433, 217
Nisini, B., Bacciotti, F., Giannini, T.,Massi, F., Eislöffel, J., Podio, L., & Ray, T. P. 2005, A&A, 441, 159
Noriega-Crespo, A., Raga, A. C., 2012, ApJ, 750, 101
Oke, J. B. 1969, PASP, 81, 11
Raga, A. C., Barnes, P. J., Mateo, M. 1990a, AJ, 99, 1912
Raga, A. C., Cantó, L., Binette, L., Calvet, N. 1990b, ApJ, 364, 601
Raga, A. C., Reipurth, B., Castellanos-Ramírez, A., Chiang, Hsin-Fang, Bally, J. 2015a, AJ, 150, 105
. 2015b, ApJ, 798, L1
Raga, A. C., Reipurth, B., Esquivel, A., Bally, J. 2016, AJ, 151, 113
Raymond, J. C. 1979, ApJS, 39, 1
Schwartz, R. D., Cohen, M., Jones, B. F., Böhm, K. H. et al. 1993, AJ, 106, 740
Solf, J., Böhm, K. H., Raga, A. C. 1988, ApJ, 334, 229

J. Bally: Center for Astrophysics and Space Astronomy, University of Colorado, 389 UCB, Boulder, CO 80309-0389, USA.
A. C. Raga & A. Castellanos-Ramírez: Instituto de Ciencias Nucleares, Universidad Nacional Autónoma de México, Ap. 70-543, C.P. 04510, Ciudad de México, México (raga@nucleares.unam.mx).
B. Reipurth: Institute for Astronomy, University of Hawaii at Manoa, Hilo, HI 96720, USA.

2.6. Proper motions of the HH 1 jet

En este trabajo se presenta un método desarrollado para el estudio de los movimientos propios de HH 1 (y 2), el cuál consiste en convolucionar las imágenes de [S II], tomadas con el HST en diferentes épocas, con "wavelets" de ancho dado, y ajustando espacialmente los picos de las imágenes convolucionadas (Raga et al., 2016a,b). En pares de imágenes, se identifican los picos vecinos y se calculan los movimientos propios con el desplazamiento resultante. Además se escribió un código para la aplicación de este método.

En este artículo tuve participacion en el diseño del nuevo algoritmo de determinación de movimientos propios y en realizar pruebas de éste con imágenes de distintos objetos (nebulosas planetarias y objetos HH, en particular el ejemplo del jet de HH 1 incluído en la sección 2.7).

Los movimientos propios parecen estar íntimamente ligados con la variabilidad de la emisión de los objetos HH. Los métodos utilizados para determinar los movimientos propios y variabilidad en el tiempo de objetos HH usando imágenes de CCD se dividen básicamente en tres tipos:

1. Ajuste por intensidad de picos (Raga et al., 1990): en donde las posiciones e intensidades de los picos se miden llevando a cabo ajustes parabólicos o Gaussianos a los máximos de intensidad de las imágenes, lo que requiere la identificación de pares de nudos en diferentes épocas.

2. Correlaciones cruzadas (Heathcote & Reipurth, 1992): se definen cajas (campos angularmente limitados en las imágenes) que son usadas para calcular correlaciones cruzadas entre pares de imágenes. El desplazamiento asociado con el pico de la correlación cruzada da el valor del movimiento propio de la emisión en las cajas seleccionadas. Este método tiene la ventaja de que es menos sensible a cambios en la morfología detallada a pequeña escala de los flujos. El principal inconveniente de este método es que las cajas se tienen que tomar de tamaños y posiciones arbitrarias, para incluír características que se juzguen como entidades bien definidas en las imágenes.

3. Otro método (Raga et al., 2012b) consiste en cubrir las imágenes con una matriz regular de cajas de correlación cruzada (llamadas "tejas"). Los desplazamientos de los picos de las funciones de correlación correspondientes a estos cuadros proporcionan un "mapa de movimientos propios" de todo el campo. En este método solo se necesita definir un tamaño para las tejas, un punto de inicio y un corte de baja intensidad. Un problema de este método es que las tejas pueden incluír solo parte de una estructura coherente, y los picos pueden desplazarse a tejas vecinas en los pares de imágenes, llevando a la

medición de movimientos propios espúreos.

El método utilizado en este trabajo combina un ajuste a las posiciones de picos con un suavizado espacial. La convolución de una imagen con un wavelet de ancho σ, mejora la relación señal-ruido a expensas de la resolución espacial y elimina las estructuras con escalas diferentes del ancho del wavelet. Como parámetros libres están el ancho del wavelet y la identificación de pares de picos en las distintas épocas.

Escogimos wavelets de tipo "sombrero mexicano". Una vez que se ha realizado la convolución con las imágenes, se llevan a cabo ajustes parabólicos a los picos de intensidad con los cuales se determina su posición e intensidad. Finalmente, se determinan los movimientos propios midiendo los desplazamientos de las posiciones de los máximos entre épocas sucesivas. Para llevar a cabo este procedimiento desarrollamos un programa que contiene una serie de módulos (escritos en Python) que ejecutan este proceso (no completamente automatizado).

Para probar este código determinamos los movimientos propios del jet de HH 1 utilizando cuatro épocas de imágenes obtenidas con el HST: 1994 (Hester et al., 1998), 1997 (Bally et al, 2002), 2007 (Hartigan et al., 2011) y 2014 (Raga et al., 2015a,b) (cubriendo un periodo de aproximadamente veinte años). Los resultados revelan que los movimientos propios esán bien alineados con el eje del chorro bipolar, con velocidades de entre 230 y 290 km s^{-1} y tal que, las velocidades más altas se encuentran en los nudos más cerca de la fuente.

Interpretamos este resultado como evidencia de un incremento de la velocidad de eyección en función del tiempo. Para verificar este resultado, se calcularon los tiempos dinámicos de los nudos y se graficaron las velocidades de los nudos en función de sus tiempos dinámicos. Esta gráfica muestra que la velocidad de eyección es mayor para tiempos más recientes.

La aceleración como función del tiempo de eyección significa que los nudos se fusionarán en una sola superficie de trabajo en el futuro. Usando un modelo de movimiento balístico, se deduce que la fusión ocurrirá en unos 450 años y en un sitio cercano a la posición actual de HH 1 (aproximadamente a $75''$ de la fuente). Este tipo de comportamiento es esperado para modelos con variabilidad en la velocidad de eyección con dos modos (ver el capítulo siguiente, Castellanos-Ramírez et al. 2018, para una explicación más detallada).

De las intensidades de los picos de [S II], en todas las épocas, vemos que para distancias mayores que $7''$ (a partir de la fuente) hay una pendiente decreciente de la intensidad con respecto a la distancia. Este comportamiento sigue una ley de potencias $I \propto x^{-3}$. Este resultado está notablemente en acuerdo con predicciones de un modelo analítico previamente desarrollado (Raga & Kofman, 1992), en donde se encuentra un régimen asintótico en el cual la intensidad tiene un comportamiento $I \propto x^{-(\kappa+1)}$, donde κ es el índice de potencia de la dependencia de la emisión de la línea como función de la velocidad del choque. Si se supone un modelo de choque plano paralelo (Hartigan et al., 1987) para [S II], este índice

toma el valor $\kappa = 2$, lo cuál indica un comportamiento $I \propto x^{-3}$, lo que significa, una notable coincidencia con las observaciones.

Revista Mexicana de Astronomía y Astrofísica, **53**, 485–495 (2017)

PROPER MOTIONS OF THE HH 1 JET

A. C. Raga[1], B. Reipurth[2], A. Esquivel[1], A. Castellanos-Ramírez[1], P. F. Velázquez[1], L. Hernández-Martínez[1], A. Rodríguez-González[1], J. S. Rechy-García[1], D. Estrella-Trujillo[1], J. Bally[3], D. González-Gómez[4], and A. Riera[5]

Received March 3 2017; accepted July 5 2017

ABSTRACT

We describe a new method for determining proper motions of extended objects, and a pipeline developed for the application of this method. We then apply this method to an analysis of four epochs of [S II] HST images of the HH 1 jet (covering a period of ≈ 20 yr). We determine the proper motions of the knots along the jet, and make a reconstruction of the past ejection velocity time-variability (assuming ballistic knot motions). This reconstruction shows an "acceleration" of the ejection velocities of the jet knots, with higher velocities at more recent times. This acceleration will result in an eventual merging of the knots in ≈ 450 yr and at a distance of $\approx 80''$ from the outflow source, close to the present-day position of HH 1.

RESUMEN

Describimos un nuevo método para determinar movimientos propios de objetos extendidos, y un código que desarrollamos para la aplicación de este método. Aplicamos este método a un análisis de cuatro épocas de imágenes del HST de [S II] del chorro de HH 1 (que cubren un período de ≈ 20 años). Determinamos los movimientos propios de los nudos a lo largo del chorro, y hacemos una reconstrucción de la historia de la variabilidad de la velocidad de eyección (suponiendo nudos balísticos). La reconstrucción muestra una "aceleración" de la velocidad de eyección de los nudos del chorro, con velocidades mayores en tiempos más recientes. Esta aceleración tendrá como consecuencia que los nudos que ahora observamos a lo largo del chorro se junten en ≈ 450 años y a una distancia de $\approx 80''$ de la fuente, en un sitio cercano a la posición actual de HH 1.

Key Words: Herbig-Haro objects — ISM: individual objects (HH1/2) — ISM: jets and outflows — ISM: kinematics and dynamics — shock waves — stars: formation

1. INTRODUCTION

The HH 1/2 outflow (discovered by Herbig 1951 and Haro 1952) has played a fundamental role in the study of collimated flows from young stellar objects (YSOs), and the associated observational and theoretical work has been reviewed by Raga et al. (2011). This system has two bright "heads": HH 1 (to the NW) and HH 2 (to the SE), centered on the "VLA 1" radio continuum source (Pravdo et al. 1985).

The VLA 1 source also has a jet/counterjet system visible at IR wavelengths (Noriega-Crespo & Raga 2012) extending out towards HH 1 and 2. Optically, only the slightly blueshifted N jet (pointing to HH 1) is visible (Bohigas et al. 1985; Strom et al. 1985), as shown in Figure 1. This optical feature has been called the "HH 1 jet". Apart from the papers mentioned above, a limited number of papers have studied some of the characteristics of the HH 1 jet:

- optical images and proper motions: Reipurth et al. (1993), Eislöffel et al. (1994), Bally et al. (2002),
- radio proper motions: Rodríguez et al. (2000),
- infrared images: Davis et al. (2000), Reipurth et al. (2000),
- infrared spectra: Eislöffel et al. (2000), García López et al. (2008).

[1]Instituto de Ciencias Nucleares, UNAM, México.
[2]Institute for Astronomy, Univ. of Hawaii, USA.
[3]CASA, Univ. of Colorado, USA.
[4]DAFM, Univ. de las Américas, Puebla, México.
[5]Universitat Politecnica de Catalunya, Spain.

Some of the most striking characteristics of HH 1/2 are their proper motions (Herbig & Jones 1981; Eislöffel et al. 1994; Bally et al. 2002; Hartigan et al. 2011) and time-variability (Herbig 1969, 1973; Raga et al. 1990; Eislöffel et al. 1994). The fact that there are now four epochs of HST images of HH 1/2, covering a time span of ≈ 20 yr (Raga et al. 2015a, b, c; 2016a, b, c) has allowed progress on both these issues.

Raga et al. (2016a, b) used the 4 epochs of HST images to determine proper motions of HH 1 and 2, finding a small acceleration for the motion of HH 1 and a small braking for HH 2 (when comparing their proper motions to the ones of Herbig & Jones 1981). They also used the photometrically calibrated HST images (Raga et al. 2016c) to evaluate the recent time-variability of the emission of HH 1 and 2 (comparing their line fluxes to the ones of Brugel et al. 1981).

For their study of HH 1/2 proper motions, Raga et al. (2016a, b) explored a new method for determining motions of angularly extended objects, based on a two-step process:

- convolving the frames of the different epochs with wavelets of chosen widths,
- spatially fitting the peaks in the (degraded angular resolution) convolved frames.

In the present paper, we apply this new method to the four available epochs of HH 1/2 HST [S II] images, in order to determine the proper motions and intensity variations of the knots along the HH 1 jet (which was not studied in the papers of Raga et al. 2016a, b). We also present a detailed description of the method, and describe a pipeline (written in Python) developed for applying this method to observational or simulated emission map time-series.

The paper is organized as follows. § 2 reviews the methods that have been used to measure proper motions in CCD frames of HH outflows. § 3 presents the new method for deriving proper motions and intensities of extended structures, and describes the Python pipeline. § 4 describes the proper motions of the knots along the HH 1 jet, and § 5 the time-variability of the [S II] emission. § 6 describes the standard attempts at using the observed proper motions to reconstruct the history of the time-variability of the ejection and to predict the future evolution of the ejected material. Finally, the results are summarized in § 7.

2. PROPER MOTIONS AND TIME-VARIABILITES OF HH OBJECTS FROM CCD IMAGES

As far as we are aware, the first attempt at measuring positions and fluxes of condensations in CCD frames of HH objects was done by Raga et al. (1990), who analyzed Hα and [O III] 5007 images of HH 1/2. These authors found the then non-trivial result that even though they had only two stars in their CCD frames (and were therefore only able to compute a scaling, rotation and translation rather than a "real" astrometric calibration of the images) they obtained positions for the HH 1/2 condensations that coincided with the forward time-projection obtained with the photographic proper motions of Herbig & Jones (1981).

Raga et al. (1990) measured the positions (and peak intensities) of the HH 1/2 condensations by carrying out paraboloidal fits to the emission peaks seen in the images. This kind of "peak fitting" procedure (fitting mostly either a paraboloid or a Gaussian) has been extensively used for obtaining proper motions of HH outflows (see, e.g., Eislöffel & Mundt 1992, 1994; Eislöffel et al. 1994).

Heathcote & Reipurth (1992) tried a different method to obtain proper motions from CCD images of HH outflows. In their analysis of images of HH 34, they defined a box (including the emission of the HH 34 jet) within which they carried out cross-correlations between pairs of images. This method proved to be a major improvement in determining proper motions of HH outflows, since instead of relying on the positions of sometimes ill-defined peaks, the proper motions were determined with the emission within a spatially more extended box. This process yielded a cross-correlation function with a much better signal-to-noise ratio (compared to the images themselves), the peak of which could be fitted to a many times surprising accuracy. This cross-correlation technique has become the standard method for determining proper motions of HH objects (see, e.g., Curiel et al. 1997; Reipurth et al. 2002; Hartigan et al. 2005; Anglada et al. 2007).

The main inconvenience of the cross-correlation method is the fact that one has to choose boxes of arbitrary shapes (mostly square boxes have been used), sizes and locations so as to include features that one judges to be well-defined "entities" within the images. This is of course inconvenient in images with complex structures of different sizes, and also some-

what problematic, since the determined proper motions clearly depend on the "cross correlation boxes" that have been chosen.

In a study of a planetary nebula, Szyszka et al. (2011) used the interesting method of covering the images with a regular array of cross-correlation boxes (which they call "tiles"). The shifts of the peaks of the correlation functions corresponding to these boxes then give a "proper motion map" of the whole field (actually, a low-intensity cut-off has to be imposed so as to avoid random motions in boxes with no visible emission structures). Raga et al. (2012a, 2013) applied this method to HH objects (with the implementation of the method being presented in detail in the latter paper).

This method of cross-correlation "tiles" has the clear advantage that one only needs to define:

- a size for the tiles,
- a "beginning point" at which to begin to draw one of the tiles,
- a "low intensity cutoff" necessary for the proper motions to be calculated.

There are of course many fewer free parameters than the ones involved in a "free choice" cross-correlation box scheme.

However, it is evident that there are complications in this method. Two of these are that:

- the tiles sometimes include only part of an apparently coherent structure (algorithmical efforts to surmount this problem are described by Raga et al. 2013),
- identifiable features sometimes are shifted away from a tile into neighbouring tiles in the image pairs (so that a shift has to be applied to one of the images before applying the division into tiles, see Raga et al. 2012a).

3. MEASURING PROPER MOTIONS OF HH OBJECTS WITH A "WAVELET TECHNIQUE": A PIPELINE

In order to try to avoid these problems, Raga et al. (2016a, b) proposed (and used) an alternative, two-step method:

- convolving the images with a wavelet of a chosen size,
- determining proper motions from spatial fits to the peaks in the convolved maps.

This method is, of course, a "peak fitting method", but it also incorporates a spatial averaging (through the convolution with a wavelet function) such as is obtained with the "cross correlation method". The only free parameter of this method basically is the half-width σ of the wavelet function (and of course, the choice of which peaks are identified as "pairs" in two different epochs!).

Convolving an image with a wavelet of half-width σ has three effects:

1. improving the signal-to-noise ratio at the expense of spatial resolution,
2. eliminating emitting structures with scales $< \sigma$,
3. eliminating structures with scales $> \sigma$.

If one convolves images with functions similar to instrumental "point spread functions" (e.g., with a Gaussian), one eliminates small scale structures, but larger scale structures in the images still remain. It is, however, unlikely that proper motions determined on images convolved with Gaussians would be substantially different from proper motions measured on convolutions with wavelets. We prefer convolutions with wavelets basically because of the mathematical properties of wavelet decompositions, which allow partial rebuildings of images with arbitrary ranges of spatial scales (see, e.g., Kajdic et al. 2012). However, this feature is not used in the present proper motion determinations.

The choice of the particular form of the wavelet function does not affect the obtained results in a substantial way. In our implementation, we have chosen a "Mexican hat" wavelet:

$$g_\sigma(x,y) = \frac{1}{\pi\sigma^2}\left(1-\frac{x^2+y^2}{\sigma^2}\right) e^{-(x^2+y^2)/\sigma^2}\,, \quad (1)$$

where σ is the half-width of the central peak. This function has an approximately Gaussian central peak, surrounded by a negative ring (such that its spatial integral is zero). Together with the "French hat" wavelet, this is one of the standard "wavelet kernels". For an astronomically oriented discussion of the properties of these wavelet kernels (along with graphic depictions) see, e.g., Rauzy et al. (1993).

The convolved maps I_σ are then calculated through the usual integral

$$I_\sigma(x,y) = \int\int I(x',y')\, g_\sigma(x-x', y-y')\, dx' dy'\,, \quad (2)$$

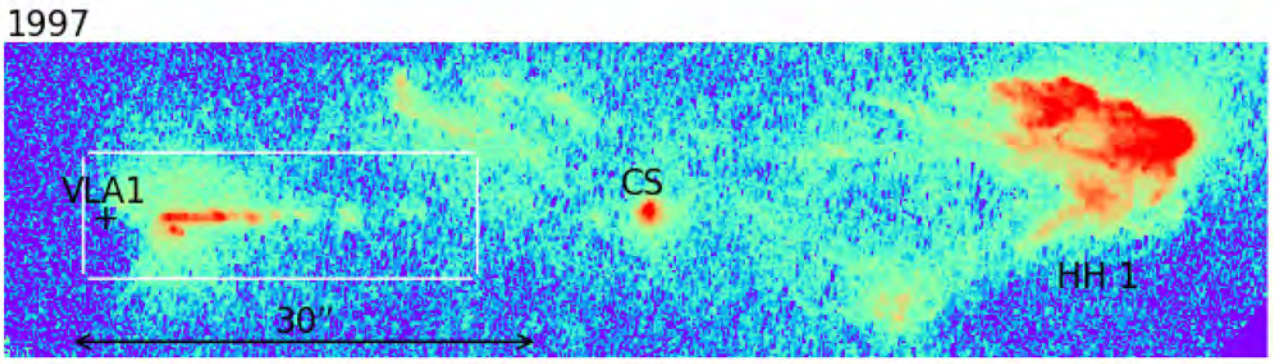

Fig. 1. [S II] image taken with the HST in 2007 of the region including the HH 1 (VLA 1) source, the HH 1 jet and HH 1 itself. The Cohen-Schwartz (CS) star is also labeled. This image (displayed with a logarithmic colour scale) has been rotated clockwise by 37° so that the axis of the outflow is parallel to the abscissa. The white box encloses the region around the HH 1 jet shown in Figures 2-4. The color figure can be viewed online.

where $I(x', y')$ is the original (i.e., not convolved) image, and (x, y) are the coordinates of the convolved image. The convolutions are carried out with a standard, "Fast Fourier Transform" method.

On the convolved image, we then carry out paraboloidal fits to intensity peaks, from which we determine the positions and intensities of the peaks. We then determine proper motions from the shifts of the positions between successive epochs.

We have developed a pipeline (written in Python) that:

1. reads an image;
2. convolves it with Mexican hat wavelets of the specified σ values;
3. finds peaks (either chosen by the user, or searches for all peaks above a given intensity threshold) and carries out paraboloidal fits;
4. has a "user confirmation and labelling" routine (with which the user can choose the relevant peaks);
5. identifies the same peaks in two or more images and calculates the proper motions (with linear least squares fits to the knot positions as a function of time).

Item number 5 allows for several possibilities:

- the more straightforward one is to calculate proper motions for the knots identified by the user with the same label in the available epochs. This is of course appropriate for images with a small number of emitting knots;
- to automatically associate the "nearest knots" detected in two successive epochs;
- to search for the nearest knot (in the following epoch), but only in the general direction away from the outflow source.

It is also possible to use the wavelet spectrum of the individual knots in order to find the knot pairs that are morphologically closest to each other, and to then use the identified pairs to calculate proper motions. This kind of "morphological evaluation" using wavelet spectra has been studied in detail by Masciadri & Raga (2004, in the context of the search for exoplanets), but has not yet been implemented in our pipeline.

Finally, our Python pipeline has routines to produce appropriately labeled plots for publication. Figures 1-4 (see the following sections) were produced with these routines. After further testing and improvements to the user interface, the routine will be available to the community.

4. PROPER MOTIONS OF THE HH 1 JET

We have taken the four epochs of [S II] HST images of HH 1/2 described by Raga et al. (2016a, b, c) obtained in 1994.61, 1997.58, 2007.63 and 2014.63 (we have not analyzed the Hα frames because the HH 1 jet is very faint in this line). Figure 1 shows a region of the 1997 frame including the position of the VLA 1 source, HH 1 and the HH 1 jet. The Cohen-Schwartz (CS) star, despite its strategic location, is apparently not associated with the outflow.

The analysis presented in this paper is restricted to the region around the HH 1 jet shown with a white box in Figure 1. The [S II] emission within this region in the four epochs is shown in Figure 2, with the knots labeled with identifications that correspond to the ones of Reipurth et al. (2000) and Hartigan et

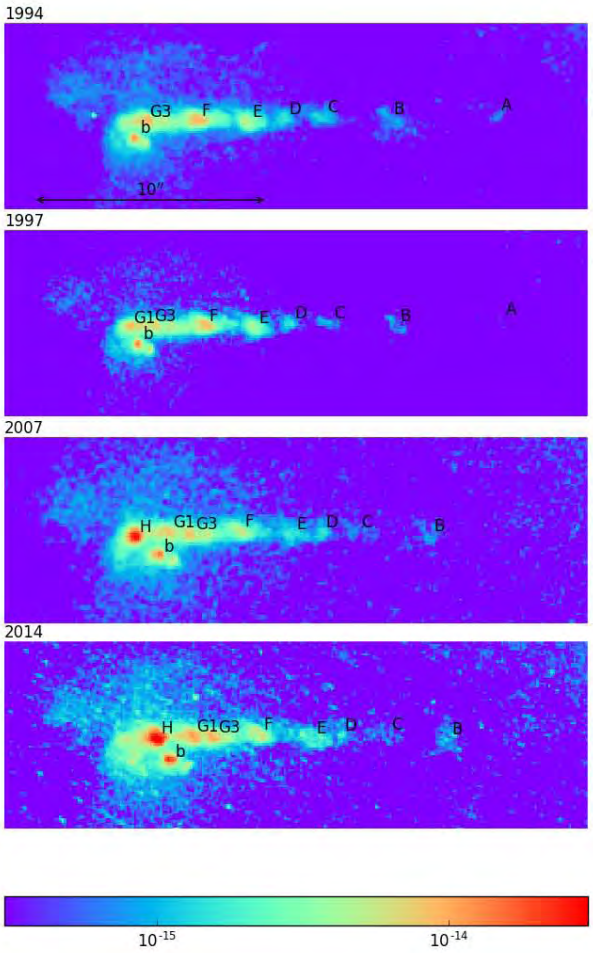

Fig. 2. The HH 1 jet in the four available epochs of [S II] HST images (see § 3). The labels used for the knots (some of them not visible in all epochs) are given. The bottom bar gives the logarithmic colour scale (in erg cm^{-2} s^{-1} arcsec^{-2}). A flat background (of 3×10^{-16} erg cm^{-2} s^{-1} arcsec^{-2} for the first three epochs and of 10^{-15} erg cm^{-2} s^{-1} arcsec^{-2} for the 2014 frame) has been subtracted. The boxes have a 30″ horizontal extent. The color figure can be viewed online.

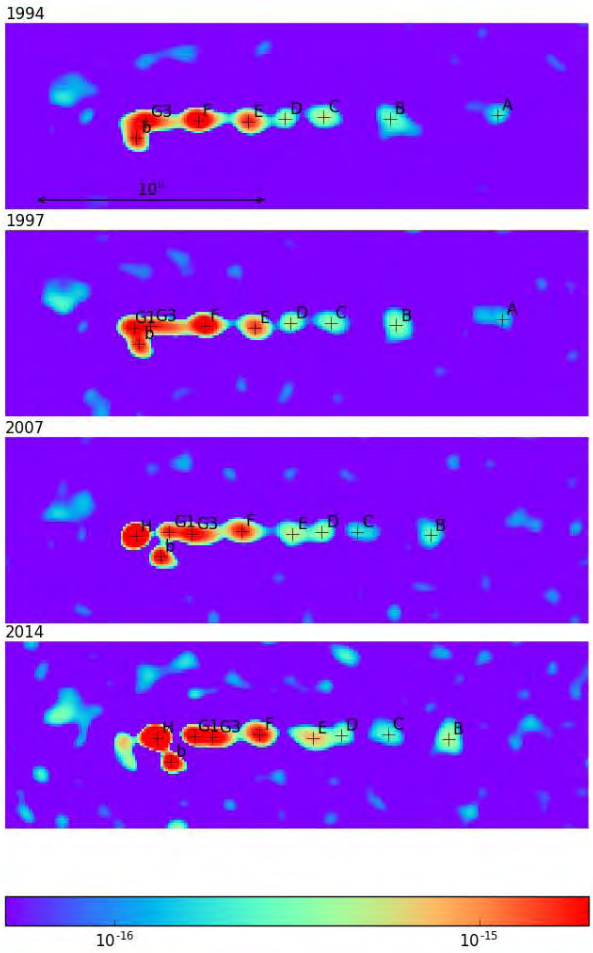

Fig. 3. The four epochs of [S II] HST images (see Figure 2) convolved with a Mexican hat wavelet of half-width $\sigma = 4$ pix (see the text). The color figure can be viewed online.

al. (2011). Also, we have labeled knot B of the HH 501 jet (see Bally et al. 2002) with a lower case "b". This outflow appears to have been ejected by another source in the vicinity of the HH 1/2 source (Bally et al. 2002).

In Figure 3, we show the four [S II] frames after convolution with a $\sigma = 4$ pix wavelet (i.e., with a central peak with a full width of 0″.8). In these convolved frames, the jet breaks up into knots with well defined peaks, to which we fit paraboloids (giving peak fluxes and the positions shown in Figure 3).

With the positions measured for the successive knots (some of them seen in all frames, but others in only two or three frames) we carry out linear least squares fits to determine their proper motion velocities. These velocities are given in Table 1 (for a distance of 400 pc to HH 1/2) and are shown in Figure 4.

The errors for the proper motion velocities given in Table 1 are calculated as follows. We estimate that the errors of the fits to the knot positions are at most 1 pixel (0″.1). This estimated error is used to calculate the errors in the proper motion velocities of knots A and H, which have measured positions in only two frames. For all of the other knots, we calculate the error in the knot positions using the standard deviation of the measured positions with respect to the (straight line) least squares fits.

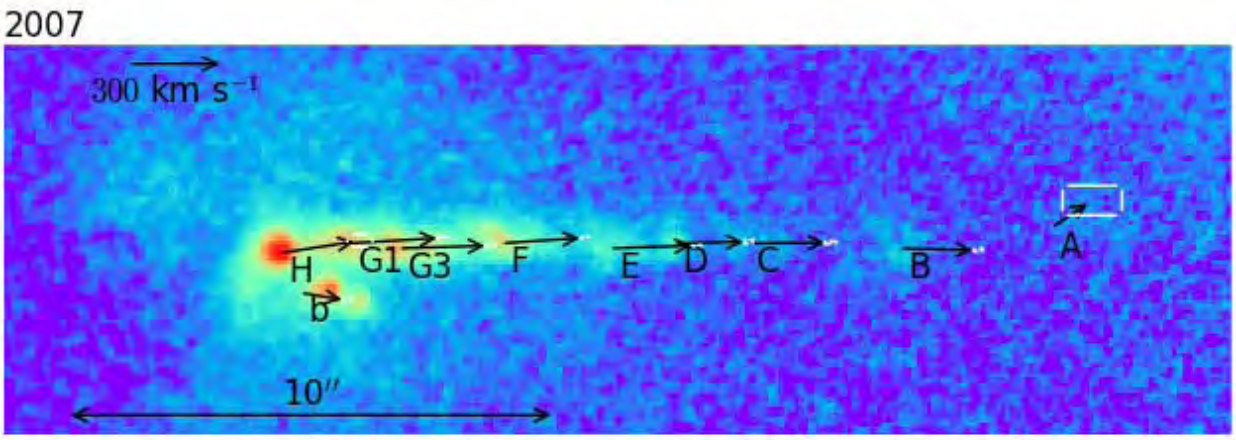

Fig. 4. 2007 [S II] image with the proper motions derived from the four available epochs (see Table 1). The scale of the velocity arrows is given by the arrow in the top left corner of the plot. The color figure can be viewed online.

TABLE 1

PROPER MOTIONS OF THE HH 1 JET

Knot	v_x[a] [km s^{-1}]	v_y[a] [km s^{-1}]
A	128 (91)	86 (45)
B	245 (12)	−6 (4)
C	258 (17)	3 (4)
D	235 (12)	5 (6)
E	271 (12)	9 (2)
F	259 (12)	18 (2)
G3	286 (13)	9 (5)
G1	288 (16)	17 (2)
H	247 (38)	38 (19)
b	149 (12)	−24 (5)

[a]The values in parenthesis are the estimated errors.

These errors (as is standard) are then propagated using the covariance matrix to calculate the errors in the proper motion velocities. Therefore, the quoted errors (see Table 1) correspond to estimates of the standard deviations.

It is clear that we do not obtain a significant result for knot A (as the errors are comparable to the determined proper motions). This is not surprising because we only see this knot in the two first epochs (which only have a time range of 3 years). For the remaining knots we do obtain proper motions along (v_x) and across (v_y) the outflow axis with reasonable errors (ranging from ≈ 10 to 40 km s^{-1}, see Table 1).

5. THE INTENSITIES OF THE KNOTS IN THE HH 1 JET

Figure 5 shows the peak [S II] intensities for knots A-I of the HH 1 jet in all epochs, obtained through paraboloidal fits to the peaks of the convolved images (see § 4). It is clear that for distances from the VLA 1 source larger than $x \approx 7''$ there is a general trend of decreasing intensities as a function of x. This trend approximately follows an $I \propto x^{-3}$ power law (shown with a dashed line in Figure 5).

Our observations do not show in a conclusive way that individual knots have intensities that "slide down" the x^{-3} slope as a function of time. This is because in the 2014 frame (intensities shown with open circles in Figure 5) we obtain systematically larger intensites for all knots than in the 2007 frame. This is a result of the fact that the HH 1 jet region has a relatively strong reflection nebula, with peak intensities aligned with the jet. This reflection nebula has a stronger contribution in the 2014 frame, which was obtained with the WFC3 camera (with a [S II] filter of 118 Å width). The first three epochs were obtained with the WFPC2 camera (with a [S II] filter of 47 Å width), and have a smaller contribution from the reflection continuum.

The observed $I_{[S\,II]} \propto x^{-3}$ dependence for large distances along the HH 1 jet (see Figure 5) is in remarkable agreement with the prediction of the analytic, "asymptotic regime" of periodic internal working surfaces of Raga & Kofman (1992). These authors note that at large enough distances from the source, the decaying working surfaces should have an intensity $I \propto x^{-(\kappa+1)}$, where κ is the index of an assumed power law dependence of the line emission as a function of shock velocity (see equation 25

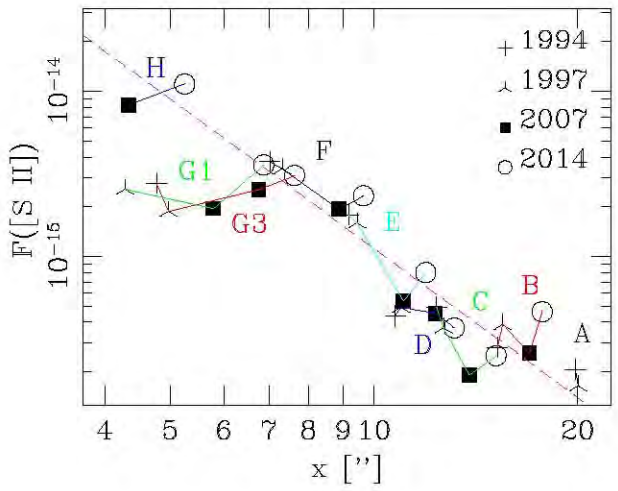

Fig. 5. Peak [S II] emission of the knots (determined from the fits to the convolved maps of the four epochs) as a function of distance from the VLA 1 outflow source. The points corresponding to the four epochs are shown with different styles of dots (as specified in the text above the plot) and the successive knots are joined by lines of different colours (with labels in the same colour giving the identifications of the knots). The color figure can be viewed online.

of Raga & Kofman 1992). If one takes the plane-parallel shock models of Hartigan et al. (1987), from the lower range of the shock velocities of their models one obtains that the [S II] intensity has a scaling $\propto v_{shock}^{-2}$. Therefore, the asymptotic regime of Raga & Kofman (1992) predicts a [S II] intensity $\propto x^{-3}$, in surprisingly good agreement with our observations of the HH 1 jet (see Figure 5).

6. THE PAST AND FUTURE EVOLUTION OF THE HH 1 JET

As can be seen in Table 1, along the HH 1 jet we see a general trend of decreasing velocities with increasing distances from the outflow source. Such a decreasing velocity trend could in principle be the result of drag due to entrainment of stationary, environmental material.

It is clear that in some of the "parsec scale HH jets" (e.g. in HH 34, see Devine et al. 1997) a progressive decrease in proper motions for the "heads" at larger distances are seen, and that this trend cannot be explained as a result of a secularly increasing ejection velocity from the outflow source (Cabrit & Raga 2000). This rather dramatic slowing down of the HH 34 "heads" is due to the fact that a precession of the outflow axis results in a direct interaction of the successive heads with undisturbed environmental material (Masciadri et al. 2002).

As the knots along the HH 1 jet are very well aligned, we would not expect them to slow down due to frontal interaction with the surrounding, stationary environment (as occurs in the giant HH 34 jet, see above). One might still have "side entrainment" into the HH 1 jet, resulting in some amount of slowing down at increasing distances from the source. This effect has recently been evaluated by Raga (2016, in terms of a somewhat uncertain "α prescription" for the entrainment velocity), who finds that in order to obtain a substantial slowing down one needs a surrounding environment (in contact with the jet beam) ≈ 10 to 100 times denser than the jet. This is unlikely to be the case in the optically visible HH 1 jet, which has already emerged from the dense core surrounding the outflow source. Also (as discussed by Raga 2016), the effect of buoyancy (which includes the gravity and the environmental pressure gradient) is negligible for the high velocities of HH outflows.

We therefore interpret the decreasing proper motion velocities (with increasing distances from the outflow source) along the HH 1 jet as ballistic motions resulting from an increasing ejection velocity as a function of time. We then take the positions of the HH 1 jet knots in the 2007 frame, and calculate the dynamical ejection times

$$t_{dyn} = -\frac{x}{v}\,, \tag{3}$$

where x is the distance from the outflow source and v is the proper motion velocity. In Figure 6, we then plot v as a function of t_{dyn}, which is the "ballistic knot" prediction of the past ejection time-variability history of the outflow source. The ejection velocity has a general trend of increasing velocities towards more recent times, which we fit with a straight line, giving:

$$u_0(\tau) = (303 \pm 15) + (0.59 \pm 0.19)\tau\,, \tag{4}$$

where $u_0(\tau)$ is the ejection velocity in km s^{-1} and τ is the ejection time in years ($\tau = 0$ corresponding to 2007, since we have used the knot positions of this epoch). The linear least squares fit (equation 4) has been calculated with the method described in Appendix A.

The ejection velocity clearly should also have a short-term variability that produces the knots that we observe along the HH 1 jet, so that the trend

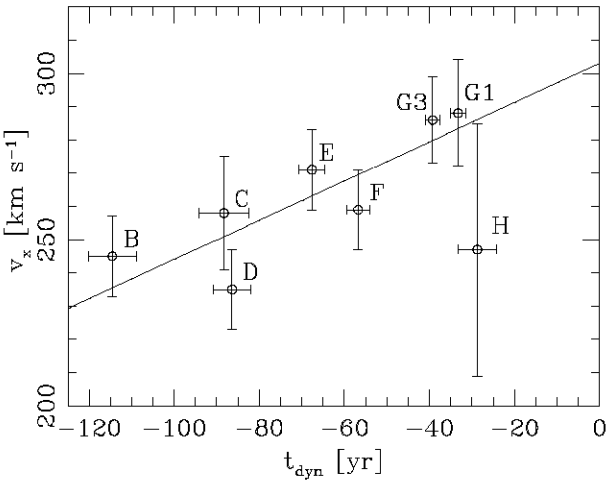

Fig. 6. Proper motion velocities of the knots as a function of dynamical ejection times (calculated through equation 3, with $t_{dyn} = 0$ corresponding to 2007). The straight line corresponds to the linear fit given in equation (4).

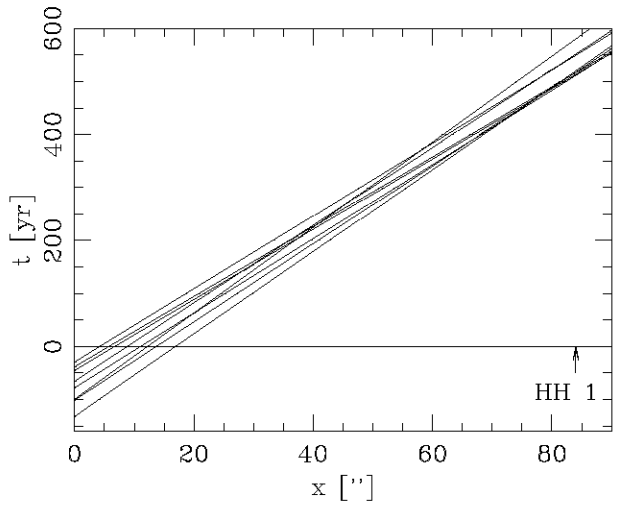

Fig. 7. Ballistic trajectories of the HH 1 jet knots on an (x, t)-plane (where x is the distance from the outflow source and t is the time measured from 2007). The present-day position of HH 1 is indicated on the bottom right of the plot.

of equation (4) would actually correspond to a long-term variability superimposed on the "knot producing" mode (see, e.g., Raga et al. 2015c).

An interesting question is whether the relatively low velocity of knot H (see Table 1 and Figure 6) is evidence that the more recently ejected, optically detected material is starting to show a decreasing ejection velocity *vs.* time trend. Given the large error of our H knot proper motion (see Figure 6), it is hard to conclude that this is indeed the case.

Also, we can obtain a second estimation of the motion of knot H as follows. We take the separation between knots H and F in the 1998.15, [Fe II] 1.64 μm image of Reipurth et al. (2000) (in which knot H is already visible), and compare it with the separation between these two knots in our 2014.63 image. From this comparison, we find that knot H has an axial motion 17 ± 2 km s^{-1}, faster than knot F. Combining this result with our knot F proper motion (see Table 1), we obtain a (276 ± 18) km s^{-1} velocity for knot H, which is consistent (within the errors) with the proper motion obtained from the optical images (see Table 1), but does not support the existence of a drop in ejection velocity associated with this knot.

In order to use the present day positions and proper motions to predict the future evolution of the HH 1 jet, in Figure 7 we plot the ballistic trajectories of the knots on a (x, t) plot (where x is the position of the knots as a function of time t). The $t = 0$ axis corresponds to the 2007 knot positions. For knot H (the trajectory with the smallest x at $t = 0$), we have used the 276 km s^{-1} velocity estimated from IR images (see above).

In Figure 7, we see that the knot trajectories have crossing points in the $x = 0 \rightarrow 80''$ distance range, at times smaller than ≈ 500 yr. Therefore, by the time the HH 1 jet knots have reached the present-day position of HH 1 (also shown in Figure 7), many knot-merging events will have occurred. This result is similar to the one found by Raga et al. (2012a) for the HH 34 jet.

In order to visualize the effect of the knot-merging events, we use the simple momentum conserving knot-merging model of Raga et al. (2012b). We take the 2007 HH 1 jet knot positions and velocities, and assign equal masses to all knots. We then follow the knot trajectories, merging colliding knots using mass and momentum conservation conditions. The knots are not assigned sizes, so that knot collisions take place at the points of trajectory crossings (see Figure 7).

The result of this exercise is shown in Figure 8. In this figure we show the knot positions at 150 yr intervals ($t = 0$ corresponding to 2007). The knots are represented as circles (centred on the knot positions) with radii proportional to the mass of the knots. It is clear that by $t \approx 450$ yr most of the knots have merged, and that at this time the position of the merged knots is slightly upstream of the present position of HH 1 (at $x \approx 4.5 \times 10^{17}$ cm or

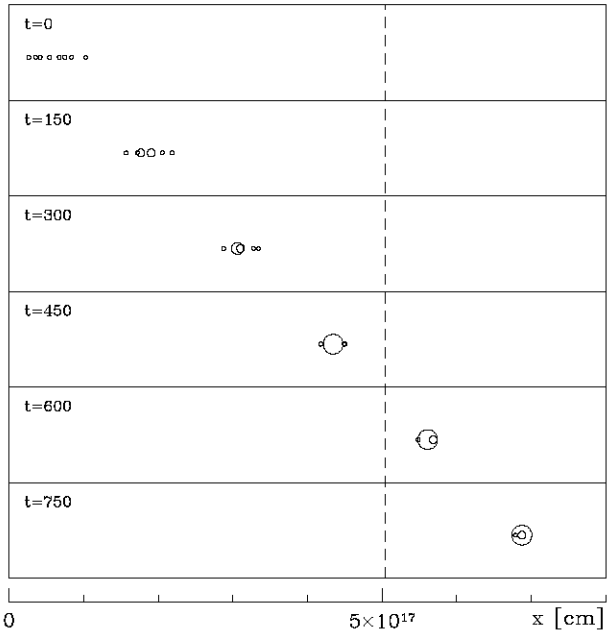

Fig. 8. Results of the "momentum conserving knot" model described in § 6. The $t = 0$ (top) frame shows the 2007 positions of the HH 1 jet knots, and the following frames show the knot positions at 150 yr time intervals. The radii of the circles (indicating the knot positions) are proportional to the mass of the merged knots. The present-day position of HH 1 is shown with the dashed, vertical line.

$75''$ at a distance of 400 pc). Therefore, the material that is being ejected now (in the HH 1 jet) will eventually form a new "head" close to the present-day position of HH 1.

7. SUMMARY

We present a discussion of the methods used in the past for measuring proper motions of HH outflows (§ 2), and a description of a new method recently developed (§ 3). This method has been implemented in a Python pipeline.

We then use this pipeline to determine proper motions of the knots along the HH 1 jet in the four available epochs of [S II] HST images (obtained in 1994, 1997, 2007 and 2014). We find proper motions that are well aligned with the outflow axis, and with values ranging from ≈ 230 to 290 km s^{-1}, with the faster velocities mostly in the knots closer to the outflow source (see § 4 and Table 1).

For each knot, we calculate a dynamical ejection time, and then plot the outflow (proper motion) velocity as a function of ejection time (see Figure 6). This plot shows that (under the assumption of ballistic knot motions) the outflow velocity has increased towards more recent times.

This "acceleration" of the ejection (as a function of ejection time) implies that the knots presently observed along the HH 1 jet will merge into a large working surface. This is seen in the crossings of the ballistic knot trajectories (see Figure 7) and in the momentum/mass conserving, "merging knot" model shown in Figure 8. From this model, we see that in ≈ 450 yr most of the HH 1 jet knots will have merged, and that at this time the position of the merged knots will be slightly upstream of the present position of HH 1 (at $x \approx 4.5 \times 10^{17}$ cm or $75''$ at a distance of 400 pc). This result is qualitatively consistent with the suggestion of Gyulbudaghian (1984) that the diverging proper motions of the condensations of HH 1 directly imply that it was formed not far upstream from its present-day position.

This kind of morphology (a large working surface at large distances, and a short chain of knots that will merge at the position of the present-day large working surface) is to be expected from models of two-mode ejection variabilities (see the analytic discussion of Raga et al. 2015c). Also, a qualitatively most similar situation has been previously found for the HH 34 outflow (see Raga et al. 2012a, b), in which the knots along the jet will merge when they reach the present-day position of HH 34S.

An important question is whether or not this kind of configuration (of knots along a jet predicted to merge at the present-day position of a large "head") is found in other HH jets. For some HH outflows, it is possible that proper motion data of sufficient accuracy might be already available, and a detailed study of the available data might yield interesting results. In other cases, future observations might be necessary in order to resolve this question.

Support for this work was provided by NASA through grant HST-GO-13484 from the Space Telescope Science Institute. ARa acknowledges support from the CONACyT grants 167611 and 167625 and the DGAPA-UNAM grants IA103315, IA103115, IG100516 and IN109715. ARi acknowledges support from the AYA2014+57369-C3-2-P grant. We thank the anonymous referee for constructive comments.

APPENDIX

A. LEAST SQUARES FIT TO THE OBSERVED v_x vs. t_{dyn} DEPENDENCE

In Figure 6, we see that the errors in v_x are probably more important than the errors in t_{dyn}, so that a traditional linear, least squares fit (in which the errors in the measured values of the abscissa are assumed to be zero) is probably reasonable. However,

in order to obtain a more convincing result, we have done a fit in which the errors in both v_x and t_{dyn} are considered.

One could in principle use a standard "errors in the two variables" least squares fit approach (see, e.g., the classical paper of York 1966), but these solutions are based on the assumption that the errors in the two variables are statistically independent from each other, and this is not the case in our "v_x vs. t_{dyn}" problem.

Given the fact that the error in the position x of the knots is much smaller than the errors in the corresponding values of v_x, the errors in t_{dyn} are given by:

$$\epsilon(t_{dyn}) = \frac{t_{dyn}}{v_x}\epsilon(v_x)\,, \tag{5}$$

which can be obtained by assuming a perturbed velocity and appropriately linearizing equation (3), or alternatively by using the standard error propagation relation.

We then proceed in the standard way, writing the "true" values of the measured points as $[t_{dyn} + \epsilon(t_{dyn}),\, v_x + \epsilon(v_x)]$, through which the linear fit passes, so that

$$v_x + \epsilon(v_x) = a[t_{dyn} + \epsilon(t_{dyn})] + b\,, \tag{6}$$

where a and b are the parameters of the linear fit that we want to calculate. Combining equations (5-6) we then find:

$$\epsilon(v_x) = \frac{at_{dyn} + b - v_x}{1 - \frac{at}{v_x}}\,. \tag{7}$$

These are the deviations from the straight line fit resulting from the displacements due to the errors in both v_x and t_{dyn}.

We now define a weighted χ^2 as:

$$\chi^2 = \sum_i \left[\epsilon(v_x)_i\right]^2 w_i\,, \tag{8}$$

where the $\epsilon(v_x)_i$ values are calculated from equation (7) with all of the observationally determined (t_{dyn}, v_x) pairs, and $w_i = 1/\sigma_i^2$, where σ_i are the estimated errors of the v_x values (see Table 1).

Now, given the measured (t_{dyn}, v_x) pairs, it is straightforward to find the values of a and b that give the minimum χ^2 (we do this by exploring numerically a range of values for a and b). It is also possible to estimate the errors of a and b by perturbing (with their estimated errors) the variables of each of the measured points, recalculating the resulting a and b values, and then using the standard error propagation formula.

When this method is applied to the knots of the HH 1 jet, one obtains $a = (0.59 \pm 0.19)$ yr and $b = (303 \pm 15)$ km s^{-1} (these are the values given in equation 4). These values are actually very similar to the $a = (0.54 \pm 0.18)$ yr and $b = (299 \pm 14)$ km s^{-1} results obtained from a standard, weighted least squares fit (in which only the errors in the ordinate are considered).

REFERENCES

Anglada, G., López, R., Estalella, R., et al. 2007, AJ, 133, 2799

Bally, J., Heathcote, S., Reipurth, B., et al. 2002, AJ, 123, 2627

Bohigas, J., Torrelles, J. M, Echevarría, J. et al. 1985, RMxAA, 11, 149

Brugel, E. W., Böhm, K. H., & Mannery, E. 1981, ApJS, 47, 117

Cabrit, S. & Raga, A. C. 2000, A&A, 354, 959

Curiel, S., Raga, A. C., Raymond, J. C., Noriega-Crespo, A., & Cantó, J. 1997, AJ, 114, 2736

Davis, C. J., Smith, M. D., & Eislöffel, J. 2000, MNRAS, 318, 747

Devine, D., Bally, J., Reipurth, B., & Heathcote, S. 1997, AJ, 114, 2095

Eislöffel, J. & Mundt, R. 1992, A&A, 263, 292

. 1994, A&A, 284, 530

Eislöffel, J., Mundt, R., & Böhm, K. H. 1994, AJ, 108, 1042

Eislöffel, J., Smith, M. D., & Davis, C. J. 2000, A&A, 359, 1147

García López, R., Nisini, B., Giannini, T., 2008, A&A, 487, 1019

Gyulbudaghian, A. L. 1984, Ap, 20, 75

Haro, G. 1952, ApJ, 115, 572

Hartigan, P. et al. 2011, ApJ, 736, 29

Hartigan, P., Heathcote, S., Morse, J., Reipurth, B., & Bally, J. 2005, AJ, 130, 2197

Hartigan, P., Raymond, J. C., & Hartmann, L. W. 1987, ApJ, 316, 323

Heathcote, S. & Reipurth, B. 1992, AJ, 104, 2193

Herbig, G. H. 1951, ApJ, 113, 697

. 1969, Comm. of the Konkoly Obs., 65 (Vol VI, 1), 75

. 1973, Information Bulletin on Variable Stars, 832

Herbig, G. H. & Jones, B. F. 1981, AJ, 86, 1232

Kajdic, P., Reipurth, B., Raga, A. C., Bally, J., & Walawender, J. 2012, AJ, 143, 106

Masciadri, E., de Gouveia Dal Pino, E., Raga, A. C., & Noriega-Crespo, A. 2002, ApJ, 580, 950

Masciadri, E. & Raga, A. C. 2014, 611, L137

Noriega-Crespo, A. & Raga, A. C. 2012, ApJ, 750, 101

Pravdo, S. H., Rodríguez, L. F., Curiel, S., et al. 1985, ApJ, 293, L35

Raga, A. C. 2016, RMxAA, 52, 311
Raga, A. C., Barnes, P. J., & Mateo, M. 1990, AJ, 99, 1912
Raga, A. C. & Kofman, L. 1992, ApJ, 390, 359
Raga, A. C., Noriega-Crespo, A., Carey, S. J., & Arce, H. G. 2013, AJ, 145, 28
Raga, A. C., Noriega-Crespo, A., Rodríguez-González, A., et al. 2012a, ApJ, 748, 103
Raga, A. C., Reipurth, B., Cantó, J., Sierra-Flores, M. M., Guzmán, M. V. 2011, RMxAA, 47, 425
Raga, A. C., Reipurth, B., Castellanos-Ramírez, A., & Bally, J. 2016c, RMxAA, 52, 347
Raga, A. C., Reipurth, B., Castellanos-Ramírez, A., Chiang, Hsin-Fang, & Bally, J. 2015a, ApJ, 798, L1
_____. 2015b, AJ, 150, 105
Raga, A. C., Reipurth, B., Esquivel, A., & Bally, J. 2016a, AJ, 151, 113
Raga, A. C., Reipurth, B., Velázquez, P. F., Esquivel, A., & Bally, J. 2016b, AJ, 152, 186
Raga, A. C., Rodríguez-González, A., Noriega-Crespo, A., & Esquivel, A. 2012b, ApJ, 744. L12
Raga, A. C., Rodríguez-Ramírez, J. C., Cantó, J., Velázquez, P. F. 2015c, MNRAS, 454, 412
Rauzy, S., Lachièze-Rey, & M., Henriksen, R. N. 1993, A&A, 273, 357
Reipurth, B., Heathcote, S., Roth, M., Noriega-Crespo, A., & Raga, A. C. 1993, ApJ, 408, L49
Reipurth, B., Heathcote, S., Morse, J., Hartigan, P., & Bally, J. 2002, AJ, 123, 362
Reipurth, B., Heathcote, S., Yu, K. C., Bally, J., & Rodríguez, L. F. 2000, AJ, 120, 1449
Rodríguez, L. F., Delgado-Arellano, V. G., Gómez, Y. et al. 2000, AJ, 119, 882
Strom, S. E., Strom, K. M., Grasdalen, G. L., et al. 1985, AJ, 90, 2281
Szyszka, C., Zijlstra, A. A., & Walsh, J. R. 2011, MNRAS, 416, 715
York, D. 1966, Can. J. Phys., 44, 1079

A. C. Raga, A. Esquivel, A. Castellanos-Ramírez, P. F. Velázquez, L. Hernández-Ramírez, A. Rodríguez-González, J. S. Rechy-García, and D. Estrella-Trujillo: Instituto de Ciencias Nucleares, Universidad Nacional Autónoma de México, Ap. 70-543, 04510, Ciudad de México, México (raga@nucleares.unam.mx).
B. Reipurth: Institute for Astronomy, University of Hawaii at Manoa, Hilo, HI 96720, USA.
J. Bally: Center for Astrophysics and Space Astronomy, University of Colorado, UCB 389, Boulder, CO 80309, USA.
D. González-Gómez, DAFM, UDLAP, Ex Hda. Sta. Catarina Mártir, C:P. 72810, Puebla, México.
A. Riera: Departament de Física i Enginyeria Nuclear, EUETIB, Universitat Politécnica de Catalunya, Comte d'Urgell 187, E-08036 Barcelona, España.

2.7. The time-evolution of the HH 1 jet modeled as a variable outflow

En este capítulo se presenta una simulación hidrodinámica numérica axisimétrica de un jet eyectado con una velocidad variable con dos modos sinusoidales, con parámetros apropiados para el jet de HH 1. De esta simulación obtenemos predicciones de imágenes de [S II], las cuales comparamos con las observaciones.

Mi contribución en el artículo es en el cálculo y realización de las simulaciones hidrodinámicas y las determinaciones de movimientos propios (en las imágenes sintéticas).

Para explicar cualitativamente la estructura de cadenas de nudos en los jets HH, se han utilizado modelos de jets variables (con eyección de velocidad dependiente del tiempo, ver la discusión en Raga et al. 2015d y referencias ahí). Estos reproducen de manera general tanto las propiedades cinemáticas como morfológicas de los jets HH. Modelos con una velocidad que varía con dos o más modos sinusoidales, han sido utilizados para simular el comportamiento de los jets HH 34 y HH 111 (ver Raga & Noriega-Crespo 1998; Raga et al. 2002; Masciadri et al. 2002).

Observaciones recientes (ver el capítulo anterior, Raga et al. 2017) muestran que el jet HH 1 consiste de una cadena de nudos alineados con el sistema HH 1/2. Este jet tiene un tamaño aproximado de $20''$ y se compone de aproximadamente 7 nudos alejándose de la fuente en dirección a la cabeza brillante (HH 1).

Del capítulo 2.6 (Raga et al., 2017) notamos lo siguiente:

- Los nudos viajan con velocidad constante.
- La intensidad de los nudos en la línea de emisión de [S II] se comporta de manera que $I_{[SII]} \propto x^{-3}$, donde x es la distancia a la fuente emisora. [1]
- La intensidad de los nudos individuales decrece con el tiempo, siguiendo también la ley $I_{[SII]} \propto x^{-3}$ (a medida que los nudos individuales se alejan de la fuente).

Con la finalidad de explorar el comportamiento de la intensidad de la línea [S II] con la posición respecto de la fuente, así como el decaimiento de la intensidad como función del tiempo, se realizaron simulaciones numéricas axisimétricas de la dinámica de gases. Para reproducir las características del jet de HH 1, se utilizó un modelo de jet cuadrado, con parámetros apropiados de una inyección de la velocidad de forma sinusoidal, con dos modos temporales: uno de "alta amplitud" y "periodo largo" y otro de "baja amplitud" y "periodo corto".

[1] Esta dependencia había sido previamente obtenida en un modelo analítico de superficies de trabajo (Raga & Kofman, 1992).

El jet se inyecta con una densidad numérica de 10^4 cm^{-3} a una temperatura de 10^3 K, y se mueve en un medio homogéneo y estacionario con densidad de 1000 cm^{-3}. Tanto el jet como el medio se encuentran en un estado neutro (con excepción del carbono y el azufre, que se encuentran una vez ionizados). Además, la simulación calcula el estado de ionización fuera de equilibrio para las siguientes especies: H (I,II), He (I,II,III), C (II,III,IV), N (I,II,III), O(I,II,III,IV), y S(II,III). Así mismo, se incluyen funciones de enfriamiento para estas especies.

Calculamos mapas de emisión de las líneas [S II] 6716+30 integrando el coeficiente de emisión que resulta de resolver el "átomo de cinco niveles" para este ión. Hemos supuesto que el eje del jet coincide con el plano del cielo.

A un determinado tiempo ($t = 950$ años en la simulación), se observa que la morfología del modelo se asemeja al objeto observado. En ambos casos hay una cadena de nudos que se extiende una longitud aproximada de $20''$ y una cabeza a una distancia aproximadamente de $80''$. Modelamos HH 1 como la primera superficie de trabajo interna del modo lento y de alta amplitud (en la variabilidad del jet) y no como la cabeza principal del jet numérico.

Ahora tomamos la emisión de [S II] obtenida a cuatro distintos tiempos en la simulación y calculamos los movimientos propios. Para calcular estos movimientos seguimos la técnica que aplicamos a las observaciones (descrita en el capítulo anterior, Raga et al. 2017). Los resultados obtenidos indican que en un diagrama posición vs. tiempo, los nudos se ajustan muy bien a una línea recta, es decir, que poseen una velocidad constante.

Si se hace una comparación de la velocidad de los movimientos propios obtenidos de la simulación numérica con las observaciones, estudiando el comportamiento de ésta como función de la distancia desde la fuente, se tiene que en ambos casos los nudos muestran una leve pendiente negativa, siendo más rápidos los nudos más cercanos a la fuente.

En la simulación, para un tiempo fijo, la intensidad de [S II] de los nudos sigue aproximadamente una ley $I_{[SII]} \propto x^{-3}$ (salvo los nudos más cercanos a la fuente). También, los nudos individuales tienen intensidades que decrecen con el tiempo siguiendo la ley $I_{[SII]} \propto x^{-3}$ a medida que se alejan de la fuente.

Con base en estos resultados, concluimos que tanto para el caso de la dependencia de la intensidad con la posición, así como la evolución temporal de la intensidad de [S II], la simulación numérica concuerda con las observaciones del jet de HH 1. Sin lugar a dudas este es uno de los mejores ejemplos en donde los modelos de jets variables reproducen exitosamente las propiedades observacionales de objetos HH.

The Astrophysical Journal, 867:29 (7pp), 2018 November 1 https://doi.org/10.3847/1538-4357/aae088

The Time Evolution of the HH 1 Jet Modeled as a Variable Outflow

A. Castellanos-Ramírez, A. C. Raga, and A. Rodríguez-González
Instituto de Ciencias Nucleares, Universidad Nacional Autónoma de México, Ap. 70-543, 04510 D.F., México
antonio.castellanos@nucleares.unam.mx, raga@nucleares.unam.mx, ary@nucleares.unam.mx
Received 2018 June 20; revised 2018 September 5; accepted 2018 September 6; published 2018 October 26

Abstract

The HH 1 jet is a chain of knots extending out to ∼20″ from the VLA 1 source of the HH 1/2 system. Four epochs of [S II] images obtained with the *Hubble Space Telescope* over a ∼20 yr period show that these knots have a time-evolving intensity as they travel away from the outflow source. We present an axisymmetric, gas-dynamic simulation of a two-sinusoidal-mode variable ejection velocity jet (including a treatment of the non-equilibrium ionization of the gas) from which we obtain predictions of the time evolution of the chain of knots close to the outflow source. Both the intensity versus position dependence (for the successive knots) and the time evolution of the [S II] intensities of the individual knots obtained from the simulations agree in a very impressive way with the HH 1 jet observations. This is one of the most striking illustrations of the success of variable jet models at reproducing the observed properties of HH jets. Also, this work represents the first attempted comparison between models and observations of astrophysical jets with both time and spatial resolution.

Key words: Herbig–Haro objects – ISM: individual objects (HH1/2) – ISM: jets and outflows – shock waves – stars: winds, outflows

1. Introduction

Although models of astrophysical jets with an intrinsic ejection variability were first explored for extragalactic jets (see Rees 1978; Wilson 1984 and Roberts 1986), they have been developed in detail for modeling Herbig–Haro (HH) jets (see, e.g., the discussion of these models by Raga et al. 2015).

Variable jet models have become the standard explanation for HH jets because they can easily reproduce (i.e., without fine tuning of the parameters of the variability) the general morphological and kinematical properties of the observed flows. It is found that jets with an instantaneous "turning on" plus a sinusoidal ejection velocity time variability (first decribed by Raga et al. 1990) or with a two-sinusoidal-mode ejection variability have characteristics similar to the "classical" HH jets HH 34 and HH 111 (discovered by Reipurth et al. 1986 and Reipurth 1989, respectively).

Though comparisons of variable jet models with a number of HH objects have been made (see, e.g., Teşileanu et al. 2014; Hansen et al. 2017), a lot of effort has concentrated on modeling the HH 34 jet. Raga & Noriega-Crespo (1998) showed that two- or three-mode ejection variability jet models could reproduce the morphology and kinematics of the HH 34 outflow. More recently, Raga et al. (2011a, 2012) tried to reproduce the morphology and kinematics of the chain of aligned knots within ∼30″ from the HH 34 source with variable jet models.

All of the papers on variable HH jets cited above are only "jet models," in which the ejection process is not modeled, and the jets are injected with more or less arbitrarily chosen conditions. There is also a considerable amount of work on modeling the ejection process (see, e.g., Zanni et al. 2007; Stepanovs et al. 2014), mostly as the result of magnetocentrifugal ejection from accretion disks and from the disk/stellar magnetosphere interaction region. Some of these models have been used to obtain predictions of the emission from so-called "microjets," extending out to ∼100 au from the outflow sources. An example of this is the work of Staff et al. (2015) who modeled microjets using time-dependent simulations with a simple, polytropic equation of state for the gas. A second example is the work of Yvart et al. (2016), who calculated microjet models with very detailed chemistry and molecular line transfer from a steady, disk wind solution.

An interesting new view of HH jets with chains of aligned knots has been provided by the analysis of four epochs of *Hubble Space Telescope* (*HST*) images of the HH 1 jet of Raga et al. (2017). This jet, first noted by Bohigas et al. (1985) and Strom et al. (1985), has around seven knots within ∼20″ from the outflow source (the VLA 1 radio source of Pravdo et al. 1985), and points toward the bright "head" HH 1. Only the slightly blueshifted HH 1 jet is visible optically, but the counterjet (pointing to HH 2) is clearly seen at 4.5 μm (Noriega-Crespo & Raga 2012). This jet has a very low excitation spectrum (e.g., with red [S II]/Hα ∼ 3; see Nisini et al. 2005), implying that the emission is formed in relatively low-velocity (10 → 30 km s^{-1}) shocks.

The four *HST* images of the HH 1 jet analyzed by Raga et al. (2017) cover a period of ∼20 yr, and show a quite remarkable time evolution of the knots:

1. the knots travel with constant (proper motion) velocities;
2. the [S II] intensities of the knots approximately follow an $I_{[S\,II]} \propto x^{-3}$ dependence (with x being the distance from the outflow source), and the knot intensities "slide down" this slope as the knots travel away from the source during the observed time period.

The first of these two points (the lack of change in the knot velocities) is of course limited by the timespan of the observations and the errors in the measured proper motion velocities. The second point, however, is a quite striking behavior which possibly indicates an important observational characteristic of HH jets.

Raga et al. (2017) point out that an $I_{[S\,II]} \propto x^{-3}$ dependence is expected from the analytic internal working surface models of Raga & Kofman (1992). Is this result reproduced by a numerical simulation of a variable jet? Does an appropriate

simulation reproduce this intensity versus position law as well as the "sliding down" time evolution of the [S II] intensities observed in the HH 1 jet? This paper attempts to answer these two questions.

2. A Model for the HH 1 jet

2.1. General Considerations

It has been shown that the emitting structure of HH jets with a chain of aligned knots close to the outflow source (with typical spacings of a few arcseconds, corresponding to $\sim 10^3$ au at the distance of the Orion star formation region) and one or more large "heads" at larger distances (with spacings of the order of an arcminute, corresponding to $\sim$0.1 pc) can be reproduced with jet models with a two-mode, time-dependent ejection velocity. This was first pointed out by Raga & Noriega-Crespo (1998), and this type of time variability has been repeatedly used to model HH jets.

The existence of an ejection velocity variability with a few modes (implied by the knot structures observed in HH jets) is a clear constraint on jet launching models. Possibilities for the production of ejection variabilities with the required characteristics have been discussed (see, e.g., Reipurth 2000; De Colle et al. 2008), but not yet fully implemented in jet launching simulations.

Even though the observations definitely imply the presence of at least two modes in the ejection variability of HH jets (see the recent discussion of Raga et al. 2015), they do not present strong constraints on the detailed characteristics of the modes. This is due to the fact that different functional forms for the modes (e.g., sinusoidal, saw-tooth, square step-functions, etc.) produce differences in the knot structures only very close to the outflow source, and soon enter the "large distance, asymptotic regime" (independent of the functional form of the modes) described by Raga & Kofman (1992). A recent discussion involving the study of different functional forms is presented by Raga & Cantó (2017).

All of what we have said in this section applies to variabilities in the outflow velocity, which produce two-shock "internal working surfaces" with maximum shock speeds comparable to the half-amplitude of the ejection velocity variability. Variability in only the ejection density (with constant ejection velocity) produces only very slow shocks, as a result of the low initial sound speed of the jet flow (of only a few km s^{-1}). Such variability only becomes interesting if the jet has a very substantial precession, so that the denser regions of the jet become exposed to a direct interaction with the surrounding environment.

The general case of time-dependent ejection velocity and density has also been studied (see, e.g., Hartigan & Raymond 1993; Cantó et al. 2000). However, the presence of a variable density produces only small effects on the time evolution of the internal working surfaces, and has no effect on the asymptotic regime of large distances from the outflow source (Raga & Kofman 1992).

Because of the lack of sensitivity of the time evolution of the internal working surfaces (in a variable jet) to the functional form of the ejection velocity variability and to the presence (or absence) of a simultaneous density variability, in this work we adopt the standard practice of considering sinusoidal ejection velocity modes and a time-independent ejection density.

2.2. Model Parameters

We compute a model of a top-hat jet with constant injection density $n_j = 10^4$ cm^{-3}, temperature $T_j = 10^3$ K, and radius $r_j = 5 \times 10^{15}$ cm, and a variable injection velocity

$$v_j(t) = v_0 + v_1 \sin\left(\frac{2\pi t}{\tau_1}\right) + v_2 \sin\left(\frac{2\pi t}{\tau_2}\right) \quad (1)$$

with an average velocity $v_0 = 300$ km s^{-1}, a "fast, low-amplitude mode" with $\tau_1 = 15$ yr and $v_1 = 25$ km s^{-1}, and a "slow, high-amplitude mode" with $\tau_2 = 500$ yr and $v_2 = 65$ km s^{-1}. This flow has a mean mass loss rate $\dot{M}_j \approx 8 \times 10^{-7}\, M_\odot$ yr^{-1} (calculated with the mean velocity v_0).

The low-amplitude mode is chosen so as to produce knots with a $\Delta x \sim v_0 \tau_1 = 1.42 \times 10^{16}$ cm $\sim 2''$ (at a 400 pc distance to HH 1), and has a low-velocity amplitude as implied by the low excitation of the spectrum of the HH 1 jet. The high-amplitude mode is chosen to produce internal working surfaces forming at a distance

$$x_c \approx \frac{v_0^2 \tau_2}{2\pi v_2} \approx 3.5 \times 10^{17} \text{ cm}, \quad (2)$$

corresponding to $\approx 1'$, which is somewhat closer to the outflow source than the present position of HH 1. This equation is strictly valid for $v_2 \ll v_0$ (see Raga & Noriega-Crespo 1998), and the full equation for the distance of formation can be found in Raga & Cantó (1998).

The jet is assumed to travel into a stationary, homogeneous environment with number density $n_a = 10^3$ cm^{-3} and temperature $T_a = 10^3$ K. All of the elements included in the simulation (see Section 2.3) are initially neutral in both the jet and the environment, except for carbon and sulphur which are singly ionized.

In order to simplify the model, we have assumed that a dynamically important magnetic field is not present (and therefore a gas-dynamic treatment is appropriate). However, relatively small magnetic fields can affect the predicted emission from the post-shock recombination regions. This can be seen in the steady, plane-parallel shock models of Hartigan et al. (1994). For shocks moving into a medium with a 10^4 cm^{-3} density (i.e., the initial density of our simulated jet, see above) and shock velocities in the 20–100 km s^{-1} range, a pre-shock magnetic field of $\sim$1 mG is necessary to produce a substantial decrease in the Hα flux emitted by the post-shock recombination region (with respect to the flux emitted by a non-magnetized shock; see Figures 14 and 15 of Hartigan et al. 1994). For pre-shock magnetic fields (parallel to the shock surface) $B_0 \leqslant 300\ \mu$G, the post-shock Hα emission has values that lie close to the emission from a non-magnetized shock. A similar result is found from magnetohydrodynamic simulations of a variable ejection jet with a toroidal magnetic field: if we scale results obtained by De Colle & Raga (2006) to the higher density of our present model, one concludes that a magnetic field of at least $\sim 500\ \mu$G is necessary to produce substantial deviations from the Hα emission found for a non-magnetized jet model. We should note that while the red [S II] emission follows the behavior of Hα for $B_0 \leqslant 300\ \mu$G, other emission lines (e.g., [O I] 6300 and [N II] 6583; see Hartigan et al. 1994) show deviations with respect to the non-magnetized case for substantially smaller values of the pre-shock magnetic field.

Another implicit simplification of our model is that we have not solved the transfer of ionizing photons and have therefore not included photoionization processes. We have only assumed that a high enough far-UV photon flux is present so as to keep C and S at least singly ionized. This is probably a reasonable approximation for the $\sim$20 km s^{-1} shocks of the "fast, low-amplitude" mode knots, because these shocks will not produce a strong photoionizing field (see, e.g., the classic paper of Shull & McKee 1979). Another possibility is that the jet could be substantially ionized very close to the source (even though this is not a feature of current models for the production of HH jets; see, e.g., Safier 1993a, 1993b; Panoglou et al. 2012). If H is substantially ionized at injection, it will recombine with an *e*-folding recombination distance

$$d_{\rm rec} \approx \frac{v_j}{n_H \alpha_H} \sim 10^{16}\,{\rm cm}, \quad (3)$$

where for the second equality we have set a flow velocity $v_j \approx 300\,{\rm km\,s^{-1}}$, an H number density $n_H \approx 10^4\,{\rm cm^{-3}}$. and an H recombination coefficient $\alpha_H \approx 2.6 \times 10^{-13}\,{\rm cm^3 s^{-1}}$. At the distance of 400 pc to HH 1, this recombination distance corresponds to $\approx 2''$. Therefore, a remnant of an initial H ionization of the jet would persist at distances from the source comparable to the positions of the knots along the HH 1 jet (see the top frame of Figure 1), providing a boost to the emission from the "fast, low-amplitude" mode knots.

Finally, we mention that the jet is initially overpressured (or "underexpanded") with respect to the surrounding environment by a factor 10. The effects of this are discussed at the end of Section 2.3.

2.3. Numerical Simulation

We have used the axisymmetric version of the "yguazú-a" code described by Kajdic et al. (2006). This code follows the non-equilibrium ionization state of H (I/II), He (I/II/III), C (II, III, IV), N (I/II/III), O (I/II/III/IV), and S (II/III). Raga et al. (2002) describe in detail the rates and the cooling terms included in this code.

The simulation was done in a five-level binary adaptive grid with a maximum resolution of 1.95×10^{14} cm along both axes, and a $(x_{\rm max}, r_{\rm max}) = (8, 1) \times 10^{17}$ cm axial $\times$ radial extent. A reflection condition is applied on the symmetry axis as well as on the $x = 0$ plane (x being the coordinate along the symmetry axis) for $r > r_j$, and an outflow condition is applied on the remaining grid boundaries. For $r < r_j$ the jet inflow condition is applied at all times on the $x = 0$ plane, with the characteristics described in Section 2.1. The jet is initially imposed within a cylinder with radius and length both equal to r_j.

From the non-equilibrium ionization state, density, and temperature obtained from the simulation, we compute red [S II] (6716+30) emission maps integrating the corresponding emission coefficient (solving the appropriate five-level atom/ion problem). For computing the [S II] maps we assume that the outflow axis lies on the plane of the sky (which is consistent with the very low $\sim 10^\circ$ angle between the HH 1/2 axis and the plane of the sky, see, e.g., Hartigan et al. 1987).

In our simulation, the jet radius is resolved with $\sim$25 grid points. From the tabulation of Hartigan et al. (1987), we see that the cooling distance behind the slowest tabulated shock (with a shock velocity $v_s = 20\,{\rm km\,s^{-1}}$), is $d_c \approx 5.4 \times 10^{14}$ cm for a pre-shock density of $10^4\,{\rm cm^{-3}}$ (we have appropriately scaled down by a factor of 10 the value of d_c given by Hartigan et al. 1987 for a pre-shock density of $10^3\,{\rm cm^{-3}}$). For the "fast, low-amplitude mode" working surfaces of our jet, the pre-shock density will initially have values similar to the jet density n_j ($=10^4$ cm), and shock velocities similar to the amplitude v_1 ($=25$ km s^{-1}) of the variability. Both the pre-shock density and the shock velocity rapidly decay as the working surfaces travel away from the source (see Raga & Kofman 1992). Therefore, in our simulations the cooling distance behind the shocks of the "fast, low-amplitude mode" knots is marginally resolved (with around three grid points) close to the point where the knots are formed, but becomes well resolved as the knots travel down the jet flow (and the pre-shock densities and shock velocities drop). Therefore, a reliable prediction of the [S II] emission of the chain of "fast mode" knots close to the injection point is obtained from our simulation.

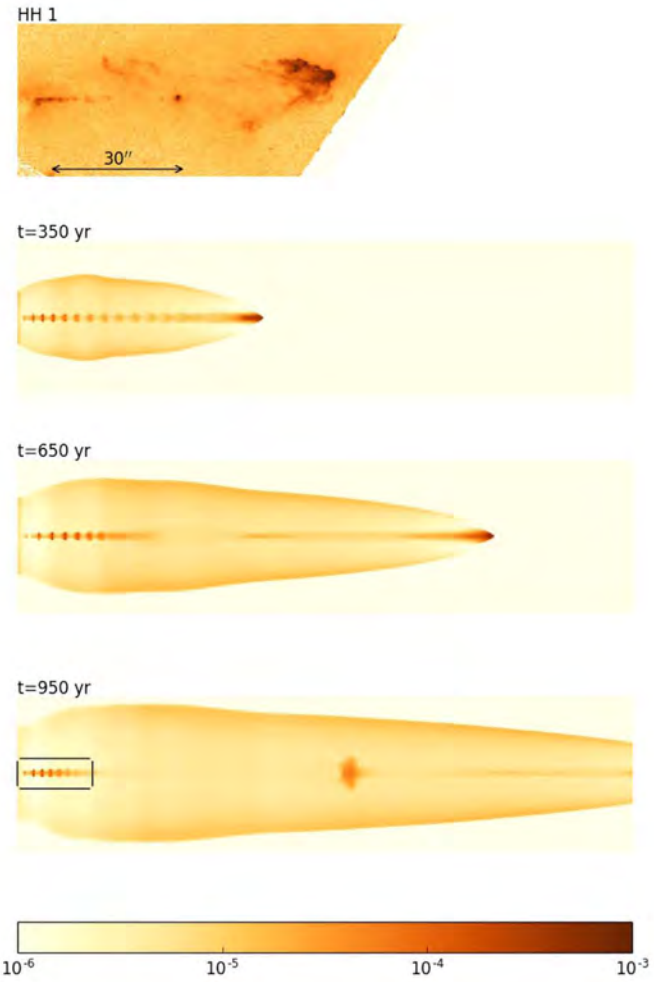

Figure 1. [S II] 6716+30 intensity maps, shown on a logarithmic scale given (in erg cm^{-2} s^{-1} sr^{-1}) by the bottom bar. Top frame: HH 1 outflow lobe *HST* image, rotated so that the outflow axis is parallel to the abscissa, and the position of the VLA 1 outflow source is located half-way up the ordinate (the diagonal cut through the image is the edge of the detector). The bright knot at $\sim 35''$ from the outflow source is the Cohen–Schwartz star, in principle not associated with the HH 1 outflow. Three botttom frames: predicted maps obtained from the numerical simulation for the three integration times shown by the labels on the top left of the frames. The extent along the outflow axis is 8×10^{17} cm, and the maps have the same scale in arcsec as the HH 1 image in the top frame for a distance of 400 pc.

A similar analysis shows that the "slow, high-amplitude" working surfaces produced in our simulation have post-shock cooling distances that are not appropriately resolved. Therefore, the prediction of the emission from the resulting, large "heads" should only be regarded as qualitative.

Figure 1 presents some of the results from our simulation. We now use the obtained results to go back to the point of the effect of the initial underexpansion of the jet beam discussed at the end of Section 2.2. If we consider a relatively advanced stage of the evolution of the flow, we find that the jet beam is in contact with a low-density, ionized cocoon, which in the region close to the outflow source has a density $n_c \sim 20\,\mathrm{cm}^{-3}$ and temperature $T_c \sim 3 \times 10^5\,\mathrm{K}$ (these numbers have been taken from the 950 yr time frame shown at the bottom of Figure 1). Therefore, the jet/cocoon pressure ratio has a value $n_j T_j/(2 n_c T_c) \sim 0.83$, so that the jet is in approximate pressure equilibrium with the surrounding cocoon. Therefore, we do not expect that strong "recollimation" or "crossing shock" cells will be formed in the jet beam (see, e.g., Young 1975, who considered an analytic approach for non-radiative flows, and Cantó et al. 1989, who considered a different analytic approach which can also be applied to radiative flows).

2.4. Predicted [S II] Maps

In Figure 1 we show the [S II] maps obtained from the simulation described in Sections 2.1 and 2.2 for integration times $t = 350$, 650 and 950 years. In the top frame of this figure, we show the 1994 *HST* [S II] image of HH 1 and its jet (see Hester et al. 1998) obtained from the *HST* archive, rotated so that the outflow axis is approximately parallel to the abscissa. In order to obtain the same spatial scale we have placed the model maps at a distance of 400 pc for HH 1.

It is clear that the $t = 950$ yr [S II] map shows a morphology that resembles the HH 1 outflow lobe. In both the observed and predicted maps there is a chain of aligned knots within $\sim 20''$ from the outflow source and a large "head" at a distance of $\sim 80''$ (this is HH 1 in the observed map, and the first "internal working surface" of the "slow, high-amplitude" mode in the simulation). The "fast, low-amplitude mode" chain of knots close to the source clearly shows a modulation resulting from the presence of the "slow, high-amplitude mode," which is described in detail by Raga et al. (2015).

If we associate the $t = 950$ yr time-frame with the HH 1 outflow lobe, HH 1 would correspond to an internal working surface, and not to the leading head of the jet. Such an association is suggested by the well known discrepancy between the high proper motion velocities and the considerably lower shock velocities implied by the line widths and the excitation of the HH 1 spectrum (see the discussions of Hartigan et al. 1987 and Raga et al. 2011b).

Having chosen the $t = 950$ yr frame, we now concentrate on the chain of knots close to the outflow source (within the black box in the bottom frame of Figure 1). This region is shown in Figure 2.

We now take five predicted [S II] images, obtained from the $t = 950$, 955, 960, 965, and 970 yr time-frames, and use them to compute proper motions of the knots within $20''$ from the injection point. We compute the proper motions by convolving the predicted [S II] maps with a $\sigma = 0\farcs4$ (corresponding to 12 pixels of the numerical simulation, assuming a distance of 400 pc to the observed object) half-width "Mexican hat" wavelet, and then measuring the positions of the peaks in the convolved frames (following Raga et al. 2017, who analyzed images of the HH 1 jet). For the intensity peaks labeled *a* through *g* in the bottom frame of Figure 2, we obtain the position (along the outflow axis) versus time dependencies shown in Figure 3. It is clear that the time-dependent positions of the knots are well fitted by straight lines, implying constant velocities. These velocities (with their errors) are shown with arrows in the bottom frame of Figure 2.

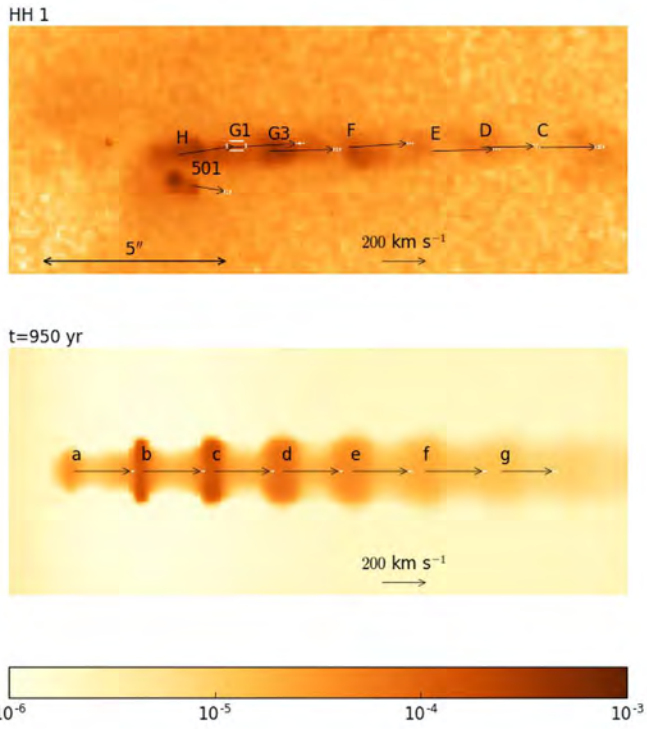

Figure 2. [S II] emission of the HH 1 jet (top) and the $t = 950$ yr [S II] map from the simulation (bottom) in the region within the box shown in the bottom frame of Figure 1, shown with the logarithmic scale given (in erg cm^{-2} s^{-1} sr^{-1}) by the bottom bar. The HH 1 jet knots (top frame) are labeled following Hartigan et al. (2011). The knot label "501" belongs to HH 501, which is a second jet and is not part of the HH 1 outflow. The knots in the simulated map (bottom frame) have been labeled *a* through *g*. The arrows give the proper motion velocities of the HH 1 jet obtained by Raga et al. (2017), and the proper motions obtained from the present simulation using the same technique. The white boxes show the errors in the determined proper motions.

In Figure 2 (top frame), we also show the proper motion velocities obtained by Raga et al. (2017) with four epochs of *HST* [S II] images of the HH 1 jet, who also measured intensity peaks in images convolved with a $\sigma = 0\farcs4$ wavelet. These authors also did not detect any accelerations/decelerations during the observed time periods. The proper motion velocities of the observed and simulated knots are shown as a function of distance from the outflow source in Figure 4. Both the simulated and the observed knots show a slight trend of decreasing velocities versus distance from the outflow source, though this trend appears to be stronger in the observed jet.

Finally, in Figure 5 we show the time evolution of the peak [S II] intensities (measured on the $\sigma = 0\farcs4$ convolutions) of the knots along the observed and simulated HH 1 jets. From the simulated maps, we show the intensities measured for the knots in the $t = 950$ and 960 yr time frames (these intensities have very small errors, not shown in the plot). For the HH 1 jet the errors of the measured intensity peaks are relatively large, so we proceeded as follows:

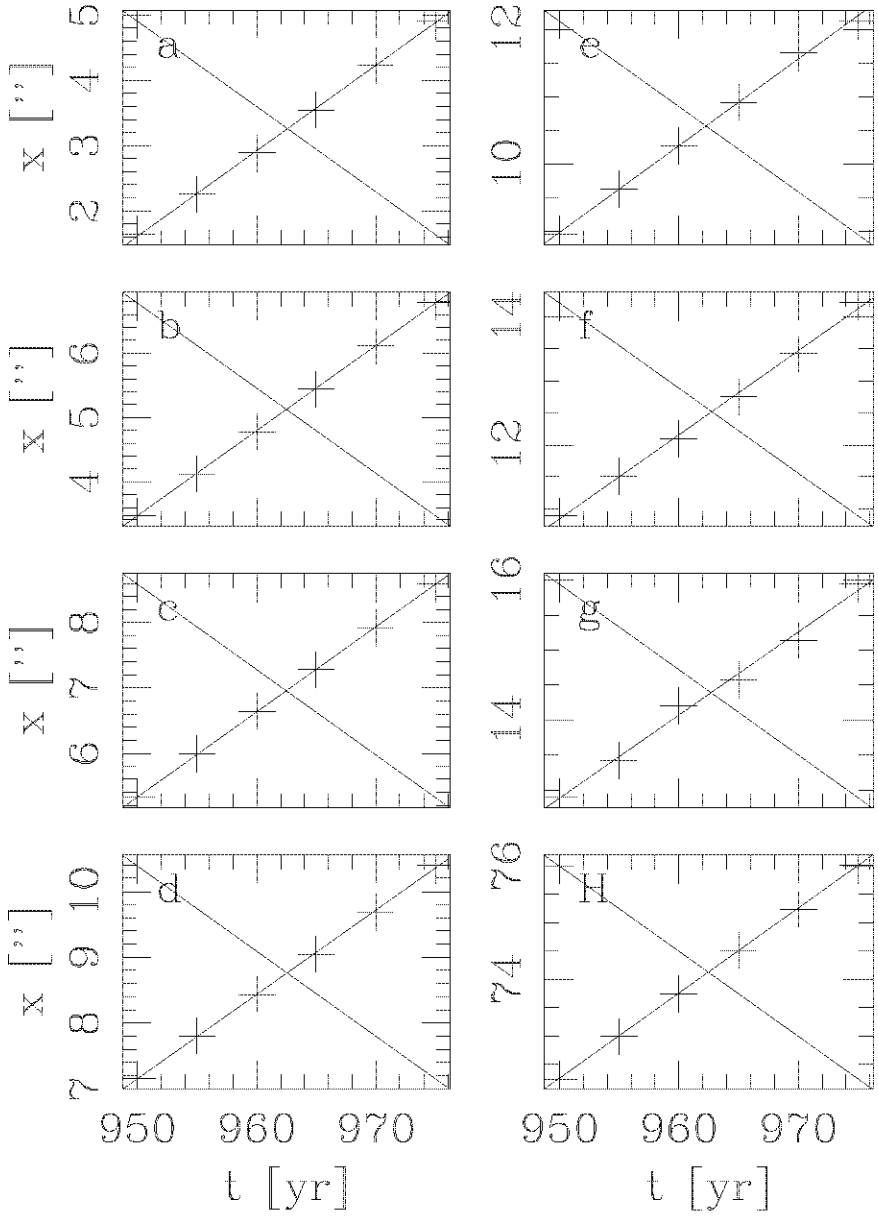

Figure 3. Distances from the source for the [S II] knots along the simulated jet. The plots are labeled *a* through *g*, corresponding to the labeled knots in the bottom frame of Figure 2. Knot *H* is the long-period-mode internal working surface that is seen at $x \approx 80''$ in the bottom frame of Figure 1. The results from linear fits to the knot positions are shown in all frames.

1. we carried out linear fits for the intensity of the observed knots versus time using the four epochs of [S II] images presented by Raga et al. (2017);
2. we then used these linear fits (and the errors computed for the fits) to calculate the HH 1 knot intensities at the time of the first epoch of Raga et al. (2017) and 10 yr later.

The intensities of the HH 1 jet knots at these two times (obtained from the fits) as well as the errors associated with the straight line fits are shown in the bottom frame of Figure 5.

3. Discussion

From Figure 5 (top frame), it is clear that for $x \geqslant 6''$ the successive knots in the simulations approximately fall on an $I_{[\mathrm{S\,II}]} \propto x^{-3}$ intensity versus position law, and that the knots slide down this curve as they travel away from the injection point. This law is predicted from the asymptotic analytic solution for a jet from a single-mode ejection velocity variability (see Raga & Kofman 1992; Raga et al. 2017). A qualitatively similar behavior is seen (with the larger associated errors) in the knots of the HH 1 jet (bottom frame of Figure 5).

The HH 1 jet [S II] knots show two clear differences with respect to the simulated jet:

1. they are brighter by a factor of ≈3.6;
2. they appear at a distance of ≈4″ from the outflow source (while in the simulation they start at ≈2″; see Figure 5).

The first of these two differences could be due to somewhat higher densities and/or shock velocities in the observed jet

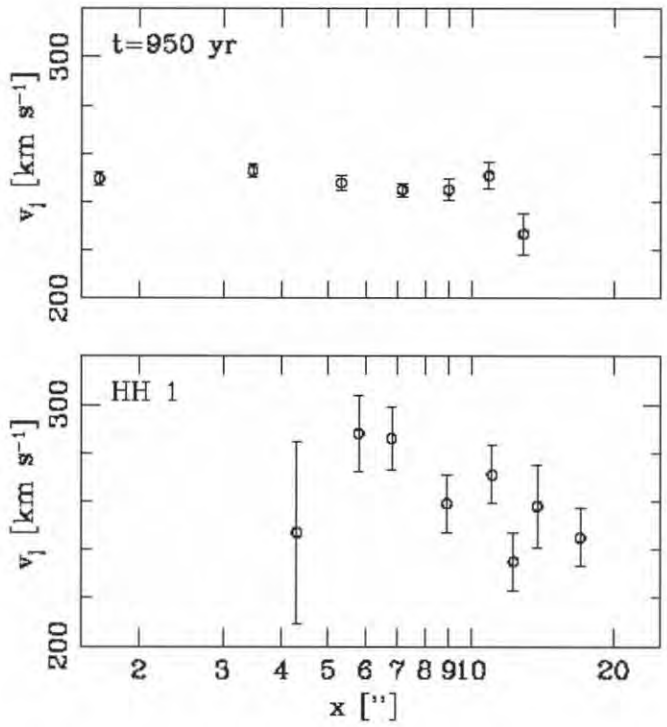

Figure 4. Proper motion velocities as a function of distance from the outflow source for the simulated jet (top) and for the HH 1 jet (bottom). The knot positions are those of the $t = 950$ yr time frame for the simulated jet, and those observed in 1994 for the HH 1 jet. The bars show the errors in the measured proper motion velocities.

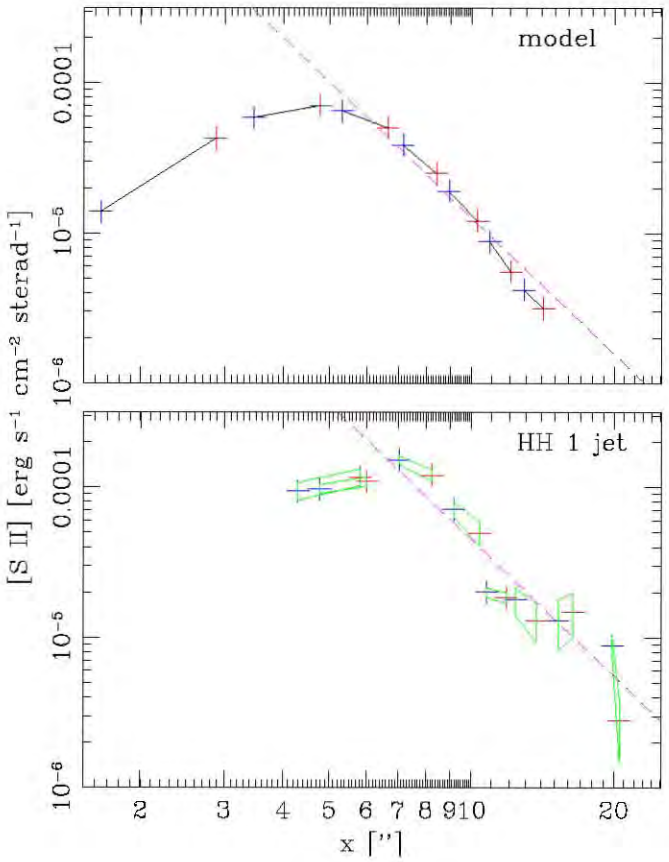

Figure 5. Peak [S II] intensities for the knots as a function of distance from the outflow source of the simulated jet (top) and the HH 1 jet (bottom) for two epochs with a 10 yr separation. The intensities of the knots in the first epoch are shown with blue crosses, and those of the second epoch with red crosses. The pairs of crosses corresponding to the same knots are joined with black lines in the simulation (top frame), and with green boxes (representing the errors of the intensities, as discussed in Section 2.3) for the HH 1 jet knots (bottom frame). Appropriately scaled $I_{[\mathrm{S\,II}]} \propto x^{-3}$ dependencies (predicted from the analytic model described in section 3) are shown with dashed lines.

knots, and a stronger effect would be present if one carried out a reddening correction. The second effect could be due to the presence of a high extinction region close to the VLA 1 outflow source, which would obscure the optical emission of the knots, while allowing the mid-IR radiation to go through (see Noriega-Crespo & Raga 2012).

We find that for different sets of two-mode variable jet parameters we obtain knots with different spacings, velocities and [S II] intensities, but that at large enough distances from the outflow source we still obtain the $I_{\mathrm{S\,II}} \propto x^{-3}$ law seen in Figure 5. We would therefore conclude that this behavior is a general property of outflows produced with either a single mode (approximately) periodic ejection variability, or with a "fast, low-amplitude" + "slow, high-amplitude" two-mode variability.

The fact that this prediction of the time evolution of the knots along an HH jet agrees with the observed time dependence of the HH 1 jet knots provides impressive evidence of the applicability of variable jet models to HH outflows. What happens in other HH jets? Do they have time -dependencies that can also be interpreted in terms of variable jets? The lengthier time sequences of calibrated, narrow-band images that are becoming available will provide the answer to this question.

We end the discussion by noting that this work is apparently the first time that a theoretical model has been compared with observations of astrophysical jets with both time and spatial resolution. In previous work, either the time evolution of spatially unresolved jets (see, e.g., the model for gamma ray bursts of Cantó et al. 2013) or "single-epoch" spatially resolved observations (see, e.g., the molecular jet models of Smith et al. 2014) have been compared with theoretical models.

We acknowledge support from the DGAPA-UNAM grants IG100218 and IN109518. We thank an anonymous referee for comments that led to the three final paragraphs of Section 2.1.

ORCID iDs

A. Castellanos-Ramírez https://orcid.org/0000-0003-3974-8449
A. C. Raga https://orcid.org/0000-0002-0835-1126
A. Rodríguez-González https://orcid.org/0000-0002-2606-8527

References

Bohigas, J., Torrelles, J. M., Echevarría, J., et al. 1985, RMxAA, 11, 149
Cantó, J., Lizano, S., Fernández-López, M., et al. 2013, MNRAS, 430, 2703
Cantó, J., Raga, A. C., & Binette, L. 1989, RMxAA, 17, 65
Cantó, J., Raga, A. C., & D'Alessio, P. 2000, MNRAS, 313, 656
De Colle, F., Gracia, J., & Murphy, G. 2008, ApJ, 688, 1137
De Colle, F., & Raga, A. C. 2006, A&A, 449, 1061
Hansen, E. C., Frank, A., Hartigan, P., & Lebedev, S. V. 2017, ApJ, 837, 143

Hartigan, P., Frank, A., & Foster, J. M. 2011, ApJ, 736, 29
Hartigan, P., Morse, J. A., & Raymond, J. C. 1994, ApJ, 436, 125
Hartigan, P., & Raymond, J. C. 1993, ApJ, 409, 705
Hartigan, P., Raymond, J. C., & Hartmann, L. W. 1987, ApJ, 316, 323
Hester, J. J., Stapelfeldt, K. R., & Scowen, P. A. 1998, AJ, 116, 372
Kajdic, P., Velázquez, P. F., & Raga, A. C. 2006, RMxAA, 42, 217
Nisini, B., Bacciotti, F., Giannini, T., et al. 2005, A&A, 441, 159
Noriega-Crespo, A., & Raga, A. C. 2012, ApJ, 750, 101
Panoglou, D., Cabrit, S., Pineau des Foreêts, G., et al. 2012, A&A, 538, A2
Pravdo, S. H., Rodríguez, L. F., Curiel, S., et al. 1985, ApJL, 293, L35
Raga, A. C., & Cantó, J. 1998, RMxAA, 34, 73
Raga, A. C., & Cantó, J. 2017, RMxAA, 53, 219
Raga, A. C., Cantó, J., Binette, L., & Calvet, N. 1990, ApJ, 364, 601
Raga, A. C., de Gouveia dal Pino, E. M., Noriega-Crespo, A., Mininni, P., & Velázquez, P. F. 2002, A&A, 392, 267
Raga, A. C., & Kofman, L. 1992, ApJ, 390, 359
Raga, A. C., & Noriega-Crespo, A. 1998, AJ, 116, 2943
Raga, A. C., Noriega-Crespo, A., Kajdic, P., et al. 2011a, RMxAA, 47, 289
Raga, A. C., Reipurth, B., Cantó, J., et al. 2011b, RMxAA, 47, 425
Raga, A. C., Reipurth, B., Esquivel, A., et al. 2017, RMxAA, 53, 485
Raga, A. C., Rodríguez-González, A., Noriega-Crespo, A., & Esquivel, A. 2012, ApJL, 744, L12
Raga, A. C., Rodríguez-Ramírez, J. C., Cantó, J., & Velázquez, P. F. 2015, MNRAS, 454, 412
Rees, M. J. 1978, MNRAS, 184, 61
Reipurth, B. 1989, Natur, 340, 42
Reipurth, B. 2000, AJ, 120, 3177
Reipurth, B., Bally, J., Graham, J. A., et al. 1986, A&A, 166, 148
Roberts, D. A. 1986, ApJ, 300, 568
Safier, P. N. 1993a, ApJ, 408, 115
Safier, P. N. 1993b, ApJ, 408, 148
Shull, J. M., & McKee, C. F. 1979, ApJ, 227, 131
Smith, M. D., Davis, C. J., Rowles, J. H., & Knight, M. 2014, MNRAS, 443, 2612
Staff, J. E., Koning, N., Ouyed, R., et al. 2015, MNRAS, 446, 3975
Stepanovs, D., Fendt, C., & Sheikhnezami, S. 2014, ApJ, 796, 29
Strom, S. E., Strom, K. M., Grasdalen, G. L., et al. 1985, AJ, 90, 2281
Teşileanu, O., Matsakos, T., Massaglia, S., et al. 2014, A&A, 562, A117
Wilson, M. J. 1984, MNRAS, 209, 923
Young, W. S. 1975, PhFl, 18, 1421
Yvart, W., Cabrit, S., Pineau des Forêts, G., & Ferreira, J. 2016, A&A, 585, A74
Zanni, C., Ferrari, A., Rosner, R., Bodo, G., & Massaglia, S. 2007, A&A, 469, 811

Capítulo 3

Astroquímica

3.1. Introducción

La astroquímica es el estudio de la formación, destrucción y excitación de moléculas en medios astrofísicos, así como su influencia en la estructura, dinámica y evolución de los objetos astronómicos. El medio interestelar en sus fases de gas difuso, nubes moleculares y núcleos densos de gas, es un entorno en el que tienen lugar procesos químicos ricos.

Algunas especies químicas actúan como agentes tanto del calentamiento como del enfriamiento, lo cual regula la temperatura del gas y por tanto influye en su evolución dinámica. Además, algunas especies (tanto atómicas como moleculares) son trazadores observacionales de distintas propiedades físicas del gas.

El hidrógeno molecular (H_2) es la molécula más abundante en el universo (ver Carruthers 1970 y referencias ahí) y domina el gas, en cantidad de masa, en las regiones de formación estelar. Sirve también como intermediario en la formación de moléculas más complejas y puede ser un enfriador importante en algunas condiciones del medio interestelar, teniendo una importante contribución al enfriamiento del universo temprano.

Otra de las moléculas más importantes en el ISM es el monóxido de carbono (CO), el cuál es el enfriador más importante (Goldsmith & Langer, 1978; Neufeld & Kaufman, 1993), y también sirve para rastrear el hidrógeno molecular (H_2) y las regiones de formación estelar (ver Bolatto et al., 2008; Leroy et al., 2008). También se encuentra el amoníaco (NH_3), el cuál es un indicador de la temperatura de un gas (Morgan et al., 2013).

Las observaciones han revelado una gran cantidad de moléculas en ciertas regiones del universo (ver `http://www.astro.uni-koeln.de/cdms/molecules`, Müller et al. 2005). Algunas de estas regiones son, por ejemplo, nubes difusas en el medio interestelar, donde la química se encuentra dominada por la fotoionización o la fotodisociación debido a la radiación producida por las estrellas jóvenes. Existen algunos objetos astrofísicos en que los procesos químicos actúan en escalas de tiempo suficientemente largas como para aproximarse al equilibrio químico. Un ejemplo de esto son las nubes moleculares sin formación estelar.

En general, las regiones moleculares presentan cambios químicos fuera del estado de equilibrio. Por ejemplo, las nubes moleculares pueden colisionar entre ellas, dando lugar a ondas

de choque que calientan y comprimen el gas, con sus respectivos cambios en el régimen químico. Las últimas etapas del colapso gravitacional aceleran el gas, incrementando su velocidad y generando turbulencia, la cual modifica el estado químico del gas. Los flujos estelares contínuos, así como las explosiones, también aceleran el gas, cambiando tanto las propiedades físicas (regiones de altas velocidades, presiones y temperaturas) como químicas del material molecular (creando, destruyendo o transportando especies).

Los modelos astroquímicos describen en general sistemas fuera del equilibrio químico. Si tomamos en cuenta la alta resolución angular y espectral de las observaciones del nuevo Atacama Large Millimeter Array (ALMA) es necesario incrementar la complejidad de las simulaciones astroquímicas. También es necesario desarrollar redes de reacciones químicas que contengan los reactivos, productos, así como las reacciones relevantes de los procesos que se tratan de simular (cinética química), y que a la vez resuelvan la dinámica de gases o la magnetohidrodinámica (ecuaciones de flujos reactivos). Esto es necesario para obtener predicciones comparables con las observaciones de interferómetros milimétricos/submilimétricos y en particular del ALMA.

En la actualidad se han desarrollado varios códigos químicos e hidrodinámicos para modelar las características de distintos objetos en el medio interestelar (ver por ejemplo Semenov et al. 2010; Grassi et al. 2014; Motoyama 2015; Ziegler 2016). También se han creado bases de datos más completas que contienen tasas de muchas reacciones químicas relevantes (McElroy et al., 2013; Smith et al., 2017).

En esta tercera y última parte de la tesis se presenta el desarrollo de un código numérico capaz de resolver las ecuaciones de una red de reacciones químicas se acopla a un código hidrodinámico. Esto nos da una herramienta con la que podremos calcular modelos con predicciones comparables a las nuevas observaciones de ALMA de flujos de estrellas jóvenes. Este cálculo se debe realizar en una malla de puntos que cubran la estructura 1, 2 o 3D del objeto que se quiera modelar.

3.2. KIMYA, a code for solving chemical reaction networks in astrophysics

En este capítulo se presenta un nuevo código que resuelve el sistema de ecuaciones diferenciales que describe el comportamiento temporal de una red química. El método de resolución es un método numérico sencillo y de fácil implementación. Éste fue probado utilizando diferentes problemas. En particular se desarrollaron el modelo de una nube oscura (McElroy et al., 2013) y la comparación con un experimento de laboratorio: formación de óxido nítri-

co durante una descarga de relámpago simulada por un láser (Navarro-González, McKay & Mvondo, 2001). Los resultados obtenidos concuerdan con los resultados experimentales.

Mi contribución en este artículo fue en la elaboración del método numérco, las pruebas del método, la implementación del método en el código hidrodinámico, la realización de las simulaciones numéricas y la discusión de los resultados.

Una red de ecuaciones químicas se representa como un sistema de ecuaciones diferenciales que contienen toda la información acerca de los procesos de creación y destrucción de las diferentes especies químicas que integran la red. Para escribir estas ecuaciones se deben conocer los reactivos, los productos, así como las reacciones relevantes. Estas ecuaciones pueden contener un gran número de reacciones, cuyas tasas de creación y/o destrucción pueden variar órdenes de magnitud entre una y otra. Como resultado de esto, estas ecuaciones no pueden ser integradas con los métodos llamados "explícitos", y reciben el nombre de "stiff" o rígidas (Gear, 1971; May & Noye, 1984).

Para lograr una integración numérica estable de este sistema de ecuaciones diferenciales utilizamos una discretización implícita. No todas las ecuaciones pertenecientes al sistema son linealmente independientes, por lo que solo hay que tomar un subconjunto de éstas. A fin de cerrar el sistema de ecuaciones se utilizan las llamadas "ecuaciones de conservación", determinadas por las densidades totales de elementos atómicos presentes en todas las especies (átomos, iones o moléculas) consideradas en la red química.

Una vez realizada esta discretización, el sistema de ecuaciones diferenciales es ahora un sistema de ecuaciones algebraicas (para las densidades de las distintas especies). Para resolver este sistema se utiliza el método de Newton-Raphson, el cuál es un método numérico estándar. Este método iterativo nos acerca a la solución del problema aplicándose un criterio de convergencia para detener las iteraciones. En el momento en que se cumple el criterio, tenemos nuestra solución. Este proceso se realiza para todas las especies y a cada intervalo de tiempo, a densidades y temperaturas dadas.

Si se quiere estudiar de forma más realista la evolución temporal de las moléculas de un gas en el medio interestelar, es necesario incluír la dinámica de gases junto con la cinética química, puesto que las tasas de cambio de las reacciones dependen fuertemente de la temperatura y densidad del gas. Esta combinación de ecuaciones se conoce con el nombre de dinámica de flujos reactivos. La manera de añadir las ecuaciones de la cinética química a las ecuaciones de la hidrodinámica es plantear un conjunto de ecuaciones de advección, con términos fuentes que contienen los procesos de creación y destrucción de las especies químicas y resolviendo numéricamente estas ecuaciones de advección junto con las ecuaciones de la dinámica de gases. Así se tiene finalmente un código numérico capaz de resolver la dinámica de distintos problemas astroquímicos.

Para la verificación del código se utilizó un test estándar de una reacción en secuencia (Braun, Herron & Kahaner, 1988) y un modelo numérico de nube oscura. Ambos modelos fueron obtenidos con el código ACUCHEM (McElroy et al., 2013), el cuál es un código que se ha utilizado previamente para realizar simulaciones numéricas de evolución química. También comparamos resultados de KIMYA con un experimento de laboratorio: la fijación de óxido nítrico, NO, durante una descarga de relámpago, que se simula en el laboratorio por un plasma generado por pulsos de láser (Navarro-González, McKay & Mvondo, 2001).

En el primer caso, los valores obtenidos coinciden plenamente con los valores reportados por ACUCHEM. En el caso del modelo de la nube oscura, se utilizó un subconjunto del conjunto total de especies y reacciones utilizadas por el ACUCHEM (13 especies y 146 reacciones contra 467 especies y 6174 reacciones). La selección de las especies y las reacciones fue hecha con el interés de reproducir los valores de las densidades de OH, CO, H_2O y H_2, las cuáles son algunas de las moléculas más importantes en el medio interestelar. Los resultados de nuestra simulación muestran que las concentraciones de H, O, OH, CO, CH y CO_2 coinciden con buena precisión con las obtenidas con el sistema más extendido y el código ACUCHEM.

Finalmente, se estudió de manera numérica la formación de óxido nítrico durante una descarga de relámpago simulada por un láser. Se utilizó una red química de 11 especies y 40 reacciones. Las condiciones iniciales suponen un gas compuesto exclusivamente de CO_2 y N_2 a una temperatura de 300 K y con una presión atmosférica.

Las simulaciones se llevaron a cabo de dos maneras: tomando un modelo de una parcela (modelo 0D) resolviendo las ecuaciones de la cinética química sin tomar en cuenta la hidrodinámica; y una simulación completa, es decir, de la hidrodinámica y química de flujo reactivo axisimétrico. En ambos casos se varió la composición química inicial del gas, cambiando la concentración inicial del $C0_2$ en el gas, χ_{CO_2}. Se compararon los resultados obtenidos con el estudio experimental. Se encontró que para cierto rango de valores de χ_{CO_2}, los resultados numéricos coinciden apropiadamente con los experimentales.

Encontramos que los cálculos que incluyen la dinámica completa del sistema (nuestras simulaciones de flujos reactivos axisimétricos) dan resultados con claramente mejor coincidencia con la composición química medida en los experimentos. Esta es la primera vez que un código de dinámica de flujos reactivos astrofísicos ha sido validado con experimentos de laboratorio.

Revista Mexicana de Astronomía y Astrofísica, **54**, 409–422 (2018)

KIMYA, A CODE FOR SOLVING CHEMICAL REACTION NETWORKS IN ASTROPHYSICS

A. Castellanos-Ramírez, A. Rodríguez-González, P. R. Rivera-Ortíz, A. C. Raga, R. Navarro-González, and A. Esquivel

Instituto de Ciencias Nucleares, UNAM, México.

Received January 30 2018; accepted April 9 2018

ABSTRACT

KIMYA is a new code for solving the system of differential equations describing the temporal behavior of a chemical network. This paper presents a simple and easy to implement numerical method and tests of its accuracy. KIMYA was designed for incorporating a chemical network into multi-dimensional gasdynamical simulations. In order to test our code we compute three numerical simulations: a model of the chemical evolution of a dark cloud (which we compare with previous calculations), and a model of nitric oxide formation during a lightning discharge simulated with a laser pulse. The latter is done with both a single parcel calculation, as well as a fully hydrodynamical/chemical model, which we compare with results from a laboratory experiment.

RESUMEN

KIMYA es un nuevo código para resolver el sistema de ecuaciones diferenciales que describe el comportamiento temporal de una red química. En este artículo presentamos un método numérico sencillo y fácil de implementar, y una evaluación de su precisión. KIMYA fue diseñado para incorporar una red química en simulaciones hidrodinámicas multidimensionales. Para probar nuestro código hacemos tres simulaciones numéricas: un modelo de la evolución química de una nube oscura (el cual comparamos con cálculos anteriores) y un modelo de la formación de óxido nítrico durante una descarga de relámpago simulada con un pulso de láser. Este último lo hacemos tanto con un cálculo de una única parcela, como dentro de un cálculo hidrodinámico/químico, y lo comparamos con resultados de un experimento de laboratorio.

Key Words: astrochemistry — hydrodynamics — ISM: molecules — methods: numerical — molecular processes — shock waves

1. INTRODUCTION

Chemical kinetics networks have applications in atmospheric chemistry, combustion, detonations and biological systems as well as in planetary, stellar and interstellar astrophysics.

In order to follow the time-evolution of a chemical system, one needs to determine the reagents and products involved, as well as the relevant chemical reactions. The resulting rate equations have to be integrated in time together with the equations that describe the time-evolution of the reactive fluid (these could be the gasdynamic or the magnetohydrodynamic equations in 1, 2 or 3D, which are coupled to the chemical network through the equation of state and possible energy gain/loss terms). The simplest possible model is a "0D" approximation, in which the chemical rate equations are integrated for a single, homogeneous parcel in which either a constant or a time-dependent density (or pressure) and temperature are imposed.

In order to follow the temporal evolution of the molecular composition of a gas, one needs to integrate the density rate of change equations for the different species contained in the gas. In order to do this, one has to construct a chemical network gathering the creation and destruction reactions for all of the different species. Such a chemical network is a system of ordinary differential equations (ODEs).

As initial conditions, we have the density for each species $n_i(t)$ (at the initial time t), and the aim of the numerical implementation is to solve this system in order to find the densities at a future time, $n_i(t + \Delta t)$.

The chemical model can include a large number of species (ranging from ≈ 10 to several thousands). The interaction between the species results in a large number of elementary reactions with rates that can in principle differ by many orders of magnitude. As a result of this fact, chemical networks (see equation 2 in § 2) are "stiff" systems of ordinary differential equations, which require special numerical integration methods.

The stiffness of a chemical network was first observed by Curtiss & Hirschfelder (1952), who noted that the so-called "explicit methods" for solving differential equations failed in the solution of some chemical reactions (though versions of explicit methods appropriate for stiff systems were later developed, see below). Dahlquist & Lindberg (1973) found that numerical instabilities resulting from the widely ranging evolutionary timescales of the different species are the main reason for the failure of explicit methods in the solution of stiff equations.

There is an extensive literature on the solution of stiff ODEs. The review of May & Noye (1984) gives an introduction to the subject, and the classical book of Gear (1971) describes appropriate numerical methods. Jacobson (2005) gives a review of many different methods for solving stiff equations.

These methods fall into two main categories:

- explicit methods: in which the solutions are marched forwards in time with the creation/destruction terms (see equation 2) evaluated at the current time. Explicit methods appropriate for stiff equations include schemes with partially time-integrated rates and/or logarithmic time-stepping,

- implicit methods: in which the creation/destruction terms are evaluated with the time-advanced densities.

While the first type of method is simpler to program and generally faster to compute, all implementations share the complexity of having many adjustable parameters (associated with having to choose different sub-timestepping schemes depending on the characteristics of the chosen network). They typically have trouble converging to chemical equilibrium and have to be specifically adjusted for solving different chemical networks. A well known example of this kind of method is the one described by Young & Boris (1973).

The implicit methods generally have guaranteed convergence to chemical equilibrium, and produce numerically stable (though not necessarily accurate) time-evolutions, regardless of the size of the timestep. However, they are computationally much slower than explicit methods, requiring iterations involving the Jacobian of the chemical network equation system. The best known method of this kind is Gear's algorithm, and variations of this algorithm are implemented in many generally used codes (see, e.g., the review of Nejad 2005).

A very important part of the chemical network is obtaining reliable values for the reaction rates. There are several databases containing experimental and/or theoretical calculations of the rate coefficients for specific temperature ranges. Examples of these are presented in the work of Baulch et al. (2005) for combustion, Crowley et al. (2010) for atmospheric chemistry, and Millar et al. (1991) and Wakelam et al. (2012) for astrochemistry.

Summaries of astrochemical codes and astrochemistry databases have recently been given by Semenov et al. (2010), Motoyama (2015) and Ziegler (2016). Since the pioneering work of Bates & Spitzer (1951), many chemical models (and the necessary numerical codes) have been developed. With the recent use of the high (angular and spectral) resolution ALMA interferometer, it has been necessary to increase the complexity of astrochemistry simulations. In particular, in order to obtain predictions that can be compared with these observations it is necessary to compute multi-dimensional models involving both the dynamics of the gas (modeled either with the hydrodynamical or the magnetohydrodynamical equations) and appropriate chemical networks. A possibility for reducing the computational time is to consider steady-state chemistry (see Semenov et al. 2010), but in order to obtain realistic results it is necessary to include the full, time-dependent chemistry in simulations of the dynamical properties of the gas.

An example of this is the code presented by Ziegler (2016). This code solves a chemical reaction network togheter with the magnetohydrodynamic equations. Also, the recently developed KROME code (Grassi et al. 2012) and the GRACKLE library (Smith et al. 2017) have chemical evolution routines that can be implemented in hydrodynamic/magnetohydrodynamic codes.

Another example is the work of Navarro-González et al. (2010), who developed a chemical

evolution code for integrating a set of chemical rate equations in order to predict the degree of oxidation and chlorination of organics in the Martian soil. This code solves the chemical kinetics model using an explicit method. This code was in good agreement with the results previously reported in others standard chemical kinetics codes (see Navarro-González et al. 2010). Nevertheless, despite the good results obtained by the code, the numerical method has difficulties converging to the correct solutions for particularly stiff reaction networks.

The aim of the present work is to present a locally developed code based on a fast, simple implicit solver for chemical networks, which is appropriate for implementations in multidimensional gasdynamic simulations. We evaluate the accuracy of this solver by computing:

- a single parcel, "dark cloud" model, which we compare with previously published results of this problem,
- a single parcel, and an axisymmetric gasdynamical model of a laser laboratory simulation of a lightning discharge.

The simulations of the laboratory experiment are used to calculate the chemical evolution of an atmospheric, laser generated, plasma bubble, which is then compared with actual measurements of the chemical species (and their densities). While a few attempts have been made in the past to evaluate the precision of astrophysical gasdynamic codes through comparisons with laboratory experiments (see, e.g., Raga et al. 2000, Raga et al. 2001 and Velázquez et al. 2001), as far as we are aware this is the first time that this type of test is done for an astrophysical chemical evolution and reactive gasdynamics code.

The paper is organized as follows. In § 2 we present the numerical method for solving the chemical networks. We describe briefly the KIMYA code in § 3. The gasdynamic equations together with the reaction network are described in § 4. In § 5 we apply KIMYA to model two phenomena: a dark cloud model, and an experimental study of the formation of nitric oxide during a lightning discharge simulated with a laser pulse. Finally, in § 6 we discuss the proper operation of the code and present our conclusions.

2. THE NUMERICAL SOLUTION OF THE NETWORK CHEMICAL RATES

A chemical network is described by the system of differential equations:

$$\frac{dn_i}{dt} = \sum \text{formation} - \sum \text{destruction}, \qquad (1)$$

where n_i is the density of species i. The first term in the right hand side of the equation contains all the formation processes and the second term all the destruction processes of species i.

If the chemical network involves only binary reactions, we have:

$$\frac{dn_i}{dt} = \sum_{j,k} f_{jk}^{(i)} n_j n_k - n_i \sum_k d_{ik}^{(i)} n_k \,, \qquad (2)$$

where n_i is the density of species i, and $f_{jk}^{(i)}$ and $d_{ik}^{(i)}$ are the (temperature dependent) rates of formation and destruction (respectively) of species i. The indices i, j, k, go from 1 to the total number of species N.

2.1. *The Newton-Raphson Iteration*

The set of the equations described above can be written, without loss of generality, as

$$\frac{dn_i}{dt} = R_i, \qquad (3)$$

where n_i are the densities of N species (i.e., $i = 1, 2, \ldots, N$).

In order to solve the system of ODEs, we use an implicit method. We do the simplest possible "implicit discretization" of the left hand side of equation (3):

$$\frac{n_i - n_{i,0}}{\Delta t} = R_i. \qquad (4)$$

where n_i are the densities at a time $t + \Delta t$, $n_{i,0}$ are the (known) densities at a time t and R_i the source terms (associated with the creation and destruction processes) evaluated with the time-advanced densities n_i.

We rewrite equation (4) as:

$$Q_i = R_i - \frac{n_i - n_{i,0}}{\Delta t} = 0, \qquad (5)$$

with $i = 1, \ldots, N$.

For very large Δt, equation (5) gives $R_i = 0$, which is the condition for chemical equilibrium. However, this condition is not sufficient to specify the chemical equilibrium, as not all of the $R_i = 0$ equations are linearly independent. We therefore only consider a subset of $p < N$ equations of the form (5), eliminating the $N - p$ equations with R_i terms which can be written as linear combinations of the R_p (with $p \neq i$) terms of the remaining rate equations.

In order to close the system of equations, we then consider a set of "conservation equations":

$$Q_m = C_m = 0, \qquad (6)$$

with $m = p, \ldots, N$. The definition of the C_m functions is given below (§ 2.2). In order to find the time-advanced densities, we then have to find the roots of the set of equations:

$$Q_i = 0;\ i = 1, \ldots, N\,, \tag{7}$$

with the Q_i given by equations (5) and (6). If we take the $\Delta t \to \infty$ limit in equation (5) this set of equations fully specifies the chemical equilibrium condition. One of the common methods to find roots of a system of equations (7) is the Newton-Raphson iteration. We apply this method to our particular problem as follows. One starts with an initial guess n_i $(i = 1, \ldots, N)$ for the time-advanced densities. Then, expanding the $Q_i(n_i)$ terms in a first order Taylor series one obtains:

$$Q_i + \sum_{m=1}^{N} \Delta n_m \frac{\partial Q_i}{\partial n_m} = 0\,. \tag{8}$$

Here, the partial derivatives are the elements of the Jacobian matrix. Both Q_i and $\partial Q_i/\partial n_m$ are evaluated at the initial guess n_m $(m = 1, \ldots, N)$ of the solution. We have then obtained a system of linear equations for the Δn_m corrections to our first guess for the time-advanced solution. This system is then solved using inversion methods for sets of linear equations (in our case, we use the standard routines of Press et al. 1993). In this way, we find an improved guess

$$n_i^{(k+1)} = n_i^{(k)} + f\Delta n_i\,, \tag{9}$$

where $n_i^{(0)}$ is our first guess for the time advanced densities, and f is a "convergence factor" that helps to reach convergence in the iteration process and is defined as:

$$f = \left(\frac{k}{N_{it}}\right)^{\beta}\ ,\ k \le N_{it}\ ;\ f = 1\,,\ k > N_{it}, \tag{10}$$

where N_{it} and β are chosen constants, and k is the current iteration number. We then recalculate the rates and Jacobians with the corrected densities ($n_i^{(1)}$), and repeat the process to obtain successively improved values for the time-advanced densities. This iteration is repeated until a convergence criterion:

$$\frac{\left|n_i^{(k)} - n_i^{(k+1)}\right|}{n_i^{(k+1)}} < \epsilon\,, \tag{11}$$

is satisfied for all species i, where ϵ is a previously chosen tolerance.

2.2. *Conservation Equations*

The conservation equations (see equation 6) are determined by the total densities of the atomic elements present in all of the atomic/ionic/molecular species that are considered in the chemical network. For example, in a pure hydrogen gas (of known total H density [H]) we have as possible species H_2 (molecular H), H I (neutral H), H II (ionized H) and electrons (as a result of the ionization of H). The associated conservation equations then are: C_H =[H]-2[H_2]-[H I]-[H II]=0, and C_e =[H II]-[e]=0 (here, the densities written in a notation of the form "[A]" correspond to the n_i of § 2.1).

In general, for an element A (participating in the chemical network) forming part of at least some of the (atomic/ionic/molecular) species n_k, the associated conservation equation is:

$$C_A = n_A - \sum_k a_k n_k = 0\,, \tag{12}$$

where n_A =[A] is the total density of element A, and a_k is the total number of A nuclei present in species k (with density n_k). There is one conservation equation of this form for each element present in the chemical network, and the resulting set of conservation equations is used together with the rate equations to guarantee convergence to the correct chemical equilibrium (see equation 6).

2.3. *Initial Newton-Raphson Guess*

For a system of equations such as (8) the convergence of the Newton-Raphson method strongly depends on the initial condition $\mathbf{n}_0$. We find that an appropriate initial guess for the time advanced densities (generally leading to a reasonably fast convergence) can be constructed as follows:

For a molecule $[aA, bB]$ composed of "a" atoms of element A, and "b" atoms of element B, we choose an initial density

$$n_i^{(0)} = \frac{1}{2}\min\left[\frac{A_T}{a}, \frac{B_T}{b}\right] \tag{13}$$

where A_T, B_T are the total densities of elements A and B (respectively). Equation (13) can be straightforwardly extended for molecules with three or more elements.

3. DESCRIPTION OF KIMYA

Whether only the chemical kinetics is calculated, or if it is used within a hydrodynamic code, the operation of KIMYA is roughly as follows. As input,

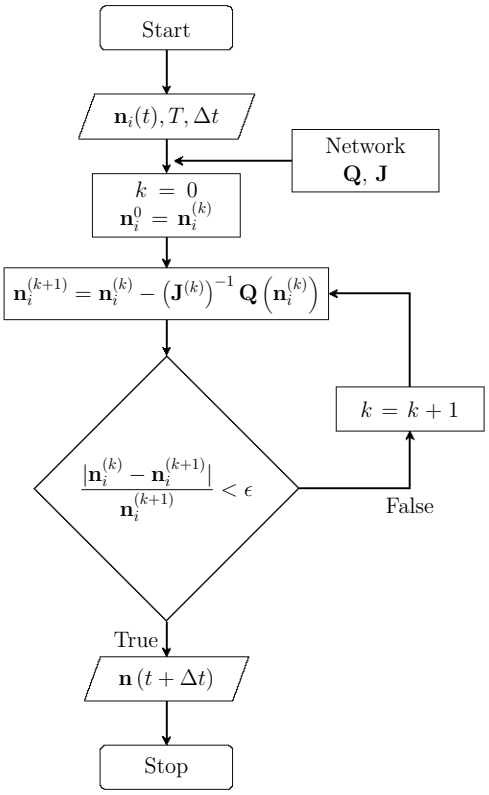

Fig. 1. KIMYA flow chart. Our code receives the initial densities of each species, the gas temperature and an arbitrary time-step and returns the time-advanced densities.

it needs the densities of all of the species and the temperature at a given time, and a timestep. With these values, the values of the Q functions and the Jacobian matrix are calculated (equation 8 of § 2). The N-R method is used to obtain the new densities (equation 9 in § 2). The time-advanced densities are iterated until the relative differences between two successive iterations meets a (previously chosen) convergence criterion. This procedure is presented in the flowchart shown in Figure 1.

We have developed a benchmark suite using the network that will be described in § 5.3, with eleven chemical species and 40 chemical reactions. As we will see later, this particular benchmark will serve to check the operation of the code when compared to laboratory experiments. We have run a benchmark test for 10^4, 10^5 and 10^6 timesteps. Our code solves a single timestep in $\approx 3.9 \times 10^{-5}$ seconds of wall-clock time. This feature is relevant when one wants to couple this solver with a multi-dimensional gasdynamic code, where one should find the solution for each species in each of the $10^4 - 10^9$ cells at every timestep.

4. THE REACTIVE FLOW EQUATIONS

KIMYA is designed for inclusion in reactive flow numerical codes. Hydrodynamic codes in one, two or three dimensions solve the gas dynamic (or magnetohydrodynamic) equations in a discretized space. In the discrete "cells", the mass, momentum, energy conservation equations are solved together with the chemical network (to which one adds advection terms for each species). Usually, in a complete simulation there are typically from 10^5 to 10^9 cells, and each one is advanced in time for thousands of timesteps, so that a fast integrator for the chemical network is clearly essential.

The gasdynamic equations are:

$$\frac{\partial \rho}{\partial t} + \nabla \cdot (\rho \mathbf{u}) = 0, \tag{14}$$

$$\frac{\partial \rho \mathbf{u}}{\partial t} + \nabla \cdot \rho \mathbf{u}\mathbf{u} + \nabla P = 0, \tag{15}$$

$$\frac{\partial}{\partial t}\left(\frac{\rho \mathbf{u}^2}{2} + \frac{P}{\gamma - 1}\right) + \nabla \cdot \left[\rho \mathbf{u}\left(\frac{\gamma}{\gamma - 1}\frac{P}{\rho} + \frac{u^2}{2}\right)\right] = G - L, \tag{16}$$

where ρ, $\mathbf{u}$ and P are the gas density, velocity and pressure, respectively. γ is the specific heat ratio. G and L are the thermal energy gain and loss (respectively) due to interaction with the radiative field or to gains/losses associated with the latent heat of the chemical reactions and/or the internal energy of the molecular/atomic/ionic species. The thermal pressure is given by

$$P = (n + n_e)kT\,, \tag{17}$$

where n is the total density (of molecules+atoms+ions) and n_e is the electron density.

The complete set of equations for a reactive flow can then be written for a 2D flow as:

$$\frac{\partial \mathbf{U}}{\partial t} + \frac{\partial \mathbf{F}}{\partial x} + \frac{\partial \mathbf{G}}{\partial y} = \mathbf{S}, \tag{18}$$

$$\mathbf{U} = [\rho, \rho u, \rho v, E, n_1, n_2, ..., n_N] \tag{19}$$

$$\mathbf{F} = \left[\rho u, P + \rho u^2, \rho uv, u(E + P), n_1 u, n_2 u, ..., n_N u\right] \tag{20}$$

$$\mathbf{G} = \left[\rho v, \rho uv, P + \rho v^2, v(E + P), n_1 v, n_2 v, ..., n_N v\right] \tag{21}$$

$$\mathbf{S} = [0, 0, 0, 0, S_1, S_2, ..., S_N] \tag{22}$$

where n_1, n_2,..., n_N are the densities of the different species. The vector $\mathbf{U}$ contains the so-called conservative variables. ρ, T y P, were defined previously,

u and v are the velocity in the x and y direction (respectively), and E is the energy written as:

$$E = \frac{1}{2}\rho u^2 + \frac{P}{\gamma - 1}\,. \tag{23}$$

The thermal pressure P is given by equation 17.

We note that the evolution equations of the chemical network were included as N continuity equations (as active scalars) and the sources S_i are given by the right hand side of equation 2. These source terms should also include the appropriate geometrical terms when considering 2D, axisymmetric flow problems. Solutions to this set of equations are presented below.

5. NUMERICAL AND EXPERIMENTAL MODELS TO CODE VERIFICATION

In order to show the characteristics of the KIMYA astrochemical code we developed three numerical simulations. We first try a standard test presented by Braun, Herron & Kahaner (1988), who used the ACUCHEM[1] code. The second test is a dark cloud model, which we describe in § 5.2. Our third test consists of a calculation of the nitric oxide formation with a laser induced plasma (meant to model a lightning discharge), which is described in § 5.3. In all cases, the maximum number of iterations mentioned in § 2.1 is $N_{it} = 40$. In all cases the code reaches the convergence criterion after a smaller number of iterations.

5.1. *Sequence Reactions Test*

In this section, we show the implementation of the KIMYA code for two reaction systems proposed by Braun, Herron & Kahaner (1988): a sequence and a reverse reaction system.

The first test is the system of sequence reactions:

$$a \rightarrow b \qquad k_1 = 2. \times 10^{-1}$$

$$b \rightarrow c \qquad k_2 = 1. \times 10^{-1}$$

$$c \rightarrow d \qquad k_3 = 1.2 \times 10^{-1}$$

where, a, b, c and d are the species. The total density is:

$$n_T = n_a + n_b + n_c + n_d\,. \tag{24}$$

[1] http://global.oup.com/us/companion.websites/9780199730728/Acuchem/

The creation and destruction rates of the species are given by:

$$\begin{aligned} \frac{dn_a}{dt} &= -k_1 n_a, \\ \frac{dn_b}{dt} &= k_1 n_a - k_2 n_b, \\ \frac{dn_c}{dt} &= k_2 n_b - k_3 n_c, \end{aligned} \tag{25}$$

and one can calculate the density of species d from the conservation equation (24).

We rewrite equations (24)-(25) in the form of equation (5):

$$\begin{aligned} Q_a &= -\frac{n_a - n_{a,0}}{\Delta t} - k_1 n_a, \\ Q_b &= -\frac{n_b - n_{b,0}}{\Delta t} + k_1 n_a - k_2 n_b, \\ Q_c &= -\frac{n_c - n_{c,0}}{\Delta t} + k_2 n_b - k_3 n_c, \\ Q_d &= n_a + n_b + n_c + n_d - n_T. \end{aligned} \tag{26}$$

The root of this set of equations then gives the time-advanced solution.

With equations (26), we can calculate the Jacobian matrix,

$$\mathbf{J} = \begin{pmatrix} -1/\Delta t - k_1 & 0 & 0 & 0 \\ k_1 & -1/\Delta t - k_2 & 0 & 0 \\ 0 & k_2 & -1/\Delta t - k_3 & 0 \\ 1 & 1 & 1 & 1 \end{pmatrix} \tag{27}$$

Then, using the set of equations (26) and the Jacobian matrix (equation 27) in equation (8) we carry out a time integration from $t = 0$ to $t = 20$. For the convergence factor (see equation 10) we set $\beta = 0.0$ (i.e., $f = 1$), and we chose an $\epsilon = 10^{-5}$ tolerance. We consider initial densities $n_a = 1$ and $n_b = n_c = n_d = 0$ (in dimensionless units).

Figure 2 shows the densities of the species a, b, c and d as functions of time (in dimensionless units); the solid, dotted, dashed and dot-dashed lines, denote the n_a, n_b, n_c and n_d densities, respectively and the diamonds the values calculated using the standard ACUCHEM code. The values obtained with our code are in very good agreement with the results obtained using ACUCHEM.

5.2. *Dark Cloud Model*

Dark clouds consist of cold ($\approx$ 10 K), dense ($10^3 - 10^6$) cm^3, and dark regions (opaque to visible and UV radiation) which are composed mainly of gas-phase molecular material. The dark clouds are

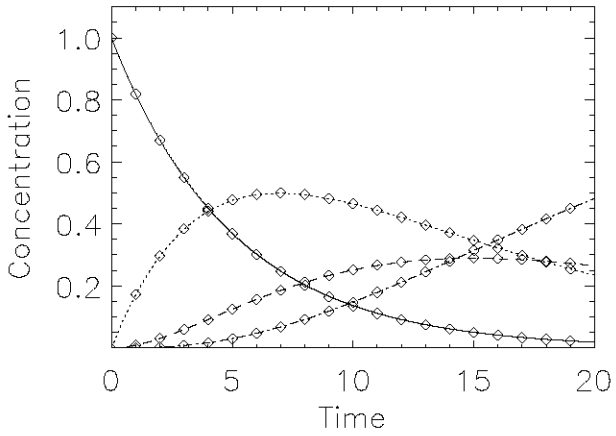

Fig. 2. Densities of species a, b, c and d as a function of time (in dimensionless units) obtained from the sequence test (see equations 24-25). The solid, dotted, dashed and dot-dashed lines, represent the n_a, n_b, n_c and n_d densities obtained with KIMYA, respectively, and the diamonds the corresponding values obtained using ACUCHEM.

very inhomogeneous, and usually present dense, filamentary structures. Also, the dust present in these condensations completely absorbs the photons of optical and UV wavelengths.

Following the work of McElroy et al. (2013), we consider an isotropic and homogeneous medium with $n(\mathrm{H_2}) = 10^4$ cm^{-3}, and $T = 10$ K. We want to compare the chemical concentrations obtained by McElroy et al. (2013), who used the complete network of the UMIST database that includes direct cosmic-ray ionization reactions, cosmic-ray-induced photoreactions and interstellar photoreactions, in the case of TMC-1. This complete network is composed of 467 species and 6174 reactions. We have chosen a reduced subset of species and reactions (13 species with 146 reactions, see below) that correctly reproduces the chemical evolution, but allows a significantly faster time-integration. We are mostly interested in reproducing the density of OH, CO, H_2O and H_2, which are some of the most important molecules in the ISM, and which dominate the molecular cooling function (see Neufeld et al. 1993, 1995).

In order to compute our (simplified) dark cloud model, we use the following selection criteria for the reactions:

- the only ionized species are those that are formed solely of hydrogen;
- the atoms taking part in the network are only H, C, and O;
- the molecules contain at most three atoms;

TABLE 1

INITIAL CONDITIONS IN KIMYA

Species i	n_i/n_{H}[1]	Species i	n_i/n_{H}
H_2	0.5	H	5.0(-5)
C	1.4(-4)	O	3.2(-4)

[1] n_H is the number density of H nuclei.
The $a(b) = a \times 10^b$ format has been used.

- the only grain-surface reaction included is the formation of H_2 due to the combination of two atoms of H:

$$\frac{dn_{\mathrm{H_2}}}{dt} = 5.2\times10^{-17}\left(\frac{T}{300}\right)^{0.5} n_{\mathrm{H}} n_{\mathrm{HI}} \quad [\mathrm{cm^{-3}\,s^{-1}}], \tag{28}$$

where n_{H} and n_{HI} are the total number of H nuclei and the density of neutral atomic hydrogen, respectively.

Taking into account these considerations, we obtain a network with 13 species (H, H^+, CH, CH_2, H_2O, OH, CO, C, C_2, O, O_2, HCO, CO_2) together with 146 reactions (including the formation in dust of H_2). We must note that, according to these criteria, direct cosmic-ray ionization reactions, cosmic-ray-induced photoreactions and interstellar photoreactions are excluded. The reaction coefficients are set to zero outside the temperature range in which they are valid.

We show the initial conditions for the dark cloud model in Table 1. The only molecule that has a nonzero concentration at the beginning of the simulation is H_2.

We ran our simulation for 10^8 yr. The results obtained are shown in Columns 2 and 5 of Table 2. Columns 3 and 6 give the values taken from the webpage of the UMIST database with RATE 12 (McElroy et al. 2013) evolved up to the same time as our KIMYA simulation.

We observe that the final concentrations of species like H, O, OH, CO, CH, and CO_2 are very similar to those reported in the UMIST homepage. This fact is important if we consider that these molecules are some of the most important for comparisons with astrochemical models and observations, since they are the most abundant in the ISM and play an important role in calculating the molecular cooling. Also, this first analysis will serve as a basis to explore and study in more detail what kind of reactions are needed in order to improve the chemical evolution of the different species.

TABLE 2

DENSITIES RELATIVE TO H_2.*

Species	Density $\log(X/H_2)$		Species	Density $\log(X/H_2)$	
	Rate12	KIMYA		Rate12	KIMYA
H	-3.60	- 3.60	C	- 4.42	- 8.43
H^+	-4.91	-10.02	C_2	-17.00	-12.43
CH	-9.96	-10.47	O	- 3.55	- 3.54
CH_2	-3.95	-11.33	O_2	- 4.03	- 4.19
H_2O	-4.33	- 6.35	HCO	-17.00	-11.25
OH	-7.93	- 7.49	CO_2	- 7.08	- 6.94
CO	-3.88	- 3.55			

*In a dark cloud model after 10^8 years.

5.3. *Nitric Oxide Formed During Lightning Discharge*

The production mechanism of nitrogen oxides by electrical discharges has been discussed by several authors, starting with the paper of Stark et al. (1996). The velocity of the shock fronts generated by laboratory scale discharges has been measured, and was found to be too slow to raise the air temperature to the ≈ 3000 K necessary for nitrogen fixation by the Zel'dovich mechanism (Zel'dovich & Raizer, 1966). The freeze out mixing ratio of NOx in air has been measured directly for low pressure discharges and was found to be of the order expected from the Zel'dovich mechanism for gas cooling over a timescale far longer than the duration of the shock front.

Navarro-González, McKay & Mvondo (2001a) presented an experimental study of the formation of nitric oxide (NO) during a lightning discharge. Lightning was simulated in the laboratory by a plasma generated with a pulsed Nd-YAG laser. They presented the experimental variation of the nitric oxide yield as a function of the CO_2 mixing ratio in simulated lightning in primitive atmospheres. The atmospheres are composed of CO_2 and N_2 at 1 bar, and all samples were irradiated at 20°C from 5 to 30 min.

Navarro-González et al. (2001b) reported an experimental assessment of the contributions of the shock wave and the hot plasma bubble to the production of nitric oxide by simulated lightning. Their results provided a picture of the temperature evolution of a simulated lightning discharge from nanosecond to millisecond time scales, and quantitatively assessed the contributions of the shock wave and the bubble to the nitrogen fixation rate by simulated lightning.

The experimental setup consisted of a pulsing Nd:YAG laser which was focussed within an enclosure with gas of the chosen initial chemical composition. In the focal region, an approximately conically shaped plasma bubble was produced in each pulse, and this plasma bubble subsequently expanded producing a central, hot gas region and an outwards moving shock. After a large number of laser pulses, the chemical composition of the enclosed gas was analyzed (see, e.g., Navarro-González, McKay & Mvondo 2001a). We then modeled this flow configuration by studying the time-evolution of hot, initially conical bubbles that expand into an initially homogeneous environment.

In order to study the formation of NO in these experiments, we applied KIMYA in two different ways: as a zero-dimensional model using the techniques shown in § 2 (using the experimentally determined time-evolution of the plasma/hot air and shock wave temperatures), and a gasdynamic model using the reactive flow equations described in § 4.

5.3.1. *Zero-Dimensional Model*

We first compute "0D" numerical simulations (i.e., single parcel models) of NO formation using a gas with atmospheric pressure and an initial temperature of 300 K. We used a gas that was initially composed only of CO_2 and N_2. We then performed a set of numerical simulations changing the initial chemical composition of the gas, that is, changing the proportion of CO_2 in the initial gas density (χ_{CO_2}, by number). The simulations were carried out for the following values of χ_{CO_2}: 0.25, 0.375, 0.5, 0.65, 0.8, 0.9, 0.975 and 0.99.

We used the temporal evolution of the temperature for the hot air bubble and the shock wave obtained experimentally by Navarro-González, McKay & Mvondo (2001a). These temperature time-evolutions are shown in Figure 3. We performed numerical integrations using these two temperature profiles, for 3000 consecutive pulses with a frequency of 1 Hz (one pulse per second).

The simulations include a chemical network of 11 species and 40 reactions. The reactions and the coefficients α and γ in the Arrhenius equation ($k = \alpha e^{\gamma/RT}$, where T is the gas temperature) are shown in Table 3, Columns 2, 3 and 4, respectively.

Figure 4 shows the number of molecules of nitric oxide formed by the laser pulse per unit energy (of the laser) versus the initial concentration of CO_2.

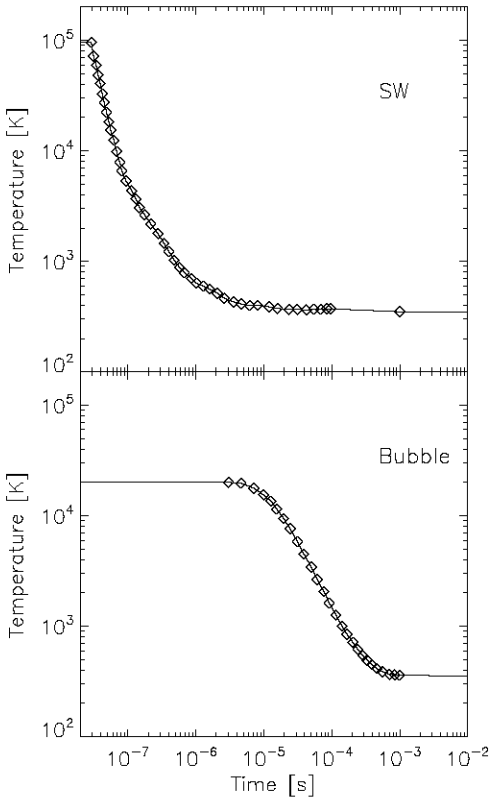

Fig. 3. Temporal evolution of the shock wave temperature (top) and the plasma/hot air temperature (bottom) obtained from a laser induced plasma with a 300 mJ per pulse discharge energy (see also Navarro-González et al. 2001b). The diamonds represent the experimental data, the solid line the fitted curve used to run the numerical models.

The dash-dotted and dashed lines are the final concentrations (after the 3000 pulses, see above) obtained for the plasma/hot air bubble (dash-dotted line) and for the shock wave (dashed line), and the diamond symbols are the experimental measurements (with their errors) for all of the gas (bubble+shock wave) presented by Navarro-González, McKay & Mvondo (2001a).

It is clear that for χ_{CO_2} between 0.25 and 0.95 the measured NO yields lie between the simulated yields obtained for the hot bubble and for the shock wave. However, for $\chi_{CO_2} \leq 0.2$ and for $\chi_{CO_2} \geq 0.95$ there are significant differences between the model predictions and the experimental results. These differences are likely to be a result of the fact that our chemical network does not have the molecular species and/or reaction rates suitable to reproduce the chemistry at very high or low initial values of χ_{CO_2}.

TABLE 3

GAS PHASE REACTIONS USED TO MODEL THE NO FORMED DURING LIGHTNING DISCHARGE

No.	Reaction	α	γ [kJ]
1	$N + N + M \rightarrow N_2 + M$	2.6×10^{-33}	-3.7
2	$N + O + M \rightarrow NO + M$	2.6×10^{-33}	-3.1
3	$N_2 + M \rightarrow N + N + M$	8.5×10^{-4}	1102.2
4	$N_2 + e \rightarrow N + N + e$	8.1×10^{-13}	0.
5	$NO + M \rightarrow N + O + M$	3.1×10^{-9}	628.5
6	$NO + N \rightarrow N_2 + O$	3.2×10^{-11}	1.4
7	$NO + O \rightarrow N + O_2$	1.2×10^{-11}	169.7
8	$NO + O + M \rightarrow NO_2 + M$	7.0×10^{-33}	-5.7
9	$NO + NO + O_2 \rightarrow NO_2 + NO_2$	3.3×10^{-39}	-4.4
10	$NO + O_2 + M \rightarrow NO_3 + M$	5.7×10^{-41}	1.8
11	$NO + NO \rightarrow N_2 + O_2$	2.5×10^{-11}	254.9
12	$NO + NO \rightarrow N_2O + O$	4.5×10^{-12}	267.7
13	$NO + O_3 \rightarrow NO_2 + O_2$	2.3×10^{-12}	11.7
14	$NO_2 + M \rightarrow NO + O + M$	1.2×10^{-12}	117.3
15	$NO_2 + O \rightarrow NO + O_2$	5.8×10^{-12}	0.7
16	$NO_2 + O + M \rightarrow NO_3 + M$	1.7×10^{-33}	-8.7
17	$NO_2 + N \rightarrow N_2O + O$	5.8×10^{-12}	-1.8
18	$NO_2 + O_3 \rightarrow NO_3 + O_2$	3.2×10^{-13}	22.1
19	$NO_2 + NO_2 \rightarrow NO + NO + O_2$	2.7×10^{-12}	109.3
20	$NO_2 + NO_2 \rightarrow NO_3 + NO$	5.7×10^{-12}	96.4
21	$NO_3 + M \rightarrow NO + O_2 + M$	4.5×10^{-13}	17.6
22	$NO_3 + O \rightarrow NO_2 + O_2$	1.0×10^{-11}	0.
23	$NO_3 + NO \rightarrow NO_2 + NO_2$	4.8×10^{-12}	-3. 6
24	$NO_3 + NO_2 \rightarrow NO + NO_2 + O_2$	1.5×10^{-13}	13.3
25	$N_2O + M \rightarrow N_2 + O + M$	3.5×10^{-10}	220.6
26	$N_2O + O \rightarrow N_2 + O_2$	2.6×10^{-10}	118.8
27	$N_2O + O \rightarrow NO + NO$	1.4×10^{-10}	114.4
28	$N_2O + NO \rightarrow N_2 + NO_2$	3.6×10^{-10}	211.5
29	$O + O + M \rightarrow O_2 + M$	1.7×10^{-34}	-6.0
30	$O + O_2 + M \rightarrow O_3 + M$	9.2×10^{-35}	-4.3
31	$O_2 + M \rightarrow O + O + M$	5.0×10^{-7}	493.0
33	$O_2 + e \rightarrow O + O + e$	4.3×10^{-11}	0.
34	$O_2 + N \rightarrow NO + O$	1.5×10^{-10}	63.1
34	$O_3 + M \rightarrow O_2 + O + M$	1.2×10^{-9}	95.5
35	$O_3 + O \rightarrow O_2 + O_2$	1.2×10^{-11}	17.6
36	$O_3 + N \rightarrow NO + O_2$	5.7×10^{-13}	0.
37	$CO_2 \rightarrow CO + O$	1.3×10^{-9}	-424
38	$CO + O \rightarrow CO_2$	1.7×10^{-33}	-12.5
39	$CO_2 + N \rightarrow NO + CO$	3.2×10^{-13}	-1710.
40	$O + CO_2 \rightarrow O_2 + CO$	2.46×10^{-11}	-220.

Figure 5 shows the evolution of the plasma temperature and numerical densities of N, N_2, N_2O, NO, NO_2, NO_3, O, O_2, O_3, CO and CO_2 for the first 18 simulated pulses. The peaks in the plasma temperature correspond to the energy injection times (i.e., to the laser pulses, which are assumed to produce instantaneous temperature rises). The concentrations of N_2, NO, O and CO_2 increase and the concentrations of N, N_2O, NO, NO_2, NO_3 and O_2 decrease in

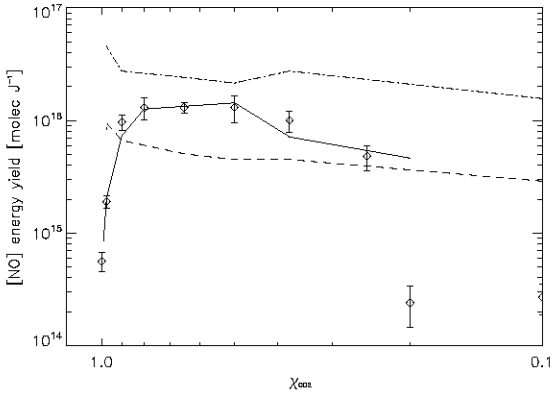

Fig. 4. The variation of the nitric oxide yield as a function of the CO_2 mixing ratio in simulated lightning for the experimental data (diamonds) and the three numerical models. The dash-dotted (plasma/hot air bubble) and dashed lines (shock wave) correspond to the zero-dimensional model. The solid line corresponds to the hydrodynamical model.

the pulses. The NO yield has a peak in each pulse, but after $\approx$ 1200 pulses it attains an almost time-independent, constant value. This is the value that is compared with the experimental measurements.

5.3.2. *Gasdynamic Model*

We computed reactive flow simulations using the WALIXCE 2D code (Esquivel et al. 2010) + KIMYA. The WALIXCE 2D code solves the gas dynamic equations (see equations 14-16 in § 4) in a cylindrical, two-dimensional adaptive mesh, using a second-order HLLC Riemann solver (Toro et al. 1994). This fusion of the two codes is named WALKIMYA-2D. To carry out the numerical simulations, we then integrate the gasdynamic equations and continuity/reaction rate equations for all species, as discussed previously in § 4.

The adaptative mesh consist of four root blocks of 16×16 cells, with 7 levels of refinement, yielding a maximum resolution of 4096×1024 (axial $\times$ radial) cells. The maximum resolution (along the two axes) is of 1.95×10^{-3} cm. The boundary conditions used are reflection on the symmetry axis and transmission everywhere else. The size of the mesh is large enough so that the choice of outer boundaries does not affect the simulation.

The timestep is chosen with the traditional CFL (Courant-Friedrichs-Lewy) stability condition of the explicit gasdynamic integrator of the WALIXCE 2D code (Esquivel et al. 2010). The same timestep is used for the (simultaneous) integration of the chemical reaction terms with the KIMYA routines.

The numerical simulations are initialized with an environment of atmospheric pressure and a temperature of 300 K. A $\gamma = 7/5$, constant specific heat ratio is assumed. The hot plasma bubble (generated in the experiment in the focal region of a focussed laser pulse) is introduced in the center of the computational mesh, as a hot, $T_0 \sim 10^4$ K cone of 0.25 cm (axial) length and $\alpha = 30°$ half-opening angle (the initial density within the cone having the environmental value, and the values chosen for T_0 are discussed below). This high pressure cone expands, driving a shock wave into the unperturbed environment. The simulations evolve until a time of 2.0×10^{-5} sec.

In order to reproduce the time-dependent evolution of the shock wave produced by an expanding, laser-generated plasma bubble, we computed simulations using initial temperatures (for the hot cone) $T_0 = 7000$, 12000 and 24000 K. Figure 6 shows the average radius of the shock wave as a function of time, and we see that the three chosen values of T_0 lead to results that lie close to the experimentally measured shock wave radius (see Raga et al. 2000, and references therein). The predictions of the chemical evolution that we present below are obtained from simulations with $T_0 = 12000$ K.

Figure 7 shows density and temperature maps for two stages of the bubble evolution. The two panels on the left correspond to density maps for evolutionary times of 2×10^{-6} and 2×10^{-5} sec, and the two panels on the right side are the temperature maps at the same two evolutionary times. At 2×10^{-6} sec, the gas which is compressed by the shock wave and a low density, inner region (with a temperature $\approx 10^4$ K) are clearly seen. At 10^{-5} sec, the shock wave is no longer visible, and the central, low density region has a $\approx$ 1000 K temperature.

The gas was initially composed only of CO_2 and N_2. We compute simulations changing the initial value of χ_{CO_2} in the same way as in the previous section.

We then solved the evolutionary densities of 11 chemical species. Figure 8 shows the density maps of CO_2, NO, O_3 and NO_2 (left, center-left, center-right and right panels, respectively) at 2×10^{-6} sec obtained from the simulation with χ_{CO_2}=0.865. The CO_2 is piled up behind the leading shock, while NO, ozone and NO_2 have been formed in the inner, the hottest region of the central bubble. Notice that ozone is also weakly formed in an extended region between the hot bubble and the shock wave.

The total NO yields obtained from the simulations are shown as a solid line in Figure 4. It is

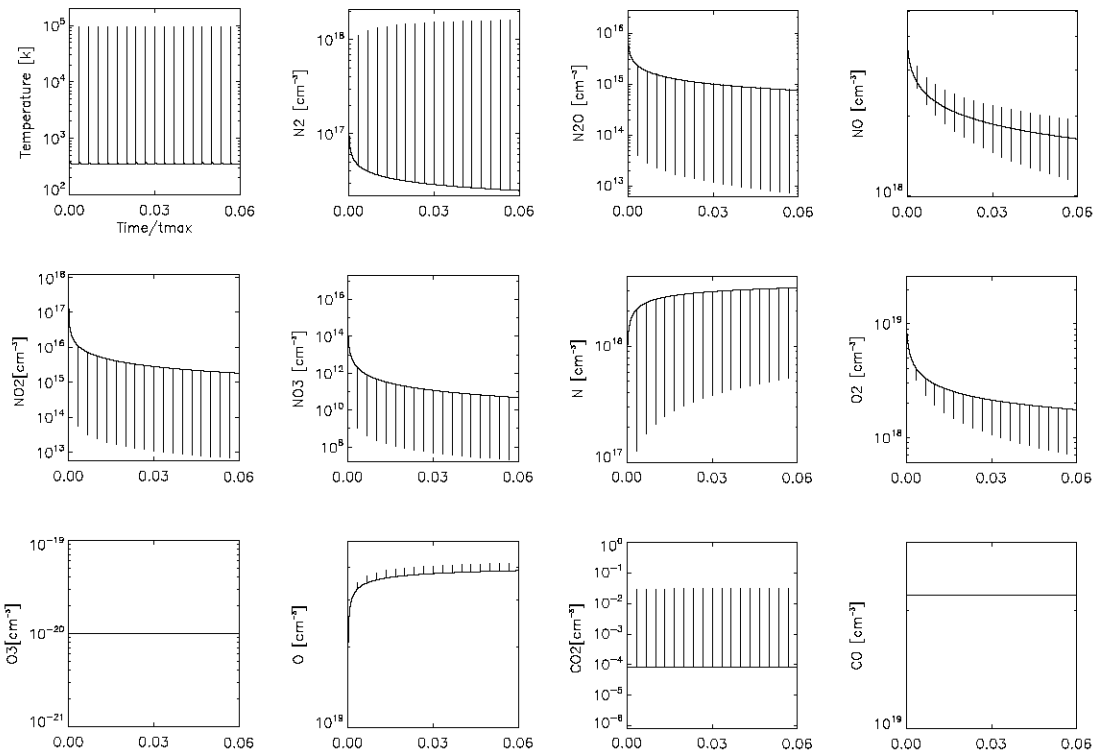

Fig. 5. The evolution of the plasma temperature and numerical densities of N, N_2, N_2O, NO, NO_2, NO_3, O, O_2, O_3, CO and CO_2 for the first 18 simulated pulses. The time is normalized by $t_{max} = 300.27$ s.

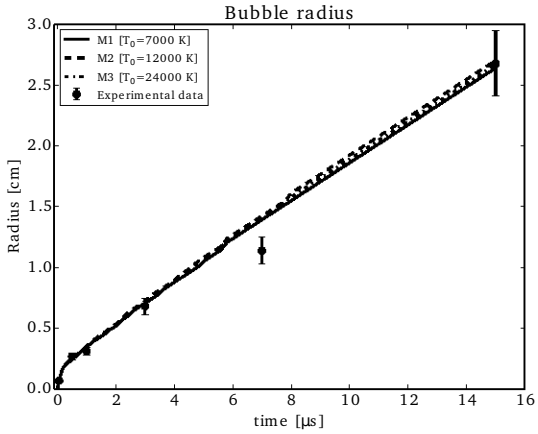

Fig. 6. Radius of the simulated bubble versus time using different initial temperatures for the hot cone: $T_0 = 7000$, 12000 and 24000 K (solid, dashed and dotted line, respectively). The symbols represent the experimental data together with their respective errors.

clear that these yields are consistent with the experimental measurements of Navarro-González, McKay & Mvondo (2001a) over most of the explored χ_{CO_2} range.

Finally, Figure 9 shows the total yield of all of the molecules included in the numerical simulations. We find that for initial CO_2 densities larger than 0.865, N_2O, NO_2, NO_3 and O_3 do not form, but in environments richer in N_2 the formation of these oxides is very important.

5.4. *Scaling of the Computational Time*

In order to illustrate the scaling of our reactive gasdynamic code as a function of the number of species and reactions, we have carried out a set of simulations similar to the ones of § 5.3.2. In these simulations we changed:

- the number of reactions (models M2a, M2b, M2c, M2d and M2e), but keeping the same number of species,
- the number of reactions and species (models M3, M4, M5 and M6).

The numbers of species and reactions used in these two sequences of simulations are given in Table 4.

In the left panel of Figure 10 (and also in Column 4 of Table 4), we show the scaled computational time as a function of number of reactions. We have scaled the computational times to the computational

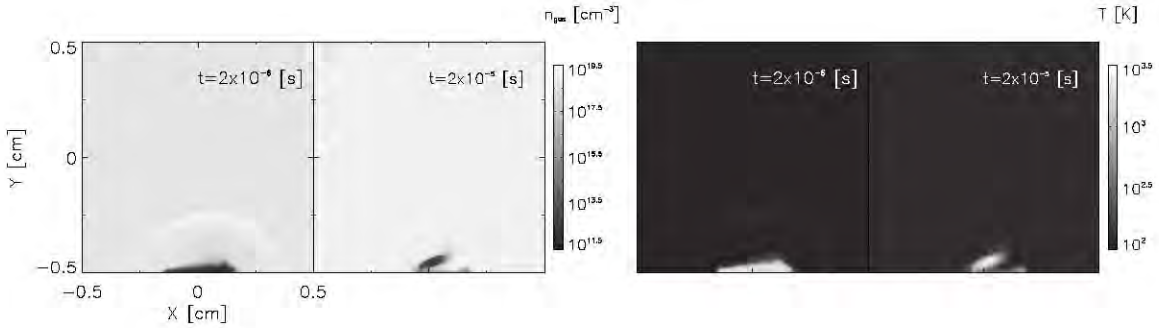

Fig. 7. Density (left) and temperature maps (right) at $t = 2 \times 10^{-6}$ and $2{\times}10^{-5}$ s (as indicated in the frames). In each panel, the left frames are the density maps and the right frames are the temperature maps.

Fig. 8. Density maps of CO_2, NO, O_3 and NO_2 at $t = 2{\times}10^{-6}$. The color figure can be viewed online.

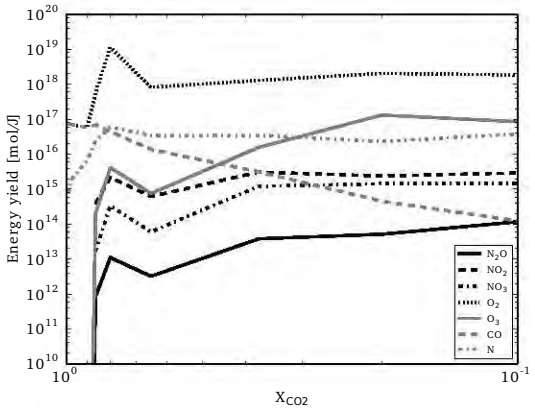

Fig. 9. The variation of the N_2O, NO_2, NO_3, O_2, O_3 and N yields as a function of the CO_2 mixing ratio in the reactive flow numerical simulations.

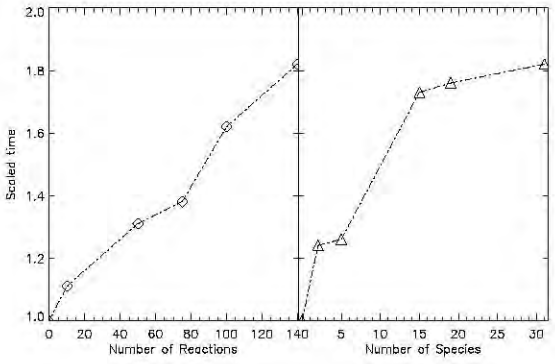

Fig. 10. Left panel: computational time vs. number of reactions for the M2a, M2b, M2c, M2d, M2e sequence (with constant number of species, see Table 4). Right panel: scaled computational time vs. number of species for the sequence of models M3, M4, M5, M6 and M2e, with increasing numbers of species and reactions (see Table 4).

time of a purely hydrodynamic simulation (model M1, with no chemical species). From these models (models M2a, b, c, d and e) we see an approximately linear increase in computational time with number of chemical reactions (left panel of Figure 10). For the case of 140 reactions (model M2e), the computational time is ≈ 1.8 times larger than that of the purely gasdynamic simulation (model M1, see Table 4).

For the sequence of models with increasing number of species and reactions (models M3, M4, M5, M6 and M2e, see Table 4) we obtain a rapid growth

TABLE 4

NUMERICAL MODELS

Model	Number of species	Number of reactions	Scaled time
M1	0[a]	0	1.0
M2a	31	10	1.11
M2b	31	50	1.31
M2c	31	75	1.38
M2d	31	100	1.62
M2e	31	140	1.82
M3	2	1	1.24
M4	5	6	1.26
M5	15	47	1.73
M6	19	82	1.75
M2e	31	140	1.82

[a]Solving only the hydrodynamic equations.

of computational time for up to 15 species, and a slower growth from 15 to 31 species (see the right panel of Figure 10).

6. DISCUSSION AND CONCLUSION

We have presented the new KIMYA numerical code for solving chemical reaction networks. This code was written in Fortran 90 and has subroutines and modules providing the tools to solve the kinetical chemistry for a reaction network chosen by the user.

In order to solve the system of ODEs, we implemented an implicit numerical solver (based on the standard, Newton-Raphson method). This method in principle converges for arbitrary values of the chosen timestep.

We simulated two problems of interest:

- a dark cloud model; we computed a single-parcel model which we compare with the previous work of McElroy et al. (2013). We find good agreement, especially for species like O, OH, H_2O, CO, and CO_2. The chemical network used for our simulation consists of 13 species: H, H+, CH, CH_2, H_2O, OH, CO, C, C_2, O, O_2, HCO, CO_2, and 146 reactions;

- laser laboratory experiments of the formation of nitric oxide during lightning discharges: we computed single-parcel models and axisymmetric reactive gasdynamic simulations, and we compared the induced chemistry with the experimental study of NO formation presented in Navarro-González, McKay & Mvondo (2001a). We computed models changing the initial chemical composition of the gas, and obtained the chemical composition after a single laser pulse and after 3000 pulses. We found that for initial CO_2 concentrations in the $0.2 < \chi_{CO_2} < 0.95$ range, a remarkably good agreement between the numerical and experimental results is obtained.

Though this second problem has no direct astrophysical application, it allows us to evaluate the precision of a reactive gasdynamic simulation, by comparing the final (spatially integrated) chemical composition obtained from the simulation with laboratory measurements. This kind of test should be attempted with different astrophysical codes to evaluate whether or not the computed chemistry converges to the appropriate solution.

We found that for a benchmark suite solving 11 chemical species and 40 chemical reactions, our code solves a single timestep in $\approx 3.9 \times 10^{-5}$ s. We found that the speed of our algorithm is sufficient for combining it with a multi-dimensional gasdynamic (or magnetohydrodynamic) code, in which the chemical evolution must be solved in $10^4 - 10^9$ computational cells.

The KIMYA code is efficient and can handle a complex set of chemical reactions that can be used in studies of interstellar chemistry, planetary atmospheres, combustion and detonation experiments, and air pollution, among others.

KIMYA can be used to solve a chemical reaction network for a "single parcel" model. Also, the code can be integrated in a full gasdynamic (or magnetohydrodynamic) simulation, computing the temporal evolution of the chemical species. The simplest possible implicit timestep (see § 2) carried out by KIMYA gives a short computational time which results in only moderate (≈ factor of 2, see § 5.4) increases over "non-reactive" hydrodynamic simulations (without a chemical network).

Although the main utility of the code is to model different phenomena in the ISM, it can also be used in other areas (see above). We found that comparisons between the numerical simulations and experiments (see § 5) show good agreement. As far as we are aware, this is the first time that an astrophysical reactive gasdynamic code has been tested with laboratory experiments. This test gives us confidence that our code is working correctly. Clearly, other reactive flow code developers could use the experimental results we have described here in order to test their codes.

As a future release, in order to make KIMYA more user friendly, we will include an automation of the chemical network generator. The code will then write the rate equations and the elements of the Jacobian matrix directly from the reactions chosen by the user. Also, we will develop procedures for defining the set of reactions, choosing the more representative reactions for a particular problem and limiting the number of species. This is not an easy task, and a substantial effort is being made to find the best way to do this, as discussed, e. g. by Wiebe, Semenov & Henning (2003) and Grassi et al. (2012) for the case of astrochemical networks.

We acknowledge support from CONACYT grant 220626 and the DGAPA-UNAM grants IA103115, IN109715, IN109518, IG100218, IN109416, PE103609.

REFERENCES

Bates, D. R. & Spitzer, L. J. 1951, ApJ, 113, 441
Baulch, D. L., Bowman, C. T., Cobos, C. J., et al. 2005, JPCRD, 34, 757
Braun, W., Herron, J. T., & Kahaner, D. K. 1988, Int. J. Chem. Kinet., 20, 51
Crowley, J. N., Ammann, M., Cox, R. A., et al. 2010, ACP, 13, 8045
Curtiss, C. F. & Hirschfelder, J. O. 1952, PNAS, 38, 235
Dahlquist, G. G. & Lindberg, B. 1973, Technical Report TRITA-NA-7302. Stockholm: Royal Institute of Technology
Esquivel, A., Raga, A. C., Cantó, J., et al. 2010, ApJ, 725, 1466
Gear, C. W. 1971, Numerical Initial Value Problems in Ordinary Differential Equations, (Englewood Cliffs: Prentice Hall)
Grassi, T., Bovino, S., Gianturco, F. A., Baiocchi, P., & Merlin, E. 2012, MNRAS, 425, 1332
Grassi, T., Bovino, S., Schleicher, D. R. G., et al. 2014, MNRAS, 439, 2386
Jacobson, M. Z. 2005, Fundamentals of Atmospheric Modeling, 2nd ed. Cambridge University Press. Chapter 10
May, R. & Noye, J. 1984, Computational techniques for differential equations, (North-Holland: Elsevier Science)
McElroy, D., Walsh, C., Markwick, A. J., et al. 2013, A&A, 550, A36
Millar, T. J., Bennett, A., Rawlings, J. M. C., Brown, P. D., & Charnley, S. B. 1991, A&AS, 87, 585
Motoyama, K., Morata, O., Shang, H., Krasnopolsky, R., & Hasegawa, T. 2015, ApJ, 808, 46
Navarro-González, R., McKay, C. P., & Mvondo, D. N. 2001a, Natur, 412, 61
Navarro-González, R., Villagrán-Muniz, M., Sobral, H., Molina, L. T., & Molina, M. J. 2001b, GeoRL, 28, 3867
Navarro-González, R., Vargas, E., de la Rosa, J., Raga, A. C., & McKay, C. P. 2010, JGRE, 115, 12010
Nejad, L. A. M. 2005, Ap&SS, 299, 1
Neufeld, D. A. & Kaufman, M. J. 1993, ApJ, 418, 263
Neufeld, D. A., Lepp, S., & Melnick, G. J. 1995, ApJS, 100, 132
Press, W. H., Teukolsky, S. A., Vetterling, W. T., & Flannery, B. P. 1993, Numerical Recipes in Fortran: The Art of Scientific Computing, (2nd ed. Cambridge, MA: CUP)
Raga, A. C., Navarro-González, R., & Villagrán-Muñiz, M. 2000, RMxAA, 36, 67
Raga, A. C., Sobral, H., Villagrán-Muniz, M., Navarro-González, R., & Masciadri, E. 2001, MNRAS, 324, 206
Semenov, D., Hersant, F., Wakelam, V., et al. 2010, A&A, 522, A42
Smith, B. D., Bryan, G. L., Glover, S. C. O., et al. 2017, MNRAS, 466, 2217
Stark, M. S., Harrison, J. T. H., & Anastasi, C. 1996, JGR, 101, 6963
Toro, E. F., Spruce, M., & Speares, W. 1994, ShWav, 4, 25
Velázquez, P. F., Sobral, H., Raga, A. C., Villagrán-Muniz, M., & Navarro-González, R. 2001, RMxAA, 37, 87
Wakelam, V. et al. 2012, ApJS, 199, 21, doi:10.1088/0067-0049/199/1/21
Wiebe, D., Semenov, D., & Henning, Th. 2003, A&A, 399, 197
Young, T. R. & Boris, J. P. 1973, nrl rept, 2611
Zel'dovich, Y. B. & Raizer, Y. P. 1966, Physics of shock waves and high-temperature hydrodynamic phenomena, (New York, NY: Academic Press)
Ziegler, U. 2016, A&A, 586, A82

A. Castellanos-Ramírez, A. Esquivel, R. Navarro-González, A. C. Raga, P. Rivera-Ortiz, and A. Rodríguez-González: Instituto de Ciencias Nucleares, Universidad Nacional Autónoma de México, Apdo. Postal 70-543, Cd. Mx., C.P. 04510, México (antonio.castellanos@nucleares.unam.mx).

Conclusiones

En esta tesis se llevó a cabo un estudio observacional, teórico y numérico de los flujos de estrellas jóvenes. En la primera parte se llevaron a cabo simulaciones numéricas 3D y observaciones de burbujas de cúmulos de estrellas masivas. La segunda parte consistió en un estudio del espectro y variabilidad temporal de las líneas de emisión de los objetos HH 1 y 2, así como un análisis observacional y numérico de los movimientos propios y variabilidad temporal del jet de HH 1. Finalmente se presentó un código numérico que resuelve las ecuaciones de flujos reactivos para explorar la evolución temporal de la composición química del gas en el medio interestelar, con clara aplicación a la interacción de flujos estelares con el material circundante .

En la sección 1.2 se presentó una serie de modelos numéricos con la finalidad de explorar los efectos de explosiones de supernova, de la metalicidad, y de la conducción térmica en la emisión térmica de rayos X (suaves y duros) de la superburbuja de un cúmulo masivo de estrellas.

En los modelos, se incluyó la inyección de masa y energía por un grupo de fuentes de viento y un evento de explosión de supernova. Además se variaron la posición de la supernova con respecto al centro del cúmulo y el tiempo de detonación. También, se calcularon modelos con metalicidad homogénea para el viento de las estrellas, el medio ambiente y la explosión de supernovas y modelos en los que estos tres componentes poseen diferentes metalicidades. Finalmente, se incluyeron los efectos de la conducción térmica.

Los modelos muestran que la contribución de la metalicidad de los vientos y el remanente de SN es insignificante para la emisión de rayos X suaves de las superburbujas, pero se vuelve importante para los rayos X duros. Por otro lado, los modelos con conducción térmica dan un aumento en la luminosidad total de los rayos X suaves. Sin embargo, a pesar de este aumento, no se alzanzan los valores observados de las burbujas cuya luminosidad se pretende modelar.

La contribución más importante a la emisión de rayos X es la explosión de supernova. El aumento en la luminosidad para el caso en que la detonación esté colocada un poco fuera del centro del cúmulo coincide en buena medida con los valores observados para el caso de las superburbujas N 70 y N 185 ($L_x \approx 10^{35}$ erg s^{-1}). La morfología simétrica de las superburbujas también coincide en estos casos. Si la explosión de supernova ocurre cerca del borde del cúmulo, el aumento de la luminosidad es mayor y coincide con los valores observados para los casos de DEM L50 y DEM L152 ($L_x \approx 10^{36}$ erg s^{-1}). La morfología de

la superburbuja simulada también presenta una deformación cerca de la región donde se ha detonado la supernova.

El trabajo presentado en la sección 2.2 desarrolla un método para calcular la emisión de líneas de Balmer. Se utiliza el equilibrio estadístico para los niveles excitados del átomo de hidrógeno considerando recombinaciones a niveles excitados y excitaciones desde el nivel fundamental. La solución a este problema se da en términos de una matriz de cascada alimentada por recombinaciones y por excitaciones colisionales.

Los resultados muestran que en el rango de temperaturas menores que 10^4 K la energía producida en las líneas de Balmer debida a las recombinaciones es dominante, mientras que, para temperaturas mayores domina la energía en estas líneas debida a las excitaciones colisionales.

Este hecho se traduce en que las recombinaciones dominan los cocientes de líneas de Balmer en el intervalo de baja temperatura, mientras que las excitaciones colisionales dominan las líneas de Balmer a alta temperatura. La aplicación inmediata de este hecho es en la observación de choques no radiativos, donde la emisión de dichas líneas (en la región inmediata post-choque) es debida a la excitación colisional.

En la sección 2.3 se describen nuevas imágenes en Hα y Hβ del sistema HH 1/2 tomadas con el HST. Estas imágenes permitieron un nuevo estudio de la estructura de emisión de líneas de Balmer en este sistema.

Las imágenes muestran que tanto para HH 1 como para HH 2 la mayor parte de la emisión de Hα proviene de zonas de recombinación, en las cuales las líneas de Balmer son producidas por la cascada de recombinación. Además, se detectan regiones filamentarias delgadas en la cabeza principal de HH 1 y 2 donde el cociente Hα/Hβ es alto. En estas zonas la distribución del cociente toma valores de hasta ~ 5 para HH 1, y hasta ~ 6 para HH 2. Este hecho se puede explicar en términos de una cascada de excitaciones colisionales ubicada en regiones con una temperatura aproximada de $1{,}5 \rightarrow 10 \times 10^4$ K, las cuales emiten líneas de Balmer excitadas colisionalmente.

Por tanto estas imágenes muestran la detección de la zona inmediata post-choque en el caso de objetos HH. Para este tipo de objetos es la primera vez que se tiene tal detección de forma concluyente.

La sección 2.4 consta de un estudio observacional de imágenes del HST de las siguientes líneas de emisión: Hα, Hβ, [O I] 6300, [O II] 3726+29, [O III] 5007 y [S II] 6716+30.

En el caso de HH 1 las observaciones muestran un valor constante de 0.35 para el cociente Hβ/Hα (caso B de la cascada de recombinación) con excepción de un filamento a lo largo del lado este de la cabeza, donde el cociente toma un valor de 0.22 (líneas de Balmer debidas a excitaciones colisionales en la región después del choque). Además, la cabeza del choque

tiene dos alas asimétricas: el ala este, más brillante en Hα, Hβ, [S II], y [O I]; y el ala oeste, más brillante en [O II] y [O III].

Para HH 2 la situación es muy similar. Los valores de Hβ/Hα son aproximadamente constantes (caso B de la cascada de recombinación). Sin embargo, cerca del borde principal la excitación colisional domina, dando como resultado unas tiras de bajo cociente Hβ/Hα. Además, existen condensaciones brillantes, detectadas en la emisión de alta excitación ([O III]), alineadas noroeste-sureste. Otras condensaciones menos brillantes, con mayores contribuciones de las líneas de baja excitación ([O I] y [S II]), se encuentran en la periferia. Un resultado interesante es que los cocientes de líneas muestran un arreglo de dos estructuras tipo choque a proa: una principal de baja excitación y otra secundaria (siguiendo de cerca a la principal) de alta excitación.

Finalmente, se encontraron correlaciones lineales entre pares de cocientes de líneas. Las pendientes observadas resultan ser muy similares en todas las regiones de HH 1 y 2. De las dependencias de estos cocientes con la temperatura, se utilizó [O I]/[SII] para evaluar el rango de temperatura y obtener mapas de temperatura de HH 1 y 2. Se encontró que los valores de la temperatura son $\sim 10^4$ K, excepto para regiones cerca del choque a proa, donde las temperaturas toman valores en el rango $3 - 5 \times 10^4$K.

En la sección 2.5 se presenta una comparación del espectro del sistema HH 1 y 2 obtenido para 3 diferentes épocas: 1978, 1994 y 2014. Las líneas analizadas son: Hα, Hβ, Mg II 2798, [O I] 6300, [O II] 3726+28, [O III] 5007 y [S II] 6716+30.

Un fenómeno interesante es que para HH 2 los cocientes de línea no dependen del tiempo en forma apreciable, pero el objeto muestra una luminosidad creciente. Por otro lado, en el caso de HH 1 los cocientes de línea también son constantes pero hay un pequeño decaimiento en el brillo como función del tiempo junto con un leve incremento en la velocidad del objeto.

A fin de explicar este comportamiento, se desarrolló un modelo de una superficie de trabajo. En el caso de HH 1, el comportamiento mostrado por las observaciones se interpreta como un chorro que se mueve dentro de un medio ambiente de densidad inhomogénea, la cual decrece a medida que el objeto se aleja de la fuente. En el caso de HH 2, el comportamiento observado se interpreta como un chorro con velocidad y pérdida de masa constante viajando en un entorno donde la densidad crece a mayores distancias de la fuente.

La sección 2.6 describe un nuevo método para determinar movimientos propios de objetos extendidos analizando el desplazamiento de los picos de las intensidades en imágenes. Este método se aplica a cuatro épocas de imágenes de [S II] del jet de HH 1 obtenidas por el HST.

El procedimiento de determinación de movimientos propios seguido por el método se puede esbozar de la siguiente manera: Se toma una imagen y se realiza una convolución con un wavelet de un semi-ancho σ escogido. Posteriormente, se calculan las posiciones e intensidades

de los picos en la imagen convolucionada. Finalmente se determinan los movimientos propios con los desplazamientos de los picos entre épocas sucesivas.

Siguiendo esta receta se determinaron los movimientos propios de los nudos pertenecientes al chorro HH 1 para 4 épocas de imágenes del HST (1994, 1997, 2007 y 2014). Estos movimientos se encuentran bien alineados con el jet, y toman valores entre 230 y 290 km s^{-1} aproximadamente, con velocidades mayores en los nudos más cercanos a la fuente emisora.

Otro resultado interesante es que los nudos a mayores distancias de la fuente muestran una pendiente decreciente de la intensidad de [S II] con respecto a la distancia del tipo $I \propto x^{-3}$, comportamiento que es predicho por un modelo analítico de jet de fuente variable.

Finalmente, calculando el tiempo dinámico para cada nudo, se encuentra que la velocidad de eyección es mayor para tiempos más recientes. Esto implica que en aproximadamente 450 años, los nudos del chorro HH 1 se alcanzarán entre ellos y formarán una gran "cabeza". Este fenómeno ocurrirá un poco más cerca de la fuente que la posición actual de HH 1 (75″).

En el trabajo presentado en la sección 2.7 se desarrolló una simulación axisimétrica de la dinámica de gases de un jet con dos modos sinusoidales para la velocidad de eyección, a fin de modelar los movimientos propios, la dependencia de la intensidad con la posición respecto de la fuente y la evolución en el tiempo de las intensidades [S II] de los nudos del chorro HH 1.

Los resultados muestran que la morfología de [S II] predicha por la simulación reproduce en buena medida la morfología presentada por el objeto, tanto en el tamaño del jet (aproximadamente 20″ en la simulación), como en la distancia de la cabeza a la fuente (de 80″ aproximadamente) y en el número de nudos a lo largo del jet (7).

Del cálculo de los movimientos propios numéricos se obtienen nudos más rápidos cerca de la fuente, lo cual coincide con las observaciones. Finalmente los nudos del jet más lejanos de la fuente siguen aproximadamente una ley $I_{[S\ II]} \propto x^{-3}$. Esto es consistente con un modelo analítico previo y con las observaciones del jet de HH 1.

En la sección 2.2 de esta tesis se desarrolló un código numérico, KIMYA, para resolver el sistema de ecuaciones diferenciales que describe el comportamiento temporal de una red química. Fue diseñado para incorporar la red química en simulaciones multidimensionales de la dinámica de gases. El código es eficiente y puede manejar un conjunto complejo de reacciones químicas apropiado para modelar el medio interestelar.

Se utilizó KIMYA para calcular un modelo de nube oscura y se compararon los resultados con una red química más extensa calculada con el código ACUCHEM, el cual es un estándar en este tipo de problemas. Se encontró un buen acuerdo, especialmente para especies como O, OH, H_2O, CO y CO_2.

Finalmente, se calcularon dos modelos de la formación de óxido nítrico debido a la des-

carga de relámpagos (simulado por un láser en el laboratorio), los cuales se compararon con un estudio experimental. El primer modelo es de una parcela simple, mientras que el segundo modelo es de flujo reactivo axisimétrico. Notamos que los resultados numéricos presentan un buen acuerdo con los resultados experimentales, y notablemente el modelo más realista (el de flujo reactivo) presenta mejor coincidencia con el experimento de laboratorio.

Referencias

Ambartsumian, V. A. 1954, Comm. Byurakan Obs., 13, 3

Arthur, S. J. 2009, The Local Bubble and Beyond, AIP Conf. Proc., 1156, 285

Bacciotti, F., & Eislöffel, J. 1999, A&A, 342, 717

Bally, J., Heathcote, S., Reipurth, B., et al. 2002, AJ, 123, 2627

Bolatto, A. D., Leroy, A. K., Rosolowsky, E., Walter, F., & Blitz, L. 2008, ApJ, 686, 948

Bohigas, J., Torrelles, J. M, Echevarría, J. et al. 1985, RMxAA, 11, 149

Böhm-Vitense, E., Cardelli, J. A., Nemec, J. M., Böhm, K. H. 1982, ApJ, 262, 224

Braun, W., Herron, J. T. & Kahaner, D. K., 1988, Int. J. Chem. Kinet., 20, 51.

Brugel, E. W., Böhm, K. H., & Mannery, E. 1981, ApJS, 47, 117

Carruthers G. R., 1970, ApJ, 161, L81

Castellanos-Ramírez, A., Raga, A. C. & Rodríguez-González, A. 2018, ApJL, submitted

Castor J., McCray R., Weaver R., 1975, ApJ, 200, L107

Chu, Y.-H., & Mac Low, M.-M. 1990, ApJ, 365, 510

Chu, Y.-H., Guerrero, M. A., Gruendl, R. A., García-Segura, G., & Wendker, H. J. 2003, ApJ, 599, 1189

Chu, Y.-H. 2008, Massive Stars as Cosmic Engines, 250, 341

Dyson, J. E., & de Vries, J. 1972, A&A, 20, 223

Gear, C. W. Numerical initial value problems in ordinary differential equations, Englewood Cliffs, N.J.: Prentice Hall.

Goldsmith, P. F., & Langer, W. D. 1978, ApJ, 222, 881

Grassi, T., Bovino, S., Schleicher, D. R. G., et al. 2014, MNRAS, 439, 2386

Gruendl, R. A., Chu, Y.-H., Dunne, B. C., & Points, S. D. 2000, AJ, 120, 2670

Haro, G. 1952, ApJ, 115, 572

Hartigan, P., Raymond, J. C., & Hartmann, L. W. 1987, ApJ, 316, 323

Hartigan, P., Frank, A., Foster, J. M., et al. 2011, ApJ, 736, 29

Heathcote, S. & Reipurth, B. 1992, AJ, 104, 2193

Henney, W. J. 1996, RMxAA, 32, 2

Herbig, G. H. 1951, ApJ, 113, 697

Herbig, G. H., & Jones, B. F. 1981, AJ, 86, 1232

Hester, J. J., Stapelfeldt, K. R., Scowen, P. A. 1998, AJ, 116, 372

Jaskot, A. E., Strickland, D. K., Oey, M. S., Chu, Y.-H., & García-Segura, G. 2011, ApJ, 729, 28

Leroy, A. K., Walter, F., Brinks, E., et al. 2008, AJ, 136, 2782

Masciadri, E., Velázquez, P. F., Raga, A. C., Cantó, J., & Noriega-Crespo, A. 2002, ApJ, 573, 260

May, R., & J. Noye. 1984. Computational techniques for differential equations, ed. J. Noye, 1-94. New York: North-Holland.

McElroy D., Walsh C., Markwick A. J., Cordiner M. A., Smith K., & Millar T. J., 2013, A&A, 550, A36

McKee C. F., Ostriker E. C., 2007, ARA&A, 45, 565

Moore, B. D., Hester, J. J., & Scowen, P. A. 2000, AJ, 119, 2991

Morgan, L. K., Moore, T. J. T., Allsopp, J., & Eden, D. J. 2013, MNRAS, 428, 1160

Motoyama K., Morata O., Shang H., Krasnopolsky R., Hasegawa T., 2015, ApJ, 808, 46

Müller H. S. P., Schlöder F., Stutzki J., & Winnewisser G., 2005, Journal of Molecular Structure, 742, 215

Navarro-González, R., McKay, C. P. & Nna Mvondo, D., 2001, Nature, 412, 5.

Neufeld, D. A., & Kaufman, M. J. 1993, ApJ, 418, 263

Noriega-Crespo, A., & Raga, A. C. 2012, ApJ, 750, 101

Oey, M. S. 1996a, ApJ, 467, 666

Oey, M. S. 1996b, ApJ, 465, 231

Ortolani, S., & D'Odorico, S. 1980, A&A, 83, L8

Pravdo, S. H., Rodríguez, L. F., Curiel, S., et al. 1985, ApJL, 293, L35

Pravdo, S. H., Feigelson, E. D., Garmire, G., et al. 2001, Nature, 413, 708

Raga, A. C., Barnes, P. J., & Mateo, M. 1990, AJ, 99, 1912

Raga, A. C., Binette, L. 1991, RMxAA, 22, 265

Raga, A. C., Mateo, M., Böhm, K. H., & Solf, J. 1988, AJ, 95, 1783

Raga, A. C. & Kofman, L. 1992, ApJ, 390, 359

Raga, A. C. & Noriega-Crespo, A. 1998, AJ, 116, 2943

Raga A. C., Velázquez P. F., Cantó J., Masciadri E., 2002, A&A, 395, 647

Raga A. C., Cantó J., Rodríguez L. F., 2012a, RevMexAA, 48, 199

Raga, A. C., Noriega-Crespo, A., Rodríguez-González, A., et al. 2012b, ApJ, 748, 103

Raga, A. C., Reipurth, B., Castellanos-Ramírez, A., Chiang, H.-F., & Bally, J. 2015a, ApJL, 798, L1

Raga, A. C., Castellanos-Ramírez, A., Esquivel, A., Rodríguez-González, A., & Velázquez, P. F. 2015b, RMxAA, 51, 231

Raga, A. C., Reipurth, B., Castellanos-Ramírez, A., Chiang, H.-F., & Bally, J. 2015c, AJ, 150, 105

Raga, A. C., Rodríguez-Ramírez, J. C., Cantó, J., Velázquez, P. F. 2015d, MNRAS, 454, 412

Raga, A. C., Reipurth, B., Esquivel, A., & Bally, J. 2016a, AJ, 151, 113

Raga, A. C., Reipurth, B., Velázquez, P. F., Esquivel, A., & Bally, J. 2016b, AJ, 152, 186

Raga, A. C., Reipurth, B., Esquivel, A., et al. 2017, RMxAA, 53, 485

Reipurth, B., & Bally, J. 2001, ARA&A, 39, 403

Reyes-Iturbide, J., Rosado, M., Rodríguez-González, A., Velázquez, P. F., Sánchez-Cruces, M. & Ambrocio-Cruz, P, 2014, ApJ, in press.

Rodríguez, L. F., Delgado-Arellano, V. G., Gómez, Y., et al. 2000, AJ, 119, 882

Rodríguez-González, A., Velázquez, P. F., Rosado, M., et al. 2011, ApJ, 733, 34

Rosado, M., Georgelin, Y. P., Georgelin, Y. M., Laval, A., & Monnet, G. 1981, A&A, 97, 342

Rosado, M., Georgelin, Y. M., Georgelin, Y. P., Laval, A., & Monnet, G. 1982, A&A, 115, 61

Rosado, M. 1986, A&A, 160, 211

Schwartz, R. D. 1978, ApJ, 223, 884

Schwartz, R. D. 1981, ApJ, 243, 197

Semenov, D., Hersant, F., Wakelam, V., et al. 2010, A&A, 522, A42

Silich, S. A., Tenorio-Tagle, G., Terlevich, R., Terlevich, E., & Netzer, H. 2001, MNRAS, 324, 191

Smith, B. D., Bryan, G. L., Glover, S. C. O., et al. 2017, MNRAS, 466, 2217

Steigman G., Strittmatter P. A., Williams R. E., 1975, ApJ, 198, 575

Toalá, J. A., Guerrero, M. A., Chu, Y.-H., & Gruendl, R. A. 2015, MNRAS, 446, 1083

Toalá, J. A., Guerrero, M. A., Chu, Y.-H., et al. 2016, MNRAS, 456, 4305

Wang, Q. D., & Helfand, D. 1991, ApJ, 379, 327

Weaver, R., McCray, R., Castor, J., Shapiro, P., & Moore, R. 1977, ApJ, 218, 377

Ziegler, U. 2016 A&A 586, A82